

# Developments towards the Technical Design and Prototype Evaluation of the PANDA Endcap Disc DIRC

Inaugural-Dissertation

zur Erlangung des Doktorgrades der Naturwissenschaften

der Justus-Liebig-Universität Gießen im Fachbereich 07

(Mathematik und Informatik, Physik, Geographie)

vorgelegt von

**Erik Etzelmüller**

II. Physikalisches Institut

AG Düren

April 2017



## Abstract

The envisaged physics program of the  $\bar{P}$ ANDA (antiProton ANnihilation at Darmstadt) experiment at the future Facility for Antiproton and Ion Research (FAIR) requires excellent particle identification over the full solid angle. The Endcap Disc DIRC (EDD) will cover forward polar angles between  $5$  and  $22^\circ$  and is one of three dedicated subdetectors for the identification of charged hadrons and the separation of pions and kaons in particular. DIRC stands for Detection of Internally Reflected Cherenkov light and implies that the emitted Cherenkov photons are trapped inside the radiator by total internal reflection.

The central part of each DIRC detector is its optical system which is responsible for a low-loss and angle-preserving transport of the Cherenkov photons. The work at hand experimentally addresses several objectives in connection with the optical components and the system as a whole. Radiator prototypes were evaluated with high precision and adapted specifications were identified based on the results. The imaging performance of the Focusing Elements (FELs) was verified and different options regarding the coupling of the individual components were evaluated. In addition a radiation hardness study of a new fused silica material provided an insight into the long term behavior of induced defects and confirmed the material to be suitable for high energy physics experiments.

A conceptual design for the mechanical integration was developed featuring a rigid optical system which is mounted into a cross-like structure. In this context the spatial constraints for the holding structure and the FELs were identified and an assembly procedure was developed. The existing prototype was revised and newly developed concepts were integrated and tested.

Furthermore a data analysis of an earlier prototype test at a mixed hadron beam at CERN was carried out. It was the first evaluation of an EDD prototype which consisted of optical components made of fused silica only and had highly segmented MCP-PMTs (Micro-Channel Plate PhotoMultiplier Tubes) for the photon detection. A single photon resolution down to  $5.68$  mrad could be achieved and a good agreement with Monte-Carlo predictions was reached. At  $3$  GeV/c a  $5\sigma$  separation of pions and protons was accomplished using a single MCP-PMT column.



## Zusammenfassung

Das  $\bar{P}$ ANDA -Experiment (*AntiProton Annihilation at Darmstadt*) ist eines der Großprojekte der Forschungsanlage FAIR (*Facility for Antiproton and Ion Research*), die zur Zeit in Darmstadt gebaut wird. Für das angestrebte Forschungsprogramm des Experiments müssen unter anderem Teilchen über nahezu den kompletten Raumwinkel identifiziert werden können. Eine besondere Herausforderung ist dabei die Unterscheidung von Pionen und Kaonen, für welchen Zweck drei Cherenkov-Detektoren im  $\bar{P}$ ANDA -Experiment verbaut werden. Der Vorwärtsbereich zwischen  $5$  und  $22^\circ$  wird hierbei vom *Endcap Disc DIRC* (EDD) abgedeckt. DIRC (*Detection of Internally Reflected Cherenkov light*) steht für die Detektion von intern-reflektierten Cherenkov-Photonen. In diesem Zusammenhang spielt das optische System eine zentrale Rolle, da es für einen verlustarmen und winkelerhaltenden Transport der Cherenkov-Photonen durch Totalreflexion verantwortlich ist.

Die vorliegende Arbeit behandelt verschiedene offene Fragestellungen im Zusammenhang mit den optischen Komponenten und dem System als Ganzes. Hierzu wurden unter anderem Prototype-Radiatoren bezüglich ihres Profils vermessen, wodurch eine Anpassung der Spezifikationen erfolgen konnte. Das Auflösungsvermögen der fokussierenden Lichtleiter (FELs, *Focusing Elements*) konnte experimentell verifiziert werden und es wurden verschiedene Kopplungsoptionen miteinander verglichen. Des Weiteren konnte eine Langzeitstudie zur Strahlenhärte eines bisher nicht untersuchten synthetischen Quarzglas durchgeführt werden.

Einen weiteren Schwerpunkt der Arbeit stellte eine Konzeption zur mechanischen Integration des EDDs dar. Kern dieses Konzeptes ist ein fest zusammenhängendes optisches System, welches mit Hilfe einer über den Detektor gespannten kreuzartigen Halterung befestigt wird. In diesem Zusammenhang wurden außerdem die geometrischen Randbedingungen festgelegt sowie eine Vorgehensweise in Bezug auf die Montage des Detektors erarbeitet. Basierend auf diesen Entwicklungen wurde der bisherige Prototyp nahezu vollständig überarbeitet.

Neben den technischen Entwicklungen wurde eine Datenanalyse zu einem Teststrahl experiment mit einem gemischten Hadronenstrahl am CERN durchgeführt. Der dort verwendete und mittlerweile überarbeitete Prototyp bestand erstmals ausschließlich aus synthetischem Quarzglas gefertigten optischen Komponenten und die Cherenkov-Photonen wurden mit hochauflösenden MCP-PMTs (*Micro-Channel Plate PhotoMultiplier Tubes*) detektiert. Hierbei wurde eine Einzelphotonenauflösung (*single photon resolution*) von  $5.68$  mrad erreicht. Die Messungen hierzu waren in guter Übereinstimmung mit den Vorhersagen durch Monte-Carlo-Simulationen. Bei einem Teilchenimpuls von  $3$  GeV/c konnte außerdem eine Unterscheidung von mehr als fünf Standardabweichungen zwischen Pionen und Protonen mit einer einzelnen MCP-PMT-Spalte erreicht werden.



## Table of Contents

<b>1</b>	<b>Introduction</b>	<b>1</b>
<b>2</b>	<b>The <math>\bar{P}</math>ANDA Experiment</b>	<b>5</b>
2.1	$\bar{P}$ ANDA at FAIR . . . . .	5
2.2	The $\bar{P}$ ANDA Detector . . . . .	6
2.3	Physics Program . . . . .	13
<b>3</b>	<b>Particle Identification</b>	<b>17</b>
3.1	Techniques . . . . .	17
3.1.1	Topology . . . . .	17
3.1.2	Energy Measurement . . . . .	18
3.1.3	Time-of-Flight . . . . .	18
3.1.4	Cherenkov Radiation . . . . .	19
3.1.5	Transition Radiation . . . . .	22
3.2	Cherenkov detectors . . . . .	22
3.2.1	Threshold Cherenkov Detectors . . . . .	22
3.2.2	RICH Detectors . . . . .	23
3.2.3	DIRC Detectors . . . . .	24
3.3	The $\bar{P}$ ANDA Endcap Disc DIRC . . . . .	26
3.3.1	Evolution of the Design . . . . .	26
3.3.2	Final Design . . . . .	28
3.3.3	Working Principle . . . . .	30
<b>4</b>	<b>Optical system</b>	<b>31</b>
4.1	Introduction . . . . .	31
4.1.1	The Optical System . . . . .	31
4.1.2	Material . . . . .	32
4.2	Radiation Hardness . . . . .	33
4.2.1	Previous Results . . . . .	33
4.2.2	Radiation Hardness of NIFS . . . . .	34
4.3	Radiator . . . . .	45
4.3.1	Requirements . . . . .	45
4.3.2	Quality Measurements . . . . .	48
4.4	Focusing Elements and Prisms . . . . .	72
4.4.1	Requirements . . . . .	72
4.4.2	Quality Measurements . . . . .	76
4.5	Optical Filter . . . . .	91
4.6	Optical Joints . . . . .	95

---

4.7	Summary . . . . .	98
<b>5</b>	<b>Mechanics</b>	<b>101</b>
5.1	Requirements . . . . .	101
5.2	Concepts and Design . . . . .	102
5.2.1	Components . . . . .	103
5.2.2	Gas System and Cabling . . . . .	106
5.3	Assembly . . . . .	108
5.4	Optomechanical System . . . . .	113
5.5	Prototype Development . . . . .	117
<b>6</b>	<b>Testbeam Analysis</b>	<b>123</b>
6.1	Introduction . . . . .	123
6.2	Setup . . . . .	123
6.2.1	Components . . . . .	123
6.2.2	Installation . . . . .	127
6.3	Calibration and Data Quality . . . . .	128
6.3.1	Laser Calibration . . . . .	128
6.3.2	Additional Offline Calibration . . . . .	132
6.4	Analysis . . . . .	138
6.4.1	Photon Yield . . . . .	138
6.4.2	Momentum and Transversal Scan . . . . .	140
6.4.3	Angle Scans . . . . .	142
6.5	Interpretation and Summary . . . . .	154
<b>7</b>	<b>Summary and Outlook</b>	<b>155</b>
<b>A</b>	<b>Appendix</b>	<b>159</b>
	List of Acronyms	165
	List of Figures	169
	List of Tables	173
	Bibliography	175

# 1 Introduction

On the hunt for new discoveries inside or outside the standard model state-of-the-art detector designs push forward the frontier of what is technically achievable to improve our understanding of the universe. Modern experiments utilizing high-energy beams consist of a diversity of subdetectors to perform different tasks such as tracking the position of a subatomic particle or measuring its energy. Many detectors require dedicated devices to identify particles types; e.g., because the resolution of the energy measurement is not sufficient to distinguish between particle types at certain momenta.

The  $\bar{\text{P}}\text{ANDA}$  experiment (antiProton ANnihilation at DArmstadt) [PAN09] at the future Facility for Antiproton and Ion Research (FAIR) [Bar07] will be a versatile detector exploring different horizons from hadron spectroscopy with a search for exotic particles and nucleon structure measurements to studying in-medium effects of hadronic particles or hypernuclei. It will provide precise tracking, energy and momentum measurements and very efficient identification of charged particles.

The latter is important as many of the detected decay products of interest are charged kaons which, without dedicated detectors for PID (Particle IDentification), cannot be properly identified and distinguished from pions at energies inside the  $\bar{\text{P}}\text{ANDA}$  detector. For this purpose three RICH (Ring-Imaging CHerenkov) detectors will be used, one conventional RICH detector with an aerogel radiator in the very forward region of the experiment, and two so-called DIRC (Detection of Internally Reflected Cherenkov light) detectors to cover polar angles between  $5^\circ$  and  $140^\circ$ . Characteristic for DIRCs are radiators which also serve as light guides enabling to build very compact detectors which allows to reduce the active area of subsequent detectors [Coy94, Kam96]. Besides a Barrel DIRC [Swa16] which covers a range between  $22^\circ$  and  $140^\circ$  the forward endcap of the  $\bar{\text{P}}\text{ANDA}$  Target Spectrometer will be equipped with an Endcap Disc DIRC (EDD) which enables PID for charged particles down to  $5^\circ$ . This is important as  $\bar{\text{P}}\text{ANDA}$  is a fixed-target experiment where a majority of particles will be detected in the forward region (see figure 1.1).

The EDD is a new type of DIRC using highly-segmented MCP-PMTs, focusing optics and a non-rectangular radiator. Since early studies in 2006 different concepts have been evaluated and tested until a working detector design has emerged which matches the requirements for  $\bar{\text{P}}\text{ANDA}$  [Mer14b]. Henceforward the work has focused on the verification of the working principle and the applicability of the envisaged components including dedicated setups for quality assurance measurements, mechanical integration and development of a readout system.

The thesis in hand addresses open questions regarding the optical system and its integration along with other parts into the  $\bar{\text{P}}\text{ANDA}$  experiment. Following this brief introduction chapter 2 will describe FAIR and the  $\bar{\text{P}}\text{ANDA}$  experiment in more detail focusing on both the physics program and the detector design. Chapter 3 will give an overview of how par-

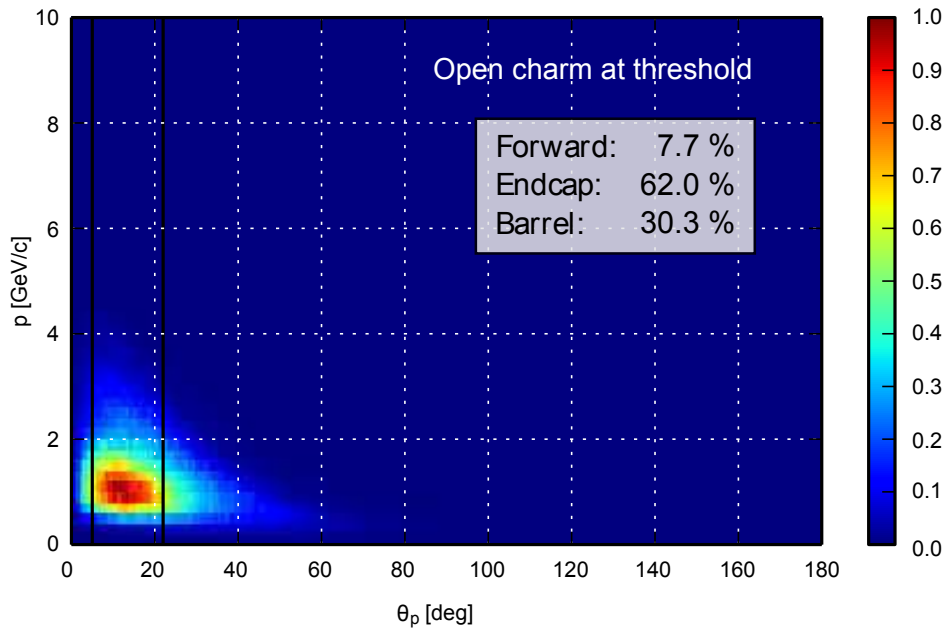


**Figure 1.1:** Combined kaon phase space distribution of the reactions  $\bar{p}p \rightarrow D^+D^-$ ,  $\bar{p}p \rightarrow D_s^+D_s^-$  and  $\bar{p}p \rightarrow h_c \rightarrow \eta_c\gamma$  at the individual production threshold as shown in [Mer14b]. The channels have not been weighted by their individual cross sections and contain all decay branches. The angular acceptance region of the Endcap Disc DIRC is indicated by two vertical black lines.

ticle identification is done in accelerator experiments. Here the focus will be on Cherenkov detectors and the  $\bar{P}$ ANDA Endcap Disc DIRC, its working principle and design in particular.

Chapter 4 deals with the optical system of the detector. After a short introduction the radiation hardness of the optical system will be addressed and in this connection a radiation hardness study of different grades of Nikon Fused Silica (NIFS) is presented. In section 4.3 different methods for the verification of the proposed specifications are introduced and a detailed study of the surface profiles of available radiators is performed. The subsequent section 4.4 contains an evaluation of the Focusing Elements (FELs) and prisms. The rest of the chapter is devoted to filter options which can limit the number of photons as well as the chromatic error and optical joints which connect the different components of the optical system.

In chapter 5 a conceptual design for the detector integration is presented along with an assembly procedure. Here the focus is set on the integration of the optical system. Besides calculations regarding the stability a new prototype is described in detail which applies several concepts for the final detector.

A detailed analysis of an earlier prototype which was tested during beamtime in May 2015 is presented in chapter 6. This was the first testbeam which contained an optical system exclusively made of fused silica components and MCP-PMTs with highly segmented anodes.

Hence it was used to verify single photon resolutions that were obtained by Monte-Carlo simulations.

Finally chapter 7 summarizes the results and provides an outlook on future actions in connection with building an Endcap Disc DIRC for the  $\bar{P}$ ANDA experiment.



## 2 The $\bar{\text{P}}\text{ANDA}$ Experiment

### 2.1 $\bar{\text{P}}\text{ANDA}$ at FAIR

The Facility for Antiproton and Ion Research (FAIR) is a large extension to the already existing Gesellschaft für Schwerionenforschung (GSI) at Darmstadt, Germany. It will push forward the knowledge in different fields of physics searching for unknown states of matter and missing information about the early universe. More than 3000 scientists from over 50 countries will benefit from this multipurpose acceleration facility which is based on four scientific pillars:

- APPA (Atomic, Plasma Physics and Applications) focuses on plasma physics with different experimental setups [Sto15],
- CBM (the Compressed Baryonic Matter experiment) will create high baryon densities in nucleus-nucleus collisions to explore the properties of super-dense nuclear matter [Fri11],
- NuSTAR (Nuclear STructure, Astrophysics and Reactions) where different experiments will investigate secondary beams of rare isotopes [NuS12], and
- $\bar{\text{P}}\text{ANDA}$  (antiProton ANnihilation at DArmstadt) which will use antiproton-proton collisions to improve our understanding of the creation of mass [PAN09].

Already existing accelerators like the UNILAC linear accelerator or the SIS-18 synchrotron are used as pre-accelerators. Together with a new p-LINAC they feed protons or heavy ions into a new large synchrotron SIS-100, where 100 stands for a magnetic rigidity of 100 Tm, with a circumference of 1100 m. In a later stage a SIS-300 will be added which increases the beam energies from 1 GeV/u to 35 – 45 GeV/u depending on the ion mass/charge ratio. A combination of both rings can be used to provide proton or ion beams in parallel for more than one experiment at the same time [Bar07]. Figure 2.1 shows an overview of the FAIR complex which besides the aforementioned accelerators provides additional rings to accumulate and store different particles as well as different targets to produce antiprotons or rare isotopes. To supply the  $\bar{\text{P}}\text{ANDA}$  experiment high energy protons are guided onto a copper production target for antiprotons [Sie12] and are subsequently accumulated in a Collector Ring (CR) where they are cooled and focused by stochastic cooling. Afterwards they are accumulated in the Recycled Experimental Storage Ring (RESR) and later stored in the High Energy Storage Ring (HESR) where the  $\bar{\text{P}}\text{ANDA}$  experiment is located. In the first building stage the antiprotons in the CR are directly injected into the HESR where they are accumulated and stored. In this so-called modularized start version neither SIS-300 nor RESR is available which reduces the achievable luminosity [FAIR09].

Inside the HESR the antiprotons have momenta between 1.5 and 15 GeV/c. A combination

**Figure 2.1:** Schematic view of existing the GSI complex with existing accelerators (blue) and the new FAIR accelerators (red) [[FAIRweb](#)].

of stochastic and electron cooling is used to achieve a high beam quality. HESR provides two modes of operation: a High Resolution (HR) mode and a High Luminosity (HL) mode. The former can store up to  $10^{10}$  antiprotons and reach a luminosity of  $2 \cdot 10^{31} \text{ cm}^{-2}\text{s}^{-1}$  with a resolution  $\Delta p/p$  of up to  $4 \cdot 10^{-5}$ . This mode allows to perform high precision resonance scans in search for new states. The HL mode requires the RESR and stores ten times more protons which leads to a luminosity of  $2 \cdot 10^{32} \text{ cm}^{-2}\text{s}^{-1}$  with a resolution  $\Delta p/p$  of  $10^{-4}$  [[Mai11](#), [Lhr06](#)].

## 2.2 The $\bar{\text{P}}\text{ANDA}$ Detector

$\bar{\text{P}}\text{ANDA}$  is a fixed-target experiment consisting of two separate parts: The Target Spectrometer (TS) with an almost  $4\pi$  coverage around the target region and the Forward Spectrometer (FS) which covers very forward polar angles between below  $10^\circ$  horizontally and  $5^\circ$  vertically with respect to the beam direction (see figure 2.2). This setup allows to detect final state particles over the full solid angle which includes measuring their momenta and identifying the particle types of the reaction products. The following section gives a brief overview of the different subdetectors used inside the  $\bar{\text{P}}\text{ANDA}$  experiment.

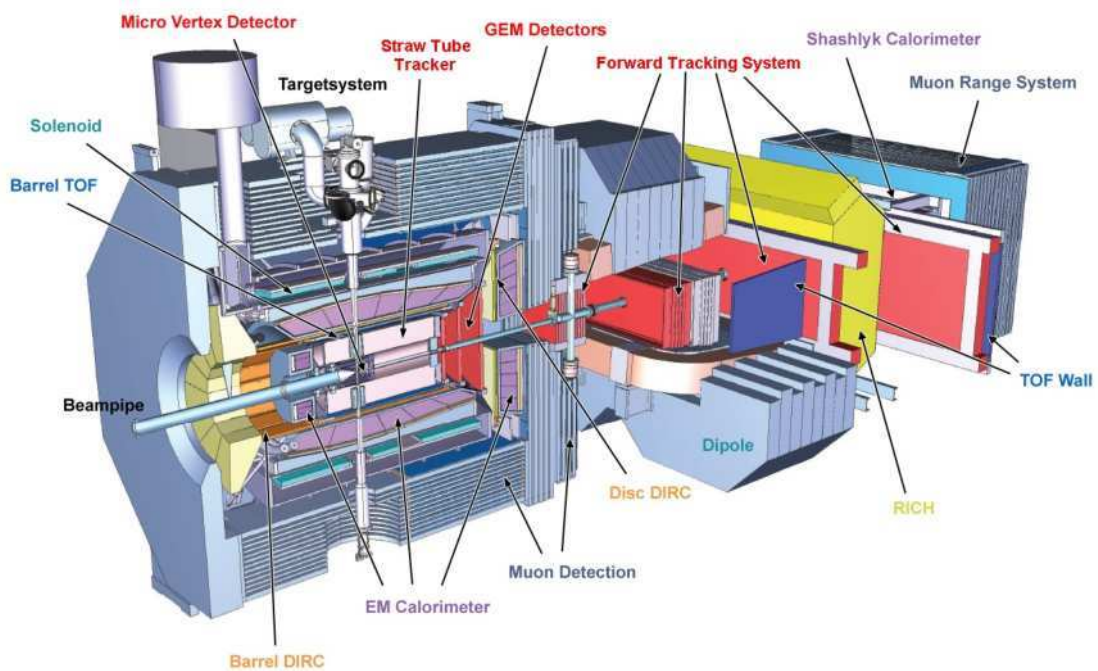


**Figure 2.2:** Cross section view of the  $\bar{P}$ ANDA detector. The antiproton beam enters from the left and interacts inside the Target Spectrometer (TS). The very forward angles are covered by the Forward Spectrometer (FS) which starts with the large dipole magnet.

## Target System

The antiproton in the beam will either interact with a pellet or cluster jet target. Both systems have to provide a very dilute and localized clump of matter without deteriorating the beam vacuum or the beam itself. In case of the pellet target a regular stream of frozen hydrogen pellets vertically traverses the beam. The pellets are produced in a triple point chamber which ensures a very regular production of droplets which are injected into the vacuum. As the pellets are produced outside of the target region on top of the detector the droplets cool down further due to surface evaporation while falling towards the interaction point. This method on one hand provides the highest target densities and a point-like interaction zone but on the other hand it has no clear time structure and is less homogeneous [TarTDR].

The cluster jet target expands compressed, pre-cooled gas through a fine nozzle. During this process the gas adiabatically cools down and forms a supersonic stream of atoms or molecules which, under appropriate conditions, form a so-called cluster. The size of these clusters is strongly influenced by the experimental conditions such as the pressure or the temperature of the gas before entering the nozzle. A constant opening of the cluster jet is provided by a skimmer and collimator in front of the vacuum. In comparison to the pellet target this option provides a homogeneous target density and time structure but no point-

like interaction zone [TarTDR].

### Tracking Detectors

The tracking of charged particles is done by several subdetectors starting with a Micro Vertex Detector (MVD) just outside the target region (see left part of figure 2.3). This device is designed to reconstruct primary interaction and secondary vertices from weak decaying particles like the  $D^0$  and achieves vertex resolutions better than  $100\ \mu\text{m}$  in longitudinal direction and several tens of  $\mu\text{m}$  in lateral direction. The detector is split into a barrel and a forward region and consists of two different layer types. The inner part is equipped with layers made of silicone hybrid pixel detectors whereas the outer part is made of double-sided silicone micro-strip detectors. A low material budget and a high radiation tolerance are the main challenges in the construction of this detector [MVDTDR].

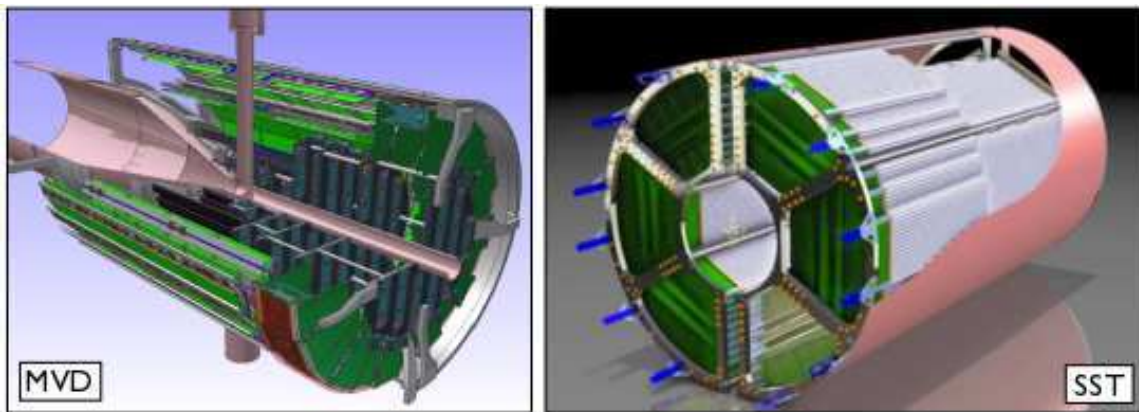


**Figure 2.3:** CAD pictures of the Micro Vertex Detector (MVD, left) [MVDTDR] and the Straw Tube Tracker (STT, right) [TrkTDR].

Right after the MVD two additional tracking detectors, a Straw Tube Tracker (STT) and a Gas Electron Multiplier (GEM) detector, provide precise tracking of charged particles. They enable the reconstruction of decay vertices of long-lived hadrons with charm and strange quark content like  $\Lambda$ -Baryons or  $K_s$  and improve the tracking inside the magnetic field to measure the momentum. The STT consists of 4636 1.5 m long single straw tubes which are arranged in several layers around the beam for full azimuthal acceptance (see right part of figure 2.3). Each tube is filled with gas and has a diameter of 10 mm. If a charged particle traverses a tube the gas is ionized and the electrons are drifting towards a thin anode wire at its center which leads to additional ionization and a measurable signal. To achieve the position resolution a precise measurement of the drift time is essential. The ions are collected by the cleading which is a conductive aluminum layer and isolated by a thin layer

of BoPET (Biaxially-oriented polyethylene terephthalate). In addition the specific energy loss of a charged particle ( $dE/dx$ ) can be measured and contributes to the identification of particles [TrkTDR]. The forward region is completed by the GEM detector consisting of three consecutive GEM discs to cover angles between  $5$  and  $22^\circ$  (see figure 2.4). Each Disc is filled with gas and consists of a two-sided readout pad which is enclosed by three GEM electrodes, a cathode foil and an entry window on each side. The electrodes are thin polymer foils, metal-coated on both sides and pierced with holes as shown in the right part of figure 2.4. When a charged particle ionizes the gas molecules electrons are accelerated by the field inside the holes and detected by the readout pad [Sau16].

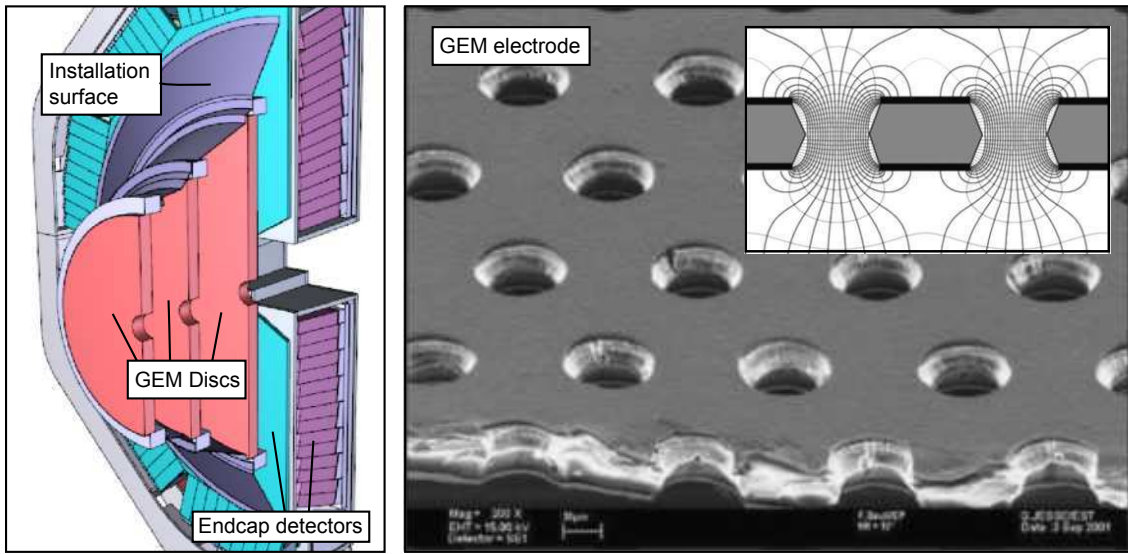


**Figure 2.4:** The Gas Electron Multiplier (GEM) in front of the  $\bar{P}$ ANDA endcap consists of three GEM discs (left). The right part shows an electron microscope picture of a section of a typical GEM electrode which is  $50\ \mu\text{m}$ . The holes pitch and diameter are  $140$  and  $70\ \mu\text{m}$ , respectively. The small picture in the top right corner shows the electric field in the region of the holes [Sau16].

In the FS the tracking is realized by six straw tube detectors similar to the STT consisting of four double layers of straw tubes each. The position resolution is reached by two layers of vertical wires and two layers of inclined wires. To properly measure the bending inside the dipole magnet two independent stations are placed in front of the magnet, one additional inside and three more behind it [TrkTDR].

## Magnets

In order to reconstruct the momentum of charged particles a strong magnetic field is essential. Inside the TS of  $\bar{P}$ ANDA a superconducting solenoid magnet will provide a homogeneous magnetic field with a homogeneity of better than 2% and a field strength of up to 2 T

over a length of 4 m. Its inner bore of 1.9 m provides space for several subdetectors. The superconductivity of the solenoid magnet is realized by a cryostat which also serves as a mechanical mount for other detectors in the TS. The return flux yoke incorporates Mini-Drift-Tubes (MDTs) and acts as an absorber for the muon detection system [MagTDR]. In the forward region a dipole magnet with a bending power of 2 Tm will enable momentum reconstruction with a resolution of better than 1% [MagTDR]. Figure 2.5 shows the magnets with a small section of the magnetic field inside the TS.

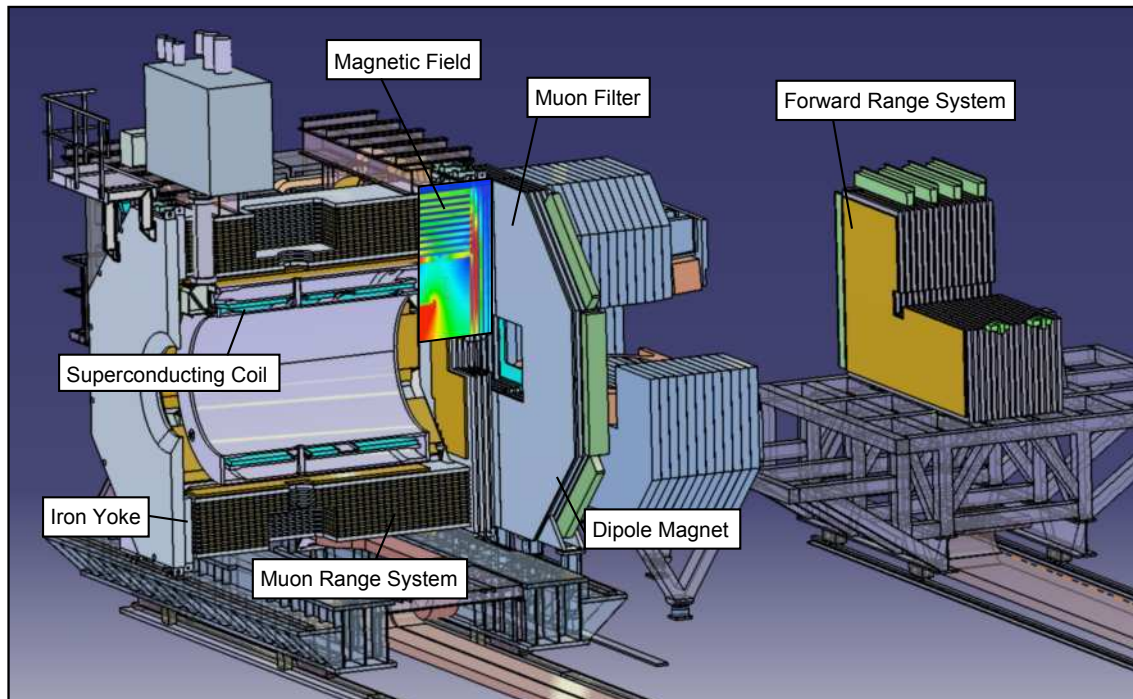


**Figure 2.5:** The solenoid and dipole magnet of  $\bar{P}$ ANDA along with the Muon detection system. A small cut-out of the magnetic field inside the TS is shown (red corresponds to the full field strength of 2 T).

### Particle Identification

Several subdetectors inside the  $\bar{P}$ ANDA experiment provide Particle IDentification (PID) for charged particles. Besides these dedicated systems other subdetectors contribute to the PID by measuring  $dE/dx$  in the tracking detectors or adding information from the calorimeters to the event topology (see also sections 3.1.1 and 3.1.2). A crucial aspect for the PID performance inside  $\bar{P}$ ANDA is the  $\pi/K$  separation. For low momentum particles a Time Of Flight (TOF) system is used. Inside the TS a Scintillating Tile (SciTil) Hodoscope based on several thousand small plastic scintillator tiles between the Barrel DIRC and the Barrel EMC provides excellent timing resolution below 100 ps which can also serve as a time reference for the Barrel DIRC to reduce background by deconvoluting the tracks of

traversing particles. The readout of the tiles is done by SiPMs [Gru16]. In the FS a TOF wall, consisting of 66 140 cm long plastic scintillators made of Bicron 406 will be placed in front of the Forward Spectrometer Calorimeter (FSC, also called Sashlyk Calorimeter). The tiles will be arranged vertically and are read out with light guides and a PhotoMultiplier Tubes (PMTs) at both ends [Bls15]. For higher momenta three Ring Imaging Cherenkov (RICH) detectors are used (see also section 3.2.2 for further details). They exploit the correlation of the opening angle of the Cherenkov cone and the speed of the particle given by equation 3.5 and use this information together with the measured momentum to determine the mass of the traversing particle. Inside the TS two DIRC (Detection of Internally Reflected Cherenkov light) detectors are placed. The central region between  $22^\circ$  and  $140^\circ$  is covered by the Barrel DIRC which consists either of 80 bars or, if the anticipated resolution can be achieved, 16 wider plates made of fused silica [BarTDR]. These radiators have precision polished surfaces to conserve the angle information of the Cherenkov photons and also serve as a light guide. At the backend of the TS the bars or plates are coupled to large expansion volumes where the photons are detected by MCP-PMTs [Swa16]. The forward region of the TS is equipped with the Endcap Disc DIRC (EDD) to cover polar angles between  $5^\circ$  and  $22^\circ$ . In comparison to the Barrel DIRC the EDD consists of four large radiator discs which together form a regular dodecagon with a cut-out for the beam pipe and the FS acceptance at its center. Focusing Elements (FELs) at the outside of the radiator discs internally focus parallel entering photons on MCP-PMTs with a highly segmented anode to determine the angle information. As this thesis is dedicated towards the development of the EDD a detailed description can be found in section 3.3. To handle the high particle energies in forward direction a conventional RICH detector is used. The Cherenkov photons will be produced inside a non-homogeneous focusing aerogel radiator. After leaving the aerogel radiator the photons are reflected off a flat mirror onto a MaPMT array [Blb15]. To ensure an efficient detection of muons inside  $\bar{\text{P}}\text{ANDA}$  a Muon Range System is installed. Similar to other detector parts it consists of a barrel, endcap and forward part. For the barrel region 13 3 cm (6 cm for the first and last layer) thick layers with an active double layer in front of the first iron plate are installed. Due to higher momenta in the forward region the endcap and forward part consist of 5 and 16 6 cm thick layers. The forward range system uses slightly different MDTs and is optimized for particles up to 10 GeV/c. In addition its resolution is good enough to be used as a hadronic calorimeter as well. Figure 2.5 shows the positions of the individual systems in the framework of the  $\bar{\text{P}}\text{ANDA}$  detector [MuonTDR].

## Calorimeters

Two different types of calorimeters are used for precise energy measurement of electromagnetically interacting particles and high energy photons. Furthermore they deliver efficient

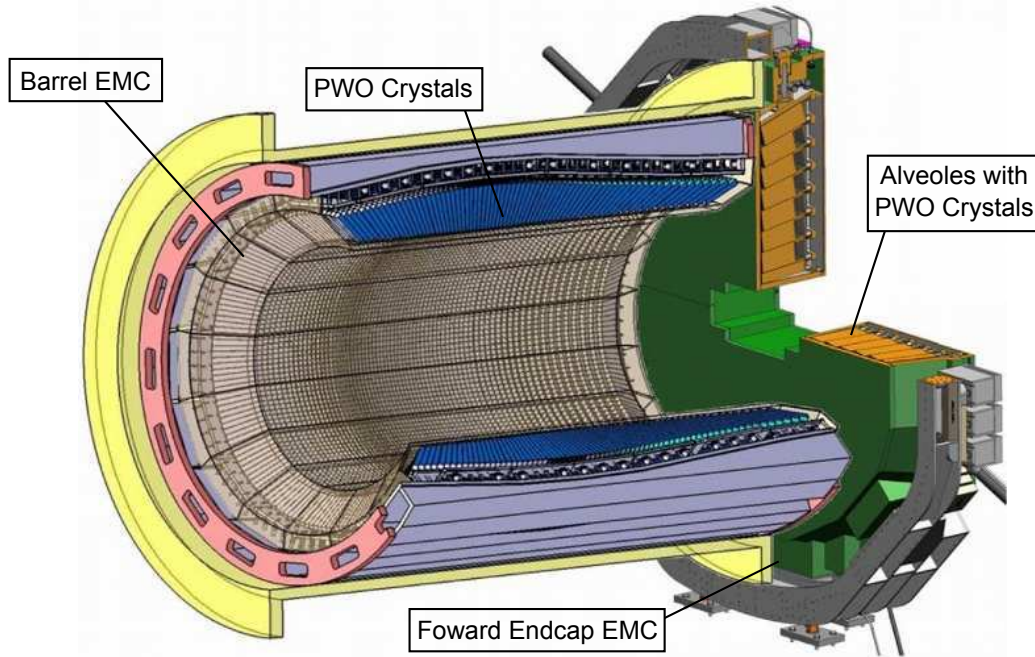


**Figure 2.6:** A CAD drawing taken from [Alb15] of the Barrel and Forward Endcap EMC. In case of the Barrel EMC 11 different geometries are used for the PWO crystals to provide a homogeneous distribution of crystals facing the interaction point of the experiment.

position information for photons. The TS is equipped with an electromagnetic calorimeter split into a backward, barrel and forward part for an almost  $4\pi$  coverage. Forward and barrel part are positioned right behind the DIRC detectors. In total 15552 lead tungstate ( $\text{PbWO}_4$ , also called PWO) crystals with different geometries are tightly arranged around the interaction point (see figure 2.6). PWO has become a favored scintillator material due to its short radiation length  $X_0$  of 0.98 cm and small Molière radius of 2 cm which allow a compact detector design. A reduced operation temperature, which is  $-25^\circ\text{C}$  for the PANDA EMCs, and recent progress towards an improved growing process of the crystals provide a higher light yield. The crystals are wrapped with a reflective foil and grouped in carbon fiber alveoles. The photons produced in the PWO are detected by Large Area Avalanche Photo Diodes (LAAPDs) and Vacuum Photo TeTodes (VPTTs). Both sensors can be operated inside a magnetic field and can cope with high radiation and low temperatures. The VPTTs have a faster response and read out the innermost parts of the Forward Endcap EMC with a low polar angle. The envisaged energy resolution  $\sigma_E/E$  is better or equal to  $1\% \oplus \frac{\leq 2\%}{\sqrt{E/\text{GeV}}}$  [EMCTDR].

The forward region is completed by the Forward Spectrometer Calorimeter (FSC). It is a shashlik-type sampling calorimeter which is made of 300 alternating layers of lead and active detector material. The latter one is a scintillator which is readout by wavelength shifting fibers which are coupled to photomultipliers. In total 378 of such modules with four

individual cells with a lateral area of  $55 \times 55 \text{ cm}^2$  and a depth of 1033 mm are installed. The performance goals are to reach a position resolution of 3.5 mm and an energy resolution of  $1\% \oplus \frac{\leq 2-3\%}{\sqrt{E/\text{GeV}}}$  [FSCTDR].

### Luminosity Detector

In order to be able to precisely determine cross sections  $\bar{\text{P}}\text{ANDA}$  is equipped with a dedicated luminosity monitoring system. It is positioned about 11 m downstream of the interaction point behind the Forward Range Muon System. The principle of the detector is to reconstruct tracks of scattered particles between polar angles of 3 and 5 mrad and fit them to simulations of the angular particle distribution to derive the time integrated luminosity. The measurement is achieved by four planes with a radius of 15 cm which are placed around the beam pipe and contain 400 pixels of High Voltage Monolithic Active Pixel Sensors (HV-MAPS) [LumTDR].

### Data Acquisition

In contrast to most accelerator experiments  $\bar{\text{P}}\text{ANDA}$  is not using a physics trigger for the event selection as the topology of some physics channels of interest cannot be distinguished from background events. This trigger-less operation leads to several 100 GBytes/s which have to be reconstructed and filtered online. The so-called SODA (Synchronization Of Data Acquisition) system is an optical network which provides a common reference time better than 20 ps RMS to fulfill this task. It is also able to synchronize the events which come from different subdetectors as some readout systems are slower than the anticipated event rate of 20 MHz in the HL mode [Kon10, Wag16].

## 2.3 Physics Program

Unlike Quantum Electrodynamics (QED), which allow a precise description of electrodynamic processes via the exchange of photons, in theory of Quantum Chromodynamics (QCD), which uses gluons with three types of color charge to describe the strong interaction, perturbative calculations work correctly only at high energies. Here the coupling constant  $\alpha_s$  becomes small and perturbation theories can be applied analogous to QED. However, at low energies QCD results deviate from experimental observations why different approaches like Lattice-QCD, where the problem is reduced to solving path integrals on a limited and discrete set of space-points (the lattice), are needed. The  $\bar{\text{P}}\text{ANDA}$  detector in combination with the HESR offers unique opportunities to explore and measure a variety of phenomena in connection with hadron physics to shed new light on non-perturbative QCD

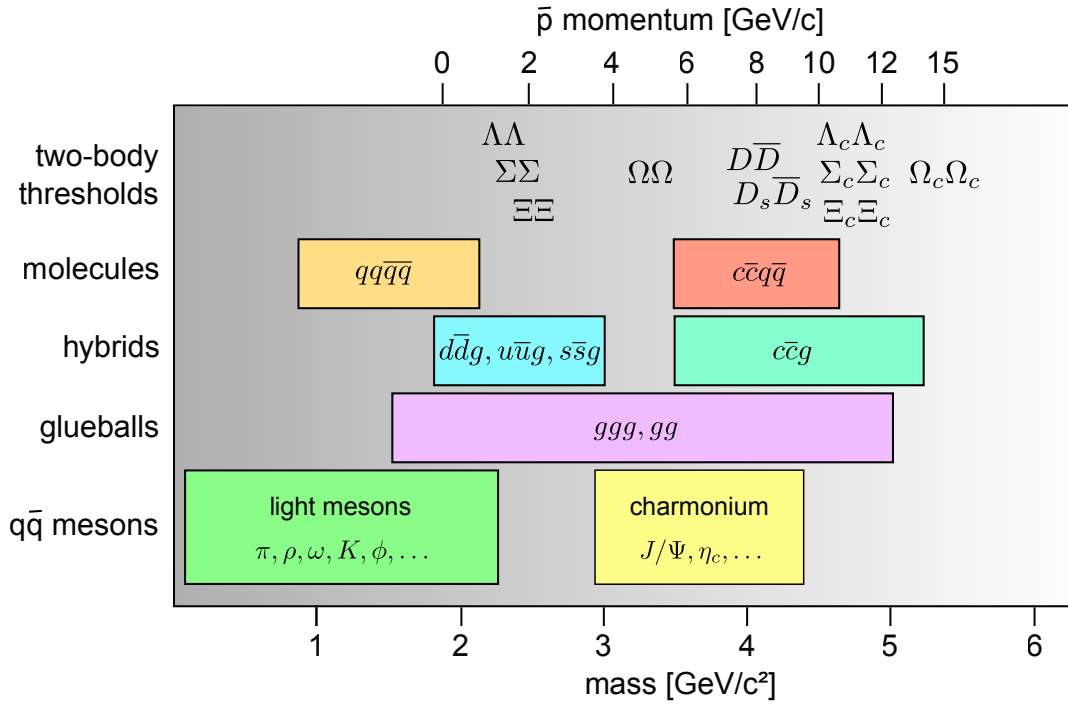


**Figure 2.7:** Overview of gluonic and ordinary hadrons which have either been discovered or are predicted by the standard model and which can be accessed with  $\bar{P}$ ANDA (based on plot in [Lhm09]).

but also enables to study the nucleon structure, hadrons in matter as well as hypernuclei. This section gives a non-exhaustive introduction to the anticipated physics program.

In contrast to  $e^+e^-$  colliders where only states equal to  $J^{PC} = 1^{--}$  can be directly produced a  $\bar{p}p$  experiment applies less restrictions on these quantum numbers. One of the advantages of  $\bar{P}$ ANDA is that these states can be precisely measured by performing a resonance scan. In this case the resolution of the measurement is only limited by the momentum spread of the antiproton beam inside the HESR.  $\bar{P}$ ANDA is able to run at energies above the open charm threshold ( $\bar{D}D$ ) and achieves center-of-mass energies of  $\sqrt{s} = 5.47 \text{ GeV}$  which allows to perform a sophisticated spectroscopy of charmonium states by collecting several thousand  $\bar{c}c$  events per day at full luminosity. An interesting candidate in this connection is the X(3872) resonance which does not fit into a simple quark model [Kal10] but was first discovered by the Belle collaboration [Cho03]. Due to its narrow peak  $\bar{P}$ ANDA allows a precise measurement of this state's width.

Another field of research will be D meson spectroscopy which has attracted much interest since discoveries of new open charm mesons at BaBar, Belle, and CLEO have shown that these new states are not well described by the present quark model predictions. Again the precision of the  $\bar{P}$ ANDA experiment will enable a precise measurement of the decay widths of these states. Besides mesons  $\bar{P}$ ANDA is well suited for a comprehensive study of baryons in the strange but also the charm sector where, due to the lack of precision measurements, a high discovery potential can be expected.

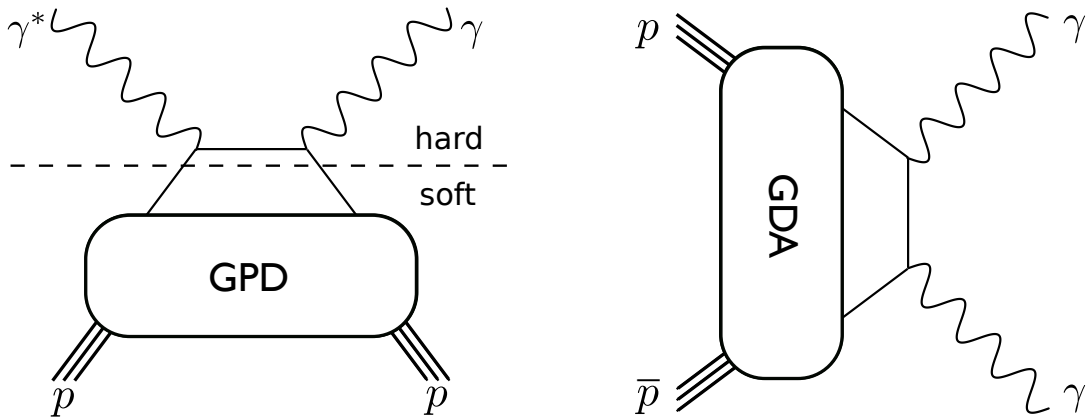


**Figure 2.8:** Handbag diagrams for Deep Virtual Compton Scattering (left) and the cross channel of the related Wide Angle Compton Scattering (WACS) which can be measured at  $\bar{P}$ ANDA. In case of Hard Exclusive Meson production (HEM) a real photon is replaced by a vector meson.

A main goal of  $\bar{P}$ ANDA is to search for gluonic excitations where gluons act as principal components. Such gluonic hadrons can be either a hybrid, which consists of two valence quarks and an excited gluon, or a glueball with two or three excited gluons and no valence quarks. Due to the additional degrees of freedom carried by the gluons these states can have exotic quantum numbers like  $J^{PC} = 0^{--}$  or  $1^{-+}$  which do not mix with nearby mesons states and therefore are easier to identify. As gluons do not carry mass inside the standard model glueballs and hybrids are supposed to yield fundamental insights into QCD. Figure 2.7 gives an overview of the mentioned states which can be accessed by  $\bar{P}$ ANDA.

Besides spectroscopy of hadronic states the structure of the nucleus can be investigated. In this context Generalized Parton Distributions (GPDs) are a promising tool to find answers to fundamental questions like the proton spin. GPDs can be accessed by Deep Virtual Compton Scattering (DVCS) or Hard Exclusive Meson production (HEM) by exploiting the factorization theorem and separating the hard part which can be computed in perturbation theory from the soft part which depends on the long distance structure of the hadron [Die03]. The crossed channel for both processes, where the soft part is described by the counterpart of the GPDs called Generalized Distribution Amplitudes (GDAs), is shown in figure 2.8 and can be measured at  $\bar{P}$ ANDA [PAN09].

In addition to proton antiproton collisions the proton target can be replaced by an atomic wire or fiber target made of carbon or other materials. This allows to investigate the modification of the life time and rest mass of hadrons containing charm quarks. Furthermore hypernuclei can be produced and studied if a secondary target is added. A hypernuclei is a nucleus which consists of nucleons whose valence quarks are not only consist of up and down quarks [PAN09].



## 3 Particle Identification

### 3.1 Techniques

In search of a complete picture of an event Particle IDentification (PID) plays an important role in particle physics experiments. For some processes it might be sufficient to distinguish only between light and heavy particles such as light leptons and hadrons whereas others require a precise determination of the final state particles. The following section intends to give a brief overview on the available techniques and their limitations.

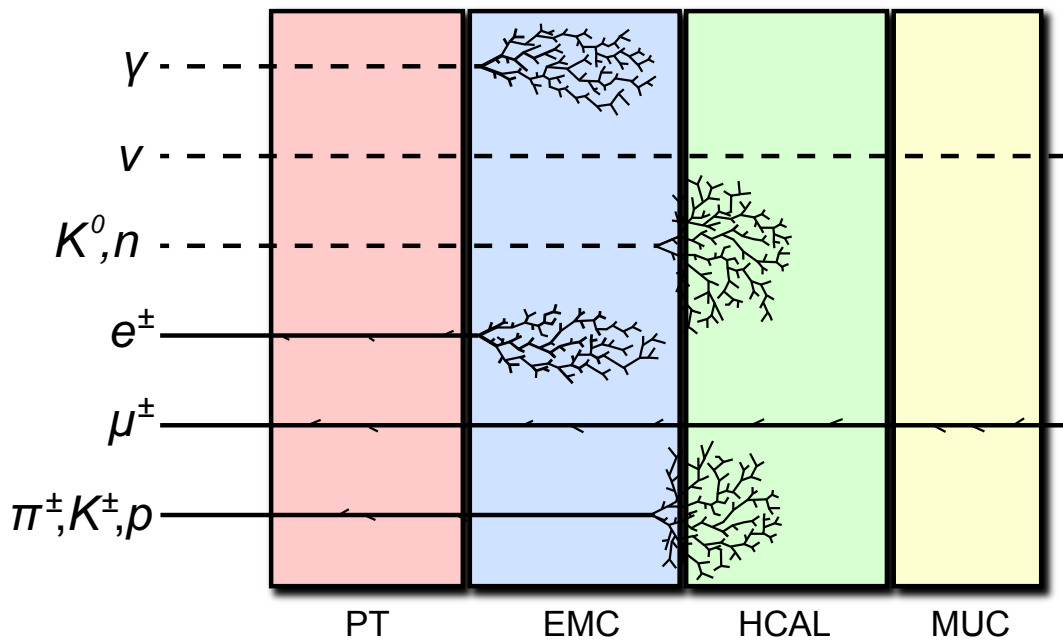


**Figure 3.1:** Sketched topologies for different particles inside a schematic detector. The abbreviations stand for Particle Tracking (PT), ElectroMagnetic Calorimeter (EMC), Hadronic CALorimeter (HCAL) and MUon Chamber (MUC). A dashed line means that the particle does not leave a signal inside the corresponding detector.

#### 3.1.1 Topology

Depending on a particle's properties such as its charge or interaction mechanisms it leaves different traces in different types of detectors. In high-energy physics experiments neutral particles like photons or neutral hadrons such as the neutron, the  $K^0$  or the  $\pi^0$  do not leave any signal until they convert into an electromagnetic or hadronic shower. Other neutral particles, the neutrinos, only interact weakly which makes them invisible for experiments which are not dedicated to their detection. Charged particles, on the other hand, ionize the matter they traverse which makes them detectable in tracking devices such as drift chambers or silicon strip detectors. Depending on the sign and amount of their charge they

take different paths inside a magnetic field which allows to distinguish between positively and negatively charged particles. Electrons and photons create electromagnetic showers by bremsstrahlung and pair production preferentially in an electromagnetic calorimeter. Electromagnetic showers typically start to develop immediately after entering a dense material. The radiation length corresponds to the mean distance when the electron or positron has lost all but  $1/e$  of its energy. They can also be characterized by their transversal spread given by the Molière radius. In contrast hadrons travel a distance, called nuclear interaction length, before they undergo an inelastic nuclear interaction and form a more complex and broad hadronic shower. The weakly decaying muons travel several meters and therefore only leave an ionizing signal in the different subdetectors.

As illustrated in figure 3.1 charged hadrons cannot be solely identified based on their topology why additional measurements have to be done in order to receive a full picture of an event.

### 3.1.2 Energy Measurement

In principle a particle can be identified by its mass which can be relativistically calculated according to

$$m = \sqrt{E^2 - p^2}. \quad (3.1)$$

Tracking in connection with a magnetic field allows to measure the momentum  $p$  of charged particles whereas the energy  $E$  of the hadron can be measured with a hadronic calorimeter. Nevertheless hadronic calorimeters are relatively large devices and their resolution is not sufficient to reliably distinguish between; e.g., a pion and kaon especially at high energies. However, an energy measurement can help contribute to PID for energies considerably below 1 GeV by also measuring the energy loss per distance  $dE/dx$ . In figure 3.2 the relation between the energy and  $dE/dx$  is plotted for different particles according to the Bethe formula [Sig06]

$$-\frac{dE}{dx} = \frac{4\pi n z^2}{m_e c^2 \beta^2} \cdot \left( \frac{e^2}{4\pi\epsilon_0} \right) \cdot \left[ \left( \frac{2m_e c^2 \beta^2}{I \cdot (1 - \beta^2)} \right) - \beta^2 \right], \quad (3.2)$$

with  $z$  being the charge of the particle in multiples of the elementary charge  $e$ , the electric constant  $\epsilon_0$ , the electron density of the material  $n$ , the mass of the electron at rest  $m_e$  and the mean excitation potential  $I$ . No PID is possible in the overlapping region which is smeared out by a limited detector resolution.

### 3.1.3 Time-of-Flight

Another way of accessing the mass of a charged particle is a Time-Of-Flight (TOF) measurement. Here the time  $\Delta t$  that a particle needs to travel between two detectors (usually

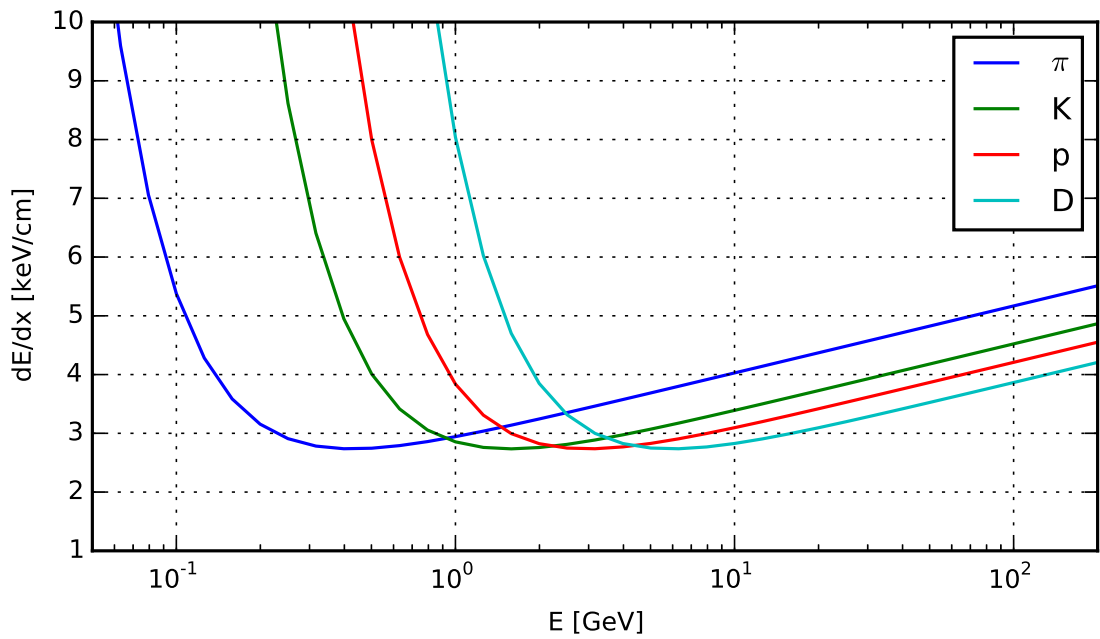


**Figure 3.2:** The Energy loss  $dE/dx$  according to the Bethe-Bloch formula versus the total energy of the particle can be utilized to identify charged particles below  $1 \text{ GeV}/c$ . The calculation was done for argon, which is a typical fill gas for drift chambers, at standard temperature and pressure.

scintillators), which are separated by a distance  $L$ , is measured. For two relativistic particles with masses  $m_1$  and  $m_2$  this time difference is given by

$$\Delta t = \frac{Lc}{2p^2}(m_1^2 - m_2^2). \quad (3.3)$$

The distance  $L$  cannot be chosen at will as it depends on the detector design and especially the position and maximum size of the calorimeters. Hence the application of a TOF system for PID is limited by the time resolution which comes with the scintillators and photon detectors which can go down to few tens of picoseconds. In addition long distances increase the probability that the particle has decayed before reaching the second measuring position.

### 3.1.4 Cherenkov Radiation

Cherenkov light is emitted when a charged particle with the velocity  $v$  traverses a transparent material under the condition that

$$v > \frac{c}{n} \quad (3.4)$$

where  $c/n$  is the phase velocity of light in the material with a refractive index  $n$ . Although it was verifiably seen by Marie and Pierre Curie around 1900 when they observed a bluish glow while experimenting with concentrated radium it took another 34 years until Pavel

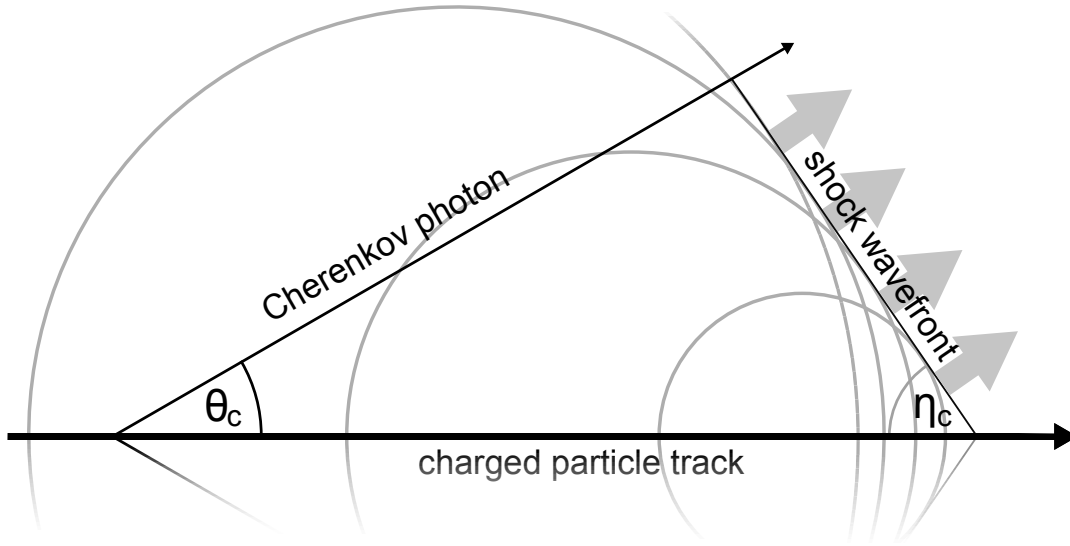


**Figure 3.3:** A schematic drawing of the charged particle track from where a Cherenkov photon is emitted along a cone with an opening angle of  $\theta_c$ . The shock wavefront and the track create the angle  $\eta_c$ .

Alexevich Cherenkov systematically investigated the nature of this effect [Che34]. Based on classical electromagnetic theory a theoretical description followed three years later by Ilya Frank and Igor Tamm [Fra37]. For their work Cherenkov, Frank and Tamm received the Nobel Prize in 1958.

The emission of Cherenkov radiation is similar to the sonic boom which is created when an object moves faster through a medium than the speed of sound in that medium. Instead of a longitudinal shock wave an electromagnetic pulse (Cherenkov photon) is emitted. The source of the electromagnetic pulse is a charged particle which polarizes the nearby atoms of the dielectric medium it traverses. When the speed of the particle exceeds the speed of light in that medium the induced polarization leads to an asymmetric dipole field along the particle's moving axis which collapses by emitting Cherenkov photons. In analogy to the sonic boom the photons are emitted in a cone around the charged particle track with an opening angle

$$\theta_c = \arccos\left(\frac{1}{n(\lambda)\beta}\right) = \arccos\left(\frac{\sqrt{p^2 + m^2}}{n(\lambda)p}\right) \quad (3.5)$$

with the relative velocity  $\beta = v/c$ , the particle momentum  $p$  and the mass of the particle  $m$ . The wavelength dependence of the refractive index  $n(\lambda)$  is a material property which can be empirically determined. It can be parametrized by Sellmeier coefficients  $B_i$  and  $C_i$  according to [Sel71]

$$n^2(\lambda) = 1 + \sum_i \frac{B_i \lambda^2}{\lambda^2 - C_i} \quad (3.6)$$

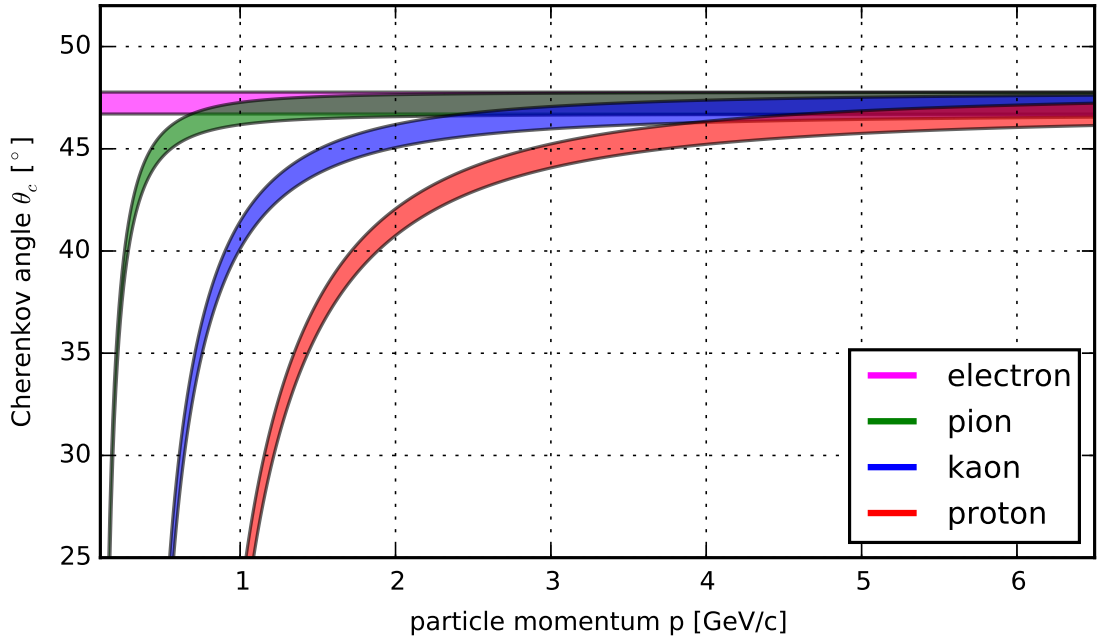


**Figure 3.4:** The above plot depicts the dependence of the Cherenkov angle versus the particle momentum in synthetic fused silica. The width of the bands illustrates smearing due to dispersion for wavelengths between 300 nm and 600 nm.

where normally only the first three coefficients  $B_1, B_2, B_3$  and  $C_1, C_2, C_3$  are given. The wavefront travels with the group velocity  $v_g = c/n_g$  where the group refractive index is given by

$$n_g(\lambda) = n(\lambda) - \frac{\lambda dn(\lambda)}{d\lambda}. \quad (3.7)$$

As optical media are dispersive the group velocity is smaller than the phase velocity which results in

$$\eta_c \neq 90^\circ - \theta_c \quad (3.8)$$

as illustrated in figure 3.3. Dispersion also leads to an intrinsic smearing of the measured Cherenkov angle. Figure 3.4 depicts the smearing of  $\theta_c$  for different particles and momenta. This chromatic error can be reduced by applying wavelength dependent filters (see also section 4.5).

Besides the Cherenkov angle the number of emitted photons is an important quantity as well. It was introduced by [Fra37] and depends on the available wavelength interval and is given by

$$\frac{d^2N}{dx d\lambda} = \frac{2\pi z^2}{\lambda^2} \alpha \sin^2 \theta_c \quad (3.9)$$

with  $L$  being the length of the path of the charged particle through the medium, the fine-structure constant  $\alpha \approx 1/137$ , the charge of the particle  $z$  in multiples of the elementary charge  $e$  and the wavelength of the emitted photon  $\lambda$ . For a quick estimation of the expected

number of photons equation 3.9 can be simplified to

$$N_{\text{photons}} = 2\pi\alpha L \cdot \left( \frac{1}{\lambda_1} - \frac{1}{\lambda_2} \right) \cdot \left( 1 - \frac{1}{\beta^2 n^2(\lambda)} \right) \quad (3.10)$$

with  $\lambda_1$  ( $\lambda_2$ ) being the lower (upper) value of the wavelength interval. Section 3.2 provides different examples of how Cherenkov light can be utilized in different detector designs to cover a wide momentum range for reliable particle identification.

### 3.1.5 Transition Radiation

A fast moving charged particle also emits photons when it passes through an inhomogeneous medium or a boundary between media with different permittivities. A first theoretical description was made by Ginsburg and Frank in 1946 [Gin46] but it took another 13 years until the first experimental evidence was found by Goldsmith and Jelley when they observed transition radiation in the visible spectrum in 1959 [Gol59]. A breakthrough in terms of PID came in 1975 when it was discovered that relativistic particles with a high Lorentz factor  $\gamma \geq 1000$  emit X-rays. These X-rays leave a large energy deposit which exceeds the average energy deposit that comes from ionization [Ava75]. The emission probability for a high energy transition radiation photon is small. This is why typical transition radiation detectors consist of several layers of foam and/or fiber where each layer provides many transitions on a microscopic scale. The layers are interleaved with gaseous detectors for tracking and measurement of the deposited energy. As a result transition radiation can be utilized to separate light from heavy particles (e.g. electrons and positrons from hadrons) up to very high momenta [And12].

## 3.2 Cherenkov detectors

### 3.2.1 Threshold Cherenkov Detectors

A simple way of using Cherenkov light for PID is realized by a Threshold Cherenkov Counter (TCC). Depending on a suitable choice of the refractive index of the radiator material and the particle's momentum a light particle, which emits Cherenkov radiation, can be distinguished from a heavy particle, which does not emit Cherenkov radiation. The threshold momentum can be calculated using equation 3.4 and is given by

$$p = \frac{m}{\sqrt{n^2 - 1}}. \quad (3.11)$$

Typically a TCC consists of a chamber filled with a radiator gas (e.g. Ne, Ar or CO<sub>2</sub>), whose refractive index can be modified by varying the gas pressure, and one or more PhotoMultiplier Tubes (PMTs) for the photon detection. This detector setup can be altered in order

to cover a larger momentum range or different particles by using more than one chamber with different gases or pressures. Figure 3.5 depicts the implication of different refractive indices on the ranges where Cherenkov radiation sets in.

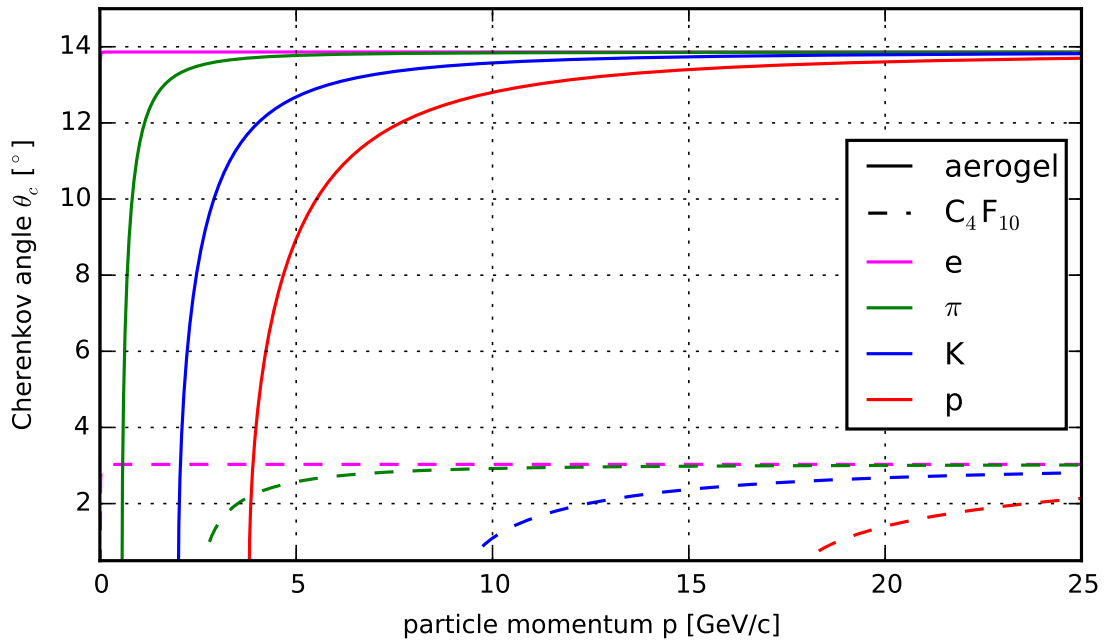


**Figure 3.5:** Similar to figure 3.4. This time the Cherenkov angles are plotted for two different refractive indices:  $n = 1.0014$  for perfluorobutane ( $C_4F_{10}$ ) and  $n = 1.03$  for aerogel which have been used in the HERMES RICH detector [Shi14].

### 3.2.2 RICH Detectors

A more sophisticated approach of utilizing Cherenkov radiation for PID comes with so-called Ring Imaging Cherenkov (RICH) detectors. As mentioned in subsection 3.1.4 Cherenkov photons are emitted along a symmetric cone around the path of the charged particle. Projecting the light that has been emitted in a small path interval on a plane which is perpendicular to the path of the particle results in a ring-like structure which is the reason for the naming of these types of detectors. The Cherenkov angle can then be determined by measuring the ring's diameter. An overview of different designs is shown in figure 3.6. The simplest setup is a proximity focusing device where the ring is just projected on a photomultiplier array. Depending on the necessary resolution this setup is impractical if a compact detector design is required. This can be overcome by a focusing design which is typically realized by a mirror, as it has been done for the CBM RICH detector at FAIR [Hon14]. A different ansatz is to build a focusing radiator which is realized by radiator slices made of aerogel with different refractive indices. Such a detector has been realized for the Belle II experiment [Pes13] and is also planned for the  $\bar{P}$ ANDA forward spectrometer [Blb15].

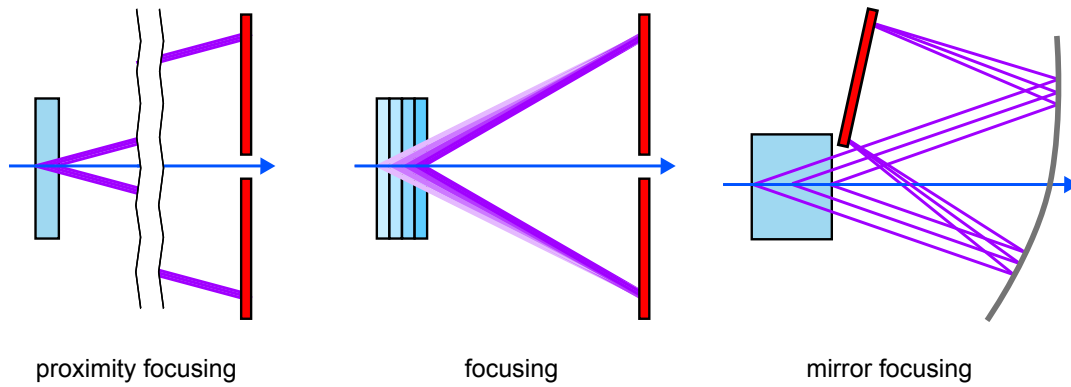


**Figure 3.6:** The figure illustrates different types of common RICH detectors. The charged particle is drawn as a blue arrow. Photo sensors are red boxes, radiators are light blue boxes. The different shades of blue in the focusing design correspond to the different refractive indices.

The design of a RICH detector is driven by the momentum range and particle types for which PID is needed. The CBM RICH for example aims at a clean electron identification up to  $8 \text{ GeV}/c$  which requires a gaseous radiator with a low refractive index. Another issue is the number of emitted Cherenkov photons which depends on the choice of material and the path length of the charged particle inside the radiator material. Moreover the radiator should show only low scintillation. In case of a gas the pressure and mixture has to be well controlled in order to not deviate from the anticipated refractive index. For aerogel one has to provide a good homogeneity and transparency of the material as well. Proper alignment is required for mirrors which also have to come with an excellent surface homogeneity and reflectivity in order to prevent photon loss and image distortion. Another interesting approach for a RICH detector was done by the HERMES collaboration who used a mirror focusing design with two different radiators which allowed to extend the momentum interval for PID (see figure 3.5).

### 3.2.3 DIRC Detectors

A special type of a RICH detector is a DIRC detector. It was first proposed for PID at B factories in 1994 [Coy94]. DIRC stands for Detection of Internally Reflected Cherenkov light which implies that the Cherenkov photons do not leave the radiator but are trapped by total internal reflection. These photons propagate through the radiator in a zig-zag-pattern while conserving the angle between the photon and the radiator surface. The DIRC principle allows a very compact detector covering only few centimeters along the path of a charged particle. Therefore it enables the design of experiments with a PID based on Cherenkov photons in the so-called barrel region. Another possibility is to replace conventional RICH detectors and therefore reduce the size of subsequent detectors in the forward or backward

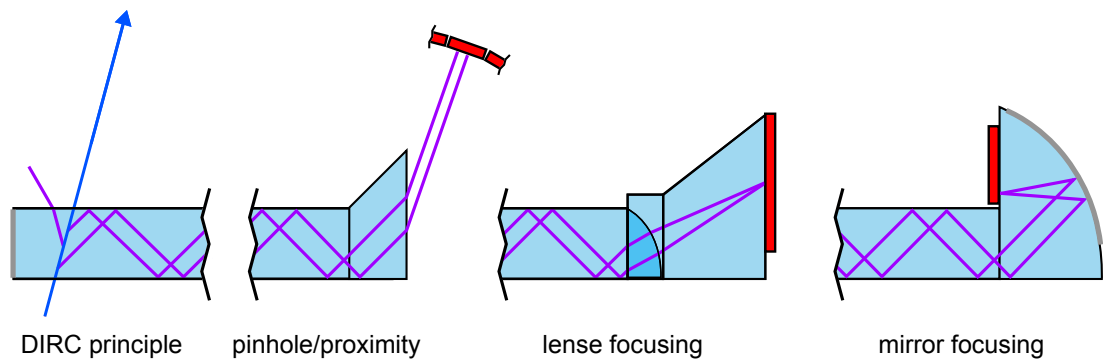


**Figure 3.7:** The figure illustrates the DIRC principle and different design options. The charged particle is drawn as a blue arrow. Photo sensors are red boxes, radiators are light blue boxes. In case of the lense focusing design the lens has a different refractive index which is drawn in a different shade of blue. Grey lines represent mirrors.

region of an experiment. Figure 3.7 gives an overview of different designs which are used in order to measure the photon angle at the end of the radiator (see also [Rat99]).

The pinhole or proximity focusing technique was used in the BaBar DIRC [Ada05] which was the first detector to utilize the DIRC principle for particle identification and achieved a  $\pi/K$  separation up to 4.2 GeV/c (with  $3.5\sigma$  separation power up to 3.5 GeV/c) [Swi05]. It consisted of 12 about 4.9 m long radiator bars made of fused silica which formed a 12-sided polygonal barrel. The bars were on one end coupled to a mirror and on the other end coupled to an expansion volume consisting of a fused silica wedge, window and a tank filled with purified water to which the photo sensors were coupled. The wedge reflects the lower Cherenkov ring image onto the upper one which reduces the number of photomultiplier tubes (PMTs) needed. Based on this design the PANDA Barrel DIRC [Swa16] has been de-

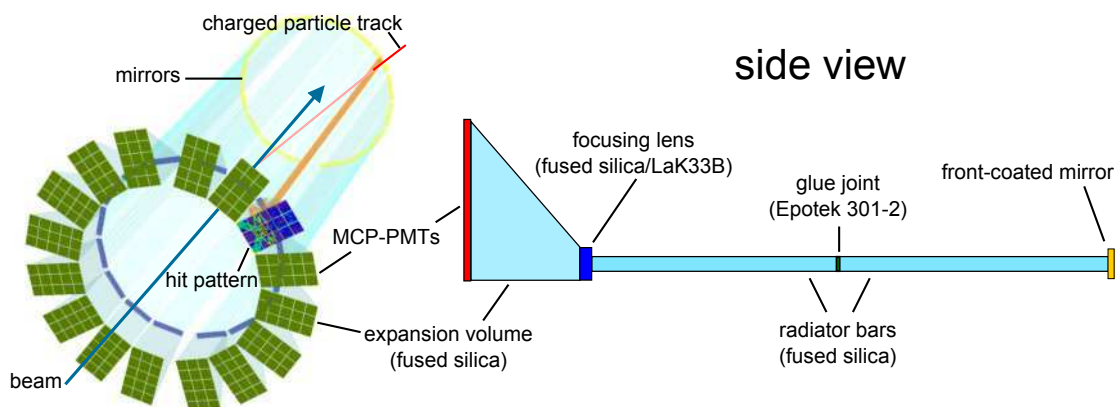


**Figure 3.8:** Example of accumulated PANDA Barrel DIRC events from a Geant simulation using narrow bars. The colored histogram shows the hit pattern from 1000  $K^+$  events at 3.5 GeV/c and  $25^\circ$  polar angle. The pictures were taken from [Swa16]. Beam arrow and naming was added.

veloped. Covering an angular range between  $22^\circ$  and  $140^\circ$  it will be capable of separating

pions and kaons up to 3.5 GeV/c with a separation power of up to  $3.5\sigma$ . There are currently two design options available: a narrow and a wide bar design [Dzh14]. The design with narrow bars allows a better reconstruction but due to the required number of polished surfaces it is more expensive (see also figure 3.8). Between the bars and the expansion volume a lens made of LaK33B [SotLAK] will be placed to improve the focusing. The expansion volumes consist of large fused silica wedges with multi-anode MCP-PMTs coupled to it. A recently realized DIRC detector is the so-called TOP (Time-Of-Propagation) counter at the Belle II experiment [Ina14]. It uses precise timing in the order of 40 ps to separate pions from kaons. The chromatic error which is typically in the order of 100 ps is reduced by a focusing mirror and 3D imaging.

The possibility of a mirror focusing design is pursued by several groups and was first discussed by T. Kamae et al. in 1996 [Kam96]. At the GlueX experiment a working group recycles old BaBar DIRC bars and builds a Focusing DIRC (FDIRC) [Dey15, Ste15] with a large expansion volume containing distilled water and mirrors while precise timing helps to reduce the chromatic error. The TORCH (Time Of internally Reflected CHerenkov light) detector [Dij14] aims at  $\pi/K$  separation up to 10 GeV/c for the LHCb experiment and uses a focusing block made of fused silica in order to measure the photon angle along with its time-of-propagation. Another detector that utilizes mirror focusing in its final design is the  $\bar{\text{PANDA}}$  Endcap Disc DIRC (EDD), the basis for this thesis, which will be discussed in the following section.

### 3.3 The $\bar{\text{PANDA}}$ Endcap Disc DIRC

#### 3.3.1 Evolution of the Design

The  $\bar{\text{PANDA}}$  Endcap Disc DIRC is designed for particle identification, especially separation of pions and kaons, with a separation power of  $4\sigma$  for momenta up to 4 GeV/c. It will cover the forward region with polar angles between  $5^\circ$  and  $22^\circ$  with a distance of 1.96 m from the interaction point. Starting at Gießen in 2006 [SmR06] different options have been evaluated and tested in order to find a design which fulfills the PID requirements. Limited space in the readout region excluded a large expansion volume for a lens or proximity focusing-based design. The proposal of a time-of-propagation measurement (TOP DIRC) [Dur09] with alternating dichroic mirrors had to be dropped because of an insufficient time resolution. In parallel a focusing design with light guides had been developed [Foh09] until a 3D-DIRC concept, which fused both concepts, was proposed and further investigated [Mer09, Dur12].

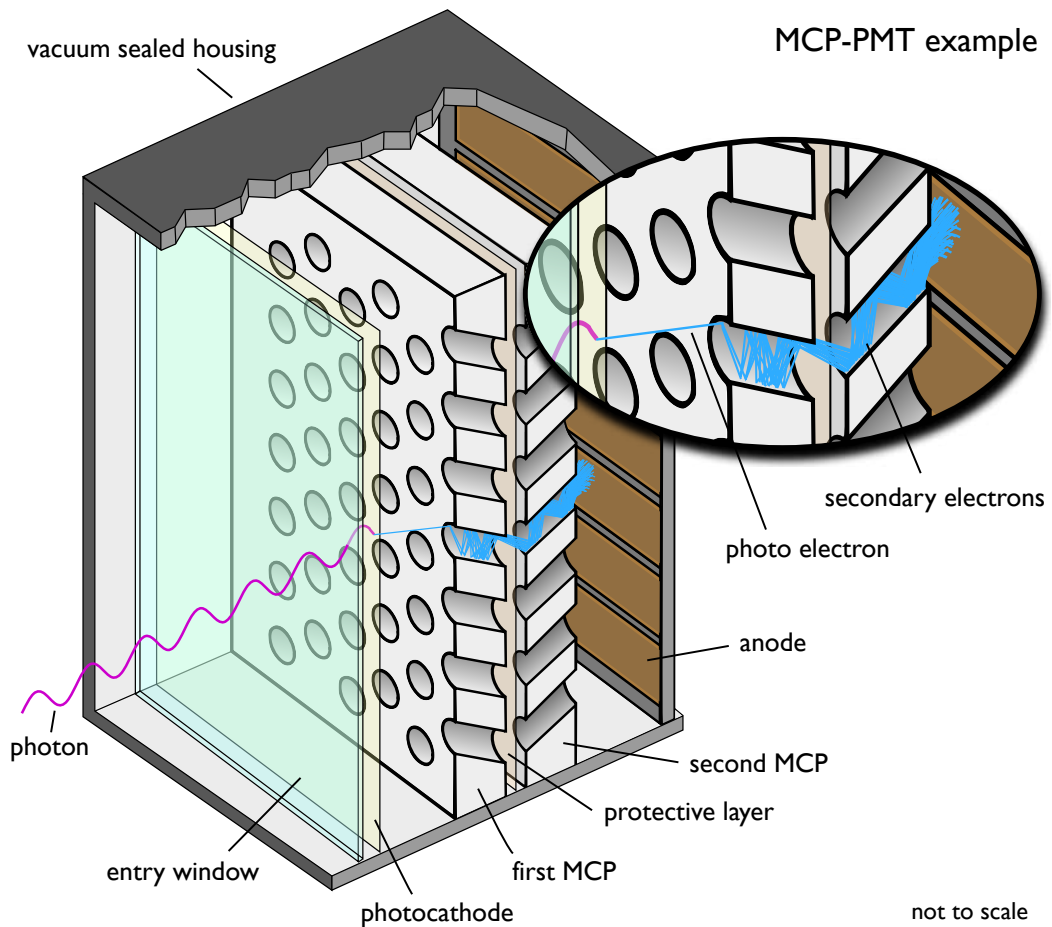


**Figure 3.9:** Schematic drawing of the MCP-PMT working principle. The depicted MCP-PMT is of the Chevron- or V-type which corresponds to the orientation of the microchannels. The incident photon (purple) enters the vacuum sealed housing through an entry window after which a photocathode is placed. From there a photo electron (blue) is emitted via the photo effect. Accelerated by the electric field inside the MCP-PMT the electron enters a capillary tube with a diameter of few  $\mu\text{m}$  where it impinges and triggers a cascade of secondary electrons which are then multiplied further. An electric signal can be detected once the secondary electrons hit the anode on the backside of the MCP-PMT. Dimensions are not to scale.

The final design was mainly driven by the choice of the photo sensors. Because the photon detection for the EDD has to be done in a magnetic field of around 0.7 T, conventional PhotoMultiplier Tubes (PMTs) are not suitable. Micro-Channel Plate PMTs (MCP-PMTs) on the other hand suffered from a low lifetime of their photocathodes which resulted in a quantum efficiency drop far before reaching the requirement of an integrated anode charge of  $5 \text{ C/cm}^2$  which is the benchmark for the  $\bar{\text{P}}\text{ANDA}$  Barrel DIRC. Hence digital Silicon Photomultipliers (dSiPMs) [Hae12] were favored at the beginning for a while. Although their dark count noise rate is quite high it would have been acceptable in connection with the anticipated event rate for the EDD. Other advantages of dSiPMs are an integrated readout

system, a high granularity and their insensitivity to the magnetic field which allows a free alignment. Nevertheless it was found that the dark count rate rises immediately when the dSiPMs are exposed to radiation which would result in unacceptable high dark count rates within months of operation. In the meantime the lifetime of the MCP-PMT photocathodes could be extended by reducing the back flow of ions from the MCPs which then impinge on the photocathode and damage it. This was achieved by improving the vacuum and applying an Atomic Layer Deposition (ALD) coating. The ALD coating also increases the emission of secondary electrons and therefore improves the gain [Uhl15]. Another strategy of improving the lifetime applied by Hamamatsu was to add a protective layer made of  $\text{Al}_3\text{O}_2$  in front of the first MCP. However, this led to a reduction of the collection efficiency as the photoelectron has to traverse the film before it can enter the micro channels why it was later placed between the two MCP stages [Jin11]. Figure 3.9 schematically illustrates the buildup of an MCP-PMT and its working principle. Extensive studies in preparation for DIRC detectors at Belle II [Hir15] and  $\bar{\text{P}}\text{ANDA}$  [Lhm16a] have shown that the lifetime for photon detection with ALD coated MCP-PMTs is sufficient to meet the EDD requirements.

### 3.3.2 Final Design

In the final design the detector will consist of four independent but identical detector parts, called quadrants. Each quadrant consists of one large fused silica radiator and 27 Read-Out Modules (ROMs) which are connected to the outer sides as depicted in figure 3.10. The ROMs combine three prisms and three Focusing Elements (FELs) with one MCP-PMT. The prisms are optically coupled to the radiator and extend it in order to allow different distances between the radiator edge and the FEL which is necessary due to the geometry of the surrounding detectors. The FELs focus the photons coming from the prism such that parallel entering photons hit the same pixel on the MCP-PMT anode. Currently two options exist for the MCP-PMTs: a PHOTONIS MCP-PMT with a segmented anode of  $3 \times 100$  pixels and a Hamamatsu MCP-PMT with a segmented anode of  $6 \times 128$  pixels. With the PHOTONIS sensor each column of 100 pixels is connected to one FEL whereas in the case of the Hamamatsu sensor two columns share one FEL. In order to reduce the chromatic error due to dispersion and limit the number of photons in order to extend the lifetime of the MCP-PMTs, a filter can be positioned between the FEL and the entry window of the MCP-PMT. The readout is foreseen to be done by ASICs (Application-Specific Integrated Circuits) which are soldered to a PCB (Printed Circuit Board). The PCB itself routes the channels and is connected to the pins on the MCP-PMT back side [Rie17]. At the moment it is planned to use so-called TOFPET ASICs by PETSys [Rol13] for the digitization of the pulses.

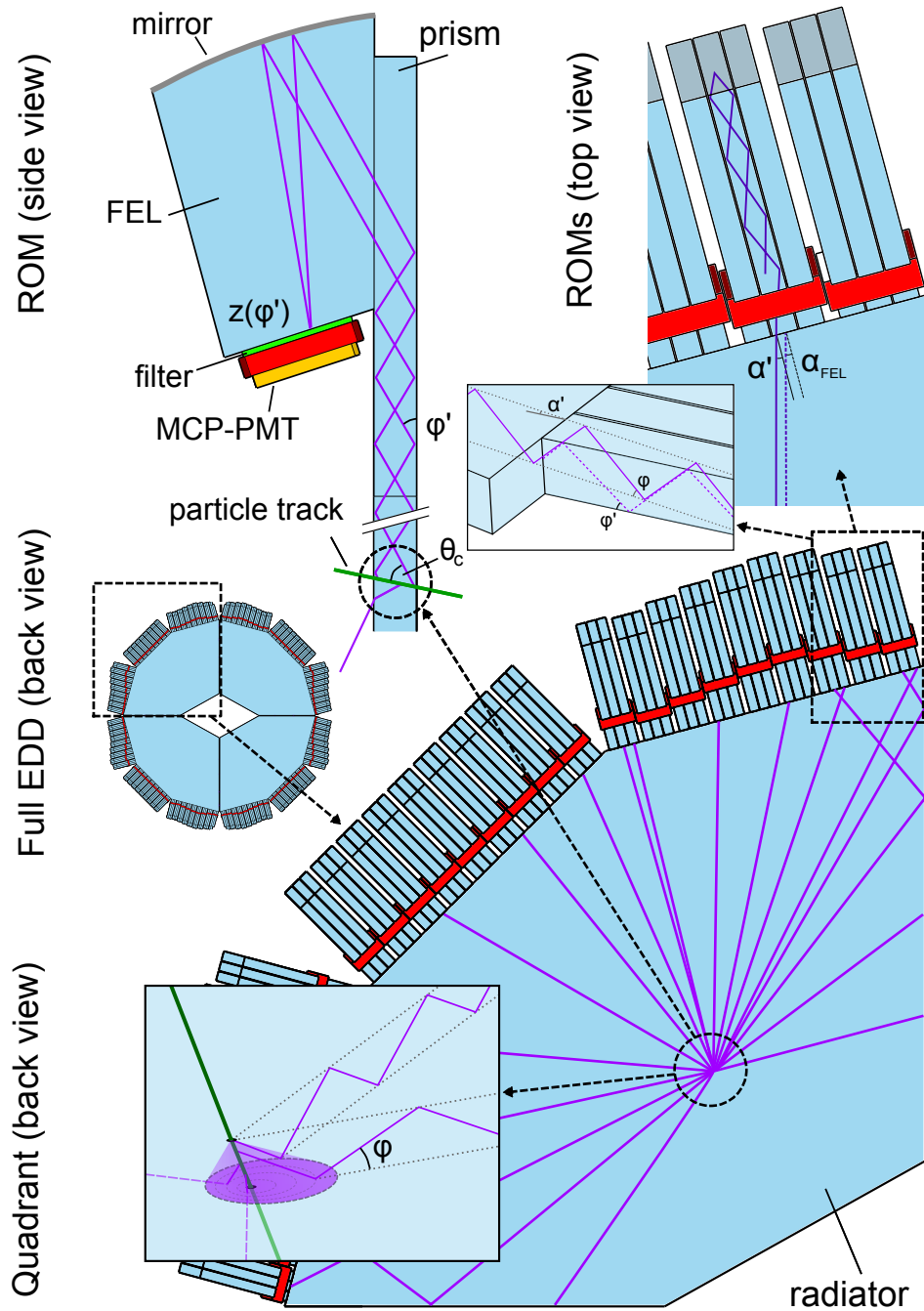


**Figure 3.10:** Schematic overview of one Disc DIRC quadrant and its working principle. Optical components are colored light blue, MCP-PMTs are colored red and the pins of the MCP-PMT anode are colored yellow. The central figure shows a fully equipped quadrant with different photon paths (purple) originating from one spot. A part of the photons is trapped by total internal reflection whereas the rest is lost by refraction on the surface. On the top right side of the drawing the impact of the bar width is illustrated. Whenever a photon enters a bar its angle  $\varphi'(\varphi, \alpha_{FEL})$  is calculated under the assumption that it entered the bar centrally. The top left part of the drawing illustrates the DIRC principle, where a charged particle (green line) passes through the radiator and Cherenkov photons are emitted along its path. The photons travel towards the edge of the radiator where they enter the prism. This prism extends the radiator and leads to the FEL, where parallel entering photons are focused on the MCP-PMT photocathode. The cylindrical-shaped surface is mirror-coated.

### 3.3.3 Working Principle

A charged particle with the four-momentum  $(E, \vec{p})$  emits Cherenkov photons along a cone with the opening angle  $\theta_c$  when traversing the radiator. Depending on the azimuthal orientation  $\phi_{\text{rel}}$  between photon path and the particle trajectory on the radiator plane, the angle  $\varphi$ , which is defined as the angle between the radiator surface and the photon path,  $\varphi$  can be calculated according to [Mer09]

$$\cos \varphi = \frac{A \cos \theta_c}{B} \pm \sqrt{\frac{\cos^2 \theta_p - \cos^2 \theta_c}{B} + \left(\frac{A \cos \theta_c}{B}\right)^2}, \quad (3.12)$$

where  $\theta_p$  is the particle angle relative to the normal of the radiator plane. The terms  $A$  and  $B$  are given by

$$A = \sin \theta_p \cos \phi_{\text{rel}}, \quad B = A^2 + \cos^2 \theta_p. \quad (3.13)$$

The photon is trapped by total internal reflection in case of

$$\varphi < \arccos(n_{\text{SiO}_2}(\lambda)) \quad (3.14)$$

and propagates towards the FELs conserving  $\varphi$ . The FEL focusing allows to measure the transformed  $\varphi'$  given by

$$\tan \varphi' = \frac{\tan \varphi}{\cos \alpha_{\text{FEL}}} \quad (3.15)$$

with  $\alpha_{\text{FEL}}$  describing the angle between the photon path on the radiator plane and the orientation of the FEL (see also figure 3.10). The angle  $\varphi'$  is determined by the position  $z$  which is given by the pixel that registers the signal. The pixel size is therefore matched with the resolution of the FEL. Due to the finite size of the FELs  $\alpha_{\text{FEL}}$  is only an approximation and, along with the tracking precision, the chromatic error and optical displacements, a main source of angle smearing. The number and hence the width of the FELs has been optimized with respect to the necessary performance requirements while reducing the number of pieces and, therefore, the number of polished surfaces [Mer14b].

The Cherenkov angle can subsequently be determined separately by

$$\theta_c = \arccos(\sin \theta_p \cos \phi_{\text{rel}} \cos \varphi + \cos \theta_p \sin \varphi) \quad (3.16)$$

for every hit. Averaging over a whole track with 16 to 25 detected photons a resolution between 1.2 and 2.0 mrad can be achieved which is sufficient to fulfill the initial performance requirements of being able to do a  $\pi/K$ -separation up to 4 GeV/c with a separation power of at least  $4\sigma$  [Mer14b].

## 4 Optical system

### 4.1 Introduction

#### 4.1.1 The Optical System

This chapter will describe and evaluate the optical system of the Endcap Disc DIRC for  $\bar{P}$ ANDA . It is composed of all parts that are traversed by Cherenkov light before hitting the MCP-PMT photocathode. Consistent with the overall detector design the optical system consists of four independent parts, one for each quadrant.

The first and largest piece in each quadrant is the radiator where Cherenkov light is emitted by relativistic charged particles that traverse the detector. Depending on their direction Cherenkov photons may then enter the prisms on the edge where they are guided into the FELs. Here they are reflected from an aluminum coated surface and focused on the MCP-PMT photocathode. Before they hit the photocathode they will pass through an optical pad, a color filter and the entry window of the MCP-PMT.

As the entry window is an integral part of the MCP-PMT, it will not be discussed at this point (details can be obtained here [Rie17]). However, depending on the choice of the MCP-PMT photocathode it might be necessary to add a wavelength dependent filter in front of each entry window.

Table 4.1 summarizes the purposes and requirements of all parts within the optical system. The following subsections will then give a detailed overview for each component along with measurements and studies for the quality assurance.

component	purpose	requirements
radiator	<ul style="list-style-type: none"> <li>• emittance of Cherenkov light</li> <li>• light guide</li> </ul>	<ul style="list-style-type: none"> <li>• high transmittance</li> <li>• high surface quality</li> </ul>
glue joint	<ul style="list-style-type: none"> <li>• optically connect ROMs to the radiator</li> </ul>	<ul style="list-style-type: none"> <li>• mechanical stability</li> <li>• high transmittance</li> </ul>
prism	<ul style="list-style-type: none"> <li>• allow variable distances between ROMs and radiator</li> <li>• light guide</li> </ul>	<ul style="list-style-type: none"> <li>• high transmittance</li> <li>• high surface quality</li> </ul>
FEL	<ul style="list-style-type: none"> <li>• focusing on MCP-PMT photocathode</li> <li>• light guide</li> </ul>	<ul style="list-style-type: none"> <li>• high transmittance</li> <li>• high surface quality</li> <li>• precise dimensioning</li> </ul>
optical pad	<ul style="list-style-type: none"> <li>• optically connect MCP-PMT to FELs</li> <li>• allow replacement of MCP-PMTs</li> </ul>	<ul style="list-style-type: none"> <li>• high transmittance</li> <li>• sufficient adaptiveness</li> </ul>
filter	<ul style="list-style-type: none"> <li>• reduce chromatic error</li> <li>• limit number of photons</li> </ul>	<ul style="list-style-type: none"> <li>• good homogeneity</li> <li>• sharp edges</li> </ul>

**Table 4.1:** This table summarizes the main purposes and requirements for each part of the optical system. The order corresponds with the path of a Cherenkov photon starting inside the radiator and entering the MCP-PMT entry window after traversing the optical pad and/or filter.

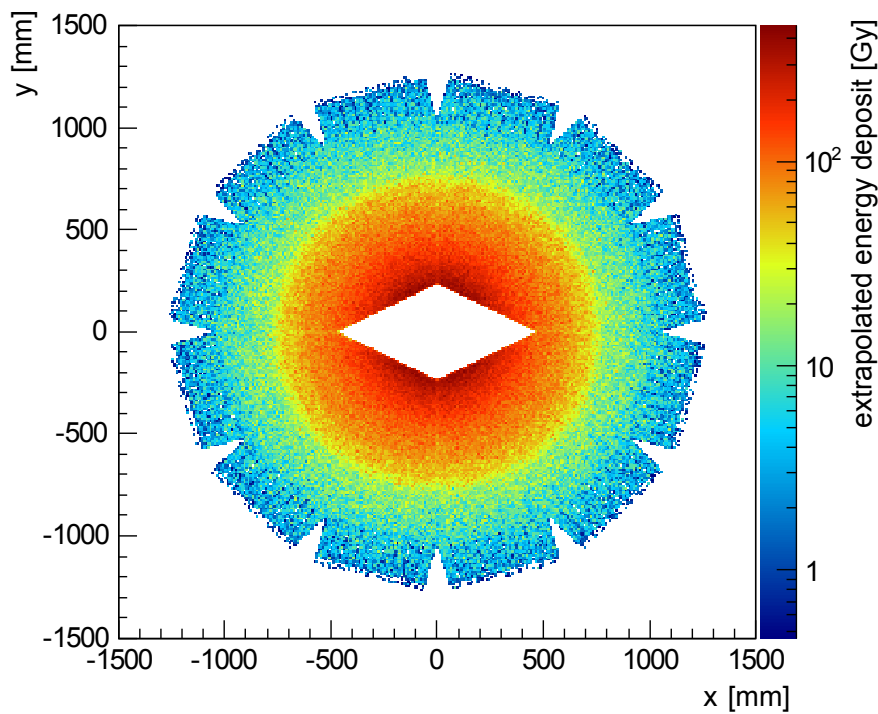


**Figure 4.1:** Energy deposit in the optical system extrapolated to 10 years at a 50% duty cycle and 10 MHz interaction rate. The amount of deposited energy clearly drops beyond a radius of 75 cm around the center as the electromagnetic calorimeter blocks this region. Further details along with the original figure can be found in [Mer14b].

#### 4.1.2 Material

The choice of materials for the optical system is fundamental for a working detector. In addition to the requirements stated in table 4.1 all components have to cope with a radiation dose of several Gy in the region where the ROMs are located and up to several 100 Gy near the center of the detector after 10 years of operation (see figure 4.1). Furthermore the choice of material has to be made with respect to economic aspects. In this context it is especially important not to overestimate price-enhancing specifications. With respect to the stated requirements only optically isotropic and transparent materials can be used in a DIRC detector. Transparent cubic crystals are very expensive to produce, especially for large dimension that are needed for a DIRC radiator. Acrylic glass on the other hand suffers mainly from radiation damage, inhomogeneities and poor processability [Hol11]. In comparison to the former two options silicon dioxide ( $\text{SiO}_2$ ) can be ground and polished to very high precision and can be produced more economically priced than other crystals. In terms of usability for a DIRC detector one has to distinguish between three different types of  $\text{SiO}_2$ .

Crystalline  $\text{SiO}_2$ , also called natural quartz, is the second-most-abundant mineral on Earth but only a small fraction has enough purity to be suitable as raw material for quartz glass.

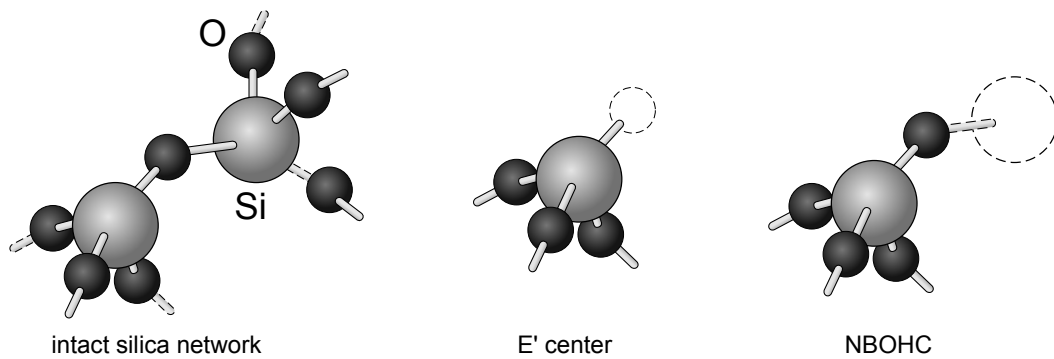


**Figure 4.2:** The left bond shows an intact silica network with a tetrahedral coordination. To its right a generic  $E'$  center is depicted where an oxygen atom is missing. The right bond shows another possible precursor where the oxygen is bridged with only one silicon atom.

Due to its birefringence it is not suitable for a high-precision optical device. In order to get an amorphous form of  $\text{SiO}_2$ , natural quartz can be crushed and melted in a hydrogen flame. This so-called natural fused silica, however, still contains impurities from the natural quartz which can be very sensitive to ionizing radiation. These impurities can be controlled and reduced to a ppb-level by artificially forming  $\text{SiO}_2$ . This is usually done by hydrolysis and oxidation of silicon tetra-chloride ( $\text{SiCl}_4$ ) in an  $\text{H}_2/\text{O}_2$  atmosphere at around  $2000^\circ\text{C}$ :



Several manufacturers provide different grades of synthetic fused silica. Many have been evaluated in the context of using them in a DIRC detector [Coh03, Hol11] such as Spectrosil<sup>®</sup> 2000 by Heraeus [Her16] or HPFS<sup>®</sup> 7980 by Corning [Cor14].

Synthetic fused silica is usually synthesized in large ingots whose transparent core is surrounded by a crust which has to be ground off. Afterwards the raw material can be inspected before being further processed. To allow shapes that differ from or exceed an ingot's cross section the material can be reheated and pressed into a new shape. The final shape will be accomplished by cutting, grinding, lapping and polishing of the raw material.

## 4.2 Radiation Hardness

### 4.2.1 Previous Results

Any material used in the  $\bar{\text{P}}\text{ANDA}$  Endcap Disc DIRC (EDD) has to withstand certain levels of irradiation. In case of the optics the used material must not develop defects which lead to an absorption of light in a region roughly between 300 nm and 600 nm. Possible effects that lead to such radiation-induced defects are described in [Mrs97] (see also figure 4.2). In short gamma irradiation produces Compton electrons and subsequently secondary electrons that

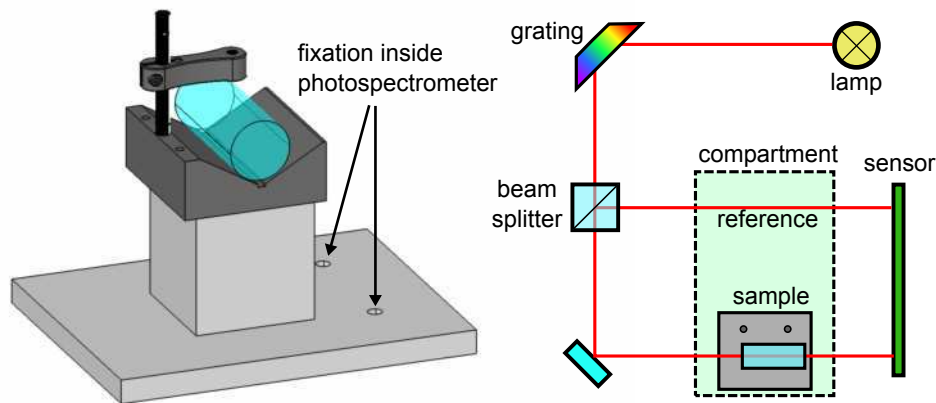


**Figure 4.3:** On the right one sees the custom mount inside the photospectrometer which allows a reproducible measurement. On the left the working principle is sketched.

create e-h (electron-hole) pairs. The carriers of the e-h pair can be captured at a precursor site and lead to a so-called  $E'$  center where an electron is missing. These precursor sites are either originating from the manufacturing process or can be induced by neutrons [Guz93] or heavy ions [Gri86] which knock off the oxygen atom leading to an Oxygen Deficient Center (ODC).

In connection with DIRC detectors various material candidates have been tested with the following outcome:

- Whereas natural fused silica shows partly severe damage and loss in transmittance even for wavelengths above 300 nm, synthetic fused silica is mostly radiation hard but develops absorption lines around characteristic wavelengths [Coh03].
- The optical degradation (peakedness) is smaller with a higher amount of interstitial hydrogen [Hok11].

#### 4.2.2 Radiation Hardness of NIFS

Nikon Corporation started to provide customer specific products made of synthetic fused silica in 2003 and hence was not on the radar for former DIRC projects. In comparison to previously known companies Nikon synthesizes fused silica as well as machines the raw material according to customer's needs. On the other hand their material Nikon Fused Silica (NIFS) has not been thoroughly tested regarding the requirements of a high-energy physics experiment.

The following subsection focuses on the radiation hardness of NIFS. For this purpose Nikon Corporation kindly provided samples of five different grades of synthetic fused silica summarized in table 4.2. NIFS-S, -U and -A undergo a slightly different treatment whereas NIFS-V is synthesized differently resulting in so-called dry synthetic fused silica which implies a low OH-content. NIFS-V' is modified compared to NIFS-V why details on the data

grade	recommended wavelength	impurities	
		OH	other
NIFS-S	UV region, visible region	<1200 ppm	<100 ppb
NIFS-U	248 nm	<1200 ppm	<50 ppb
NIFS-A	193 nm	<1200 ppm	<0.2 ppb
NIFS-V	193 nm	<100 ppm	<0.2 ppb
NIFS-V'	193 nm	-	-

**Table 4.2:** Overview of the available NIFS samples. The value in the **impurities** column **other** represents each element (Li, Na, K, Mg, Ca, Al, Ti, Cr, Fe, Cu) individually [NIFS].

are not presented.

The study was based on a previous study carried out by M. Hoek et al. [Hok11] which focused on samples of Heraeus Suprasil 2A and Suprasil 311 with different hydrogen contents. The NIFS samples for this study, which was partly described in [Etz16], were cylindrically shaped with a length of 60 mm and a diameter of 25 mm. The length of the sample should not be too short in order to be more sensitive towards the induced absorption length. The flat top and bottom surfaces were polished. The transmittance measurement was done using a Hitachi U-3200 spectrophotometer which was operated with a deuterium arc lamp only. This lead to some artifacts in the transmittance measurements for the Balmer line  $D_{\beta}$  at 486 nm and the Fulcher band emission between around 560 to 640 nm (compare figure 4.4). However, this circumstance does not effect the value of the radiation hardness measurements as it is based on a relative measurement. The experimental setup inside the Hitachi U-3200 spectrophotometer is depicted in figure 4.3. Here it was important to have a reliable mount for the samples as the positioning inside the compartment is crucial for a reproducible measurement. Each sample was measured twice in two different positions, where the sample was rotated by  $180^{\circ}$  around the cylindrical axis. The transmittance was then determined by averaging these four measurements. Before the first measurement each sample was cleaned using ethanol. Figure 4.5 illustrates the possible impact when the cleaning is not done carefully. Residues of ethanol cause characteristic absorption lines which later on could distort or falsify the measurement.

#### 4.2.2.1 Irradiation with 1000 Gy

The irradiation of the samples was done at a  $^{60}\text{Co}$ -source at the Strahlencentrum Gießen. The source could be accessed via an annular slider. At the time of irradiation the dose rate amounted to approximately 100 Gy per hour [Kra15] resulting in a total of 10 hours of irradiation. All five samples were irradiated at once in the same compartment. After the

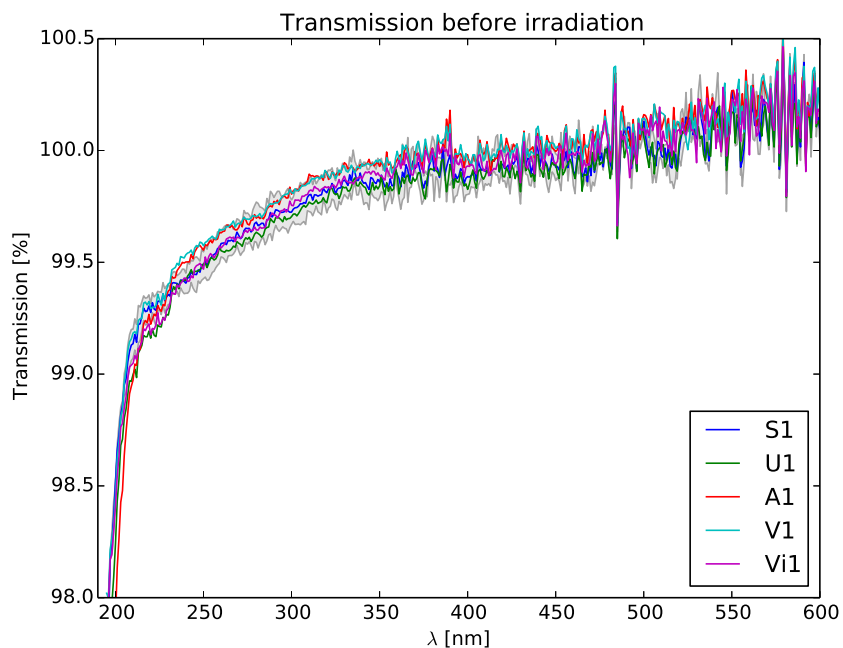


**Figure 4.4:** Transmittance of all NIFS samples before any irradiation. The filled gray area corresponds to the maximum error of the NIFS-S sample as this had the largest uncertainty which arose from different values after rotating the sample. The spike at 486 nm is supposed to be caused by the Balmer line  $D_{\beta}$  for hydrogen  $H_{\beta}$ .

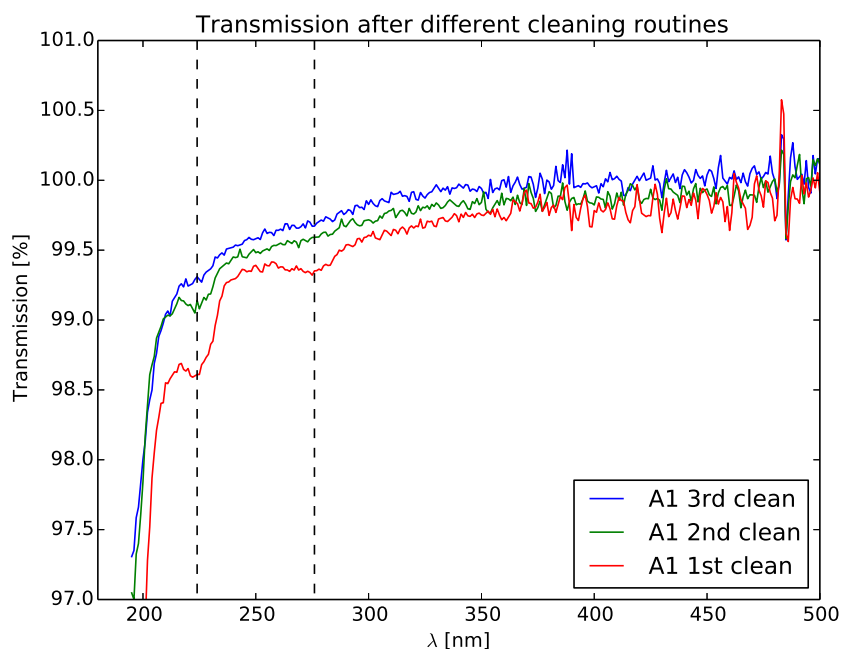


**Figure 4.5:** Impact of a different cleaning routine on the transmittance. The cleaning was done using ethanol which, if not completely removed by firm rubbing, leads to significant losses at 224 nm and 276 nm.

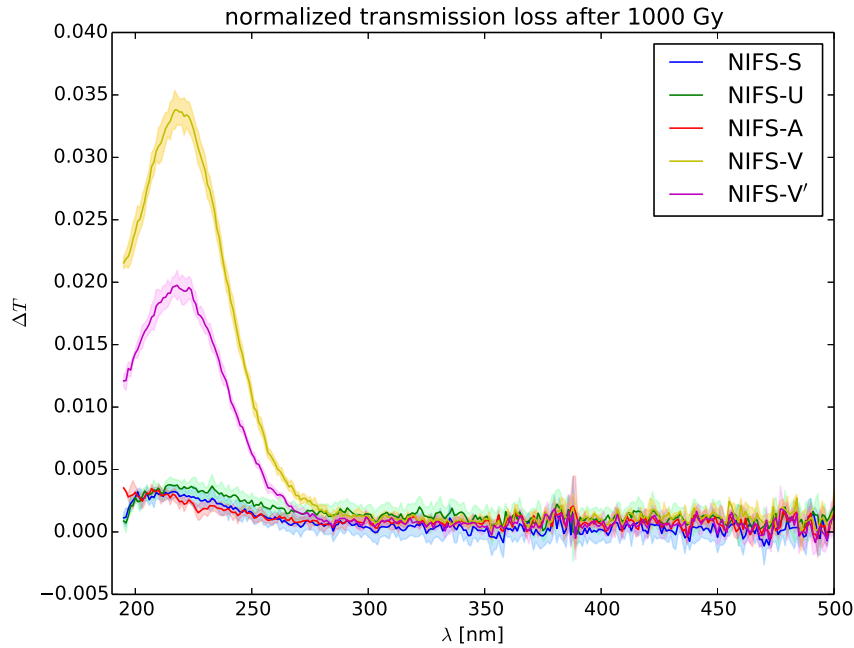


**Figure 4.6:** Normalized transmittance loss after irradiation with a dose of 1000 Gy. The samples NIFS-V and NIFS-V' which contain less OH show a larger change in transmittance.

irradiation the transmittance measurement was repeated as described above but without an additional cleaning.

Subsequently the normalized transmittance loss  $\Delta T$  was calculated according to

$$\Delta T = \frac{T_{\text{before}} - T_{\text{after}}}{T_{\text{before}}} \quad (4.2)$$

with  $T_{\text{before}}$  ( $T_{\text{after}}$ ) representing the values obtained before (after) the irradiation. The wavelength dependent results are shown in figure 4.6. A clear difference can be observed between the two NIFS-V samples and the rest. This is in agreement with previous results which identified a clear correlation between the OH content of synthetic fused silica and the damage due to ionizing radiation [Hok11]. Another observation is the reduced damage of NIFS-V' in comparison to NIFS-V. This leads to the assumption that NIFS-V' underwent an additional treatment which increased the OH content of the originally dry fused silica. The wet samples NIFS-S, -U and -A show no significant transmittance loss. The position of the peak is in accordance with the  $E'$  center at around 5.8 eV (215 nm) which most likely comes from a dangling silicon bond [Sku05]. Another typical defect which comes from a dangling oxygen bond, also called Non-Bridging Oxygen Hole Center (NBOHC, see also figure 4.2), at 4.7 eV (260 nm) cannot be observed for NIFS.

As the Cherenkov photons will travel up to 1.5 m inside the EDD and a much larger distance in the Barrel DIRC it is necessary to quantify the radiation damage subject to the path length. The transmittance of light after traversing a material of length  $x$  with an attenuation

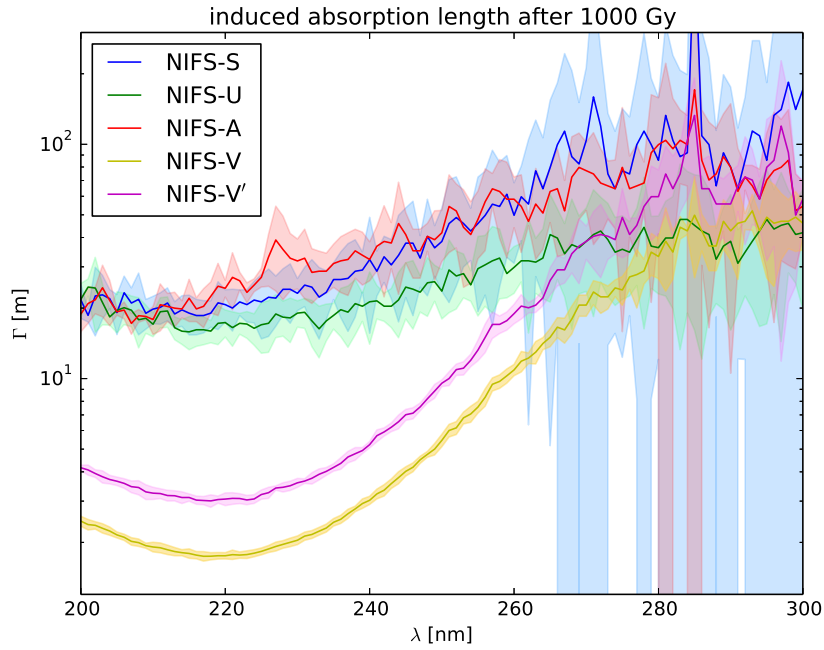


**Figure 4.7:** Absorption length after irradiation with a dose of 1000 Gy.

length  $\lambda$  is given by

$$T(x) = e^{-x/\lambda}. \quad (4.3)$$

In the present case the so-called induced absorption length  $\Gamma$  is of interest which replaces the attenuation length  $\lambda$  and is calculated according to

$$\Gamma = -\frac{l}{\ln(1 - \Delta T)} \quad (4.4)$$

where  $l$  is the length of the sample (6 cm) and  $\Delta T$  the normalized transmittance loss as defined in equation 4.2. In figure 4.7 the induced absorption length is plotted for all samples. For wavelengths between 200 nm and 260 nm the wet samples NIFS-S, -U and -A reach values slightly below 20 m whereas the dry samples peak at 2 m (NIFS-V) and 3 m (NIFS-V'). In consideration of the requirements for the EDD all materials could be used in terms of radiation hardness, as the envisaged wavelength region lies above 300 nm which is not affected. Nevertheless future experiments might depend on photons in the middle or far ultraviolet region and possibly also have to deal with an even higher radiation dose. Therefore this study was later extended to evaluate long-term effects and later on repeated with a dose of 5000 Gy.

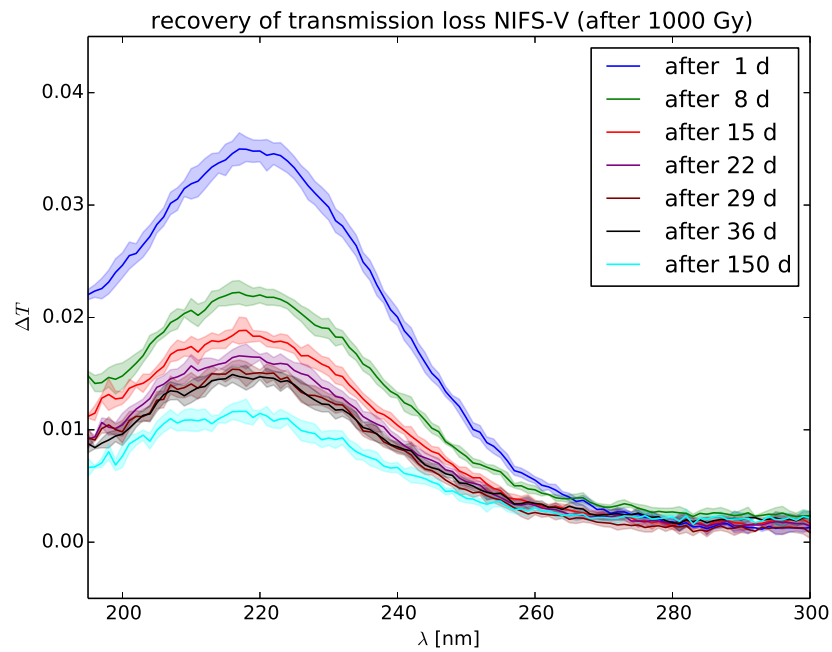


**Figure 4.8:** Recovery of the normalized transmittance loss after irradiation with 1000 Gy for NIFS-V.

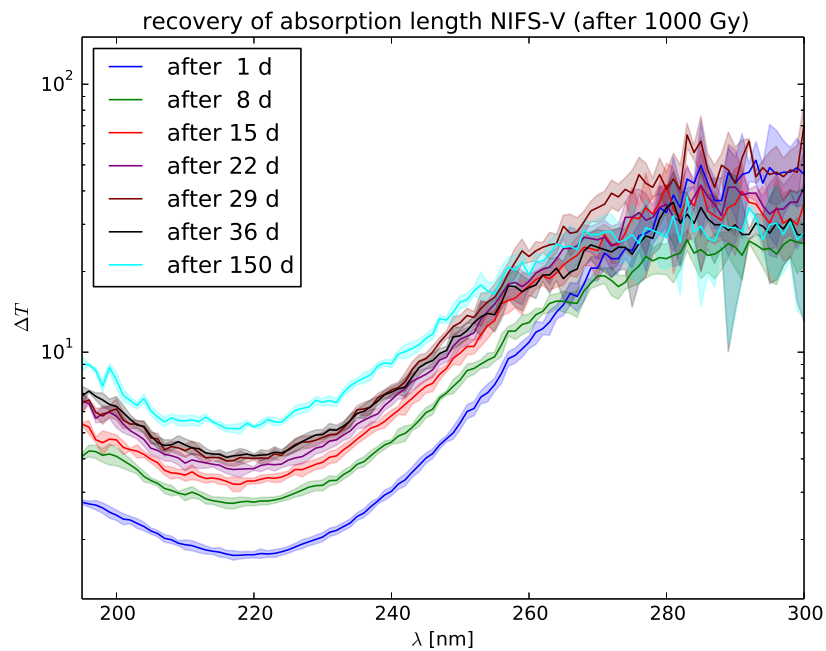


**Figure 4.9:** Recovery of the induced absorption length after irradiation with 1000 Gy for NIFS-V.

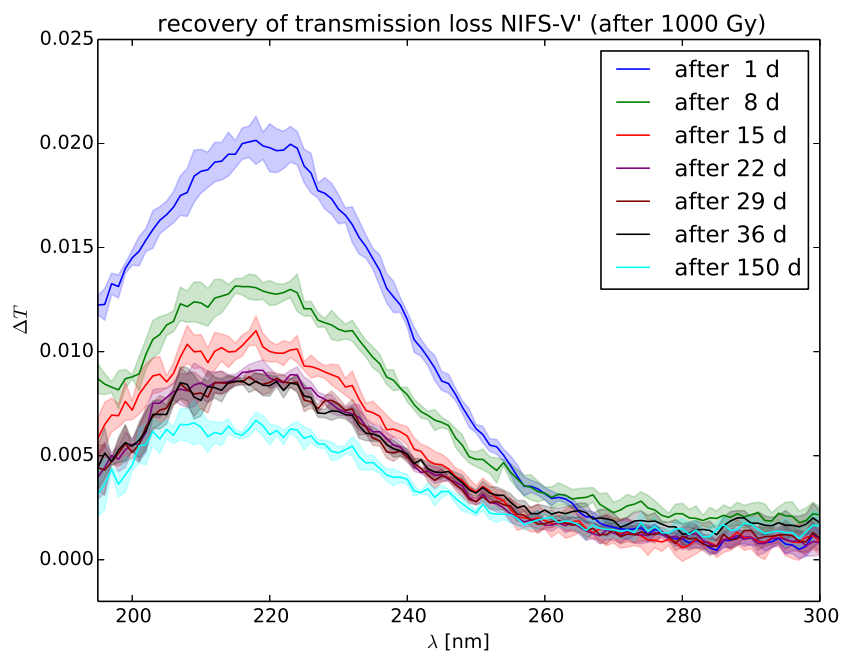


**Figure 4.10:** Recovery of the normalized transmittance loss after irradiation with 1000 Gy for NIFS-V'.

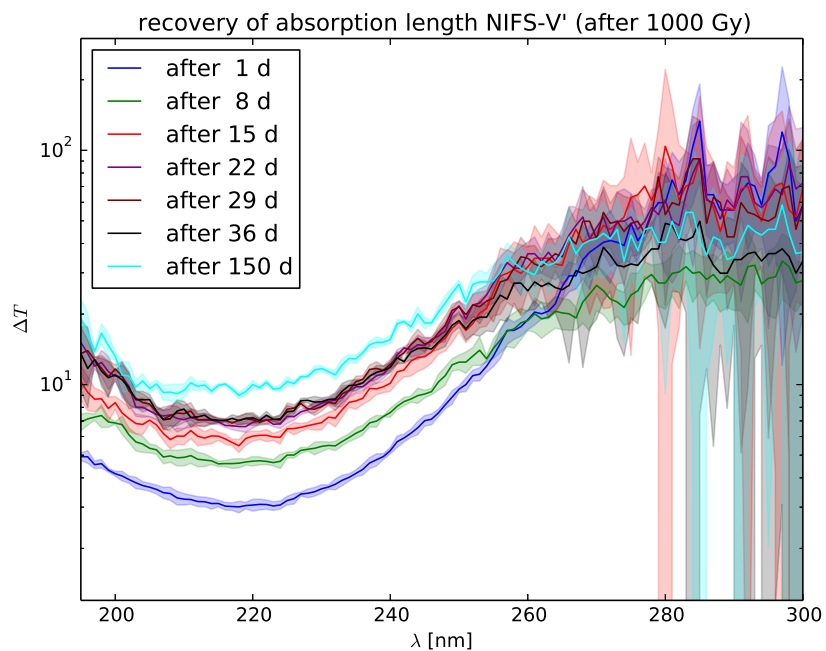


**Figure 4.11:** Recovery of the induced absorption length after irradiation with 1000 Gy for NIFS-V'.

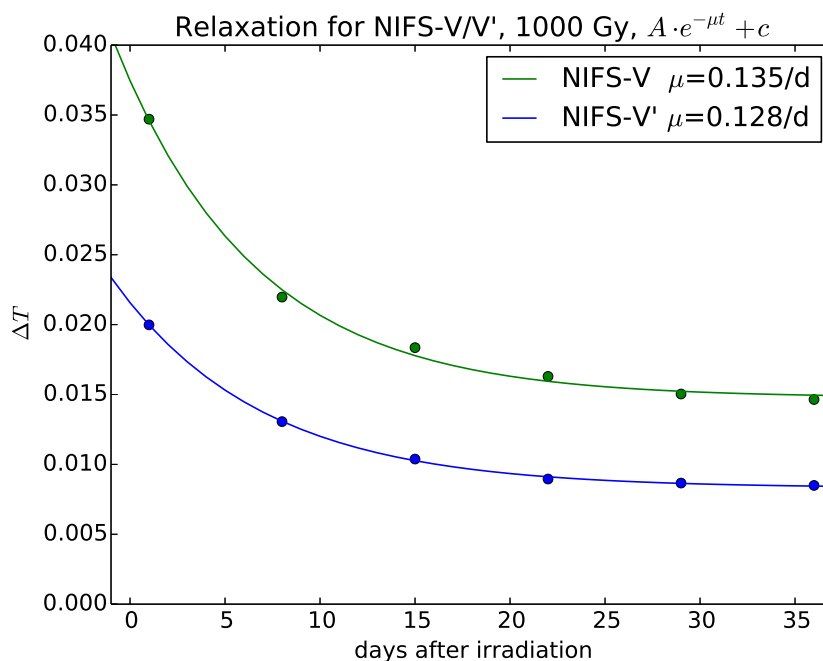


**Figure 4.12:** Relaxation plot after irradiation with a dose of 1000 Gy. The data points match the amplitudes around 220 nm.

The transmittance measurement of the irradiated samples was repeated on a weekly basis as described above for six consecutive weeks. An additional measurement was done after 150 days before the probes were irradiated again for the 5000 Gy study. Between the measurements the samples were stored in individual membrane boxes in a light-tight compartment at room temperature. No additional treatment was applied. As the wet samples showed hardly any damage only the dry samples NIFS-V and -V' were evaluated. Figures 4.8 and 4.9 show the induced transmittance loss and the absorption length for NIFS-V. The same can be obtained from figures 4.10 and 4.11 for NIFS-V'. The obtained data suggests an exponential recovery within the first six weeks. The recovery for the doped NIFS-V' and NIFS-V are similar as shown in figure 4.12.

#### 4.2.2.2 Irradiation with 5000 Gy

The irradiation of the samples was repeated with an additional radiation dose of 4000 Gy which leads to a total irradiation of 5000 Gy. This is about  $10\times$  the expected maximum energy deposit at the central region of the detector and hence interesting with respect to a higher safety but also possible defects at different energies which have not been observed for the 1000 Gy study.

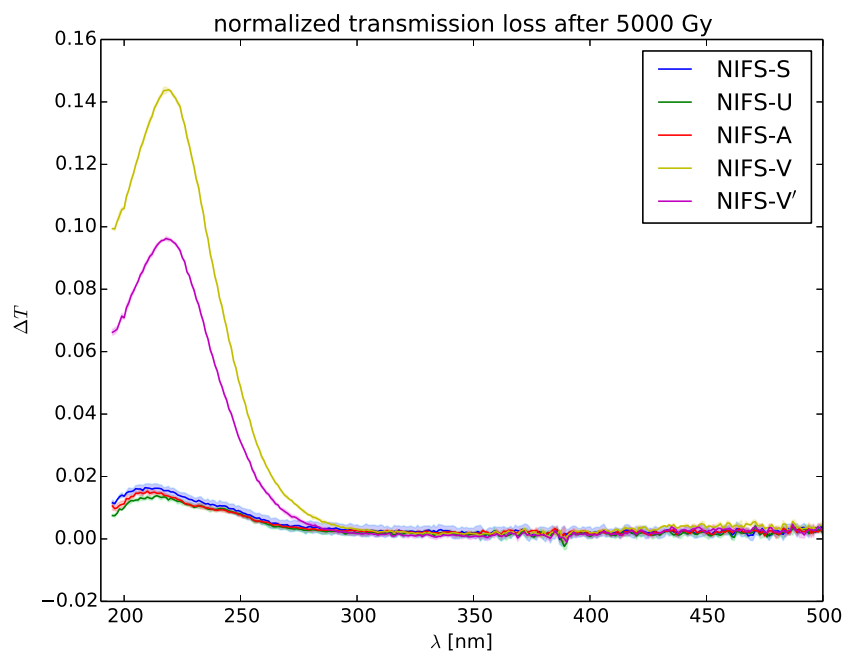


**Figure 4.13:** Normalized transmittance loss after irradiation with a dose of 5000 Gy. The samples NIFS-V and NIFS-V' which contain less OH show a larger change in transmittance.

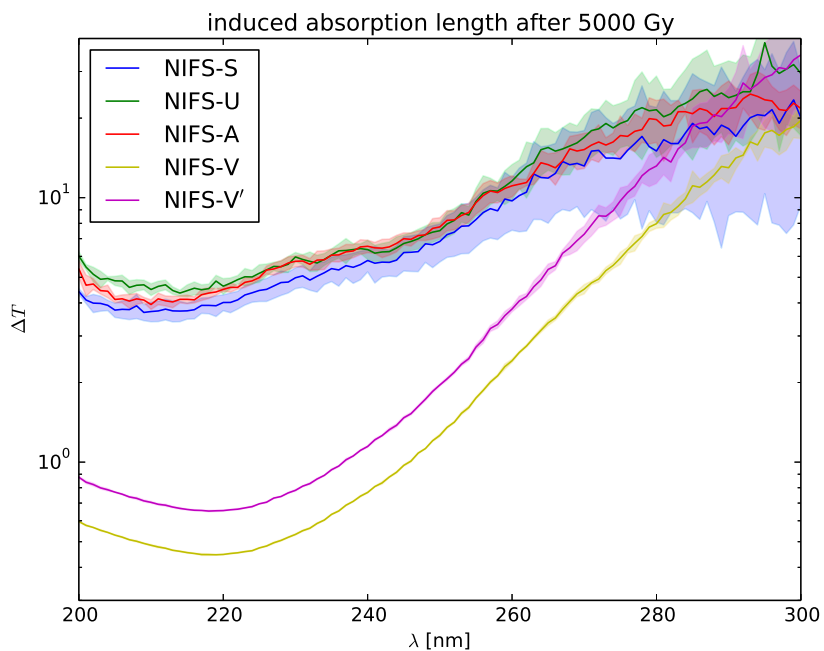


**Figure 4.14:** Absorption length after irradiation with a dose of 5000 Gy.

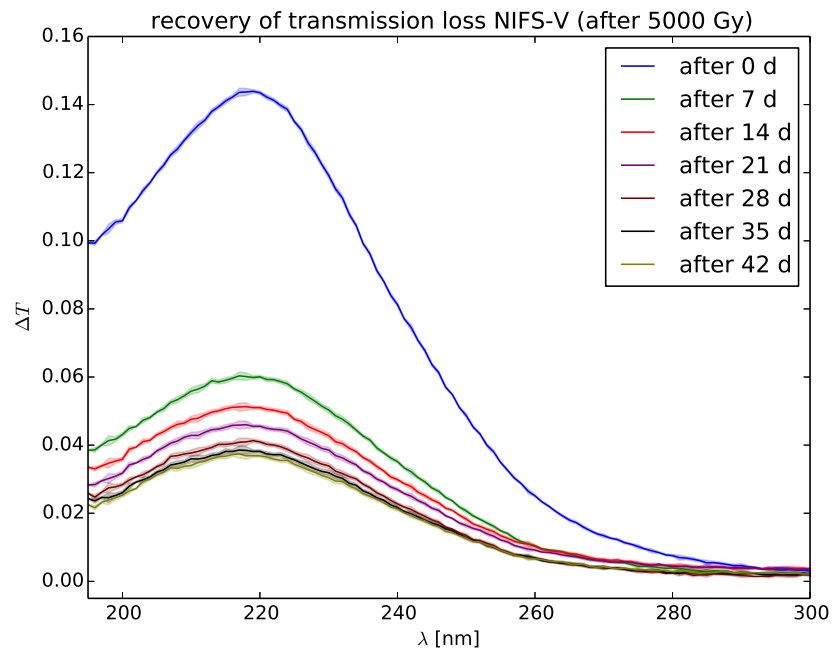


Figure 4.15: Recovery of normalized transmittance loss after irradiation with 5000 Gy for NIFS-V.

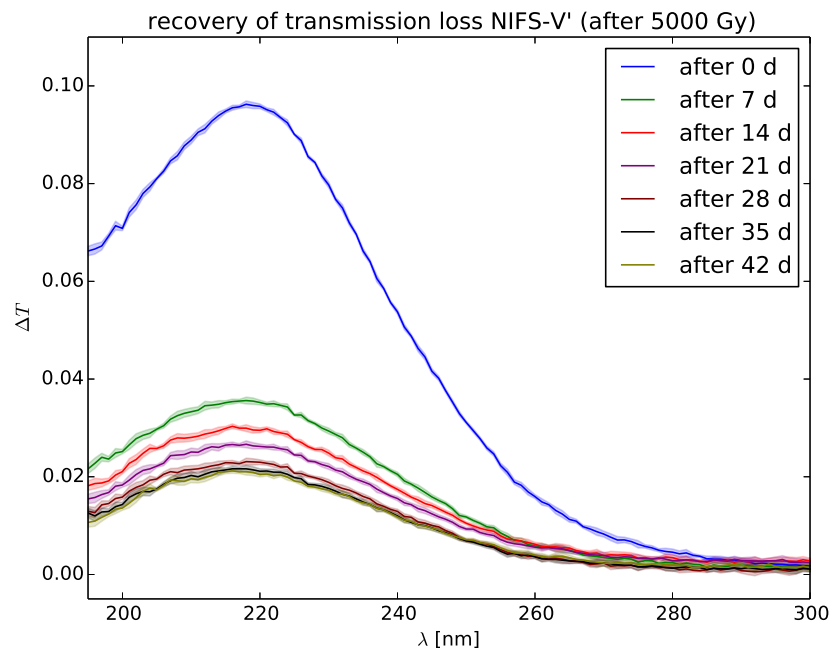
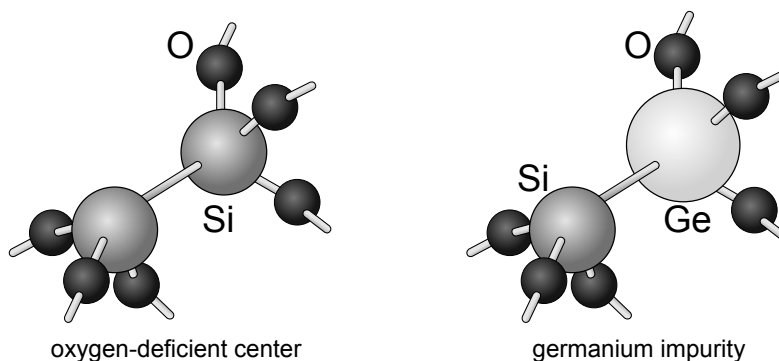


Figure 4.16: Recovery of normalized transmittance loss after irradiation with 5000 Gy for NIFS-V'.

Figures 4.13 and 4.14 show the normalized transmittance loss and induced absorption length after the irradiation with 5000 Gy. The previously present absorption band around 215 nm does not suggest any saturation in comparison to the measurements obtained at 1000 Gy despite the relatively high radiation. For the wet samples NIFS-S, -U and -A an additional absorption between 240 nm and 250 nm becomes visible. The source of this absorption could be a germanium impurity which is depicted in figure 4.17. As the germanium impurity in NIFS-A is smaller than for NIFS-S and -U but the effect appears similar for all three samples this explanation is rather improbable. Besides one would expect an absorption band around 300 nm which is created in the same way as the  $E'$  center in an intact silica network. Another reason could be the previously mentioned ODC (see also figure 4.17). Although neutrons and heavy ions are not directly emitted by the  $^{60}\text{Co}$ -source it is possible that these defect centers are created by related processes. As no absorption line was visible before and after the irradiation with 1000 Gy it seems likely that the ODCs were created during the continuing irradiation. As the  $E'$  defect dominates the spectra for NIFS-V and -V' an absorption line can not be clearly observed. The creation of new ODCs also leads to a continuous creation of  $E'$  centers which can be validated by the rise in the transmittance loss.



**Figure 4.17:** The left bond shows an oxygen-deficient center and the right bond a germanium impurity.

In the style of the previous measurement the normalized transmittance loss was measured for seven weeks. Figures 4.15 and 4.16 contain the wavelength dependent normalized transmittance loss for NIFS-V and -V'. The amplitudes of each week are summarized in figure 4.18. The data points at zero days have been excluded from the fit. The deviation for the data points at zero days could be explained by a different fast healing process. In comparison to the relaxation after the irradiation with 1000 Gy the healing process has slowed down. Interestingly the coefficient  $\mu$  for NIFS-V and NIFS-V' became almost equal. The observed relaxation depicts an important property of synthetic fused silica glasses and NIFS in particular. In addition to a rapid self healing which becomes obvious directly after the irradiation of wet and dry fused silicas a long-ranging process continues to repair defect

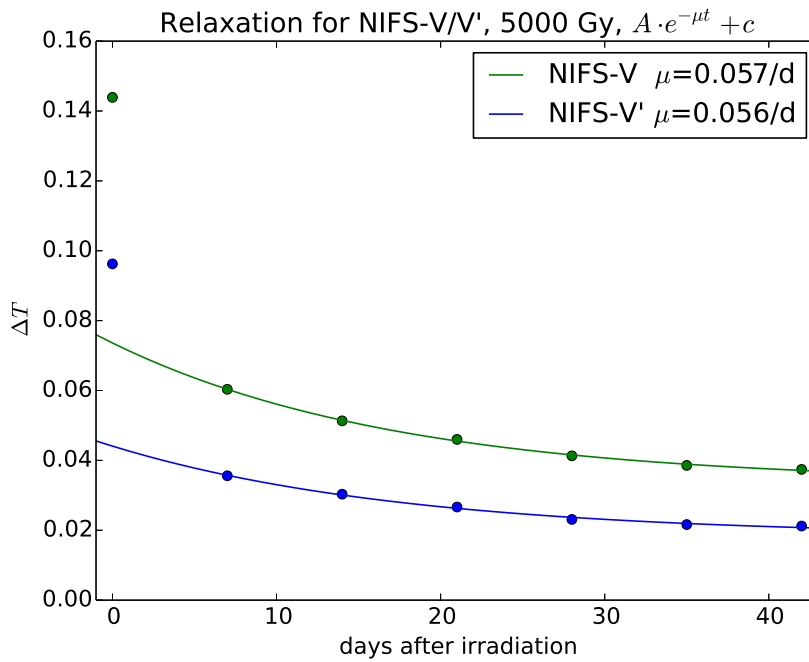


**Figure 4.18:** Relaxation plot after irradiation with a dose of 5000 Gy. The data point at 0 days was excluded from the fit.

centers in the long term. Therefore, when talking about radiation hardness, it is not sufficient to quantify only the induced transmittance loss but one also has to take into account the time period of the exposure. Whereas the samples were irradiated within several hours the same amount of radiation inside the  $\bar{P}$ ANDA Endcap Disc DIRC will be induced over several years. Based on the presented data all NIFS types are usable in the  $\bar{P}$ ANDA DIRC detectors. Experiments which require a high transmittance below 300 nm have to evaluate whether the usage of NIFS-V or -V' is necessary for their performance goals and with respect to the amount and time period of the irradiation.

## 4.3 Radiator

### 4.3.1 Requirements

The Disc DIRC consists of four large fused silica radiators where the Cherenkov photons are emitted by traversing charged particles. Together they form a regular dodecagon which lies within a circle with a radius of roughly 1 m. The center has a rhombic opening of 96 cm in x and 48 cm y-direction which leaves space for the antiproton beam and the acceptance region of the  $\bar{P}$ ANDA Forward Spectrometer. The dodecagonal shape was chosen with respect to the alignment of the MCP-PMTs to the magnetic field, the available space due to the surrounding mechanics and to minimize the number of polished surfaces. The geometry

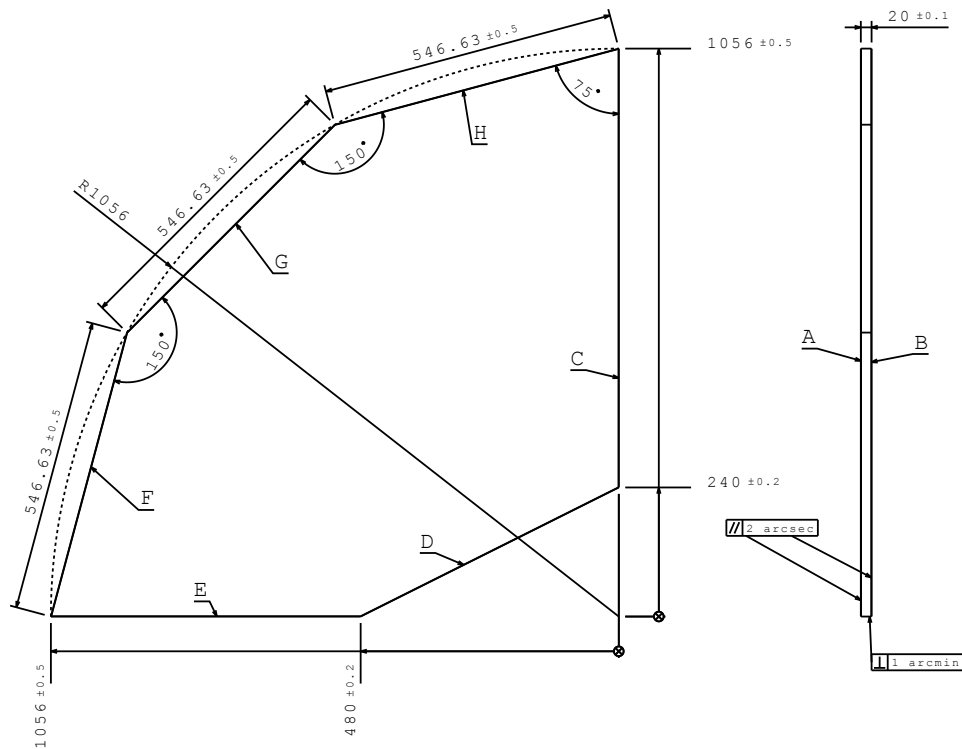


**Figure 4.19:** The technical drawing shows the shape and the corresponding dimensions and tolerances of the radiator.

for one radiator is shown in a technical drawing in figure 4.19 along with the corresponding dimensions and tolerances. The radiators will not be optically contacted to each other. Early proposals envisaged one large connected radiator which turned out to be impractical because of its size. In addition the segmentation into four independent radiators and therefore quadrants carries the advantage of a modular setup. A general challenge in connection with the radiator is its size and shape. Only few manufacturers operate polishing machines which can handle diameters above 60"  $\approx$  1.5 m. This is why the radius of the dodecagon was initially limited to 1056 mm. In this connection the option of six sixth instead of four quadrants had been evaluated. It was found that despite a larger overlap of the photon pattern the separation worked in a similar way [Mer14c]. Nevertheless as this option is not beneficial from an economical point of view it was not pursued. Another general concern are sharp corners (like C-H and E-F, see figure 4.19) which require very careful handling. As stated in table 4.1 the radiator has to provide a high transmittance and surface quality. These requirements are necessary in order to provide a sufficient amount of Cherenkov photons for the reconstruction but also to preserve the angle information. Typically synthetic fused silica possesses excellent transmittance properties with attenuation lengths far above 100 m for the relevant wavelengths. Another inherent property is the chromatic dispersion

category	side	specification
form error	A, B	slope $\leq 50 \mu\text{rad}$
	A, B	$\sigma_{\text{slope}} \leq 5 \mu\text{rad}$
TTV	A, B	$\leq 15 \mu\text{m}$
	C, E, F, G, H	25 $\mu\text{m}$ Peak-to-Valley (PV)
roughness	A, B,	1.5 nm RMS
	C, E, F, G, H	5 nm RMS
scratch/dig	all sides	80/50 or better
edge chips	all sides	10 chips/m and $\leq 1 \text{ mm}$
chamfers		< 0.5 mm for long sides < 2 mm for corners

**Table 4.3:** Surface specifications of the radiator. The Letters refer to the technical drawing in figure 4.19. TTV stands for total thickness variation.

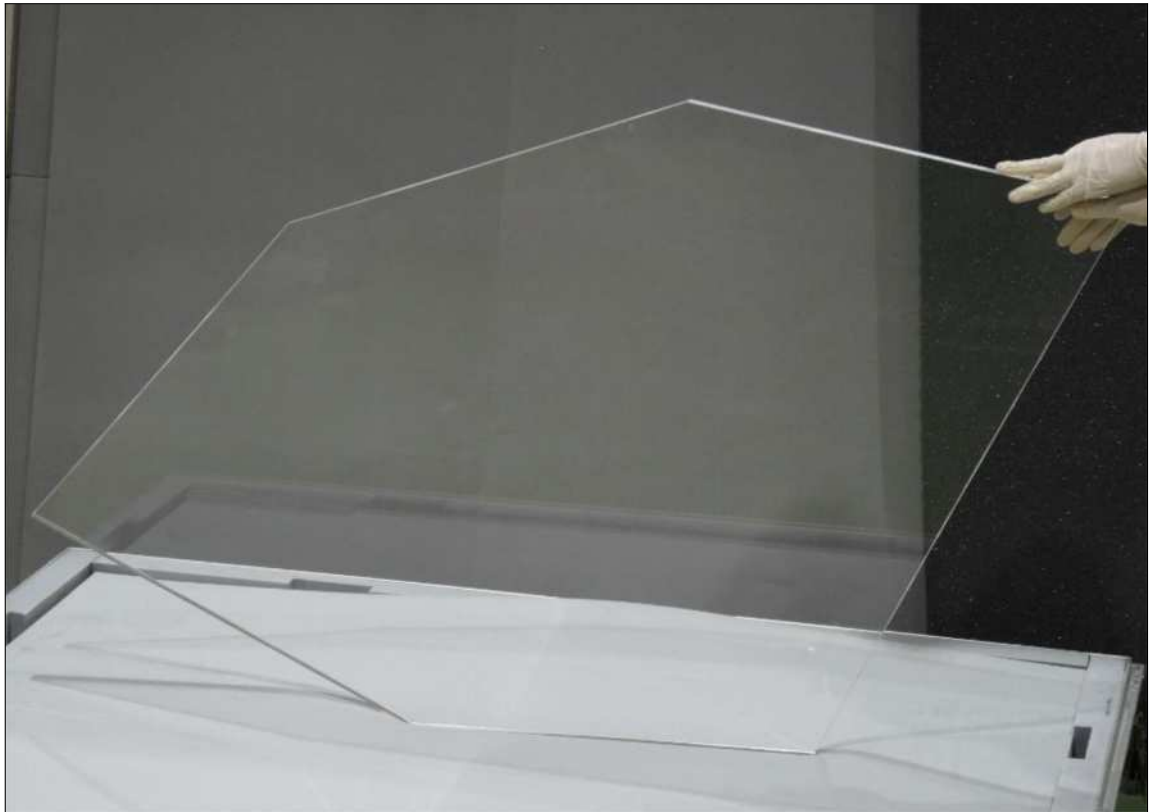


**Figure 4.20:** The first trial of producing a radiator for the  $\bar{\text{P}}\text{ANDA}$  Disc DIRC according to the specifications named in figure 4.19 and table 4.3. Courtesy of Nikon [Sug15].

which can be quantified by the Abbe number

$$v = \frac{n_D - 1}{n_F - n_C} \quad (4.5)$$

where  $n_D$ ,  $n_F$  and  $n_C$  correspond to the refractive indices at the wavelengths of the Fraunhofer spectral lines D-, F- and C (589.3 nm, 486.1 nm and 656.3 nm respectively). A typical Abbe number for synthetic fused silica is 67 which indicates a low dispersion. Another internal figure of merit is the homogeneity of the material. Inhomogeneities might lead to diffraction-like patterns (also called lobes) [Coh03]. They can be avoided by an appropriate production process. In the case of DIRC detectors also the surface quality is of utmost importance as Cherenkov photons can be reflected more than one hundred times off surfaces by total internal reflection. Therefore the surface roughness has to be controlled. In comparison to barrel-shaped DIRCs such as [Ada05, Swa16, Ina14] the photon paths are typically shorter for the EDD and hence the number of reflections and the demands on the surface roughness are lower. As the Cherenkov photons do not have more than one reflection from any side surface (C or E) comparably low requirements are imposed on the surface roughness and the size of the chamfers. The same applies to the surfaces F, G and H to which the ROMs are coupled via the prisms. The preservation of the photon angle has to be achieved by a high parallelism and a low form error of the two large surfaces A and B. On the other hand according to the previous line of argument precision requirements for perpendicularity of the side surfaces C, E, F, G, H is not very high in comparison to other DIRC designs. Table 4.3 completes figure 4.19 with surface related specifications.

Nowadays optical manufacturers have developed techniques for lapping and polishing of fused silica which enables them to produce optics with highly parallel surfaces and a excellent surface roughness. It is important to mention at this point that this is even feasible for very large optics with untypical geometries like the EDD radiator as can be seen in figure 4.20. The following subsections continue to discuss the impact of the form error and the roughness in the framework of the EDD and justify the choices made in table 4.3. In addition different measurement techniques to verify them experimentally are being presented.

## 4.3.2 Quality Measurements

### 4.3.2.1 Transmittance and Reflectance

#### Transmittance

The transmittance of a material is usually quantified by the attenuation length  $\Lambda$  or the attenuation coefficient  $\mu = 1/\Lambda$ . It is a wavelength dependent property which is caused by absorption and scattering inside the medium. Absorption occurs when photons excite single atoms, molecules or the lattice whereas scattering is dominated by Rayleigh scattering.

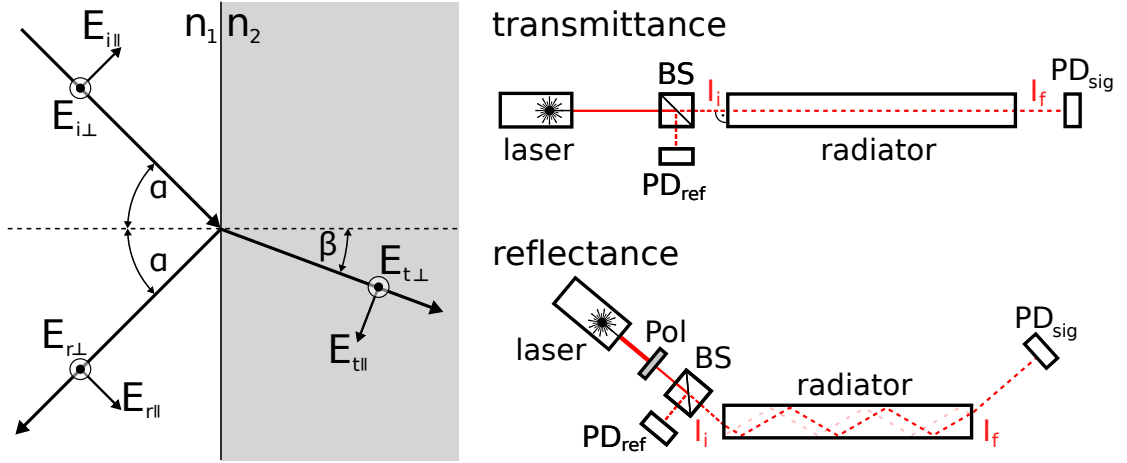


**Figure 4.21:** The left part defines the angles and amplitudes of the incoming, reflected and transmitted electromagnetic waves at the boundary of two media with different refractive indices. The top right part illustrates a typical setup for a transmittance measurement of a large optical sample. The modified setup for the reflectance measurement is shown in the bottom right part. *Pol* stands for polarizer, *BS* for beam splitter and  $PD_{ref}$  ( $PD_{sig}$ ) for the reference (signal) photo diode.

Impurities alter the lattice and therefore the transmittance (see also section 4.2). The requirement for the attenuation length  $\Lambda$  has to be chosen in such a way that not too many photons are lost. Typical values for synthetic fused silica exceed 100 m [BarTDR, Hol11, Wan16] which in conjunction with radiation-induced defects as described in 4.2 does not restrict its usage.

The transmittance can be measured by coupling a laser beam with intensity  $I_i$  into the optical component and measuring the outgoing intensity  $I_f$ . This result has then to be properly corrected for Fresnel losses which depend on the wavelength, the polarization, the angle of incidence and the angle of refraction when leaving the optical component. These losses can be calculated using the Fresnel equations which describe the behavior of a plane, electromagnetic wave which moves between two media of different refractive indices. They were derived by Augustin-Jean Fresnel from Maxwell's equations. Depending on the polarization of the electromagnetic wave the ratio of the initial ( $E_i$ ) and the transmitted/reflected ( $E_t/E_r$ ) amplitude is given by

$$t_{\perp} = \frac{E_{t\perp}}{E_{i\perp}} = \frac{2N_1 \cos \alpha}{N_1 \cos \alpha + \frac{\mu_{r1}}{\mu_{r2}} N_2 \cos \beta}, \quad (4.6)$$

$$r_{\perp} = \frac{E_{r\perp}}{E_{i\perp}} = \frac{N_1 \cos \alpha - \frac{\mu_{r1}}{\mu_{r2}} N_2 \cos \beta}{N_1 \cos \alpha + \frac{\mu_{r1}}{\mu_{r2}} N_2 \cos \beta}, \quad (4.7)$$

$$t_{\parallel} = \frac{E_{t\parallel}}{E_{i\parallel}} = \frac{2N_1 \cos \alpha}{N_1 \cos \beta + \frac{\mu_{r1}}{\mu_{r2}} N_2 \cos \alpha}, \quad (4.8)$$

$$r_{\parallel} = \frac{E_{r\parallel}}{E_{i\parallel}} = \frac{N_1 \cos \beta - \frac{\mu_{r1}}{\mu_{r2}} N_2 \cos \alpha}{N_1 \cos \beta + \frac{\mu_{r1}}{\mu_{r2}} N_2 \cos \alpha}. \quad (4.9)$$

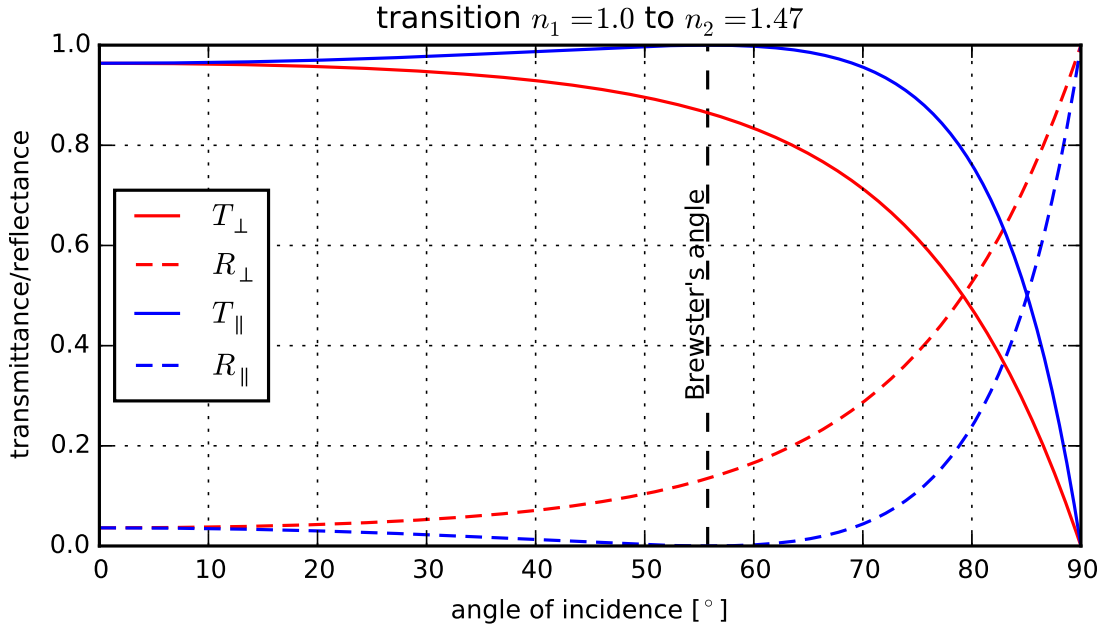


**Figure 4.22:** Transmittance and reflectance according to Fresnel equations for a transition between vacuum and quartz. At the Brewster's angle of  $55.77^\circ$  parallel polarized light is fully transmitted.

Here  $N$  denotes the complex refractive index  $N = n + ik = \sqrt{1 + \chi}$  and  $\mu_r$  the relative permeability, and the indices represent the different materials. The left part of figure 4.21 illustrates the remaining quantities. For DIRC related measurements, where the transition happens usually between dielectric materials, equations 4.6-4.9 can be reduced to

$$t_{\perp} = \frac{2n_1 \cos \alpha}{n_1 \cos \alpha + n_2 \cos \beta}, \quad (4.10)$$

$$r_{\perp} = \frac{n_1 \cos \alpha - n_2 \cos \beta}{n_1 \cos \alpha + n_2 \cos \beta}, \quad (4.11)$$

$$t_{\parallel} = \frac{2n_1 \cos \alpha}{n_1 \cos \beta + n_2 \cos \alpha}, \quad (4.12)$$

$$r_{\parallel} = \frac{n_1 \cos \beta - n_2 \cos \alpha}{n_1 \cos \beta + n_2 \cos \alpha}. \quad (4.13)$$

The intensities which correspond to the transmittance ( $T$ ) and reflectance ( $R$ ) are then given by

$$T_{\perp/\parallel} = \left| \frac{n_2 \cos \beta}{n_1 \cos \alpha} t_{\perp/\parallel}^2 \right|, \quad (4.14)$$

$$R_{\perp/\parallel} = \left| r_{\perp/\parallel}^2 \right|. \quad (4.15)$$

As the speed of light and the direction differs between the two media according to Snell's law

$$n_1 \sin \alpha = n_2 \sin \beta \quad (4.16)$$

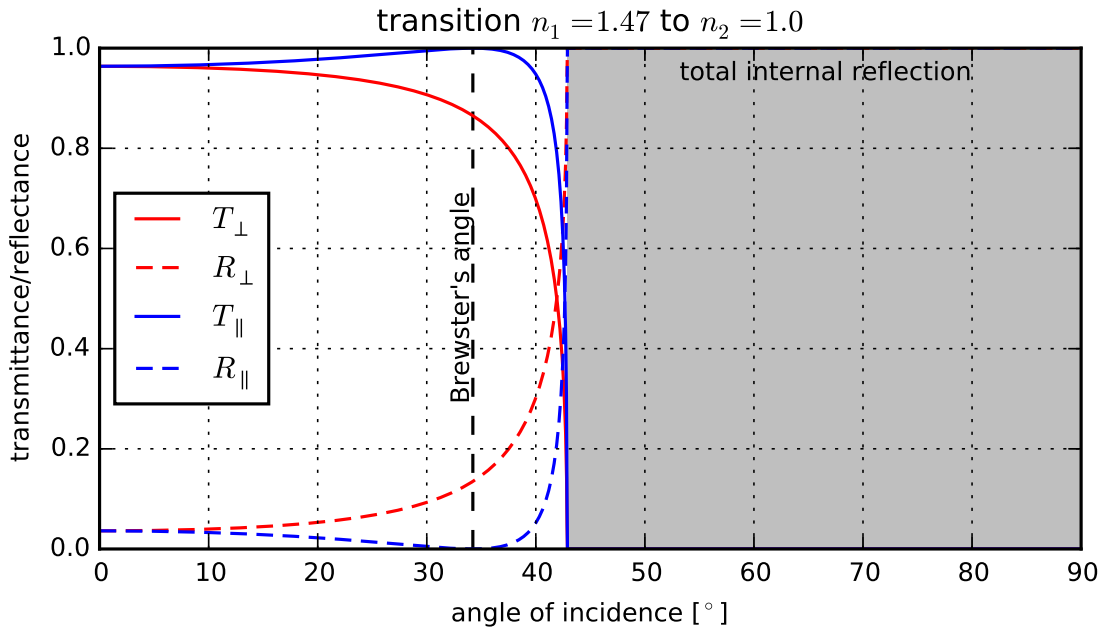


**Figure 4.23:** Transmittance and reflectance according to Fresnel equations for a transition between vacuum and quartz. Besides Brewster's angle at  $34.22^\circ$  light is completely reflected by total internal reflection for angles larger  $42.86^\circ$ .

and

$$v_1 n_1 = v_2 n_2 = c \quad (4.17)$$

the transmittance  $T$  is not equal to the square of transmitted amplitude  $t$ . Due to conservation of energy the transmittance and reflectance are related by

$$T_{\perp/\parallel} + R_{\perp/\parallel} = 1. \quad (4.18)$$

Figures 4.22 and 4.23 illustrates the transmittance and reflectance for perpendicular and parallel polarized photons between the vacuum and fused silica and vice versa. For the transition into the optically less dense medium the onset of total internal reflection occurs at

$$\theta_{tot} = \arcsin \frac{n_2}{n_1} \quad (4.19)$$

as shown in the second plot. In both cases Brewster's angle

$$\theta_B = \arctan \frac{n_2}{n_1} \quad (4.20)$$

defines the angle of incidence where parallel polarized photons are fully transmitted. It can be used to calibrate the polarizer and/or the angle of incidence of the initial photon beam. In case of a transmission measurement laser light can be coupled into and out of the sample perpendicularly ( $\alpha = 0^\circ$ ), provided that two distant surfaces are parallel. This reduced

equations 4.10-4.13 to the much simpler form

$$T_{\alpha=0^\circ} = \frac{4n_1n_2}{(n_1 + n_2)^2}, \quad (4.21)$$

$$R_{\alpha=0^\circ} = \left( \frac{n_1 - n_2}{n_1 + n_2} \right)^2 \quad (4.22)$$

where the transmittance and reflectance is also independent of the polarization of the light. A typical setup for a transmission measurement is depicted in the top right part of figure 4.21. A collimated laser beam is split into two parts: one for a reference measurement and the other for probing the sample. According to equations 4.21 and 4.22 the probing beam is then traversing the sample perpendicularly if possible. The outgoing intensity measured at the signal photo diode is then given by

$$I_f = I_i \cdot T_{n_1 \rightarrow n_2} \cdot \tau \cdot T_{n_2 \rightarrow n_1}. \quad (4.23)$$

The attenuation length  $\Lambda$  is calculated according to

$$\Lambda = -\frac{l}{\ln \tau}, \quad \tau = \frac{I_f}{I_i (T_{\alpha=0^\circ})^2}. \quad (4.24)$$

Equation 4.23 does not include corrections for higher orders which are considered in the more general equation

$$I_f = I_i \sum_{j=0}^k T_{\alpha=0^\circ}^2 \cdot R_{\alpha=0^\circ}^{2j} \cdot e^{-(2j+1)\frac{l}{\Lambda}}. \quad (4.25)$$

Expressed in numbers the correction for a transition from quartz in a vacuum is around 3.5% for no ( $j = 0$ ), 0.12% for two ( $j = 1$ ) and  $1.4 \cdot 10^{-4}\%$  for four internal reflections ( $j = 2$ ). In the context of a transmittance measurement for a Disc DIRC radiator the following aspects have to be taken into account:

- the final Disc DIRC radiator does not have any parallel side surfaces. Therefore the described standard setup must be altered and a polarizer has to be added as the measurement cannot be done at  $\alpha = \beta = 0$ . On the other hand no higher corrections have to be included,
- the accuracy of the beam angle of incidence has to be determined in order to assign a correct systematic error,
- the laser has to run stable. As the collimation of the beam is not perfect the setup might be extended by additional optics prior to the beam splitter and/or polarizer,
- a halo of the laser beam might be accidentally reflected into the sensor by the radiator which has to be taken into account for in the systematic error.

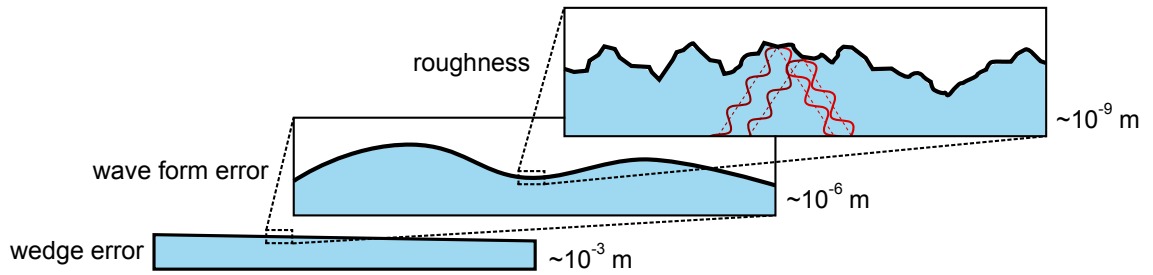


**Figure 4.24:** Illustration of different kinds of surface errors. Taking a look at the full size only large deviations such as a wedge error can be obtained. Zooming in on a microscopic level the surface structure shows so-called wave form errors which normally are a result of vibrations during the polishing procedure. A further magnification reveals the surface roughness and allows a phenomenological derivation of photon loss despite total internal reflection.

## Reflectance

The reflectance coefficient is defined as the ratio of the actual to the theoretical value of the light intensity reflected from a surface. Loss of intensity for reflections is connected to the surface roughness  $h$  which is defined by

$$h = \sqrt{\frac{1}{n} \sum_{i=0}^n z_i^2}, \quad (4.26)$$

with  $z$  being height differences of the profile from the mean surface level [Mrd07].

The setup for the reflectance measurement is shown in the bottom right corner of figure 4.21. In addition to the transmittance measurement setup a polarizer must be added as the angle of incidence has to be chosen unequal to zero and such that a high number of internal reflections  $N$  is provided. In analogy to equation 4.23 the intensity of the outgoing beam  $I_f$  is given by

$$I_f = I_i \cdot T_{n1 \rightarrow n2} \cdot \tau \cdot \rho^N \cdot T_{n2 \rightarrow n1} \quad (4.27)$$

with the reflectance coefficient  $\rho$  and the modified internal transmittance  $\tau$ :

$$\rho = \sqrt[N]{\frac{I_f}{I_i \cdot T_{n1 \rightarrow n2} \cdot \tau \cdot T_{n2 \rightarrow n1}}}, \quad \tau = e^{-\frac{\sqrt{l^2 + (Nd)^2}}{\Lambda}}. \quad (4.28)$$

$l$  and  $d$  being the radiator length and thickness. The value of  $\Lambda$  can either be taken from a previous transmittance measurement or be determined simultaneously with  $\rho$  by carrying out a series of measurements with varying angles of incidence or numbers of reflections. As illustrated in figure 4.24 the decrease in intensity can be explained by destructive interference due to deviations in the surface profile. Unlike shown in the sketch these deviations usually amount to only a very small fraction of the photon wavelength and are connected to atomic structure of the material. The relation between the reflectance coefficient and the

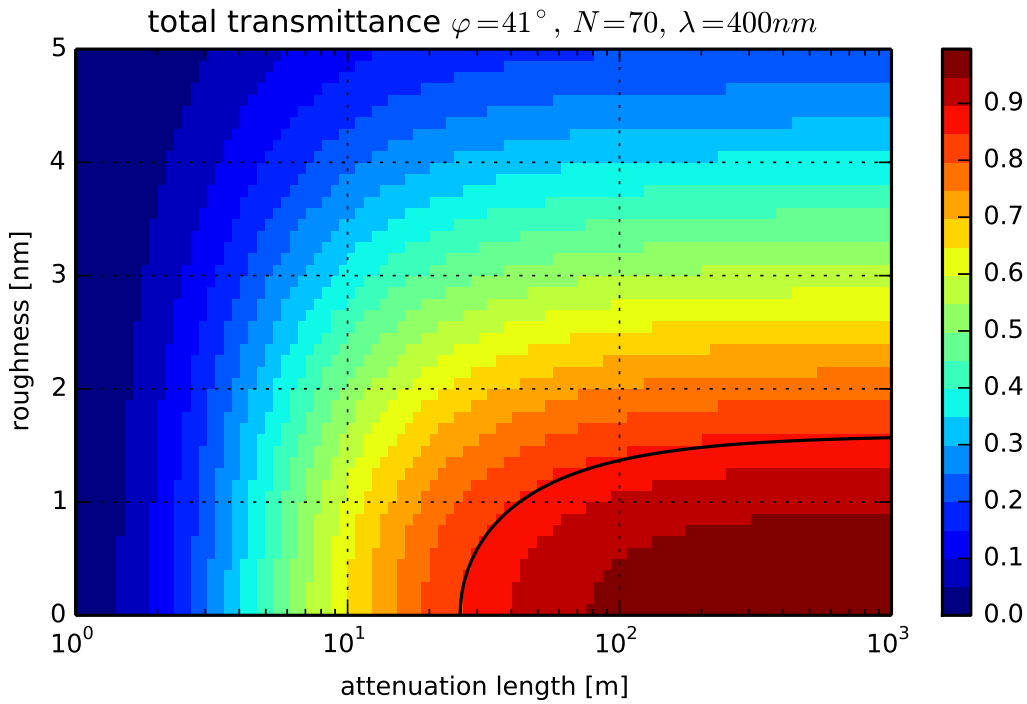


**Figure 4.25:** The total transmittance for different roughness values and attenuation lengths. For attenuation lengths above 400 m the transmittance only depends on the surface roughness. The black line indicates a total transmittance of 85%.

surface roughness can be derived using scalar scattering theory (e.g. see [Bec63]) and leads to

$$h = \frac{\lambda \sqrt{1 - \rho}}{4\pi n \cos \theta}. \quad (4.29)$$

A measurement of the Disc DIRC radiator surface roughness has to consider the following aspects:

- since no parallel side surfaces exist for the final Disc DIRC radiator light should be coupled in via prisms which adds an additional source for errors,
- as the angle of incidence of the laser beam differs from  $0^\circ$ , the polarization has to be adjusted and included in the systematic error,
- the laser has to run stable which usually is the case after several hours. As the collimation of the beam is not perfect the setup might be extended by additional optics prior to the beam splitter and/or polarizer,
- a halo of the laser beam might be accidentally focused by the radiator which has to be taken into account for in the systematic error,

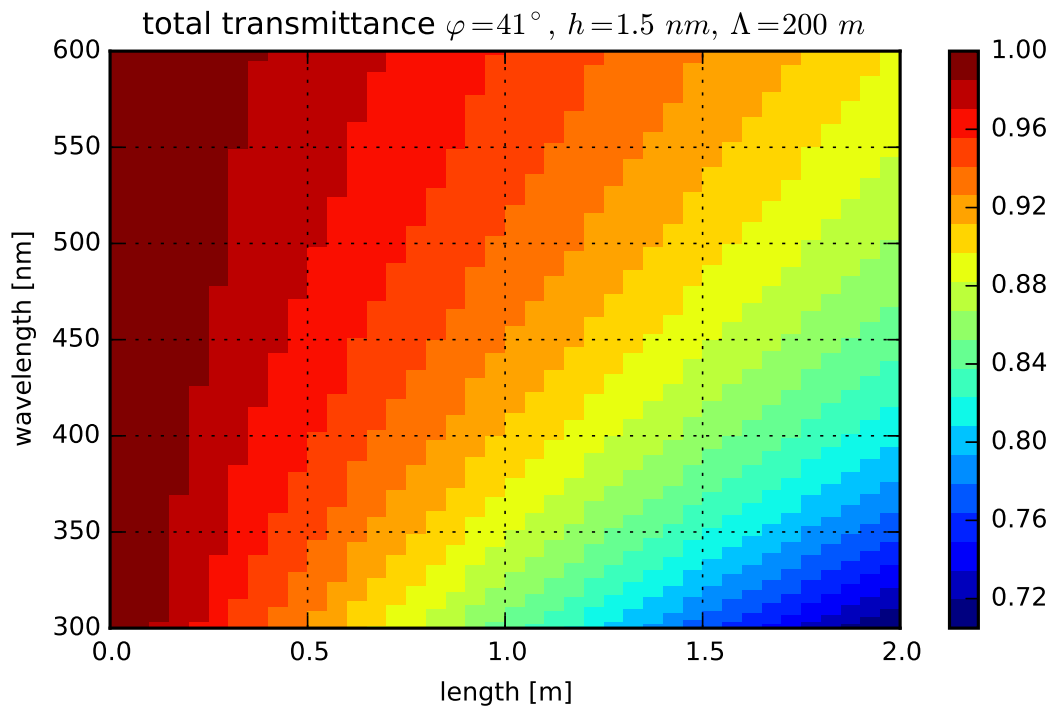


**Figure 4.26:** The total transmittance for different roughness values and projected path lengths. Shorter wavelengths show a rapid decrease in transmittance.

- any dust or residues on the radiator surface might lead to additional light losses which should be avoided by properly cleaning the radiator.

The impact of surface roughness and attenuation length on the total transmittance of photons on their way through the radiator towards the ROMs is calculated in figure 4.25. The calculation was done for the worst case scenario where the charged particle traverses the radiator at the farthestmost position with an angle  $\varphi = 41^\circ$  between the photon path and the radiator surface which results in a projected path length of 1.5 m (projected on the x-y-plane). Here the light travels a total distance of roughly 2 m inside the radiator and is reflected 100 times off its surface. For the given scenario no significant improvement can be obtained for attenuation lengths above 400 m. Even attenuation lengths below 100 m allow a total transmittance above 80% subject to the condition that the surface roughness is small. A more complete picture of the situation can be obtained by taking into account figure 4.26 where surface roughness and attenuation length are fixed according to the minimum requirements stated in table 4.3. Therefore the wavelength and the projected path length of the photon are varied which also brings to mind why photons with smaller wavelengths are further suppressed as expected from a pure transmittance measurement. This effect might even be more excessive due to surface contaminations or other effects [Coh03]. For convenience the figure also assumes a constant attenuation length for different wavelengths.

### 4.3.2.2 Profile Measurement

The surfaces of the  $\bar{P}$ ANDA Endcap Disc DIRC are meant to be perfectly planar. In reality this demand can only be partly satisfied as indicated in figure 4.24. Besides the previously treated roughness a so-called wave form error can be observed. This error usually originates from the polishing process and occurring vibrations. The application of different polishing methods might also lead to multiple overlapping wave patterns. Unlike the surface roughness the wave form is not a source for light loss but leads to non conservation of the angle  $\varphi$  between the photon trajectory and the surface plane. In this connection a profile measurement shall investigate the form of a delivered radiator in order to estimate the smearing due to wave form errors and therefore also to qualify the sample.

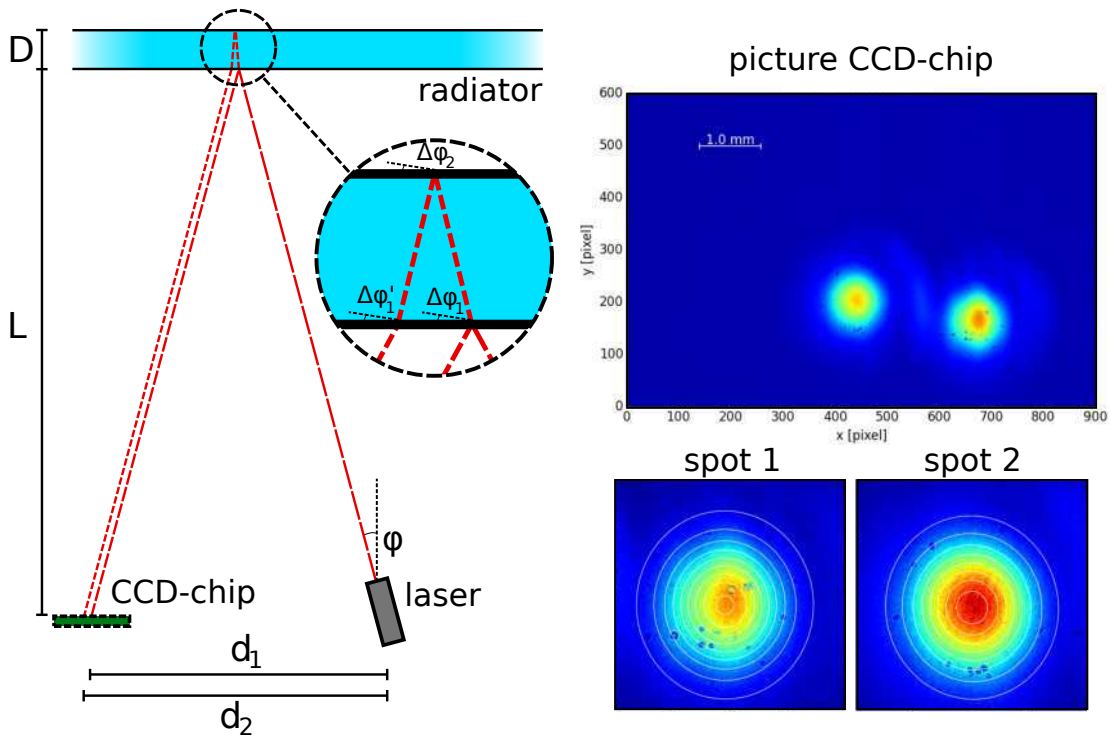


**Figure 4.27:** The left part schematically shows the top view of setup for the surface profile measurement. The top right picture is a colored example picture taken by the CCD chip which shows the direct (indirect) reflection off the (back-) surface of the radiator and the corresponding 2-dimensional-fits using a Gaussian.

In general different methods for surface measurements which are based on tactile (e.g. a profilometer with a diamond stylus) or non-tactile methods (e.g. white light interferometry) are available. The challenge which comes with DIRC radiators is their large size which currently exceeds the capabilities of many producers on the market. Following the need for a large-scale measurement with micrometer precision a non-tactile setup was developed

similar to [Foh11] which can be used for in-house quality measurements. Instead of a direct profile measurement the setup allows to quantify the thickness variation of the sample. As the Cherenkov photons propagate along a zig-zag-path this variation is of high importance to quantify the performance of the radiator.

## Setup

The temporary setup was realized on an optical table. At one end of the table a linear stage with a translation length of 1.2 m was positioned vertically. A second linear stage was mounted horizontally and centric on the vertical stage's carrier forming a cross-like structure. The carrier of this second linear stage was equipped with a platform on which a laser and a programmable CCD chip by Jenoptik with a  $36 \times 24 \text{ mm}^2$  full frame active area was mounted. This setup allowed to scan an area of roughly  $1 \text{ m}^2$ . The radiator was then placed upright on the opposite side of the optical table (see schematic drawing in figure 4.27).

The underlying idea is to measure the relative position changes of the reflections off the radiator with the CCD chip and to derive the slope deviation using this information. For the measurement two reflections are used:

- a direct reflection off the surface facing the laser and CCD chip,
- an indirect reflection off the back surface of the radiator.

In principle the direct reflection allows a measurement of the front surface according to

$$\begin{aligned}
 \Delta d_1 &= d'_1 - d_1 \\
 &= L \tan(\varphi + \Delta\varphi) + L \tan(\varphi + \Delta\varphi + 2\Delta\varphi_1) - 2L \tan \varphi \\
 &\approx L(\varphi + \Delta\varphi) + L(\varphi + \Delta\varphi + 2\Delta\varphi_1) - 2L\varphi \\
 &= 2L\Delta\varphi + 2L\Delta\varphi_1.
 \end{aligned} \tag{4.30}$$

where  $d_1$  ( $d'_1$ ) is the position of the reflection on the CCD chip before (after) moving the platform to a new position. Small-angle approximation is valid as the deviations are very small in reality. Rearranging the equation leads to an expression for the slope deviation for the front surface:

$$\Delta\varphi_1 = \frac{\Delta d_1}{2L} - \Delta\varphi. \tag{4.31}$$

$\Delta\varphi$  is the deviation of the laser angle which occurs as the linear stage is not perfectly planar. The surface profile could therefore only be measured if the deviation of the laser angle is very small in comparison to the waviness of the surface profile or precisely known. To work around this deficit the indirect reflection is taken into account revealing information of the

back surface. The formula is hereby derived according to

$$\begin{aligned}
\Delta d_2 &= d'_2 - d_2 \\
&= L \tan(\varphi + \Delta\varphi) + D \tan\left(\arcsin\left(\frac{1}{n} \sin(\varphi + \Delta\varphi + \Delta\varphi_1)\right) - \Delta\varphi_1\right) + \\
&\quad D \tan\left(\arcsin\left(\frac{1}{n} \sin(\varphi + \Delta\varphi + \Delta\varphi_1)\right) - \Delta\varphi_1 + 2\Delta\varphi_2\right) + \\
&\quad L \tan\left(\arcsin\left(n \sin\left(\arcsin\left(\frac{1}{n} \sin(\varphi + \Delta\varphi + \Delta\varphi_1)\right) - \Delta\varphi_1 + 2\Delta\varphi_2 - \Delta\varphi'_1\right)\right) + \Delta\varphi'_1\right) - \\
&\quad L \tan\varphi - 2D \tan\left(\arcsin\left(\frac{1}{n} \sin\varphi\right)\right) - L \tan\left(\arcsin\left(n \sin\left(\arcsin\left(\frac{1}{n} \sin\varphi\right)\right)\right)\right) \\
&\stackrel{\varphi'_1 = \varphi_1}{\approx} L(\varphi + \Delta\varphi) + \frac{D}{n}(\varphi + \Delta\varphi + \Delta\varphi_1) - D\Delta\varphi_1 + \frac{D}{n}(\varphi + \Delta\varphi + \Delta\varphi_1) - D\Delta\varphi_1 + 2D\Delta\varphi_2 + \\
&\quad L(\varphi + \Delta\varphi) + 2L\Delta\varphi_1 - 2nL\Delta\varphi_1 + 2nL\Delta\varphi_2 - 2L\varphi - 2\frac{D}{n}\varphi \\
&= 2(nL + D) \left( \frac{\Delta\varphi}{n} + \frac{\Delta\varphi_1}{n} - \Delta\varphi_1 + \Delta\varphi_2 \right).
\end{aligned} \tag{4.32}$$

$d_2$  and  $d'_2$  are the positions of the indirect reflections on the CCD chip before and after moving the platform to a new position. The position of the reflection is also influenced by the slope deviation  $\Delta\varphi_1$  when the laser enters and  $\Delta\varphi'_1$  when it leaves the radiator. The assumption  $\varphi'_1 = \varphi_1$  is valid in good approximation and leads to a much simpler expression which can subsequently be rearranged to

$$\Delta\varphi_2 = \frac{\Delta d_2}{2(nL + D)} - \frac{\Delta\varphi}{n} - \frac{\Delta\varphi_1}{n} + \Delta\varphi_1. \tag{4.33}$$

As the deviation of the laser angle  $\Delta\varphi$  appears here as well it can be eliminated by combining equations 4.31 and 4.33 to get the relative slope deviation between the front and back surface of the probed radiator:

$$\Delta\Phi = \Delta\varphi_2 - \Delta\varphi_1 = \frac{\Delta d_2 - \Delta d_1 \left(1 + \frac{D}{nL}\right)}{2(nL + D)}. \tag{4.34}$$

The relative slope deviation is almost directly proportional to the relative distance variation of the two reflections. It also shows that the measurement is relatively robust against errors as the refractive index  $n$  is precisely known,  $D$  can almost be neglected and depending on the length  $L$  the relative error becomes very small. The radiator can then be scanned horizontally and vertically to map the relative slope deviations of the surface and the relative slope  $\Phi$  can be calculated by integrating over the observed values for the slope deviation according to

$$\Phi_i = \Phi_{\text{offset}} + \sum_{j=0}^i \Delta\Phi_j, \tag{4.35}$$

where  $\Phi_{\text{offset}}$  technically has to be added because a relative measurement is not able to obtain any information on a possible wedge error. In order to get the relative thickness

variation of the radiator surfaces another integration step has to be performed given by

$$\Delta D_i = \Delta D_{\text{offset}} + \sum_{j=0}^i \Phi_j \cdot \Delta s, \quad (4.36)$$

where  $\Delta s$  represents the step size of the linear stage between two measurements.

In practice scans were performed by automatically moving the laser beam over a predefined area of the surface with a predefined discrete step size. For each step an image of the reflections on the CCD chip was taken and saved to the hard disc. This process was controlled by a LabVIEW program. The images were later analyzed individually by finding both spots and fitting their shapes with a 2-dimensional Gaussian function

$$f(x, y) = A \exp \left( - \left( \frac{(x - x_0)^2}{2\sigma_x^2} + \frac{(y - y_0)^2}{2\sigma_y^2} \right) \right). \quad (4.37)$$

In the rare case that a fit did not converge properly an exception was thrown, otherwise the positions  $x_{0,1}$ ,  $x_{0,2}$ ,  $y_{0,1}$  and  $y_{0,2}$  were then passed on to the integration. Hereby exceptions from the fitting routine were corrected by assigning the mean value from the measured neighboring points.

In order to execute the measurement properly the following steps are recommended:

- although the precision of the measurement scales with the distance  $L$  as can be seen in equation 4.34 it has to be chosen with care. Depending on the frequency and amplitude of the wave form error the reflexions on the CCD chip might overlap or even cross due to a large lever which causes problems in the reconstruction.
- in connection with the previous statement the laser beam angle should be chosen carefully. If chosen too large the CCD chip might not be large enough. On the other hand both reflexions could interfere and hamper the fitting of the spots.
- a pre-scan should confirm that all reflections stay within the frame of the CCD chip.
- depending on the size and quality of the laser beam additional optics such as a pinhole aperture or an attenuator should be added.
- the images were saved in the TIFF format to not lose any information. Therefore, if possible, it is recommended to narrow down the field of view in order to save disc space and speed up the subsequent analysis.
- due to vibrations during the movement of the linear stages a certain waiting time should be added before the image is taken.

## Measurements

The first measurement was done using the group's first synthetic fused silica radiator which has also been used for a testbeam experiment in 2013. This so-called old prototype radiator has the dimensions  $500 \times 500 \times 20 \text{ mm}^3$  with cut-outs at the four corners. It is made of Spectrosil<sup>®</sup> 2000 by Heraeus [Her16] who was also responsible for polishing the large surfaces without accepting any specifications. The radiator had to be placed 700 mm away from the CCD chip in order to avoid intersecting reflections. Before the two dimensional scan was commenced several one dimensional scans were performed with different step sizes in order to find a compromise regarding time and precision. Figure 4.28 shows the result for the calculated slope and thickness variation. For the step sizes 20 and 40 mm the substructure cannot be resolved whereas 1 and 2 mm hardly reveal additional details. In case of 5 and 10 mm the obtained slope is slightly shifted according to their value. The impact on the thickness variation is obvious for 20 and 40 mm. The remaining lines are in good agreement within a sub  $\mu\text{m}$ -range. Hence the step size for two dimensional scans was chosen to be 10 mm.

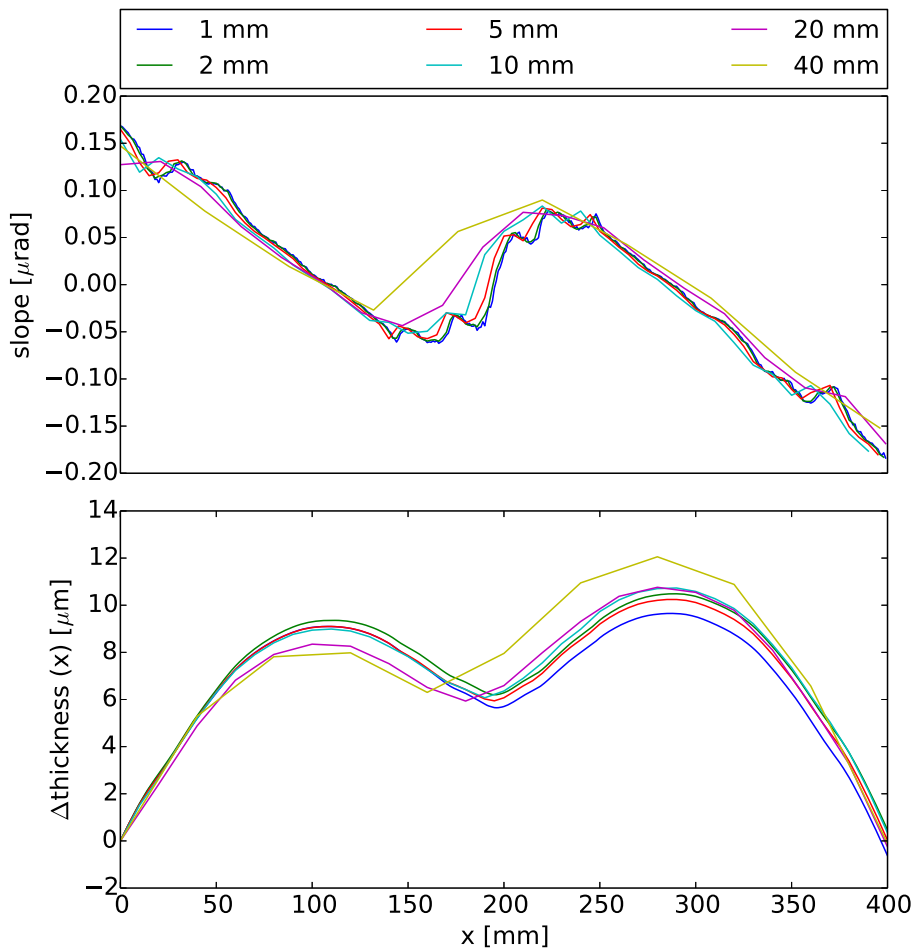


**Figure 4.28:** Profile scan of the old prototype radiator for different step sizes. In the present case a step size of 20 or 40 mm only gives a good approximation without revealing some of the details.

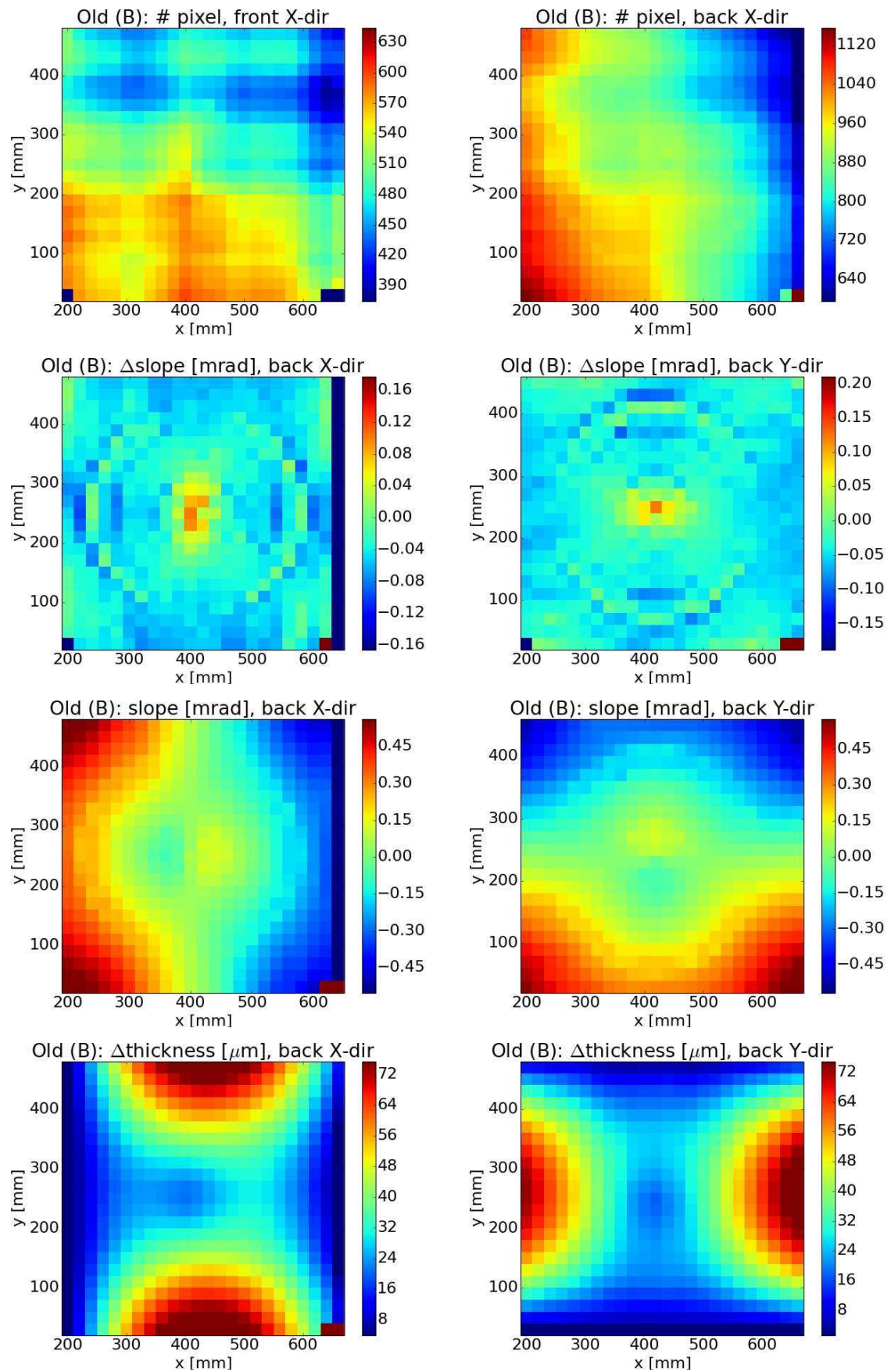


**Figure 4.29:** From top to bottom: recorded positions of reflections, calculated slope derivation, calculated slope and calculated thickness variation of the old prototype radiator. The top row shows only the data for the x-axis whereas the rest is the result for x and y.

The different plots in figure 4.29 summarize the measurements and calculations for one side of the radiator. In the top row of figure 4.29 the measured positions of the direct (front X-dir) and indirect (back X-dir) reflection in x-direction are shown. The bottom corners show a clear offset which are due to reflections of chamfers from a cut-out section facing inwards. The left plot in the second row shows the horizontal slope derivation calculated from the relative position changes which can be obtained from the previously mentioned plots in the top row according to equation 4.34. The position plots which are used to calculate the vertical slope derivation in the right picture of the second row are not shown (additional plots of the opposite side including the position measurements for both axes can be found in the appendix figures A.2 and A.3). Equation 4.35 was used to get the relative slope of the radiator surfaces by integrating over the data in the previous plots as depicted in the third row. Finally the thickness variation for each one-dimensional scan is calculated by equation 4.36 taking into account the chosen step size. The total thickness variation can be obtained by a direct gradient approximation which is shown in figure 4.30. The plots there show two independent measurements which were done each with a different front surface facing the CCD chip. Both measurements show a very good agreement as expected.

As previously mentioned the relative thickness variation does not contain any information on the wedge error. The integration constant  $\Phi_{\text{offset}}$  in equation 4.35 is therefore determined by

$$\Phi_{\text{offset}} = \frac{1}{N} \sum_{j=0}^N \Delta\Phi_j. \quad (4.38)$$

This leads to a balancing shift in case of the relative slope and a tilting of the distribution in case of the relative thickness measurement so that the average slope is zero and therefore also the artificial wedge disappears.

Especially the plots in figure 4.30 nicely depict the wave form error which may arise during the polishing process as mentioned before. Under the assumption that the surface profile is symmetric, the center of the radiator represents an about  $5 \mu\text{m}$  deep crater valley within a protruding ring with a diameter of roughly 250 mm. Figure 4.31 contains the results for precision vertical scans at five different horizontal positions with a step size of 1 mm which allow a more detailed view (horizontal scan results are shown in figure A.4). Especially in the central part of the radiator large slope deviations are present. A noticeable but typical effect is the rapidly increasing slope at both ends of the radiator which has to be reduced as much as possible. Otherwise it can lead to large deviations for slightly varying photons paths.

Based on the measurements the old prototype radiator would not qualify as a DIRC radiator. The relative slope exceeds 0.3 mrad at the outer parts of the radiator and the total thickness variation is too large.

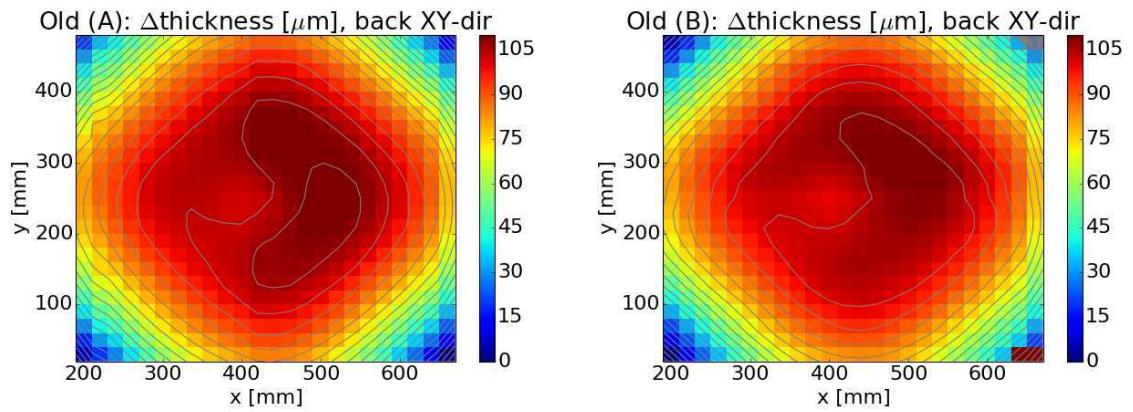


**Figure 4.30:** By performing a two-dimensional numerical integration the total thickness variation is calculated as shown in the above plots for the old prototype radiator. They were obtained during two independent measurements, each with another large surface facing the translation stages.

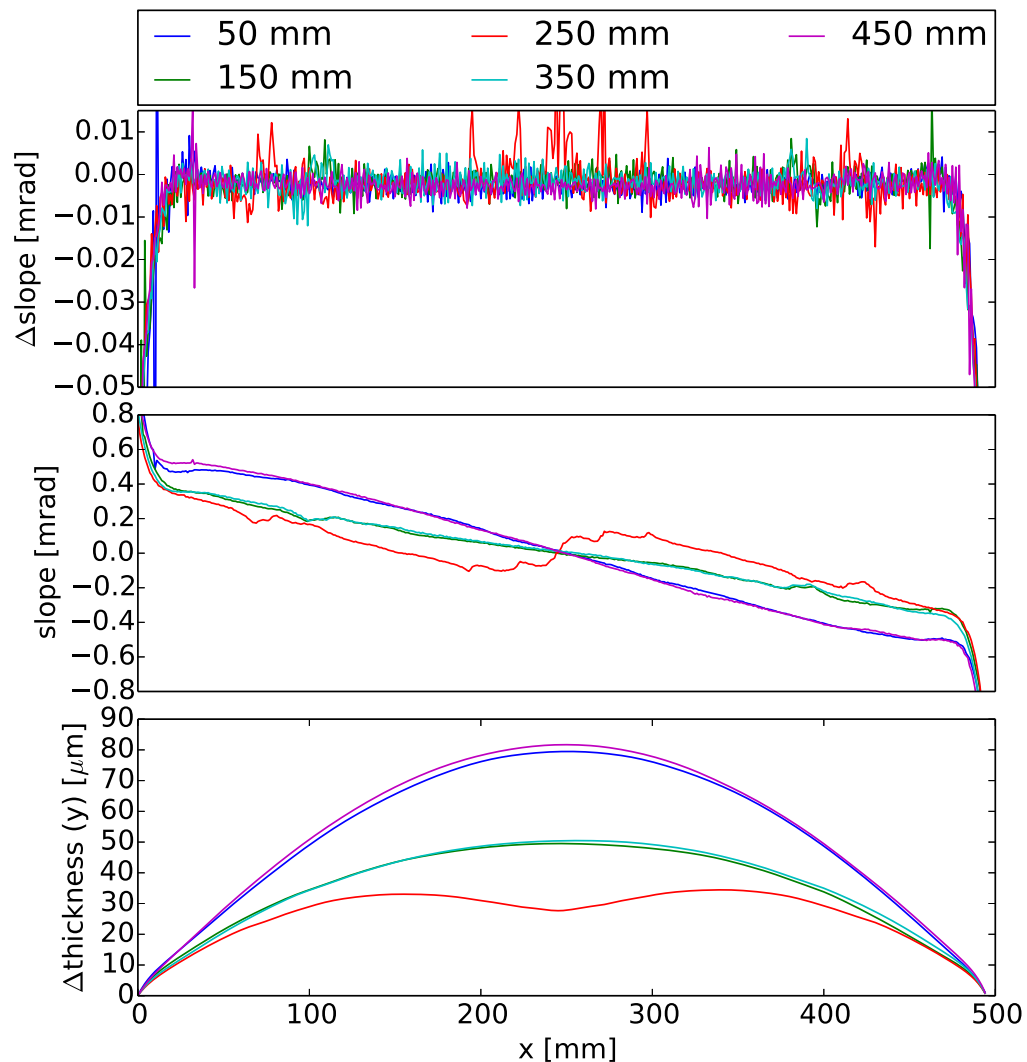


**Figure 4.31:** Fine vertical scan of the old prototype radiator at different x positions as indicated in the legend.

Prior to the CERN testbeam in 2015 Nikon Corporation provided a prototype radiator with the same dimension as the previous. This radiator was manufactured according to pre-defined specifications and conform to the final radiator requirements. A short summary together with the metrological results provided by Nikon are summarized in table 4.4. At this point the achievement of 0.64 nm surface roughness should be emphasized in connection with the previous subsection 4.3.2.1. Analogous to the previous measurement of the old prototype radiator the Nikon prototype radiator was investigated regarding its shape. During the pre-measurements it turned out that a much larger lever (distance  $L$ ) could be chosen as the thickness variation was much smaller than for the old prototype radiator. An overview of the measured data and the subsequent calculations is shown in figure 4.32 (additional results for the measurement of the opposite side facing the CCD chip can be found in figure A.5 and A.6). Already the similarity of the direct and indirect reflection measurements indicated a much flatter thickness variation. In addition the slope is monotonically increasing by approximation which results in concave lens like thickness variation. This is nicely visible in the plots in figure 4.33 which show the total thickness variation obtained from both sides facing the CCD chip individually. Again precision scans were done to further investigate the different profiles. Figure 4.34 (figure A.7) show the results for the horizontal (vertical) scans. The edges of the slope measurement proves that the polishing was done up to the very edge of the radiator. In addition the slope stays below  $50 \mu\text{rad}$  for the whole surface. In comparison to the old radiator only one large valley can be seen resulting in a concave shape of the radiator. One can get a good confirmation of the result by comparing the obtained total thickness variation of the in-house measurement ( $13.5 \mu\text{m}$ ) to the result provided by Nikon ( $12.5 \mu\text{m}$ ).

category	specification	result
parallelism	$< 5 \text{ arcsec}$	$2.47 \text{ arcsec}$
form error (faces)	$< 20 \mu\text{m PV}$	$< 7.254 \mu\text{m PV}$
form error (sides)	$< 25 \mu\text{m PV}$	$< 12.38 \mu\text{m PV}$
roughness (faces)	$< 2 \text{ nm RMS}$	$< 0.64 \text{ nm RMS}$
roughness (sides)	$< 5 \text{ nm RMS}$	$< 0.88 \text{ nm RMS}$

**Table 4.4:** Some major specifications and inspection results for the Nikon prototype radiator. The naming faces corresponds to the two large  $50 \times 50 \text{ cm}^2$  large surfaces whereas sides stands for the remaining four surfaces with the dimension  $50 \times 2 \text{ cm}^2$  (cut-outs at the corners are not considered).

Another important value is the RMS slope error  $\sigma_{\text{slope}}$  which leads to the statistical photon error

$$\sigma_{\text{ph}} = \sqrt{N} \cdot 2\sigma_{\text{slope}}, \quad (4.39)$$

with  $N$  being the number of reflections [Mer14b].

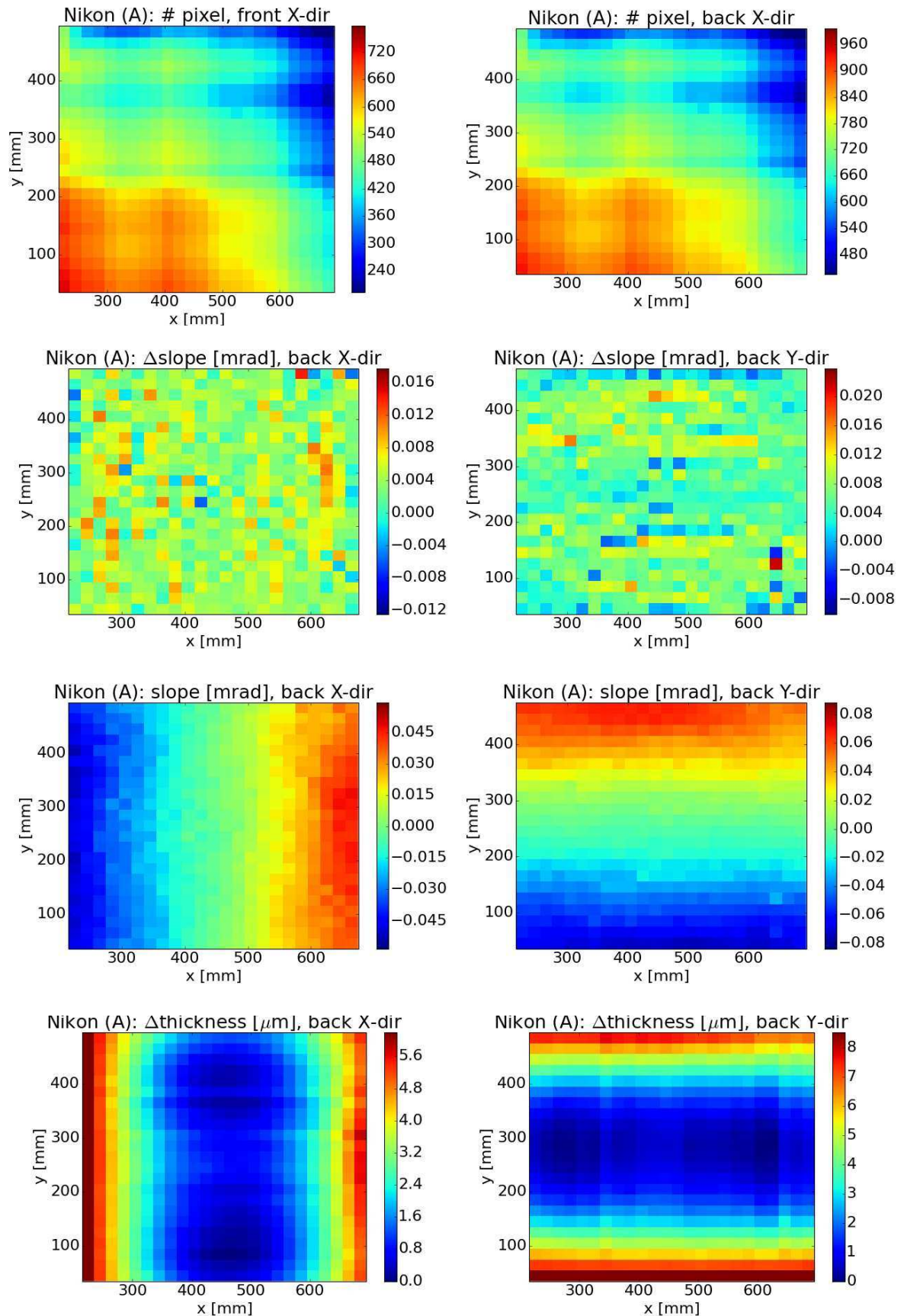


**Figure 4.32:** From top to bottom: recorded positions of reflections, calculated slope derivation, calculated slope, calculated thickness variation of the Nikon prototype radiator. The top row shows only the data for the x-axis whereas the rest is the result for x and y.

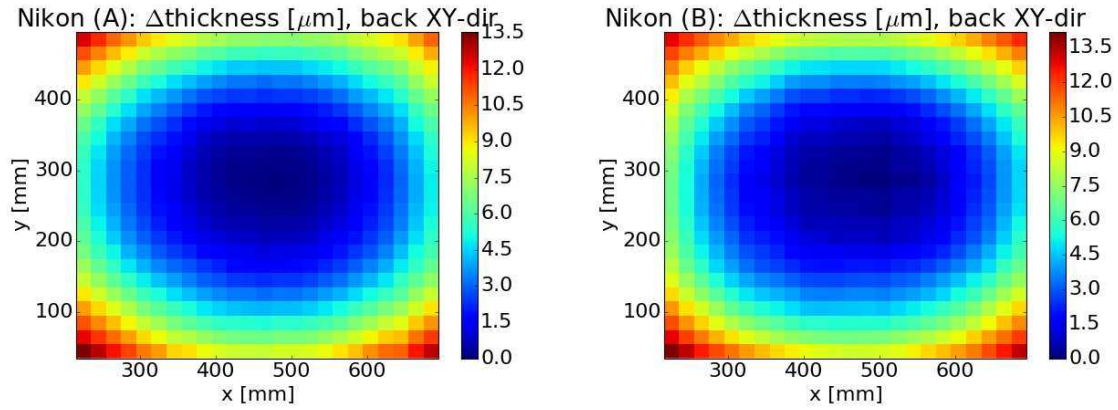


**Figure 4.33:** By adding the individual thickness variations in  $x$  and  $y$  the total thickness variation is calculated as shown in the above plots for the Nikon prototype radiator. They were obtained during two independent measurements, each with another large surface facing the translation stages. The agreement between both measurements underlines the robustness and precision of the setup.

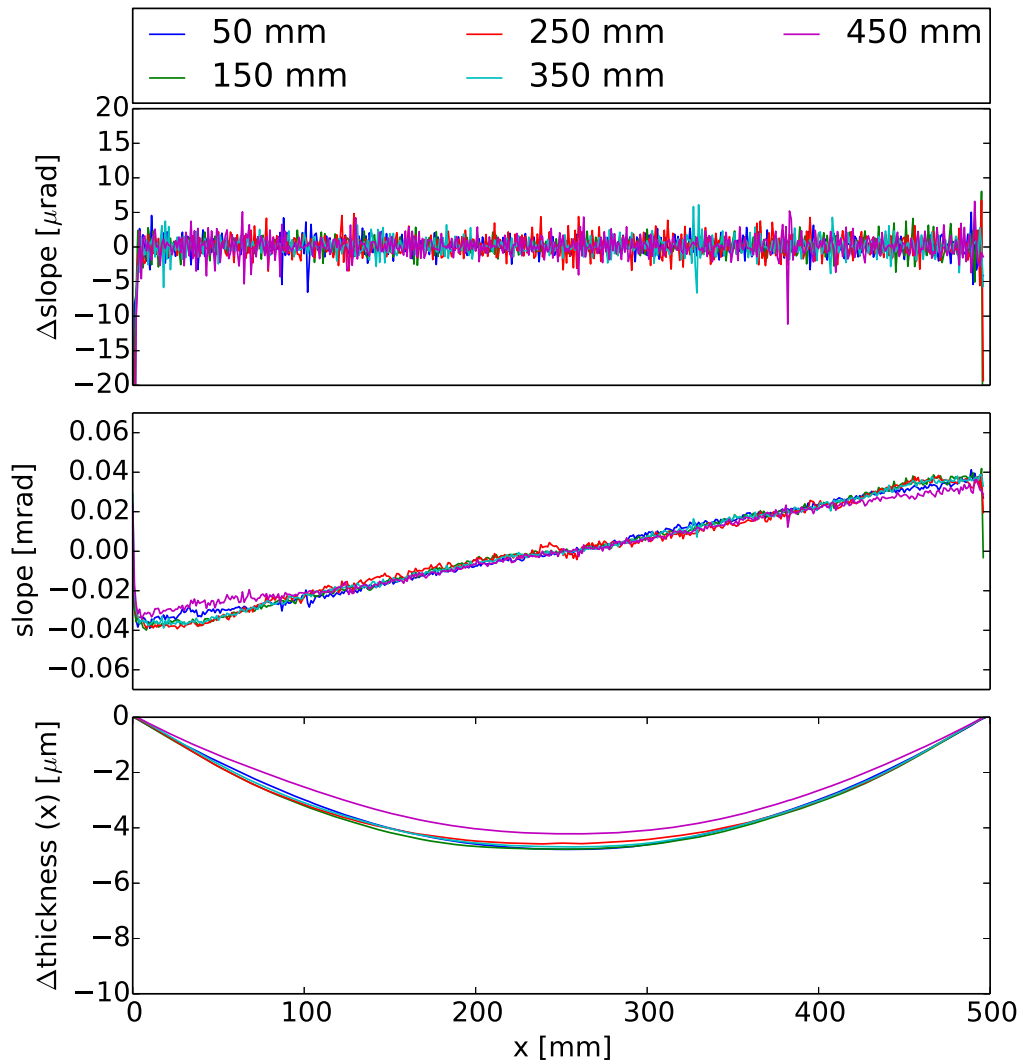


**Figure 4.34:** Fine horizontal scan of the Nikon prototype radiator at different  $y$  positions as indicated in the legend.

Figure 4.35 shows the deviation from a fit with a one-dimensional first order polynomial to the slope at  $y = 250$  mm in figure 4.34. The RMS value corresponds to  $2.43 \mu\text{rad}$  which would lead to a statistical photon error  $\sigma_{\text{ph}}$  of only  $40 \mu\text{rad}$  for 70 reflections. In comparison to initial demands of a  $\sigma_{\text{slope}}$  of  $18 \mu\text{rad}$  the obtained value allows to redefine previous specifications. The measurement is also instructive in the context of the capabilities of Nikon Corporation as they have not been involved in any Disc DIRC (prototype) application until now. Based on the profile measurements the Nikon radiator quality is suitable for DIRC applications.

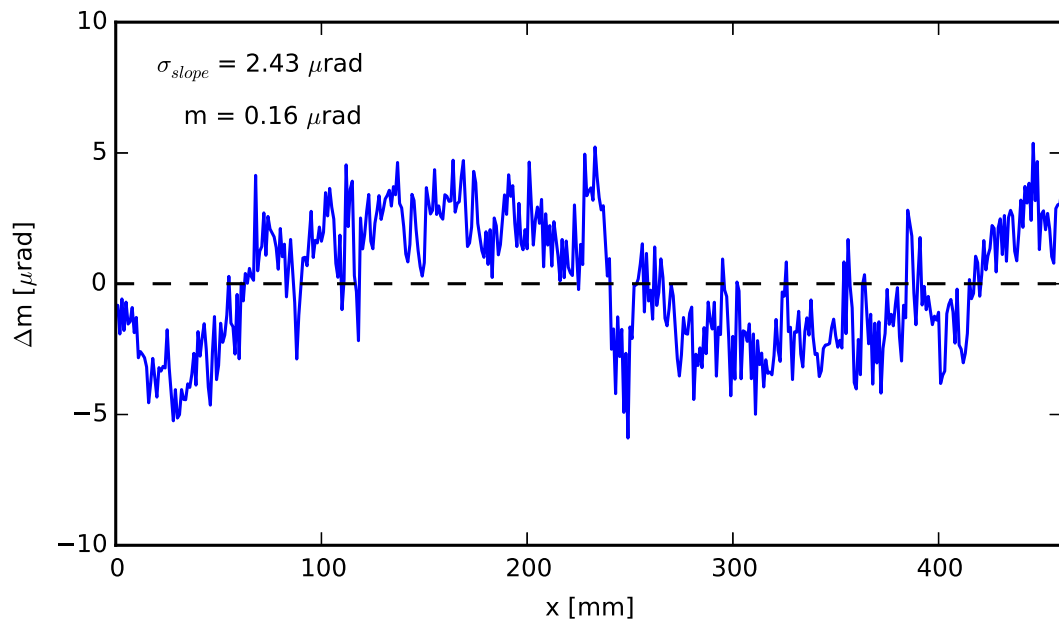


**Figure 4.35:** Deviation of the slope from a perfectly linear progression.  $m$  represents the slope of the fit of the slope at  $y = 250$  mm in figure 4.34 and  $\sigma_{\text{slope}}$  the RMS error.

### Systematic Errors

To derive the systematic error which arises from the small angle approximation and the assumption  $\phi'_1 \approx \phi_1$  (see equation 4.32) the algorithm was tested with different surface profiles. The following example depicted in figure 4.36 used the data obtained with the Nikon prototype radiator as input data.

It clearly demonstrates the impact of the linear stages on the measurement of the front surface. In the presented case the deviation of the linear stage is exemplary chosen to be a sine wave with an amplitude similar to the surface profile. However, the relative slope and total thickness variation is well reconstructed as shown in the bottom plot with a systematic error of  $0.16 \mu\text{m}$  in the present case. This error can be further reduced by choosing the angle  $\phi$  of the laser closer to the surface normal of the radiator. In comparison to this a smaller

step size of the scan is only a second order improvement.

Another source of error is the deviation of the slope from a perfectly continuous function (e.g. a one dimensional polynomial as shown in figure 4.35). This statistical error also comes into effect when the surfaces are scanned which may lead to deviations between the scans made from opposite sides. Only a subtle difference of around  $100 \mu\text{m}$  can be obtained by comparing their maximum profile heights which is in agreement with the formula 4.39 for 500 reflections.

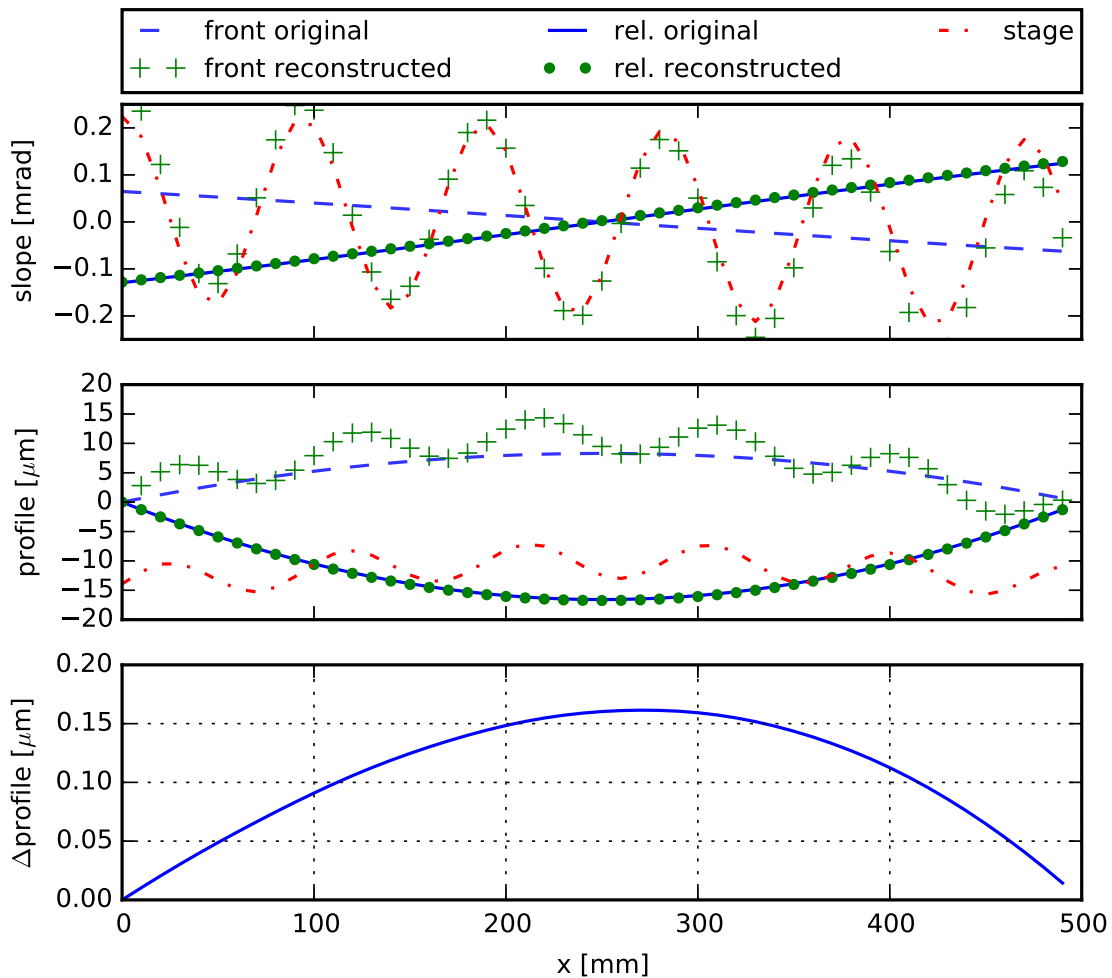


**Figure 4.36:** The above plots are created using sample data that was processed by the reconstruction algorithm in order to check the method for systematic errors. The two top plots show the original front slope and profile (solid blue lines) as well as the the relative slope and profile (dashed blue lines). The latter is almost completely hidden behind the green dots which represent the reconstructed values for the relative slope and profile. The green pluses are the reconstructed values for the front slope and profile which are dominated by the form of the linear stages which carries the laser and CCD chip (dot-dashed line). The bottom plot shows the difference between the original and the reconstructed thickness variation (slope deviations of the surface are disregarded for simplicity).

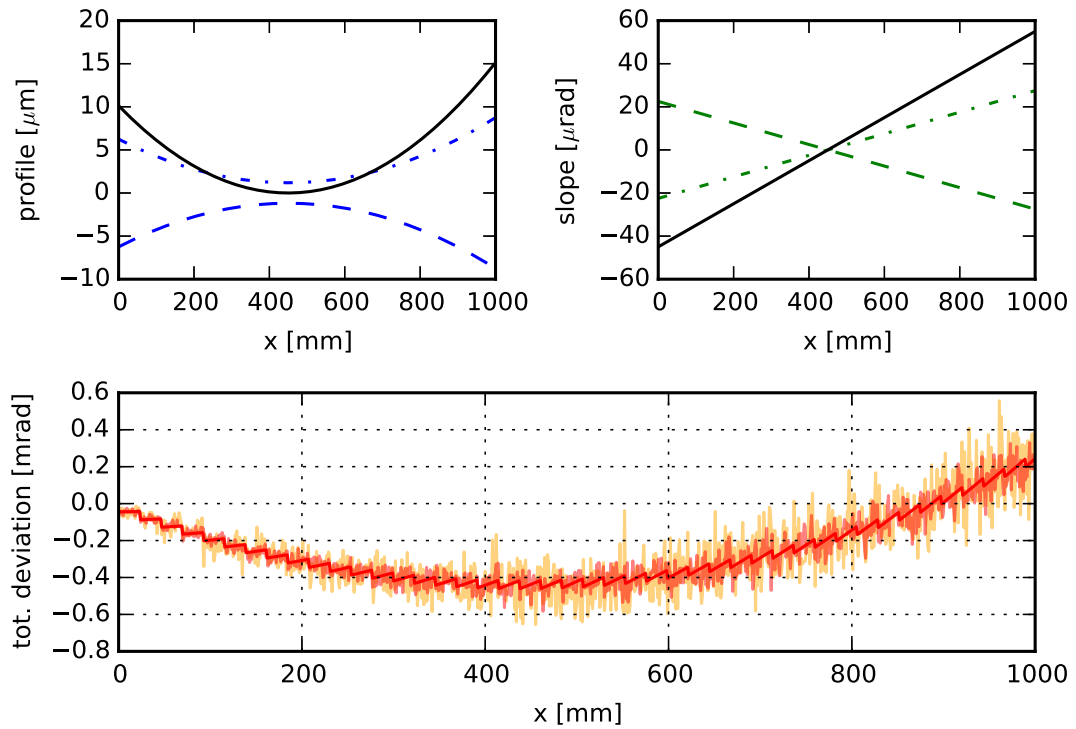


**Figure 4.37:** The top left plot shows the front (dashed), back (dot-dashed) and relative surface profile (solid line). The top right plot shows the corresponding slopes. The wedge error is  $5 \mu\text{rad}$  and the maximum relative slope was chosen to be  $50 \mu\text{m}$  with a resulting TTV of  $15 \mu\text{m}$  for the whole surface. The bottom plot shows the total deviation of the photon angle with respect to the projected path length inside the radiator. The redish (yellowish) fluctuations in the background illustrate the impact of a slope error of  $2.5 \mu\text{rad}$  ( $5.0 \mu\text{rad}$ ). The maximum deviation within any 10 cm interval is 0.49 mrad.

### Transport Error Estimation

The transport error estimates the angular deviation of the Cherenkov photon due to the imperfection of the radiator surfaces and was defined as

$$\sigma_{\text{trans}} = \sigma_{\text{ph}} + N \cdot \delta_{\text{wedge}} \quad (4.40)$$

in [Mer14b]. In figure 4.37 the situation for the steepest angle  $\varphi = 41^\circ$  is shown for a possible radiator profile. The maximum spread of total deviations is about 1.3 mrad but a clear pattern can be obtained and utilized in order to loosen the specifications on the statistical photon and wedge error. In case of the wedge error it was already stated in [Mer14b] that “it might become necessary to correct for this systematic error instead of avoiding it”. A possibility which arises from the measurements of the radiator shape is an additional correction for slope deviations of the radiator. Therefore the following considerations assume that corrections can be done with sufficient knowledge of the radiator profile and the position of origin of the Cherenkov photon. A large uncertainty arises from the number of reflections

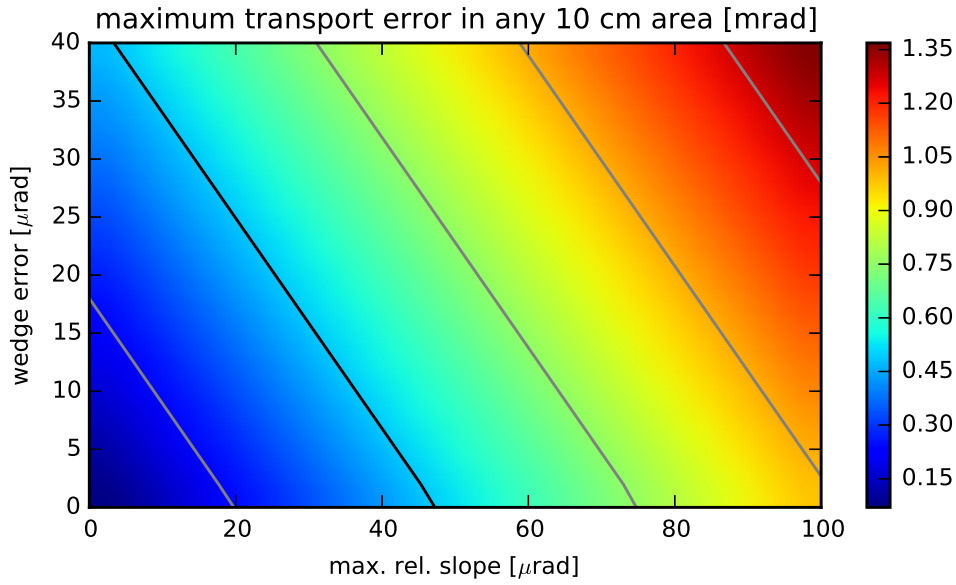


**Figure 4.38:** The wedge error and maximum relative slope are varied in order to obtain their impact on the total transport error. Only the maximum value for any 10 cm interval is shown. The underlying surface structure is shown in figure 4.37 where the maximum transport error of 0.5 mrad is indicated by the black line. The gray lines are drawn with a distance of 0.2 mrad.

which cannot be perfectly determined due to different possible paths. In addition the starting position of the photon is smeared along its path due to the non perpendicularity of the traversing charged particle. Nevertheless ambiguities in the paths are small in comparison to other DIRC designs. The original specifications for the requirement of the transport error  $\theta_{\text{trans}} \leq 0.5$  mrad is hence modified to be valid only within a limited aperture around the traversing particle's path. As a benchmark case a photon with an angle of  $\varphi = 41^\circ$  between the photon's path and the radiator surface is chosen. The maximum projected path length is 1 m. The corresponding aperture is then chosen to be 10 cm in diameter around the origin of the Cherenkov light which corresponds to roughly five reflections off the surface. In this context equation 4.40 can be complemented to

$$\sigma_{\text{trans}} = \sigma_{\text{ph}} + N \cdot \sigma_{\text{wedge}} + \sigma_{\text{form}}. \quad (4.41)$$

One has to bear in mind that the actual form of the radiator surface is crucial for the correct application of specifications such as wedge error, total thickness variation (TTV) or slope error. Hence  $\sigma_{\text{form}}$  can be quantified but cannot be directly used or measured. This requires a good communication with the manufacturer who on the other hand needs to have a high knowledge of his capabilities. The previous measurements for the Nikon prototype radiator were used as a sample for the now following considerations. It is important to mention that the actual absolute surface forms are not relevant in first order and only the relative slope and thickness are causing the observed deviations. In figure 4.38 the maximum relative

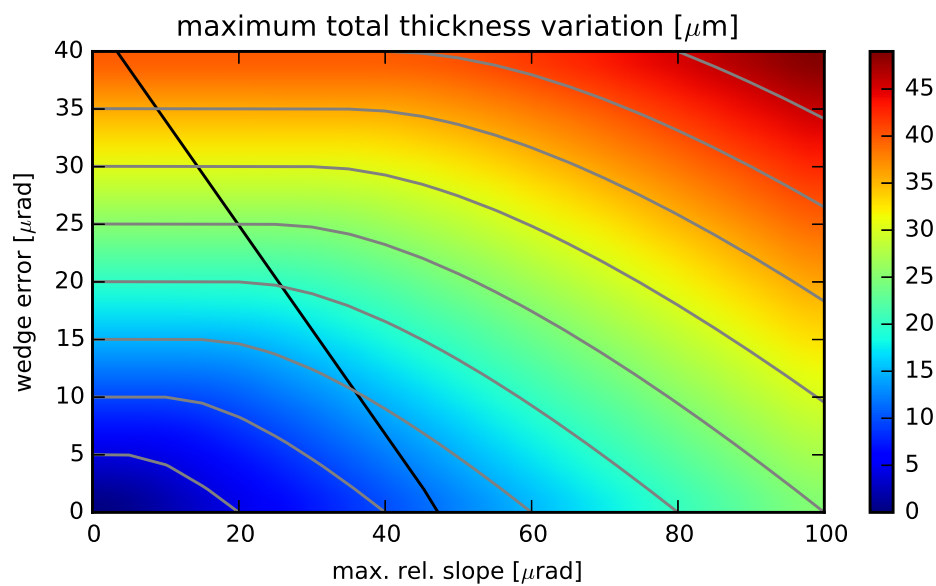


**Figure 4.39:** Total thickness variation (TTV) for the whole radiator surface. The parameter variation is the same as shown in figure 4.34. The corresponding threshold value for the transport error is again indicated by the black line.

slope and the wedge error are varied and the maximum transport error in any 10 cm area is plotted. The slope variation is supposed to be linear. Also a RMS slope error with a RMS value of  $5 \mu\text{rad}$  has been added. Typically the wedge error can be controlled better which results in a relative slope error of around  $40 \mu\text{rad}$  for a wedge error below  $5 \mu\text{rad}$ . The same plot can be made plotting the total thickness variation which is often used as a figure of merit for flat optics. This was done in figure 4.39 where the threshold for the transport error is drawn again as a reference only. The characteristic differs from the transport error distribution but it turns out that a TTV below  $15 \mu\text{m}$  is adequate.

### Future Measurements

The presented measurement setup does not allow to measure a wedge error or the perpendicularity of the front and side surfaces. The wedge error or parallelism can be measured using an autocollimator at different positions. An autocollimator could also be used to determine an absolute relative slope between the two surfaces at certain spots and therefore be used to calibrate the profile measurement. In conjunction with a penta-prism the perpendicularity can be measured as well [BarTDR]. Although the setup is limited to measure an area of up to  $1 \text{ m}^2$  which was sufficient for the available prototypes, larger radiators could be measured by doing several measurements of individual sections and stitching them together afterwards.

## 4.4 Focusing Elements and Prisms

### 4.4.1 Requirements

A Focusing Element's (FEL) main purpose is the internal focusing of parallel entering Cherenkov photons on the MCP-PMTs photocathode. During the evolution of the Disc DIRC different proposals have been made for different detector designs as shown in figure 4.40. One possibility is to choose a geometry such that total internal reflection is valid for any possible reflection off the surface (see e.g. Erlangen design for a WASA Disc DIRC [Foh11] or early proposals for a focusing Disc DIRC for  $\bar{P}$ ANDA [Foh07, Cow11]). More compact solutions are possible if the curved focusing surface can be coated with a mirror (see e.g. [Dur12]). Another option is to make a symmetric FEL with two sensors. This design is insensitive to angle misalignments with respect to the radiator. In case of the  $\bar{P}$ ANDA EDD MCP-PMTs are used and have to be aligned to the magnetic field which leads to a larger FEL volume. Instead of a polynomial function the curved focusing surface now has a cylindrical shape which slightly simplifies the manufacturing process [Mer14a].

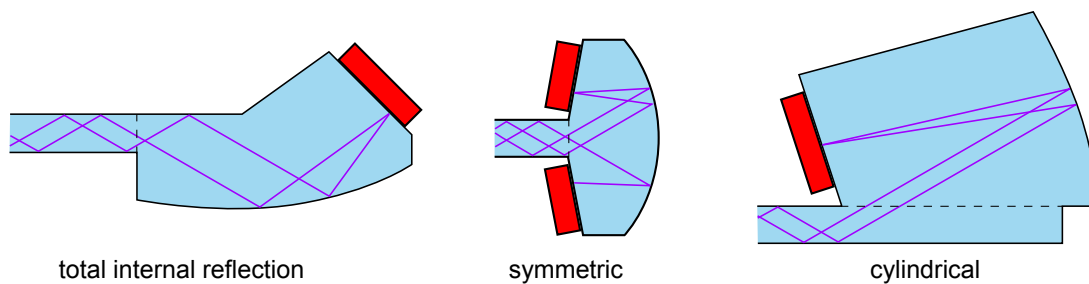


**Figure 4.40:** The figure shows some examples of different FEL types. The left one does not need any mirror coating as the condition for total internal reflection is always present. The design shown in the middle part is symmetric which avoids defocusing due to bad alignment. The right design corresponds to the cylindrical FEL for the  $\bar{P}$ ANDA Disc DIRC.

#### 4.4.1.1 Prisms

As described in section 3.3, the design had to be changed as the available space had already been determined by neighboring detector parts. This excluded the possibility of symmetric FELs and led to the introduction of the prisms (sometimes called bars). The prisms extend the radiator but are part of the ROMs by definition. Their height is equivalent to the thickness of the radiator whereas the width corresponds to the FEL width of 16 mm [Mer14a]. The optical properties have to be chosen according to the previously discussed requirements for light loss and the conservation of the photon angle. Figure 4.41 and table 4.5 summarize the specifications.

category	side	specification
form error	A, B, C, E, F	$2\lambda$ PV on wavefront
roughness	A, B, C, E, F	2 nm RMS
scratch/dig	A, B, C, E, F	5/5x0.2;L5x0.004;E0.2
chamfers	all sides	< 0.2 mm

**Table 4.5:** Surface specifications of the prism

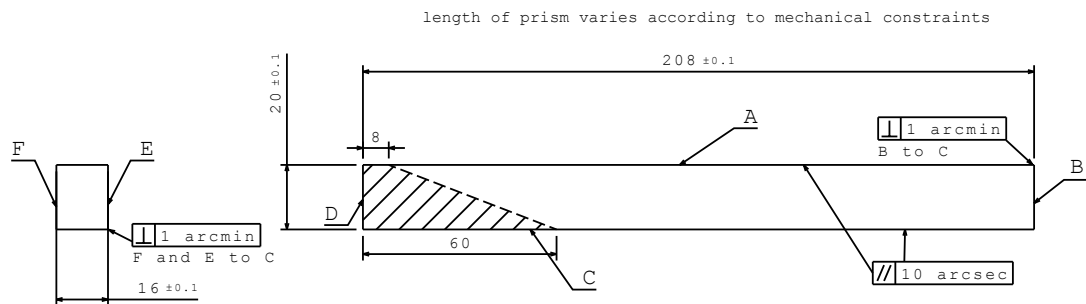


**Figure 4.41:** The technical drawing shows the shape and the corresponding dimensions and their allowed tolerances of the prism. The hatched surfaces are not relevant for the photon transport and hence can be in contact with mounts.

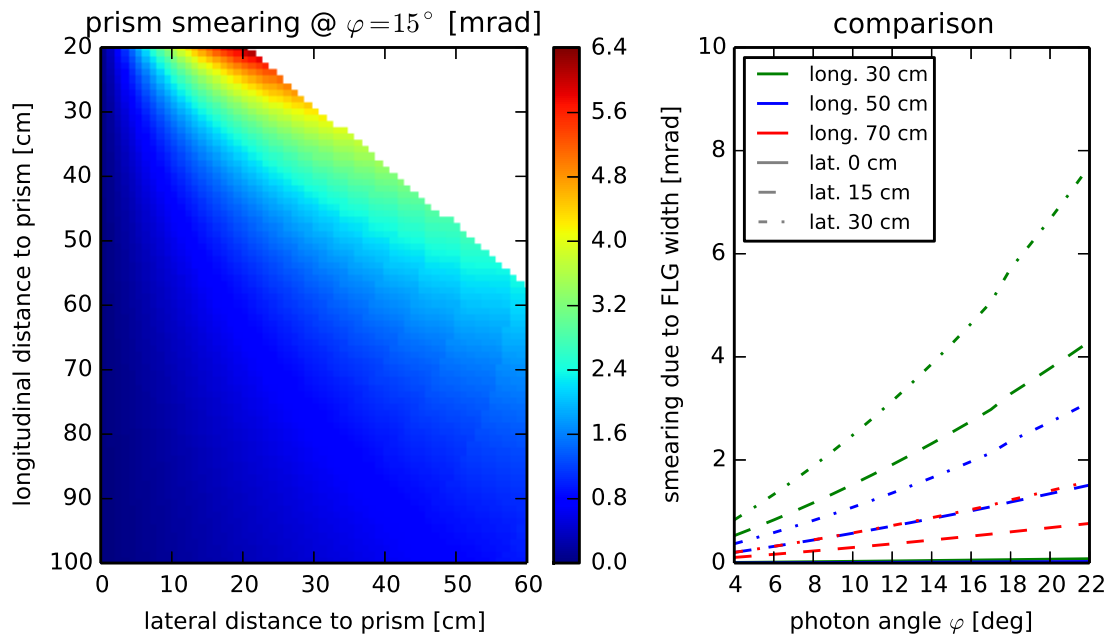


**Figure 4.42:** Left: Geometric angle smearing due to the FEL/prism width of 16 mm for different distances at a polar angle of the traversing charged particle of  $15^\circ$ . Right: Smearing for different particle angles and positions on the radiator (lateral and longitudinal distances to the prism entry).



- the range of the imaging function which also has to be compatible with the MCP-PMT anode,
- the minimum position of the imaging function on the FEL side C in order to leave enough space for the MCP-PMT itself including PCBs and possible plugs.

The optimization was repeated by an independent and custom made two dimensional ray tracing macro which has also been used to reevaluate the proposed tolerances. Additional specifications are summarized in table 4.6. The form error of  $\lambda/2$  Peak-to-Valley (PV) turned out to be quite challenging for many manufacturers. However, it does not have to be applied to the shaded parts of side A. According to these specifications three FEL prism pairs have been manufactured by Berliner Glas KGaA for first investigations. Table 4.7 summarizes the metrological results provided by the manufacturer. Here all dimensions stay well within the allowed tolerances. The Al coating was accurately applied up to the edge of side A as well. Early concerns that the coating might cover small parts of sides E and F, which would have still been acceptable, could be dispelled after optical inspection.

category	side	specification
form error	A	$\lambda/2$ PV on wavefront
	C, D, E, F	$2\lambda$ PV on wavefront
roughness	A, E, F	2 nm RMS
	C, D	2 nm RMS
scratch/dig	A	5/1x0.1;L1x0.002;E0.1
	C, D, E, F	5/5x0.2;L5x0.004;E0.2
coatings	A	Al-coating
chamfers	all sides	< 0.2 mm

**Table 4.6:** Surface specifications of the FEL

dimension	value	tolerance	FEL (S2)	FEL (S6)	FEL (S8)
offset x	146.02 mm	$\pm 0.1$ mm	0.0098 mm	0.0060 mm	0.0154 mm
offset y	39.0 mm	$\pm 0.1$ mm	0.0110 mm	0.0161 mm	0.0076 mm
radius	287.77 mm	$\pm 0.2$ mm	0.0112 mm	0.0002 mm	-0.0081 mm
thickness	16.0 mm	$\pm 0.1$ mm	-0.03 mm	-0.02 mm	-0.02 mm
angle	108.0°	$\pm 0.02^\circ$	0.0046°	0.0023°	< 0.0001°
form side A	cylindric	$\lambda/2$ PV	$0.1\lambda/0.6\lambda$ PV	$0.2\lambda/0.7\lambda$ PV	$0.2\lambda/0.8\lambda$ PV

**Table 4.7:** Quality measurements provided by Berliner Glas. The form error of side A shows two values. The first one is for the relevant region on the surface whereas the second value is for the whole surface. The measured deviations are in agreement with the specifications.

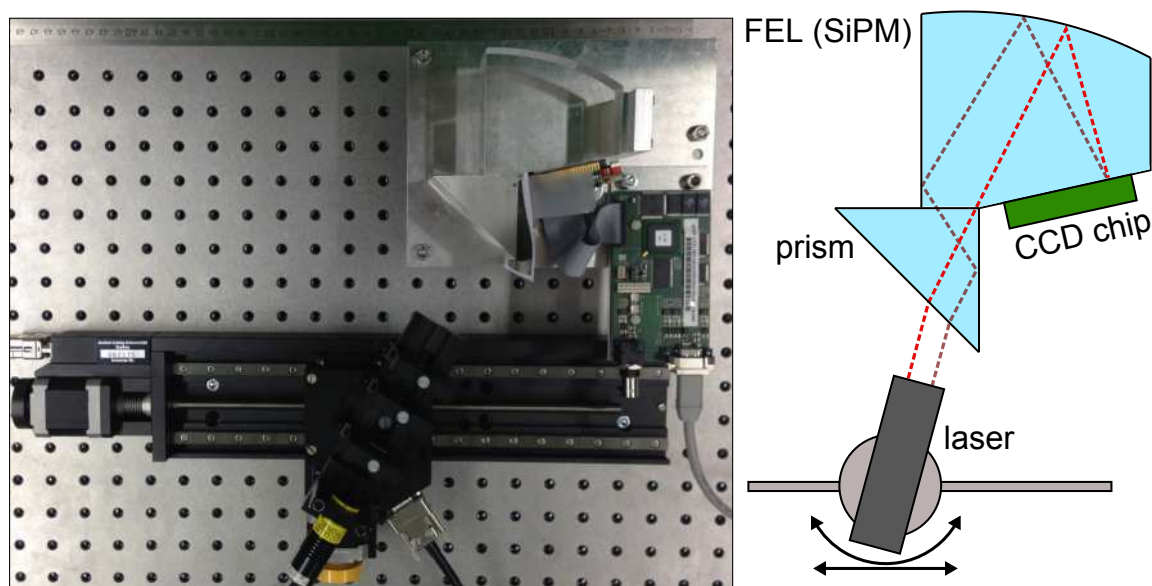


**Figure 4.44:** Picture and schematic drawing of the quality measurement setup for the SiPM FEL. All angles could be measured without changing the position of the prism or the CCD chip.

## 4.4.2 Quality Measurements

### 4.4.2.1 dSiPM FEL

The background for in-house quality measurements was to demonstrate the performance with respect to the focusing capabilities of the FELs. Before the MCP-PMT FELs became available the developed setup was used to investigate a dSiPM FEL which was made of fused silica in preparation for a previous Disc DIRC prototype. The setup itself is shown in figure 4.44. It consists of a plate where the FEL was mounted along with the CCD chip, a coupling prism which was optically contacted to the FEL using fused silica optical matching liquid by Cargille [CML6350] and a laser which was mounted on a linear stage with a rotary stage on top. The angular position of the prism with respect to the entry side of the FEL had to be manually calibrated to avoid a double focusing spot. Therefore the laser was widened using two lenses and positioned such that part of the beam had two additional reflections off the coupling prism and the FEL whereas the other part of the beam directly traversed the coupling between the two components. The imaging was then evaluated at different positions using the CCD chip (see figure 4.45). Subsequently the orientation of the coupling prism was corrected and the evaluation was repeated until a smooth transition could be obtained.

The linear stages were programmed such that a full scan could be done automatically. Due to refraction the angle of the laser  $\beta$  had to be converted into the angle  $\alpha$  (see figure 4.46),

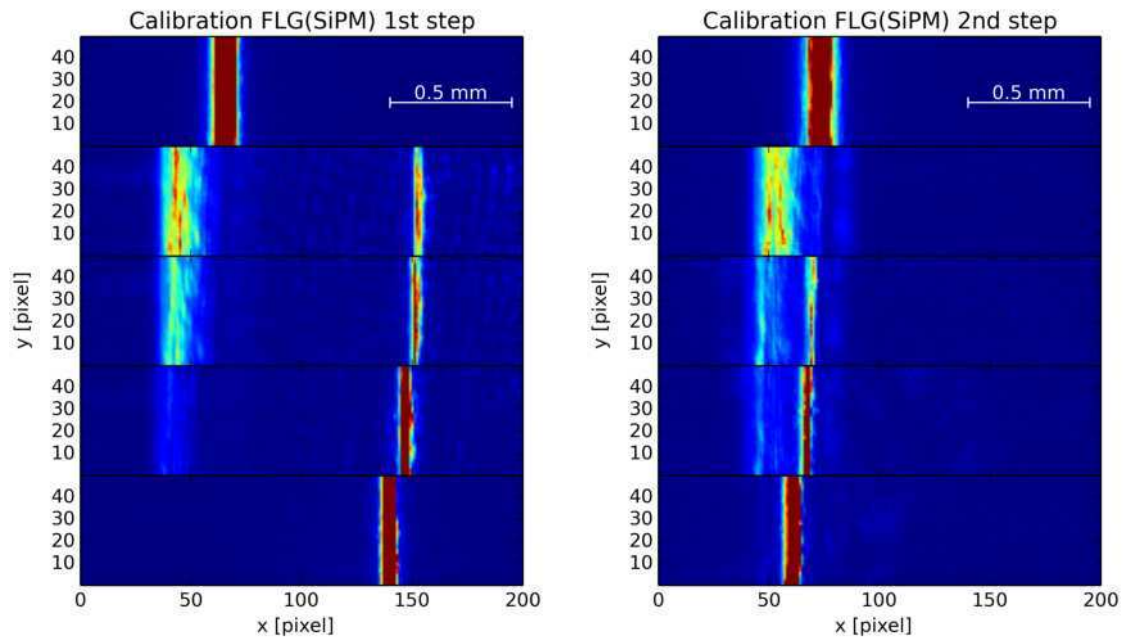


**Figure 4.45:** The plots shown above demonstrate the calibration procedure for the FEL scans. From top to bottom the laser is slightly moved along the linear stage leading to a different photon path with additional reflections. The left (right) plots are without any (with a) correction applied to the orientation of the coupling prism. This procedure has to be further iterated to get a smooth transition.

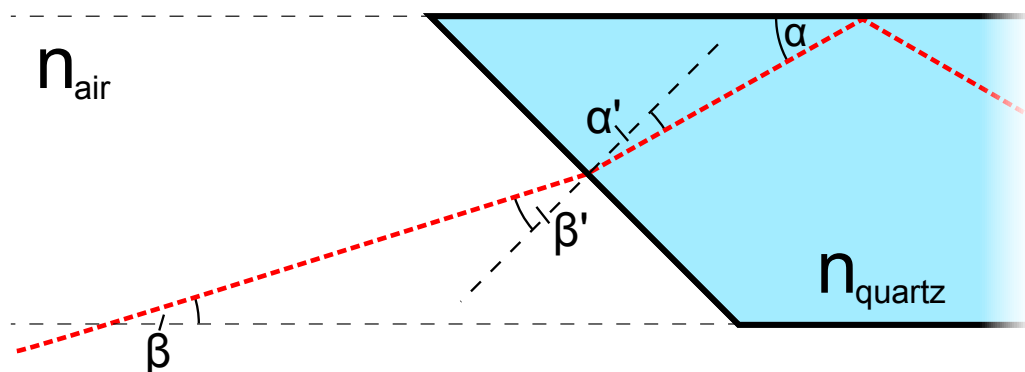


**Figure 4.46:** The drawing above illustrates the conversion of angles for coupling of laser to the prism and light guide.

which corresponds to  $\varphi$  as seen in equation 3.12, according to

$$\beta = 45^\circ - \arcsin(n \cdot \sin(45^\circ - \alpha)), \quad (4.42)$$

$$\alpha = 45^\circ - \arcsin\left(\frac{1}{n} \cdot \sin(45^\circ - \beta)\right), \quad (4.43)$$

with  $n_{\text{air}} \approx 1$  (see also figure 4.46). A picture of the FEL's focal plane was then taken for different positions and angles of the laser with the CDD-chip. Afterwards the pictures were analyzed as shown in figure 4.47 by projecting the entries on to the horizontal axis and applying a Gaussian fit. The left part of figure 4.47 draws a dot for each analyzed picture according to its position.

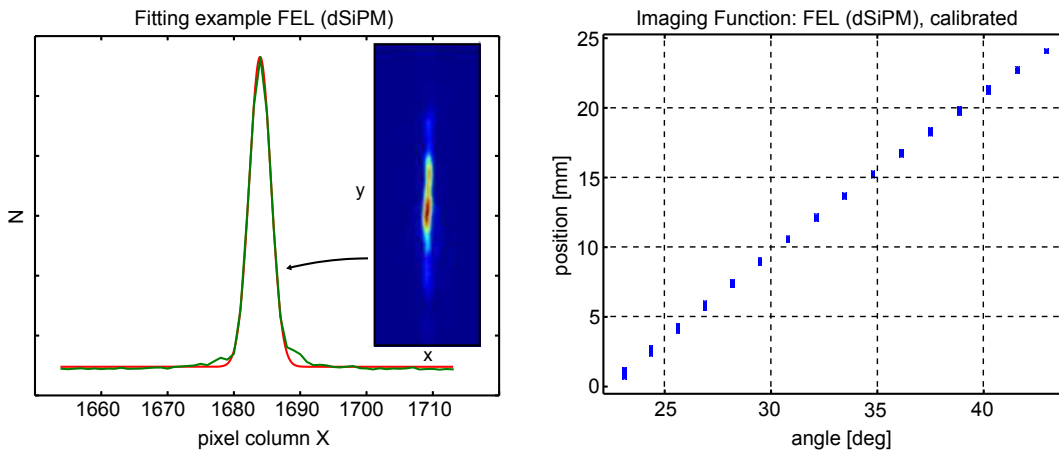


**Figure 4.47:** The left picture contains a two-dimensional projection of snippet of the CCD image for a single position which is fitted with a Gaussian in order to determine the mean value and the width of the spot. The right part contains all the mean values that have been measured for the SiPM FEL.

Due to the CCD chip's pixel size of  $9 \mu\text{m}$  the spot width can be determined with high precision. However, the angle of incidence itself is error-prone due to

- divergence of the laser beam,
- dispersion ( $\pm 10 \text{ nm}$ ),
- tolerance of the rotary stage,
- misalignment of the coupling prism.

The main error arises from the misalignment of the coupling prism which can in principle be corrected. Therefore an additional measurement was done with the existing setup as depicted in figure 4.48. At first the deviation of the laser at a  $0^\circ$  position ( $\varphi_1$ ) was calculated by taking the deviation at two different Measurement Positions (MPs). In a second step the laser was rotated by  $90^\circ$  using the precision rotary table to reflect off the prism surface. Again the deviation was calculated at two different MPs in order to obtain  $\varphi_2$

$$\varphi_1 = \arctan\left(\frac{d_1}{L_1}\right) \approx \frac{d_1}{L_1}, \quad \varphi_2 \approx \frac{d_2}{L_2}, \quad (4.44)$$

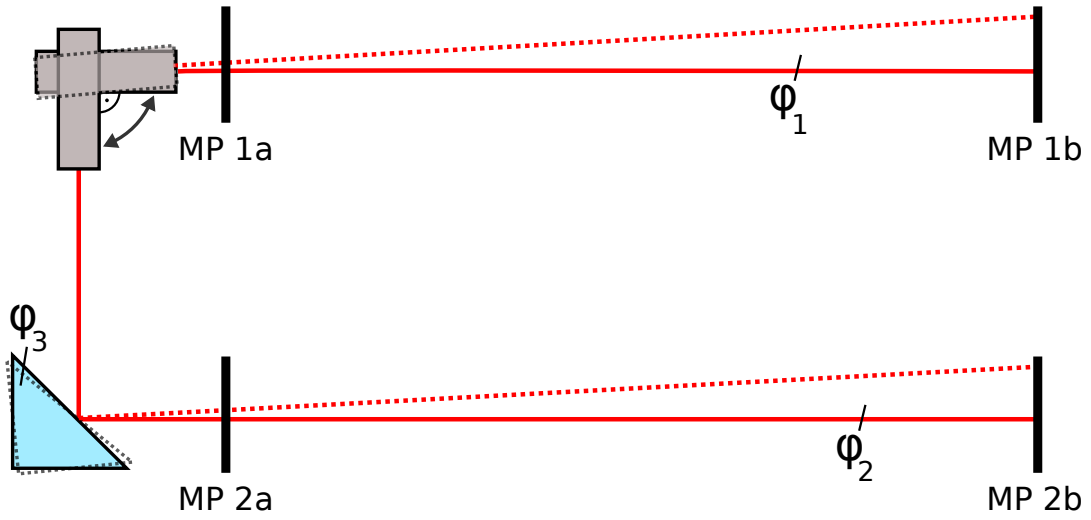


**Figure 4.48:** The drawing above illustrates the setup for correction of the angle due to misalignment of the laser or the prism. MP stands for measurement position and depends on the available space.

with  $L$  being the distance between the MPs and  $d$  the differences of the deviations from the mean position. Both angles can be used to calculate the misalignment of the coupling prism  $\varphi_3$  according to

$$\Delta\varphi_2 = 2\Delta\varphi_3 - \Delta\varphi_1 \quad \Rightarrow \quad \Delta\varphi_3 = \frac{\Delta\varphi_2 - \Delta\varphi_1}{2} = \frac{1}{2} \left( \frac{d_2}{L_2} - \frac{d_1}{L_1} \right). \quad (4.45)$$

The error due to the misalignment of the prism also doubles for the transmitted light which leads to shift of the angle  $\beta$  (see equation 4.42) of

$$\beta' = \varphi_1 - \varphi_3 \quad (4.46)$$

$$= \frac{d_1}{L_1} - \frac{d_2}{2L_2} + \frac{d_1}{2L_1} = \frac{1}{2} \left( \frac{3d_1}{L_1} - \frac{d_2}{L_2} \right) \quad (4.47)$$

with the corresponding error

$$\Delta\beta' = \sqrt{\left( \frac{3\Delta d_1}{2L_1} \right)^2 + \left( \frac{\Delta d_2}{2L_2} \right)^2} \quad (4.48)$$

where the errors  $\Delta L$  have been neglected.

This information was used to create the left plot in figure 4.49 where each entry corresponds to an angle of incidence. The vertical error bar indicates the spot width whereas the horizontal error bar represents the angle uncertainty. In the right part the spot width and RMS value for each angle is plotted separately.

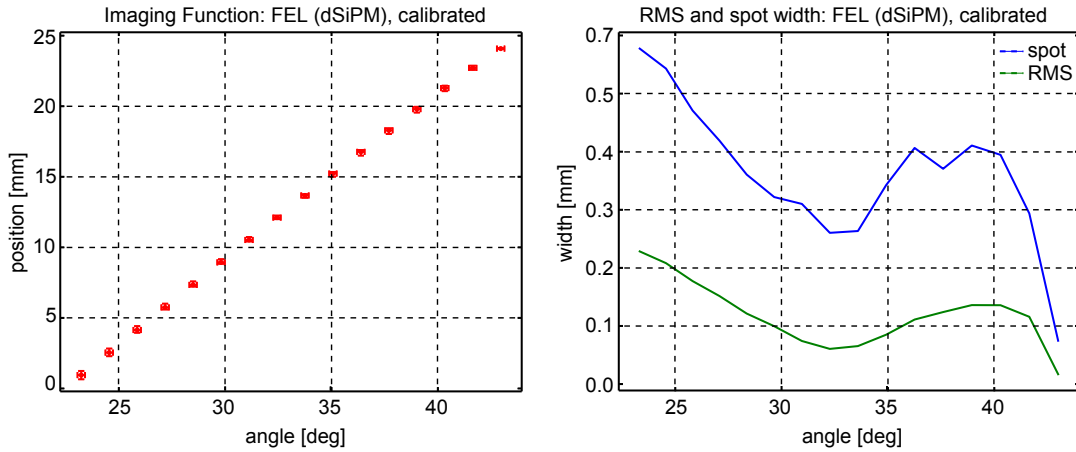


**Figure 4.49:** Left: Imaging function for the SiPM FEL. The error bands in x direction indicate the uncertainty regarding the laser angle whereas the error bands in y direction correspond to the measured spot width. Right: Spot width and RMS for each angle.

#### 4.4.2.2 MCP-PMT FELs

After the arrival of the MCP-PMT FELs the present setup was slightly altered to mount and evaluate the new samples. As shown in figure 4.50 a new plate was designed which contained a custom made clamp to fix the FEL and an elongated hole in order to move the CCD chip along the focal plane of the FEL. This became necessary as the width does not cover the full range of the focal plane. In addition the chip had to be used vertically for mechanical reasons. In total three FEL-prism pair prototypes were delivered. Two FELs were shipped separately (S6 and S8) and have been evaluated first without the prisms attached. Therefore the coupling prism was directly coupled to side D. Due to the limited size of the coupling prism it had to be moved along the surface to cover the full range of possible photon paths. The size of this range can be calculated according to

$$d_{\text{range}} = 2 \frac{D}{\tan \varphi} \quad (4.49)$$

with  $D$  being the thickness of the radiator/prism and  $\varphi$  being the angle between the traversing photon and the face surface of the radiator (see equation 3.12). This translates into a distance  $d_{\text{stage}}$  which is required to be scanned in order to get the range  $d_{\text{range}}$

$$d_{\text{stage}} = 2 \frac{D}{\tan \alpha} \sqrt{\frac{3}{2} - \sqrt{2} \cos \alpha} \sqrt{\frac{3}{2} - \sqrt{2} \sin \alpha}. \quad (4.50)$$

Both, the coupling prism and the CCD chip, had to be moved manually which inhibited a fully automated setup. On the other side it was not necessary to align the coupling prism as no defocusing reflections occur in this setup. Figure 4.51 shows a long time exposure of different photon paths at  $\varphi = 31^\circ$  which nicely demonstrates the focusing properties of the FEL.

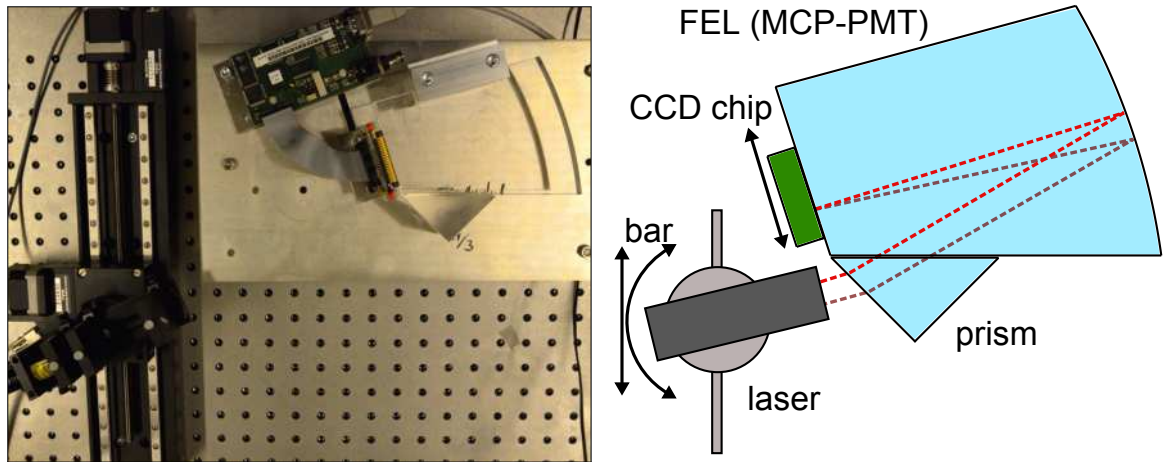


**Figure 4.50:** Picture and schematic drawing of the quality measurement for the MCP-PMT FEL. In order to scan all required angles the positions of the coupling prism and the CCD chip have to be varied.

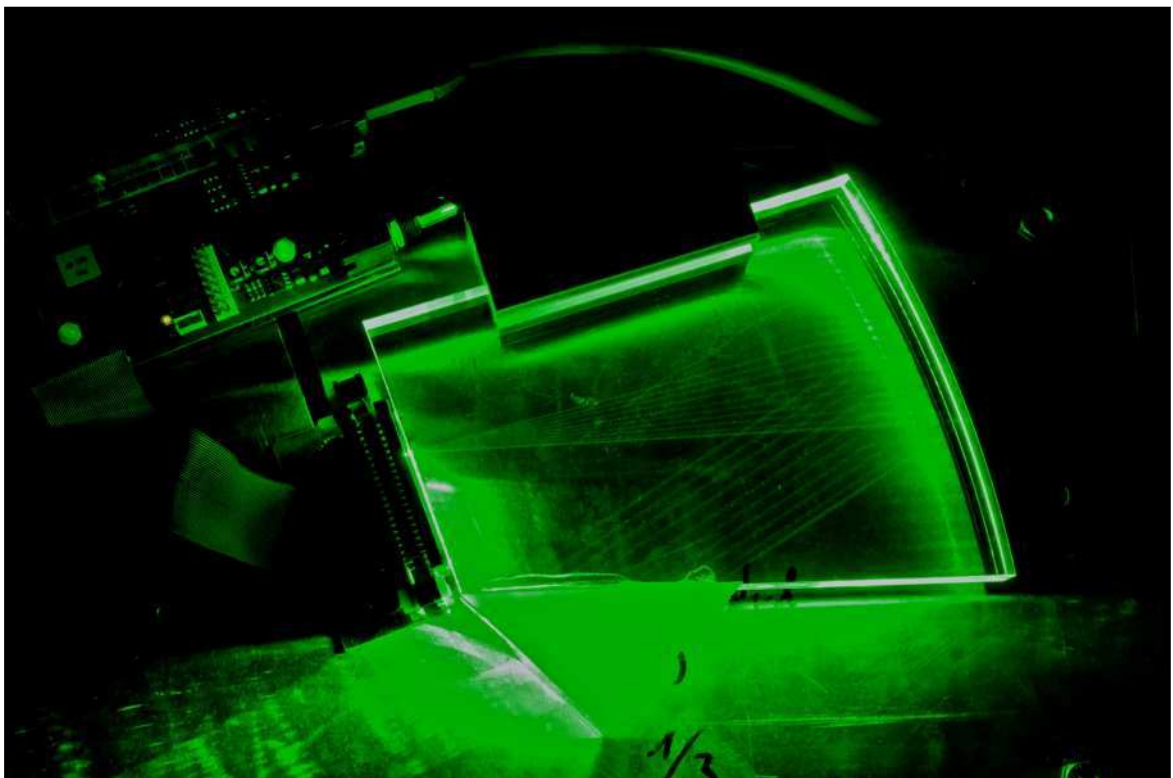


**Figure 4.51:** A picture of the FEL focusing taken with long time exposure for different laser positions. The coupling prism was directly contacted to the FEL.

The third FEL (S2) was coupled with the prism via optical contact bonding. This bonding is achieved without any gluing as the molecules on the surfaces are attracted by van der Waals forces, hydrogen bonds and dipole-dipole interaction. This can only be achieved if the distances between the surfaces are below 1 nm and hence requires ultra parallel surfaces which must be clean and free of any contamination. The advantage of this coupling method is the absence of any additional material and hence a source of additional photon loss but more importantly no additional boundaries where Fresnel reflections can occur which would distort the imaging. After the first inspection the FELs S6 and S8 were also contacted with a prism using a custom made gluing setup. After a careful cleaning of the components the gluing was done according to the following procedure in a clean room (letters and numbers correspond to the steps shown in figures 4.52 and 4.53):

- A. Positioning: The gluing setup contains thin distance plates made of glass which are attached to each block to avoid any glass to non-glass contact.
  - 1.-2. The FEL is first positioned against a fixed orientation block which also determines the distance between the focal plane of the FEL (side C) and the front surface of the prism (side B). Prior to this step a tape is attached to the FEL in order to cover the glue joint.
  3. A rotatable connection block is attached to the FEL to hold it in position. It only touches the sides of the FEL side A to avoid any damage to the coated mirror.
  4. The prism is positioned with respect to the orientation block and the FEL. The distance between the FEL and prism is determined by a 100  $\mu\text{m}$  thin plastic foil. Therefore the FEL can be readjusted as well.
  - 5.-7. Before removing the plastic foil, the connection blocks are moved against the prism to fix it.
- B. Inspection: The gap is carefully inspected using a magnifying glass prior to the injection of the glue.
- C. Gluing: Two different glues were used for the bonding: NOA-61 by Norland [Noa61] which is a UV curing glue and Epicol 348990 by APM Technica [APMEpi] which is a two component epoxy resin. NOA-61 was carefully applied directly from the tube and - after it covered the full area between the two components - was cured using a handheld UV source. The Epicol glue was delivered in a bi-pack which allowed a bubble free mixing without additional equipment. After mixing it was loaded into a blunt cannula and carefully applied to the gap. The FEL-prism pair was left inside the setup for 48 hours for curing.
- D. Cleaning: Prior to the curing glue residues were carefully removed from the surfaces.

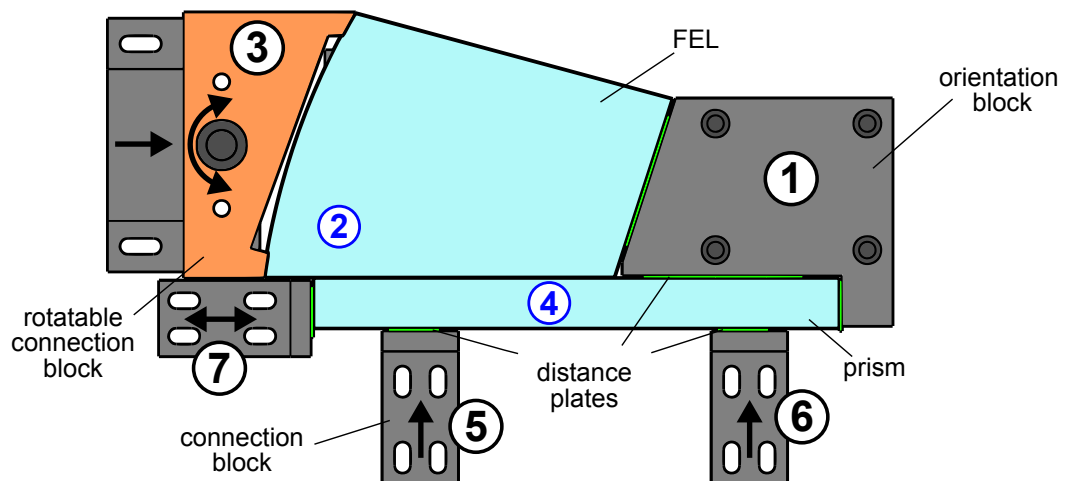


**Figure 4.52:** The drawing shows the device for gluing of the FEL-prism pairs, the circled numbers indicate the order in which the components are used.

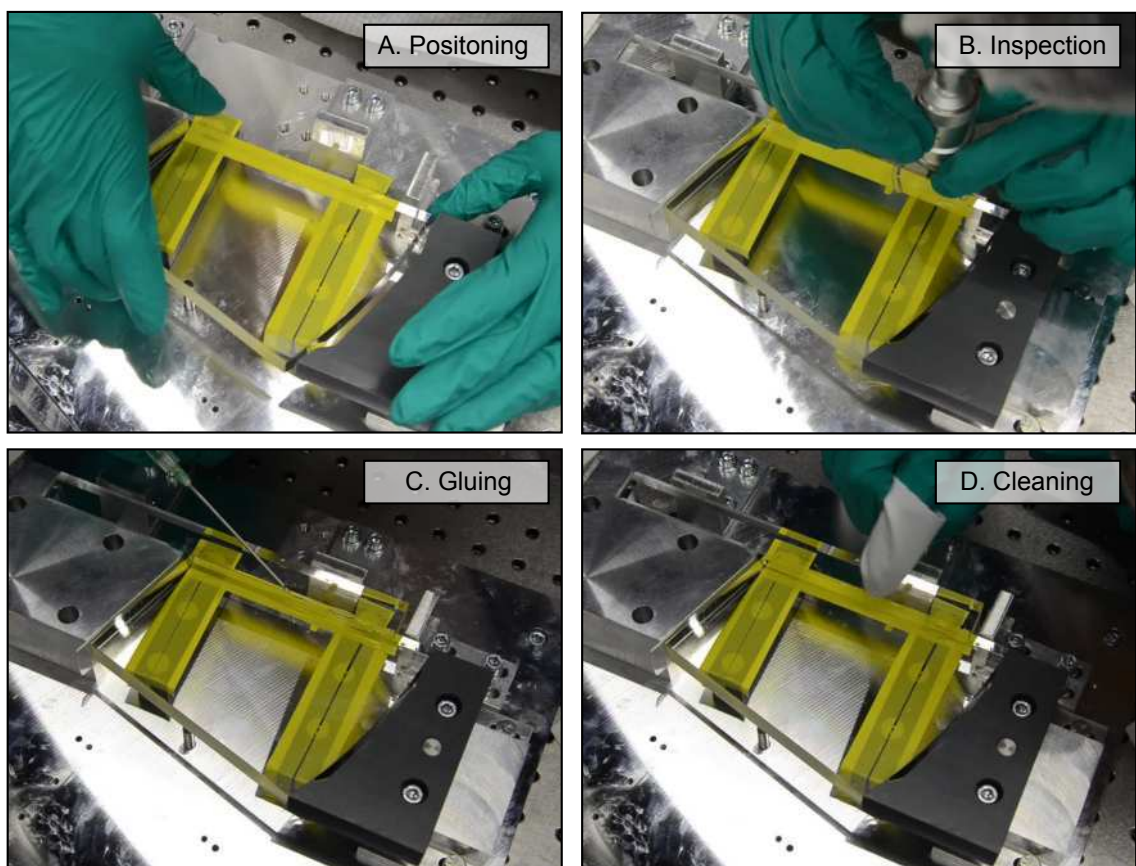


**Figure 4.53:** From top left to bottom right: First the FEL and prism are properly positioned inside the gluing device and the gap is carefully inspected. Afterwards the glue is applied using an injection. Finally any residues are wiped off before a final inspection was done.

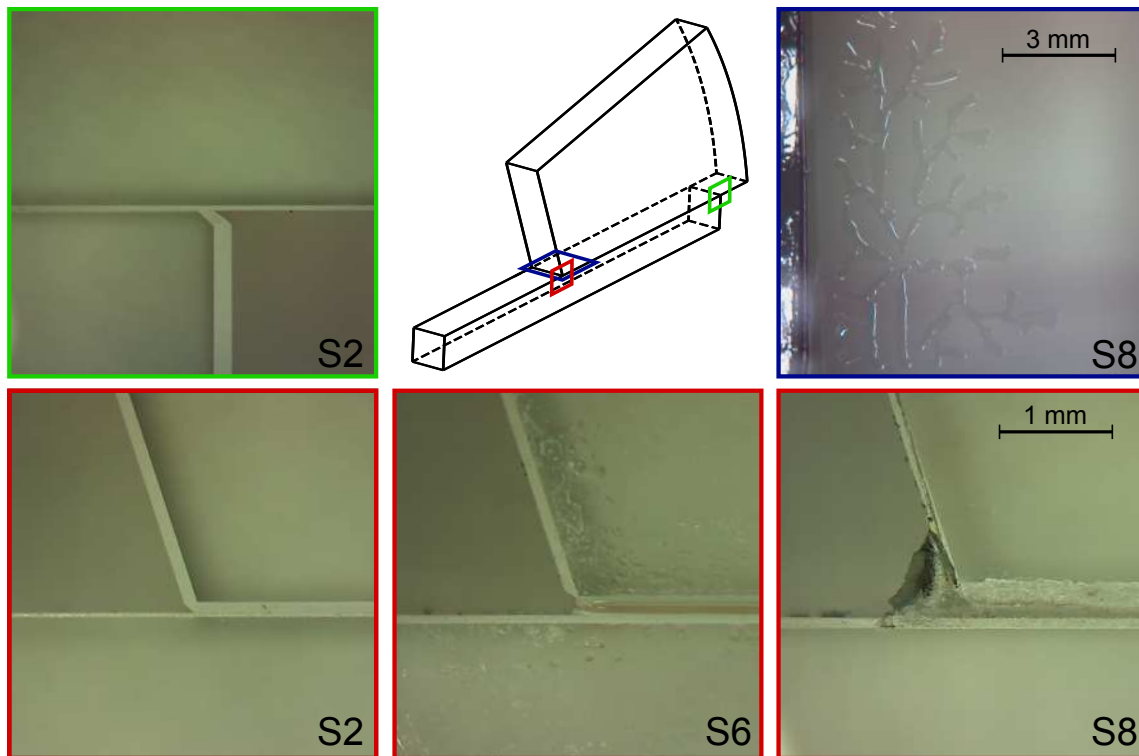


**Figure 4.54:** The framed images show magnified pictures of the couplings between the FELs and prisms. The color of the frame refers to the position where the picture was taken according to the sketch. The bluish framed picture on the top right shows the inclusion defect after 24 hours.

As only little practical experience regarding the bonding of optical components was available the gluing of the components was also done in order to anticipate the future course in this context. First the optical joints were inspected using a hand-held electronic microscope. In figure 4.54 some observations are summarized. First of all one can observe a visually perfect coupling for S2 which is done with optical contact bonding. The S6 FEL was contacted using Epicol 348990. The backside of the FEL, which faced the plate of the gluing device and was taped, showed a lot of unwanted residues on the surface which leads to photon loss and image distortion. Further investigations led to the assumption that it is not practicable to apply the tape prior to the alignment of the components, which was necessary because of a contact area below the glue gap. Nevertheless the coupling itself was achieved without bubbles or inclusions.

The last FEL (S8) was bonded using NOA-61. For this trial the taping was minimized which helped to achieve a cleaner surface. Unfortunately some glue was concentrated at the acute angle between the prism and the FEL. This causes photons, which are meant to be reflected off the prism surface, to scatter into the FEL. Another critical defect occurred later on when an at first small air bubble developed into a large-scaled branching. After two days it stopped developing further and covered almost the full FEL width of 16 mm

with a length of about 10 mm. One reason could be that the curing of the inside glue was not sufficient which stimulated the growth due to mechanical forces by the hardening glue.

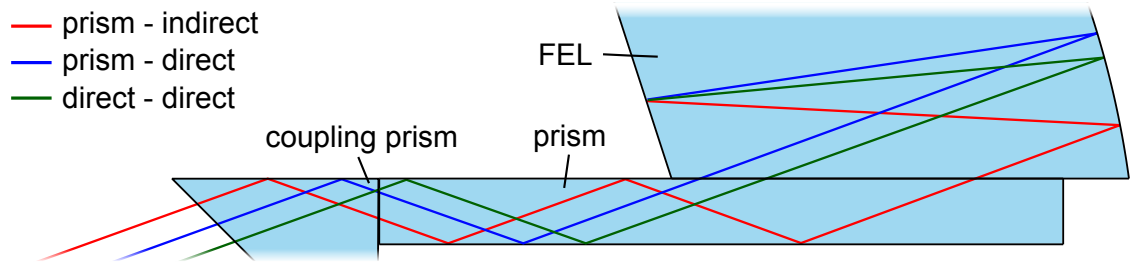


**Figure 4.55:** The above drawing illustrates the setup for scanning the FEL-prism pair. Three characteristic light paths are highlighted. Two of them (red and blue) are reflected off the coupling prism before entering the prism. One (red) also has two additional reflections inside the prism.

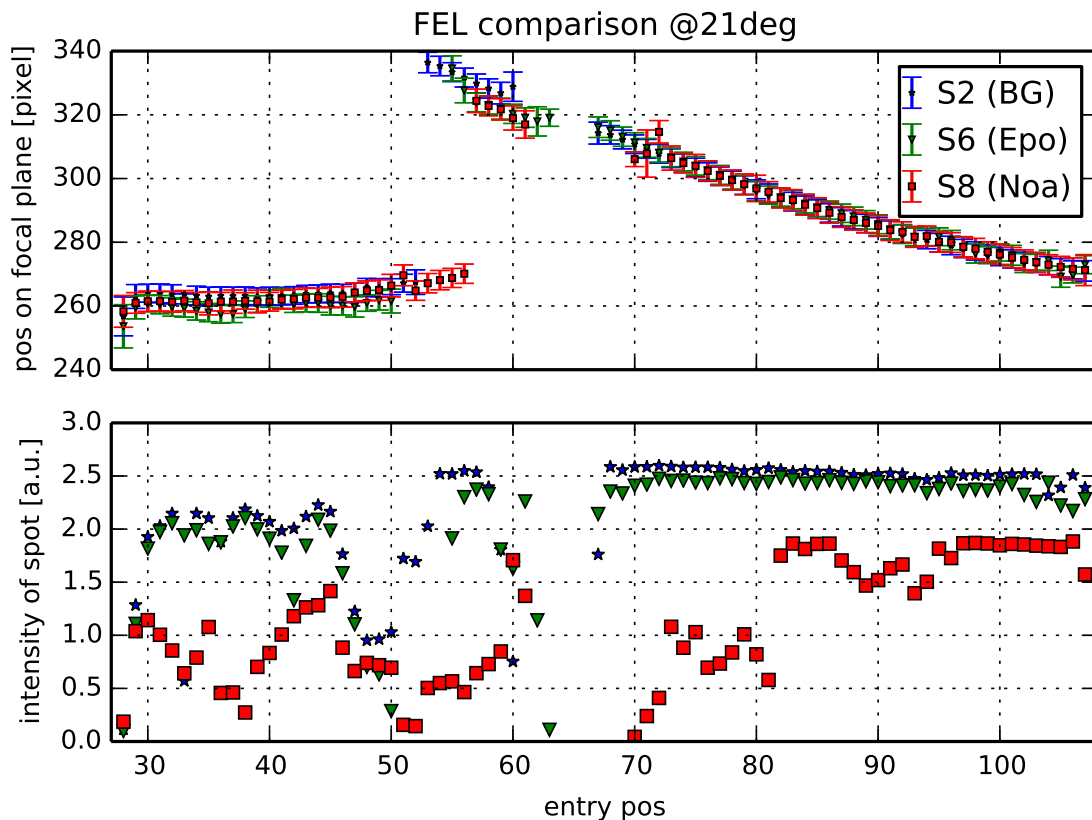


**Figure 4.56:** Scan of all available FELs connected to prisms at  $21^\circ$ . S2 was non-adhesively contacted by Berliner Glas (blue stars), S6 (green triangles) and S8 (red squares) were glued using APM Epical 348990 [APMEpi] and NOA-61 [Noa61]. The glue joint for S8 turned out to be deficient after it developed a large net of bubbles which leads to a crucial absorption especially for smaller angles and low entry positions. Bad data points have been removed from the plot. The error bars correspond to one standard deviation from the Gaussian fit. One pixel corresponds to  $9 \mu\text{m}$ .

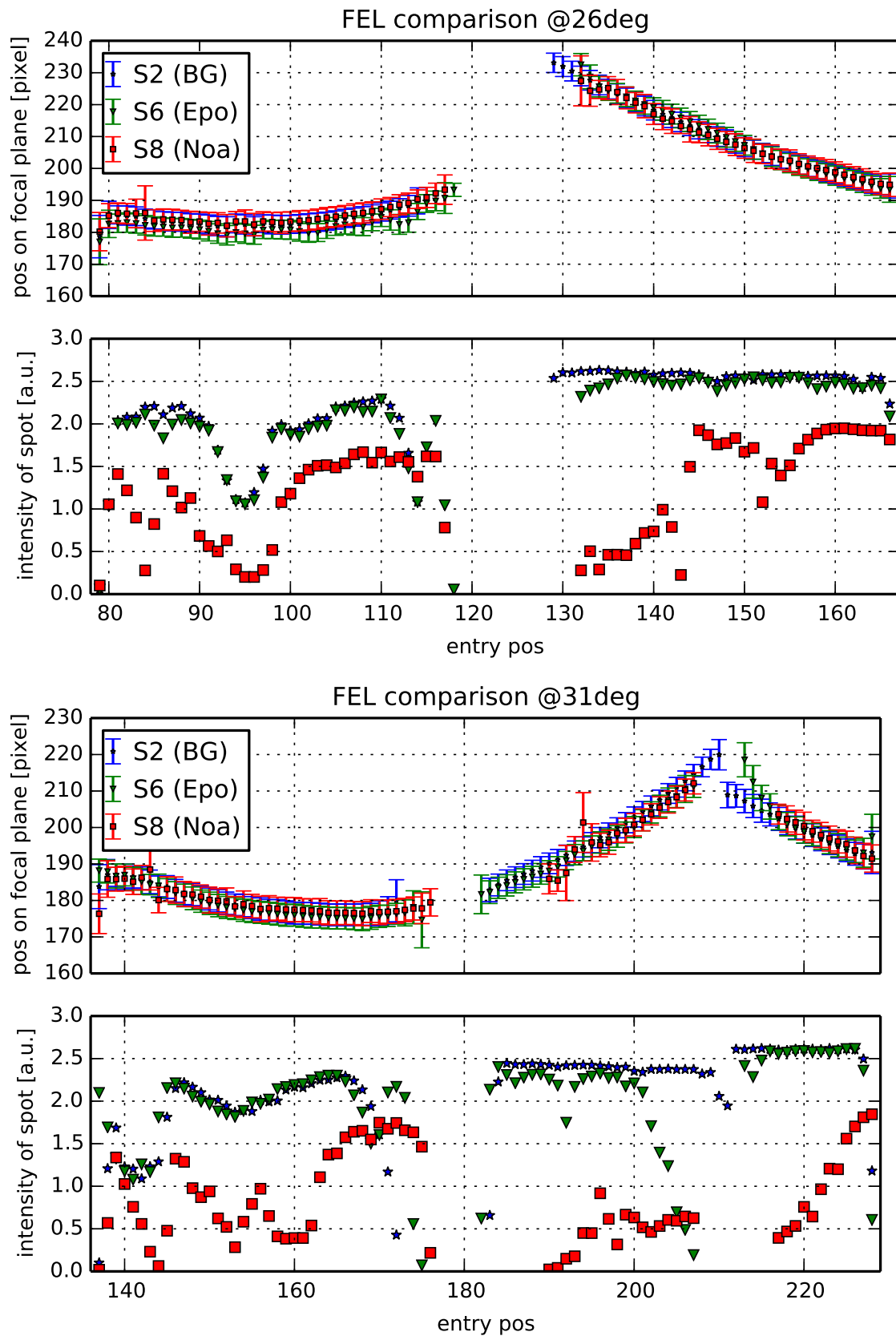


**Figure 4.57:** Comparison of FEL performance at 26 and 31° (for further explanation please refer to figure 4.56).

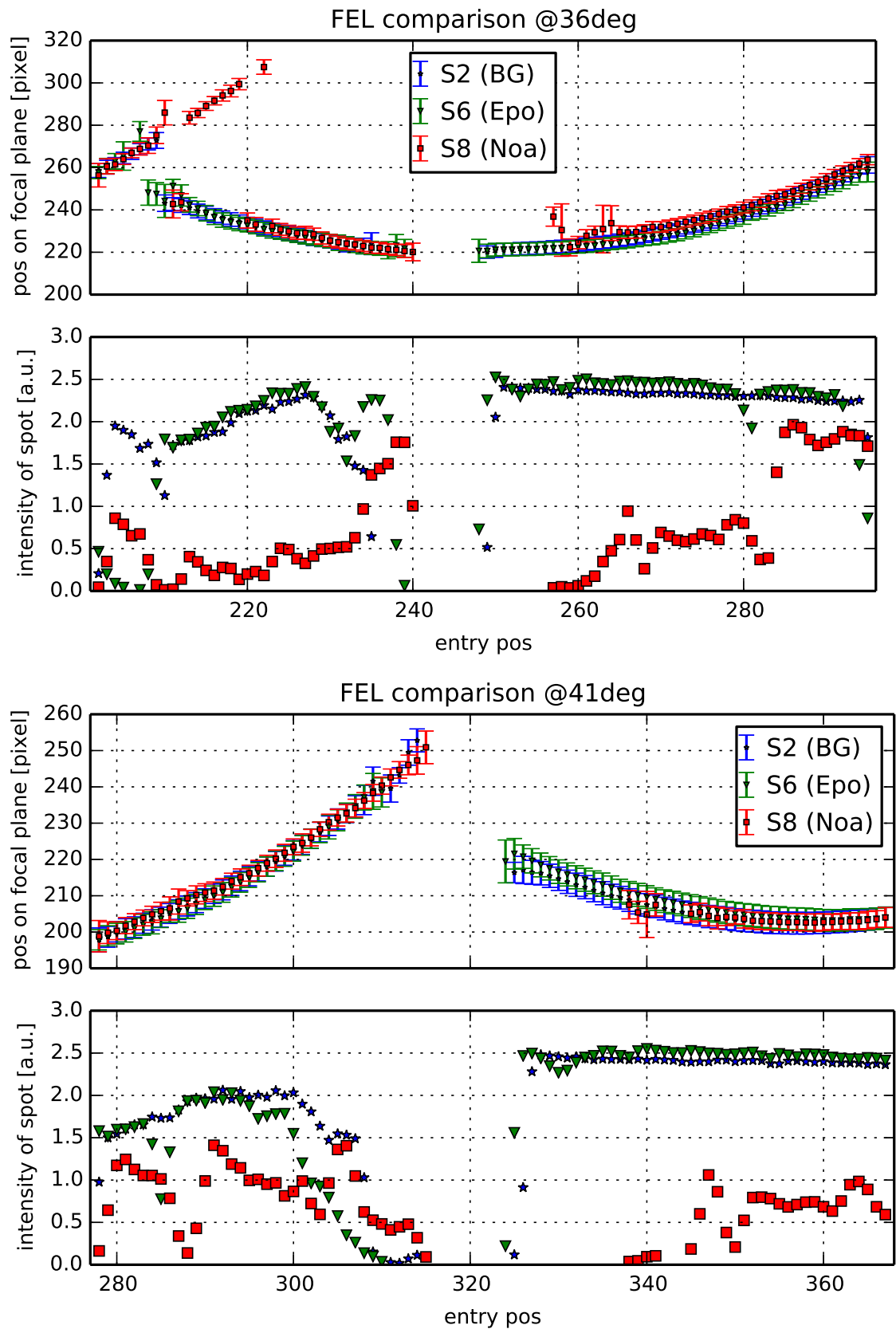


**Figure 4.58:** Comparison of FEL performance at 36 and 41° (for further explanation please refer to figure 4.56).

After the curing was completed all FEL-prism pairs were evaluated. With the prism attached to the side D of the FEL the setup was slightly altered by placing the coupling prism such that it extended the prism (see figure 4.55). Analogous to the dSiPM FEL measurement the alignment of the coupling prism had to be calibrated. Figure 4.56 shows the result for the scan at  $\varphi = 21^\circ$  (data points with a large deviation from the mean curve have been excluded). The top part of the figure shows the position of the spot on the CCD chip versus the position of the linear stage. The spot width is defined as the difference between the minimum and the maximum of the entries. Two discontinuities can be obtained in the spectrum. The first one between entry position 50 and 60 comes from a direct entry inside the FEL which causes a shift in the photon path (compare red and blue paths in figure 4.55). The jump for the NOA-61 spectrum is slightly shifted which can be explained by the additional glue inside the corner of the acute angle. The second discontinuity at around 65 is caused by the chamfer of the coupling prism which leads to uncontrolled scattering. The same behavior can be obtained from figures 4.57-4.58 which show the measurements between 26 and 41°.

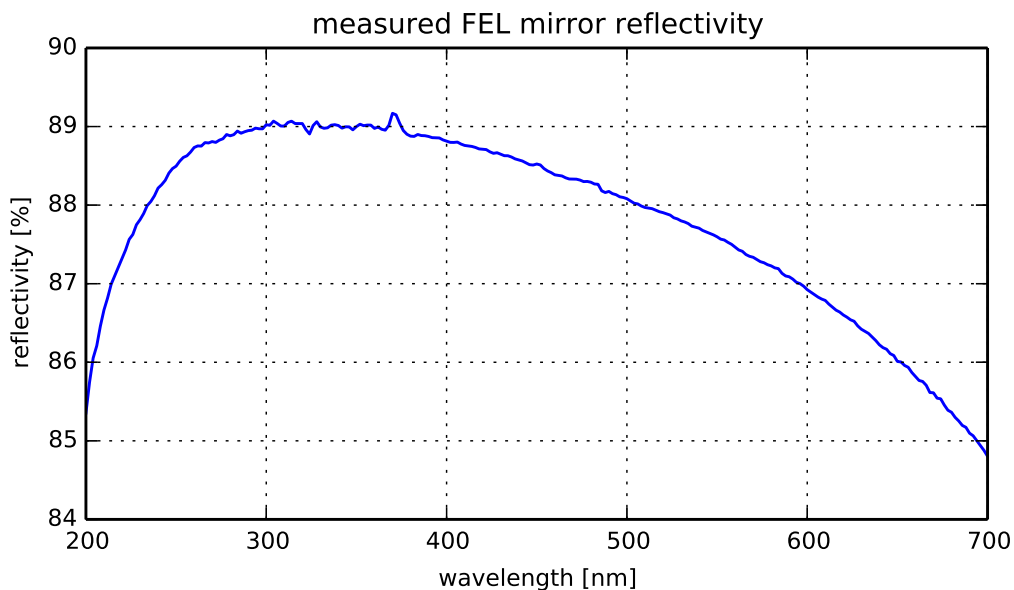


**Figure 4.59:** The above data shows the reflectivity of the Al coating on side A of the FEL. The data was provided by Berliner Glas and was recorded using a coated prism test piece and an unpolarized light source with an angle of incidence of  $28^\circ$  ( $45^\circ$  in air) [Fie17].

The bottom part shows the amplitude of the spot which corresponds to the integral of the Gaussian fit of the projection and hence is proportional to the transmittance (see figure 4.47). As no reference channel was available the measured amplitudes are not corrected for possible fluctuations of the laser beam. Moreover the exit angle of the photons varies between 4

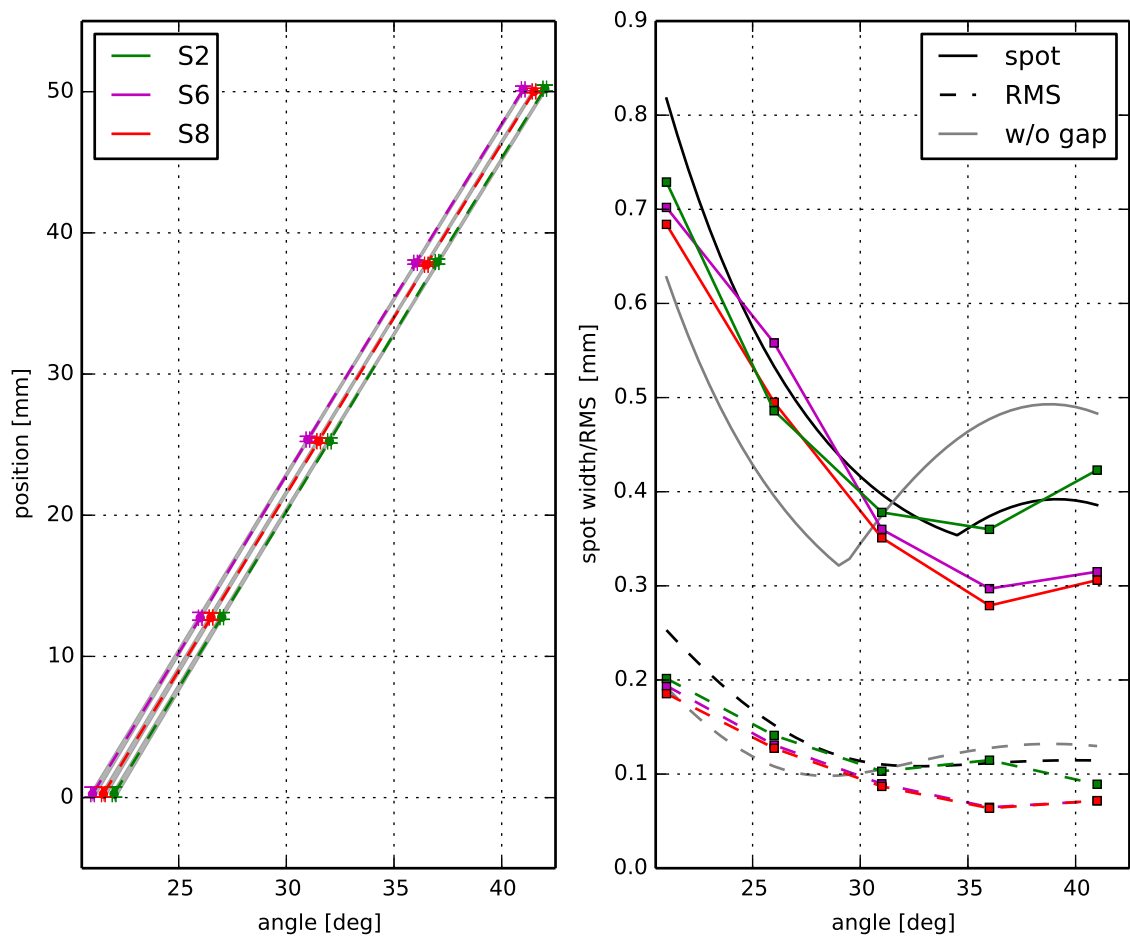


**Figure 4.60:** Left: Measured imaging function for all MCP-PMT FELs (S2 and S8 have been shifted to the right by  $0.5^\circ$  and  $1^\circ$  for a better display). Right: Spot width and RMS for the FELs. The black lines represent data obtained by simulation. The gray lines show the original spot widths and RMS values with a directly coupled 2 mm entry window.

and  $25^\circ$  which would require slightly different values for the Fresnel corrections. Nevertheless some important conclusions can be drawn from the recorded data. The amplitudes are higher for the entry positions to the right as the photons have less reflections of the surfaces and a steeper angle with respect to the exit surface C of the FEL. The performance for S6 which was epoxy glued is very similar to the optical contact bonding which is supposed to be the best choice. In case of the NOA-61 bonded S8 the amplitude is fluctuating and strongly suppressed after the reflection step due to the defect described above (in case of the  $41^\circ$  scan around 25% of the photons are immediately lost). In this connection one also has to bear in mind that the transmission inside the FEL depends on the angle of incidence with respect to the curved surface A. The reflectivity of the coating is also wavelength dependent and varies in the order of 10% within the relevant region (see figure 4.59). Although the epoxy bonding shows a good performance the NOA-61 bonding visualizes

the possible risks of gluing the FEL prism pairs in-house. Along with the advantages of an optical contact bonding regarding the transmission performance it is recommended to outsource this production step along with the fabrication of the optical components.

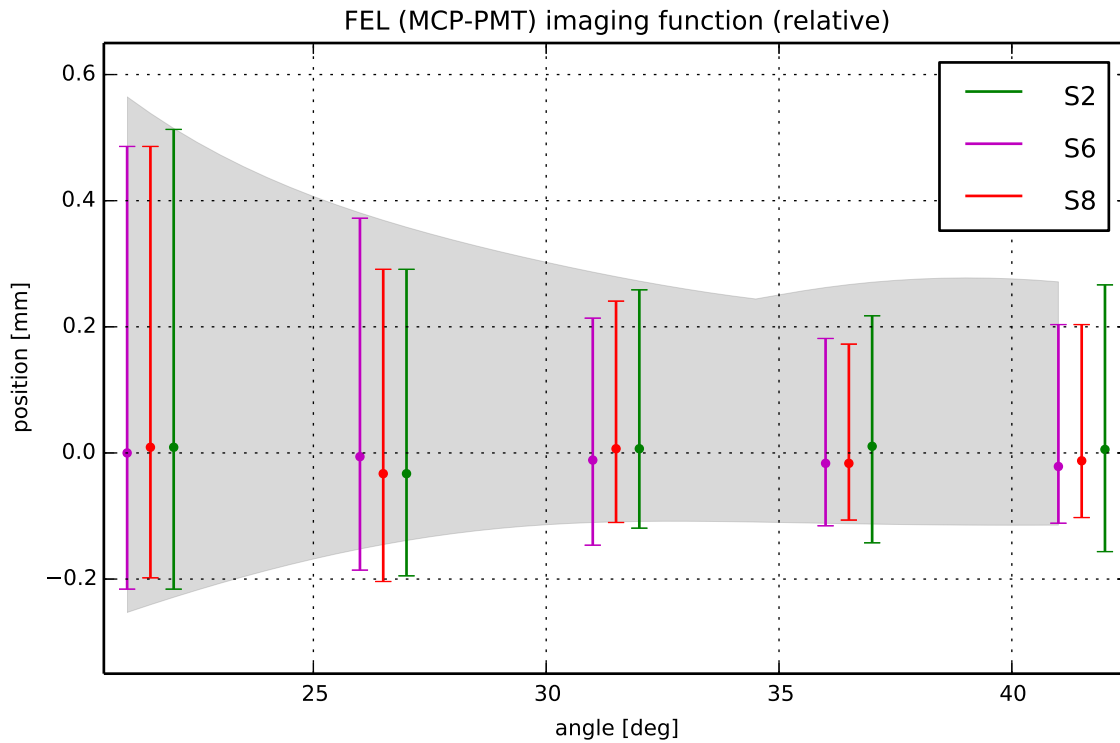


**Figure 4.61:** The above plot contains the data from the left part of figure 4.60 but shifts the data according to the mean value of the simulated data. The error band and bars correspond to the maximum spot width.

To quantify and compare the focusing properties such as imaging function, spot width and RMS to the theoretical predictions of the FELs, a small gap (1 mm) consisting of air and an entry window between the FEL side A and the CCD chip was added to the ray tracing macro for the geometry optimization. Such a gap leads to a different imaging function as well as different RMS and spot width values. As the CCD chip was smaller than the total width of the image, each position change of the chip was calibrated with respect to the previous position. In case of S6 and S8 the previous measurements without the bonded prisms were used as they are not distorted by defects due to the glue joints. Figure 4.60 summarizes the measured values. In case of the imaging function all FELs show a linear behavior according to the prediction. To get a better impression of the result figure 4.61 shows the relative positions of the reflections where a value of 0 corresponds to the simulated position on the CCD chip. Both figures show a good agreement regarding the spot width and RMS value. The measurements for S6 and S8 which were done with the same setup are almost

identical. The deviation of the S2 measurement most probably comes from the different measurement setup as the curves in figures 4.56-4.58 coincide. Altogether the MCP-PMT FELs show the desired performance and present a valid and feasible solution for focusing optics in a tight spatial environment.

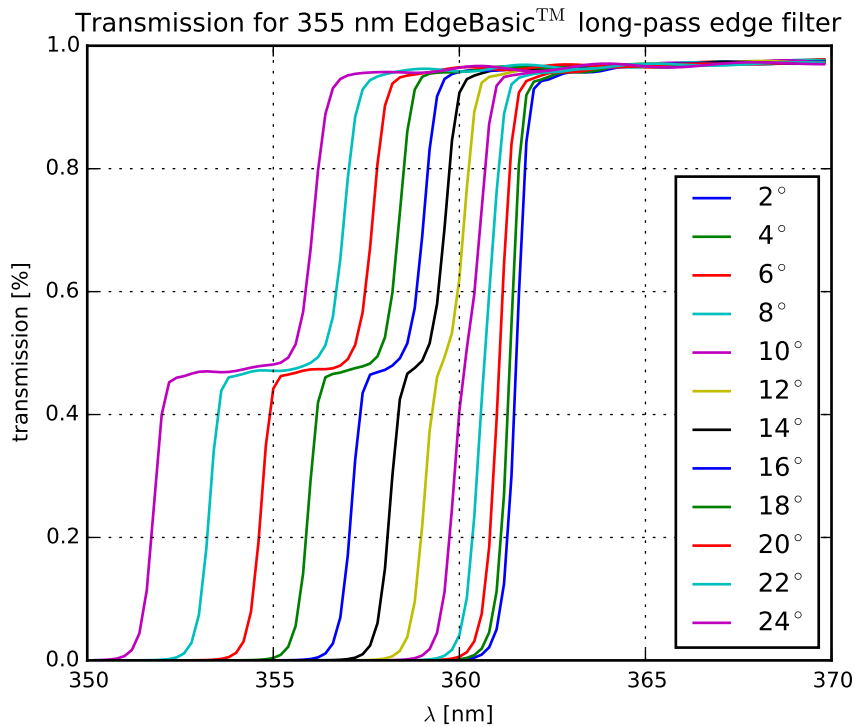


**Figure 4.62:** Transmission for 355 nm EdgeBasic™ long-pass edge filter for angles of incidence between 2° and 24° degrees. Data taken from [Semweb].

## 4.5 Optical Filter

Dispersion and the resulting chromatic error is an inherent property of any RICH detector. As described in section 3.1.4 it depends on the radiator material and does not only smear out the Cherenkov angle but also the time-of-propagation of the Cherenkov photons. One approach of limiting the chromatic error was to use a special prism made from lithium fluoride (LiF) which corrects for the angular deviation [Foh09]. The downside of this idea are the high costs for LiF in comparison to SiO<sub>2</sub>. A more economic approach are optical filters which can be added to the setup. As the resolution scales with  $1/\sqrt{N}$  it is important to identify the appropriate wavelength interval. Although the number of photons is higher in the UV region the dispersion is higher as well which results in monotonically decreasing value of  $d\theta_c/dN$  towards smaller wavelengths which is only modified by absorption edges of the fused silica or the quantum efficiency of the MCP-PMT photocathode. In case of the PANDA Disc DIRC two different kinds of filters come into consideration: a long-pass edge

filter to cut off wavelengths below a certain threshold and a single-band bandpass filter which can only be traversed by photons within a given wavelength interval. The transmission properties of these filters depend on the angle of incidence of the light and hence should be placed in front of the MCP-PMT entry window. Figures 4.62 and 4.63 show the wavelength dependent transmission for two standard filters at angles of incidence between  $2^\circ$  and  $24^\circ$ . For higher angles the transmission becomes more polarization dependent and shifts towards higher energies. The presented single-band bandpass filter shows a similar behavior for wavelengths between 305 and 315 nm but the edge is less steep (A.8 shows a narrower bandpass filter with a more uniform distribution).

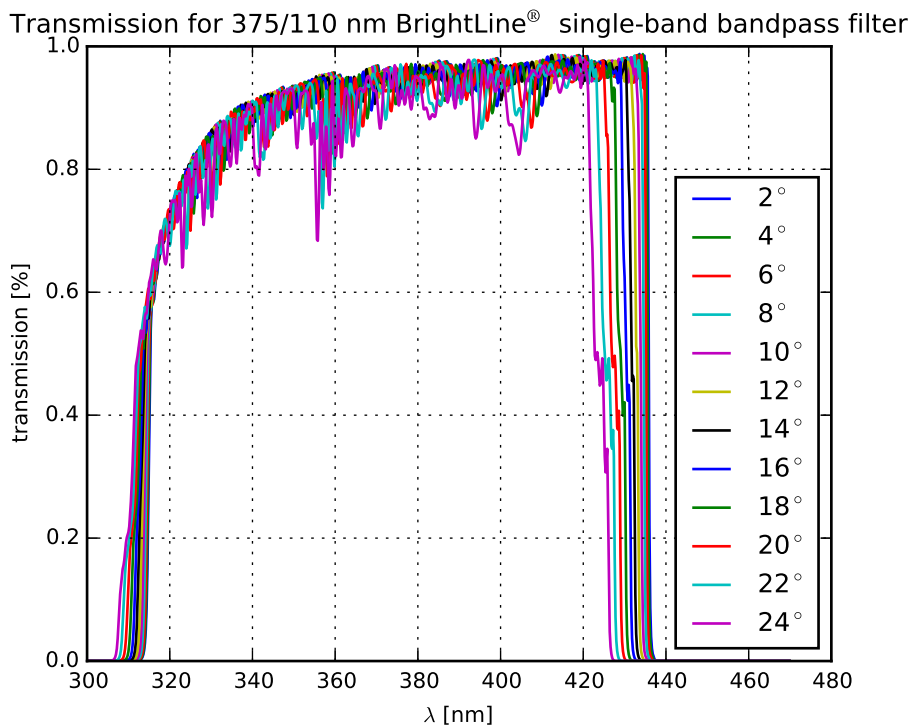


**Figure 4.63:** Transmission for 375/110 nm BrightLine® single-band bandpass filter for angles of incidence between  $2^\circ$  and  $24^\circ$  degrees. Data taken from [Semweb].

The transmission of the filters has to be folded with the photon distribution given by the production probability, the transmittance of the fused silica optics (see sections 3.1.4 and 4.3.2.1) and the quantum efficiency of the MCP-PMT photocathode. The underlying photon distribution was taken from a Monte-Carlo simulation which includes all possible angles for 3 GeV/c hadrons. In figures 4.64 and 4.65 six different options are compared. The black dashed-dotted line in figure 4.64 corresponds to the original photon distribution which is scaled by a factor 1/3 in comparison with the other distributions. The blue distribution in both figures represents the photon yield with the blue photocathode by PHOTONIS (Hi-QE-blue) [PHO16] whose quantum efficiency peaks at around 30% and aims at wavelengths in the UV- and visible high energy spectrum.

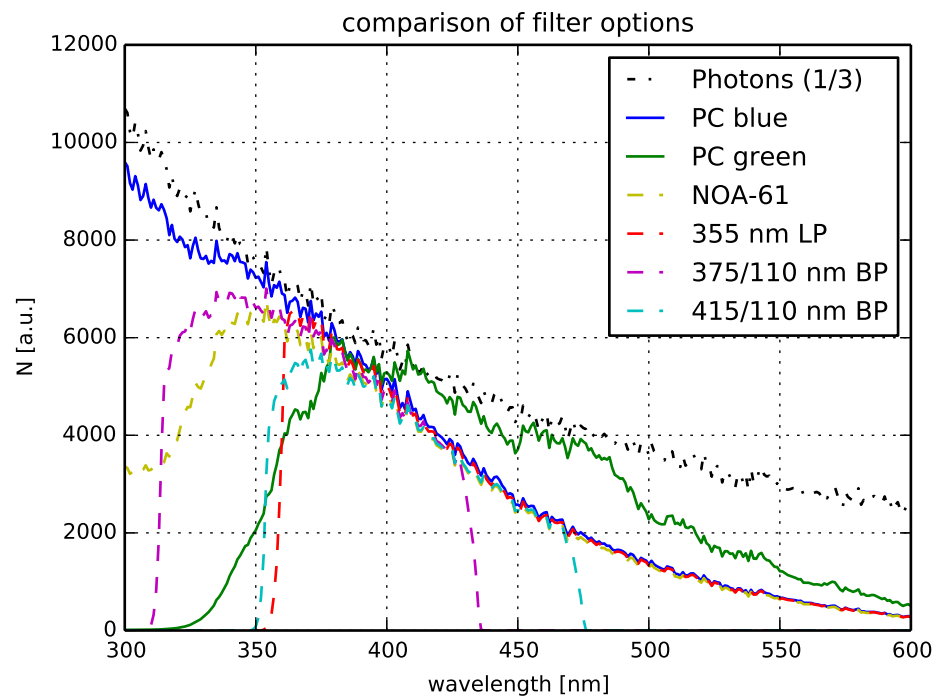


**Figure 4.64:** Comparison of transmission for different filters and photocathode options (the quantum efficiencies for the photocathodes were kindly provided by PHOTONIS [Pin16]). All filters are applied on the blue photocathode.

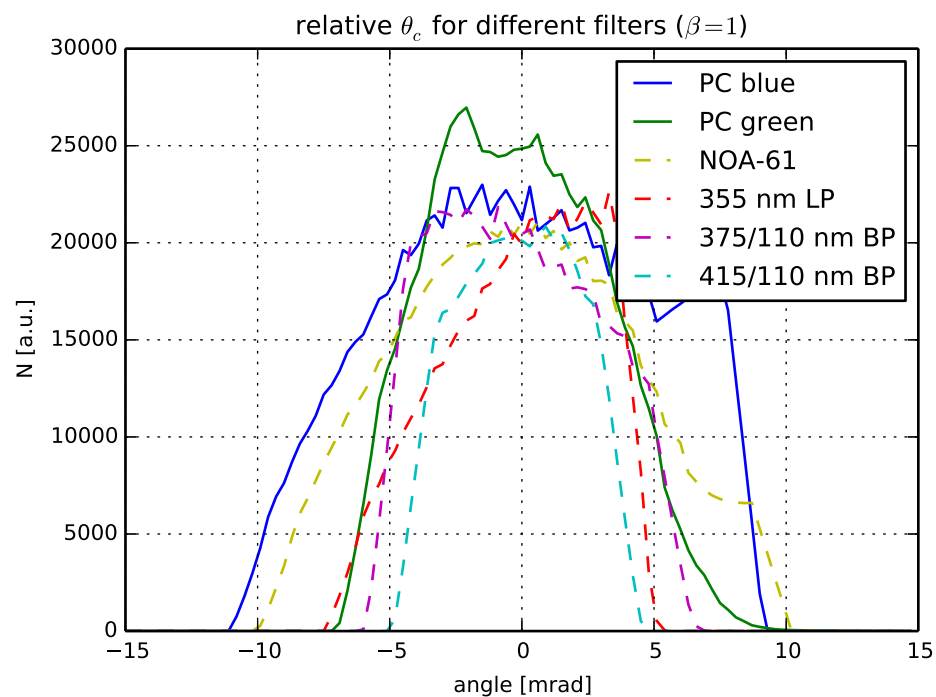


**Figure 4.65:** Comparison of the chromatic error for different filter and photocathode options. All filters are applied on the blue photocathode. The distributions were centered around 0 hence do not show the resulting position shift.

As the dispersion is larger at higher energies, which are favored by the blue photocathode, the chromatic error is large for this option. An improvement can be made by applying the filters presented above which are drawn as dashed lines inside the figures. The filter option 415/110 nm BP corresponds to an artificially shifted 375/110 nm BrightLine<sup>®</sup> single-band bandpass filter which is similar to a dielectric bandpass filter for the wavelength interval 360 – 465 nm which was proposed in [Mer14b]. A new option is a green photocathode (Hi-QE-green) which is sensitive towards higher wavelengths. Figure 4.65 indicates a narrower distribution for the green photocathode which is comparable with the filters. The RMS values for each option is shown in table 4.8. This table also contains the expected number of photons per track and the statistically weighted chromatic error. This number shows that the performance of the green photocathode is comparable to the edge filter option and slightly worse than the best bandpass filter option.

Another reason for the introduction of filters was the limitation of the number of photons to reduce the total anode charge and therefore delay the lifetime limit of the MCP-PMT sensors. In this connection the bandpass filter is still the best option as it has about 40% less photons than the green photocathode without any filter. As manufacturers further improve the lifetime limits of the MCP-PMTs and photocathodes and the demands of the PANDA experiment regarding the integrated luminosity have been changing the argument regarding the number of photons might become less relevant.

The figures also include NOA-61 [Noa61] as an option, which becomes less transparent for wavelengths below 350 nm. NOA-61 is a candidate for the glue joint between the radiator and the prism but as the edge is not sharp enough the chromatic error cannot be reduced. In this context a photocathode which is insensitive to wavelengths below 350 nm is an interesting option for a less complex and probably more economic EDD as less components are needed. Nevertheless this photocathode has not been tested regarding radiation hardness and lifetime which is crucial for its application. It is recommended to further investigate on this option for the aforementioned reasons.

Option	$\sigma_{\text{chrom}}$ [mrad]	$N_{\text{Ph}}$	$\sigma_{\text{chrom}} / \sqrt{N_{\text{Ph}}}$ [mrad]
PC blue	4.80	56	0.64
PC green	3.15	41	0.49
NOA-61	4.38	45	0.65
355 nm LP	2.84	31	0.51
375/110 nm BP	2.97	34	0.51
415/110 nm BP	2.13	24	0.44

**Table 4.8:** Chromatic error and photon yield for different filter and photocathode options.

## 4.6 Optical Joints

The significance of optical joints for the experiment has already been addressed throughout the previous sections. An optical joint is necessary whenever two optical components are connected in order to form the optical system. Like other optically relevant parts the joints must have a high transparency and conserve the photon angle. Often joints are realized by an optical matching gel or liquid (also called optical grease) which has similar properties as the main optics (i.e. fused silica) regarding the refractive index. This minimizes the chance of unwanted Fresnel reflections and provides a high transmittance. Figure 4.66 shows the transmittance measurement for three different optical greases: Silicone Grease EJ-550 by Eljen Technology [EJ550], Fused Silica Matching Liquid Code 06350 [CML6350] and Optical Gel Code 0607 [COG607] by Cargille.

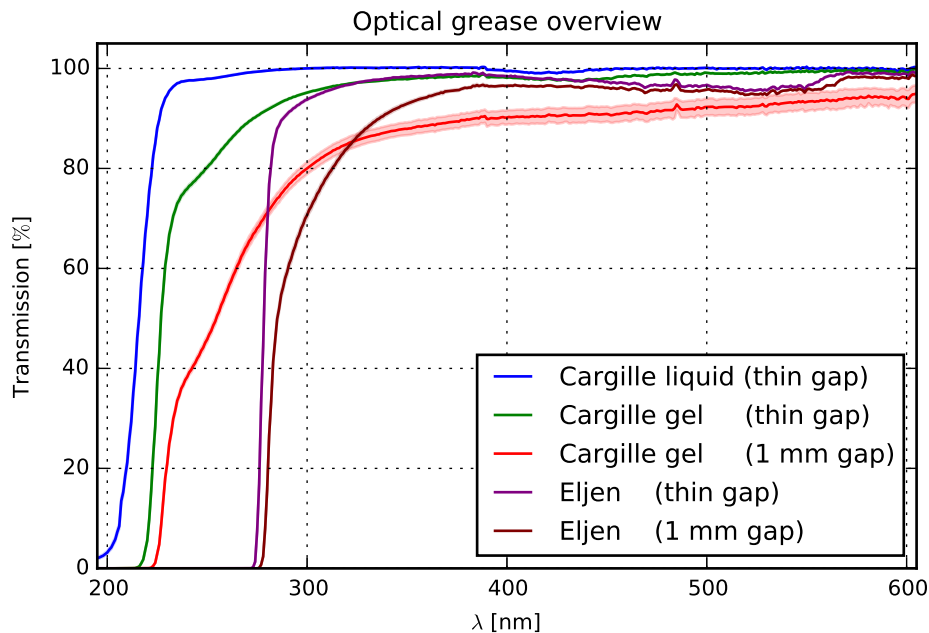


**Figure 4.66:** Overview of three different optical grease with different thicknesses.

In case of the gels two samples, a thin sample where the gel was pressed between two quartz glass plates and a 1 mm thick sample, were prepared. The values were obtained with the same setup as shown in section 4.2. A reference measurement was made with a thin quartz glass plate which was later subtracted from the measurement with the grease between two thin quartz plates. Therefore no additional corrections were made regarding Fresnel losses. All thin samples show a very high transmittance into the UV region where the performance of the Cargille couplings is slightly better. Both thick samples show a drop in transmittance in comparison to their thin counterparts which becomes more relevant towards lower wavelengths. The results of the measurement can be used as an input for Monte-Carlo sim-

ulations and are important in order get a better understanding of the photon yield. The matching gels or liquids come with the advantage that they are relatively easy to apply and remove and are available off-the-shelve. However, depending on the application they are not a good choice because of viscous flow.

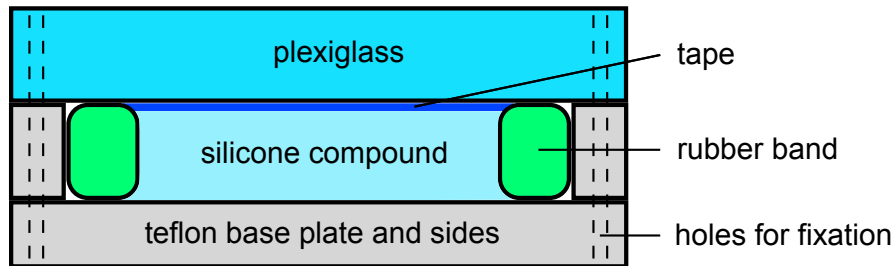


**Figure 4.67:** The schematic illustrates a side view of the setup for the optical pad production developed at KEK.

Another option are optical pads (sometimes called optical cookies). They are made on a silicone basis and can be commercially purchased (i.e. BC-634 A or BC-637 Optical Interference Pads by Saint-Gobain Ceramics & Plastics, Inc [BC634]) or individually molded. In preparation for the Belle II TOP counter TSE 3032 by Momentive [TSE3032], a two-component, low viscosity, transparent silicone rubber, was intensively studied [Fur14]. Other candidates for optical pads are RTV 615 by Momentive [RTV615] and Elastosil<sup>®</sup> RT 601 by Wacker Chemie AG [RT601] which are both available on the European market. Both materials have yet to be tested regarding their radiation hardness and transmittance over a wide wavelength interval. As only limited information about the molding procedure of the optical pads used at Belle II is available figure 4.67 schematically shows the used setup. The following production sequence was applied:

- Mix the two components and remove bubbles in a vacuum (in case of the Belle II optical pads the mixing ratio was altered from 100:10 to 100:2.5 which contains less hardener).
- Prepare the setup by applying tape or foil to the plexiglass side and place a rubber band inside the teflon structure before closing the setup with the plexiglass top.
- Fill in the mixed silicone and cure it preferably in an oven (40°C for 40 hours).
- Remove the cured pad from the teflon base and apply a membrane for protection. The other side should stick to the tape which can be removed from the plexiglass top. The rubber band has to be removed from the sides.
- The optical pad can now be cut into a dedicated format. Before using it as a joint between two optical components the tape has to be removed.

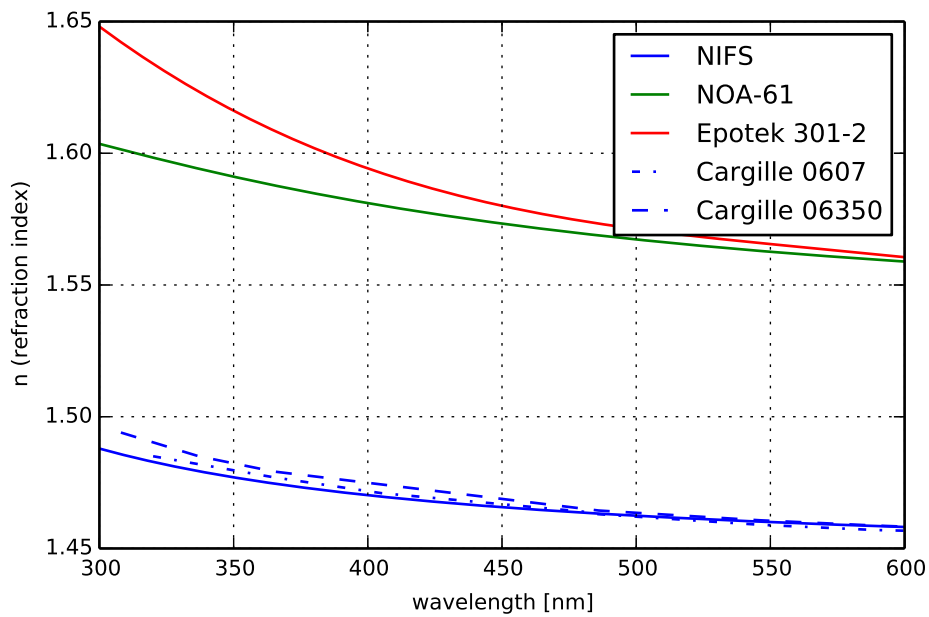


**Figure 4.68:** Wavelength dependence of synthetic fused silica (NIFS) [NIFS], UV-curing adhesive NOA-61 [Noa61] and two component adhesive Epotek 301-2 [EPO301, Vav01] along with optical grease produced by Cargille [CML6350, COG607].

The production of optical pads requires proper training in a dust free environment as the surfaces are fragile and attract dust particles. The coupling with optical pads can be improved by applying an optical matching liquid. In comparison to optical grease the refractive index is not well matched ( $n_{D,TSE3032} = 1.406$ ). Due to the vacuum inside the MCP-PMT the entry window is slightly concave which has to be taken into account when the pads are produced by evaluating the proper elasticity.

A third way of coupling is given by gluing the optical components. Typical candidates for this purpose are Epotek 301-2 [EPO301] which is a two-component epoxy or NOA-61 [Noa61] which is an UV-curing adhesive. The previously introduced APM Epicol 348990 [APMEpi] has not been studied in the context of a high-energy physics experiment so far. On the other hand especially Epotek 301-2 has been thoroughly tested for the use in previous experiments [Ada05]. Gluing provides a permanent connection but has to be applied carefully as defects such as bubbles or misalignment cannot be corrected once the material is cured. Other adhesives like the UV-curing NOA-68 can be separated in chlorinated solvent such as methylene chloride but the bond is not as strong.

In figure 4.68 the wavelength dependence of the refractive indices of different adhesives and optical grease products are plotted.

component	transm.	angular dev.	comment
tracking	-	$\approx 1$ mrad	depends on $dE/dx$ , MCS and the tracking resolution
radiator	>85%	< 0.5 mrad	transmission mainly depends on the number of reflections and surface roughness
glue joint	>99%	-	depends on the thickness of the glue joint and its refractive index
prism	>99%	0 – 7 mrad	depends on the track position with respect to the prism
FEL	80-92%	< 1 mrad	transmission mainly depends on the reflectivity of the coated mirror
optical pad	>95%	-	depends on the thickness of the optical pad and its refractive index
dispersion	90-95%	< 4.8 mrad	angular deviation depends on the choice of the filter and photocathode (see table 4.8)
MCP-PMT	< 33%	< 1 mrad	mainly depends on the Q.E. of the photocathode and the pitch of the anode pixels

**Table 4.9:** The table summarizes the influence of different detector parts with respect to the single photon resolution. Besides the optical system the external tracking as well as the MCP-PMT sensor contribute to the overall performance. The transmission values are wavelength dependent and in case of the dispersion only apply to the chosen band.

## 4.7 Summary

Although the realization of an Endcap Disc DIRC in first order depends on the lifetime of MCP-PMT sensors its feasibility is also reliant on the availability and machinability of the components which form the optical system. Therefore this chapter covered all relevant parts and provided needed measurements of critical components.

With Nikon Corporation a new manufacturer was introduced. Their fused silica products were tested for radiation hardness which also allowed a new look at the long-term behavior of radiation induced damage for dry fused silica. The form error of two prototype radiators was evaluated with an in-house measurement. These results helped to better understand the demands that have to be set regarding the specifications of such optics. In addition the measurements can be used to correct for form errors which might become relevant in future experiments. For the first time FELs for the MCP-PMT design have been manufactured and tested regarding their focusing properties which is a necessary measurement to prove the working principle of the Endcap Disc DIRC.

It is not possible to quantify the performance of the optical system by a single number as the

transmission and angular deviations of the photons depends on the position of the hadron track, its angle and the wavelength of the emitted photon. In this context a track position which is in the far prolongation of a prism with a steep angle leads to the best single photon resolution. In case of the averaged track resolution the relative position between the prisms and the track changes along with the projected angles. Other imaging errors are a result of waves on the radiator surface, the focusing capabilities of the FELs, the resolution of the MCP-PMT anode and the width of the FELs and prisms. They can be controlled by setting proper specifications. The chromatic error is an inherent property and can be reduced by applying optical filters or a different MCP-PMT photocathode. The imaging as well as the chromatic errors scale with the square root of the number of photons when the track resolution is calculated. Track related errors such as an error in the measurement of the track angle and position on the radiator or the error due to energy loss or Multi Coulomb Scattering (MCS) directly affect the Cherenkov angle resolution and cannot be influenced or reduced by higher photon statistics.

Table 4.9 summarizes the contribution of different detector parts as well as the external tracking towards the single photon resolution.



## 5 Mechanics

### 5.1 Requirements

Designing the mechanical support and structure has so far played only a subordinate role during the development of a working Endcap Disc DIRC design. In the framework of this thesis different concepts and design options were developed and investigated. In this regard the mechanical design has to fulfill the following requirements:

- usage of non-magnetic and radiation-hard materials,
- removability of certain components for maintenance,
- secure and precise assembly and alignment,
- low material budget,
- economically priced construction.

The listed conditions have to be fulfilled in a tight spatial environment as the EDD will be mounted on the support of the endcap calorimeter in front of its thermal insulation. This space was originally reserved for a Disc DIRC using SiPMs [Foh09] which had to be replaced by a design using MCP-PMTs [Mer14a] (see also section 3.3.1). These MCP-PMTs have to be aligned with the magnetic field which requires much larger FELs and occupies more volume in the readout region. Figure 5.1 gives an overview of the available space inside the endcap holding structure (EMC support). The left part of the figure shows the available space in z-direction which is limited by the insulation of the Endcap EMC and its supply lines [EMCTDR]. The minimum distance is given by the insulation with 42 mm where the radiator will be placed. The available space for the FELs and sensors varies from 242 mm to 148 mm. The latter value leaves only a total distance of 22 mm below and above the FEL-prism pair. In the x- and y-plane the minimum allowed distance between the EMC insulation and the FEL amounts to 35 mm whereas at least 10 mm have to be reserved between the rear edge of the FEL and the EMC support. In addition the dodecagonal symmetry of the EDD is neither present in the Endcap EMC nor its support structure which further restricts the available space. For demonstrable reasons not all requirements from the above list can be satisfied at the same time. The MCP-PMTs, for example, contain Kovar which is a ferromagnetic material. Although aluminum is paramagnetic it has a high conductivity which becomes noticeable during rapid variation of an external magnetic field such as a quench. In principle alternative materials like ZERODUR® [SotZER] or carbon fiber are available but in comparison to aluminum they are more expensive and their machinability is not as good.

The necessity of radiation hard materials is more relevant with respect to the optical and electrical components. In this regard extensive studies have been done by different DIRC

groups and were complemented by this thesis where the radiation hardness of a new type of fused silica was measured (see section 4.2). Besides radiation hardness the impact of out-gassing of materials such as glues, sealing and packaging has to be taken into account and for many materials a dedicated evaluation was done [Coh00].

The presence of passive material to stabilize and mount the detector cannot be avoided. The Disc DIRC radiator itself is a 2 cm thick homogeneous fused silica block with a radiation length  $X_0$  of 27.05 g/cm<sup>3</sup> and a nuclear interaction length  $\lambda_I$  of 97.8 g/cm<sup>3</sup> [PDG14]. During the conception stage of the mechanical design the necessity of a feasible assembly always had to be borne in mind. Temporary mounts require a lot of space and hence not all parts can be made exchangeable. Nevertheless, especially electronic parts and sensors are prone to having defects and will be individually removable.

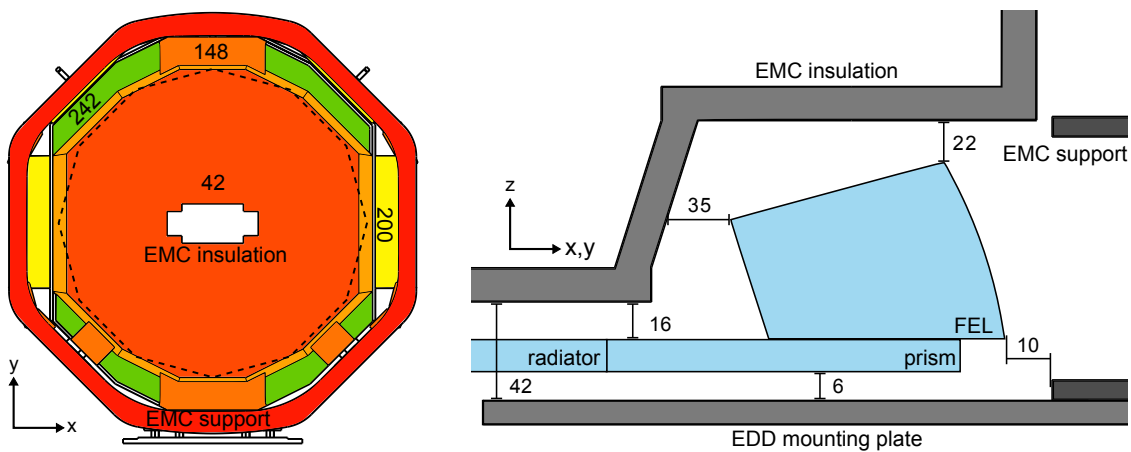


**Figure 5.1:** The illustration summarizes the constraining distances to the surrounding detectors. The left part shows a downstream view of the EMC endcap with the available space along the z-axis. The dashed line represents the DIRC radiator boarder. The right part also indicates the available space in the readout region for the FELs.

## 5.2 Concepts and Design

The anticipated mechanical design differentiates between large-, medium-, and small-scale components. Large-scale components (mounting plate and stabilizing cross) exceed the size of a quadrant and have to carry a major load (see also figure 5.2), medium-scale components (radiator cover and ROM housing) protect the optical system from outside influences and small-scale components (connection blocks and ROM cases) summarize small key components which are necessary to mount the radiator or smaller components such as sensors or electronics. The following section will introduce the concepts behind these components.

## 5.2.1 Components

### Mounting Plate

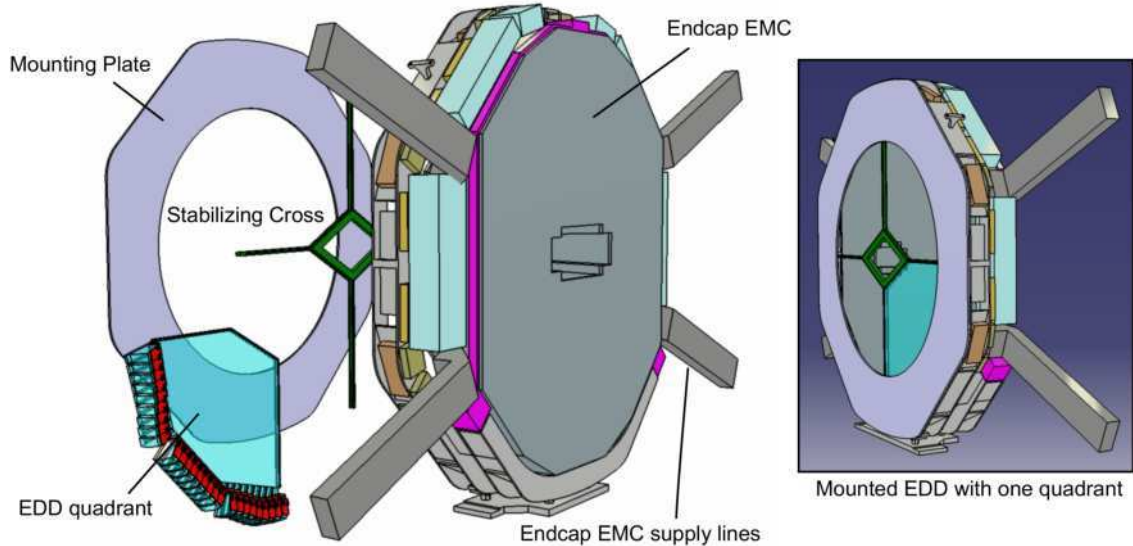


**Figure 5.2:** The picture illustrates the purpose of the large-scale components mounting plate and stabilizing cross and how they are applied.

The largest component is the so-called Mounting Plate (MP). It is a 15 mm thick plate which will be screwed onto the upstream side of the Endcap EMC support and has the same outer dimensions. For this reason all screws on the EMC outer frame which would have interfered with the MP are countersunk. The endcap EMC support measures more than 2.5 m in diameter and is divided into two pieces at 3 and 9 o'clock. Due to its size it is recommended to divide the MP into two pieces as well at 6 and 12 o'clock preferably. It will consist of aluminum and has to carry the entire weight of the Disc DIRC. In order to not unnecessarily increase the material budget a circular hole with a radius of at least 850 mm will be cut-out.

As the EDD will be added to the  $\bar{P}$ ANDA experiment during a later stage a deformation of the Endcap EMC support cannot be ruled out. Finite Element Analysis (FEA) predicts a deformation of as much as 13 mm along the y-axis [EMCTDR]. Therefore eight so-called orientation holes were added to the upstream side of the endcap EMC support frame (see figure 5.3). To safely mount the EDD during a later stage of the experiment more holes will be required and added using a drilling stencil which can be adjusted using the orientation holes.

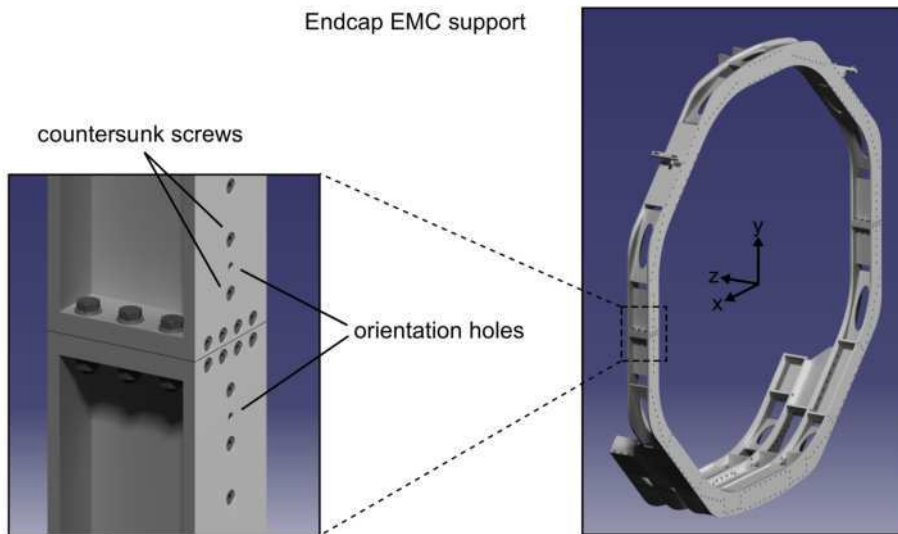


**Figure 5.3:** A CAD picture of the Endcap EMC showing the changes which have been made in order to mount the Endcap Disc DIRC.

### Stabilizing Cross

The MP is subdivided into four regions (quadrants) by a Stabilizing Cross (SC). It has a rhombic cutout in its center where the acceptance region for the Forward Spectrometer lies. The main purpose of the SC is to keep the four quadrants in position. This is realized by 1 – 2 mm thin U-profiles which are attached to each other to form a double-T-profile with a strengthened middle part. In this regard it is unavoidable to add additional material in the Endcap EMC acceptance. As the SC has to withstand the weight of the two upper quadrants a compromise has to be found between the profile thickness and height (see figure 5.4). It is planned to rivet the U-profiles along the four long arms of the cross and weld them in the corners by cutting out a triangle of the salient material and bending them according to the radiator geometry. First tests have already been done in this regard (see section 5.5) and support this idea of building a stable cross structure. The SC will be clamped taut to the MP to avoid any shifts in z-direction and displacement of the quadrants.

The inside of the SC will also provide suspensions for the EDD radiator which have to be manually added once the SC profile and radiator dimensions have been precisely measured. Using this method a good suspension of the radiators can be achieved.

### Radiator Cover

The optical system and photo sensors have to be operated in a gas- and light-tight environment. As the SC only covers the small surfaces which do not have ROMs attached the large openings have to be sealed. One of the requirements for the sealing is that it has to have only a small contribution to the material budget as it will cover the full acceptance region

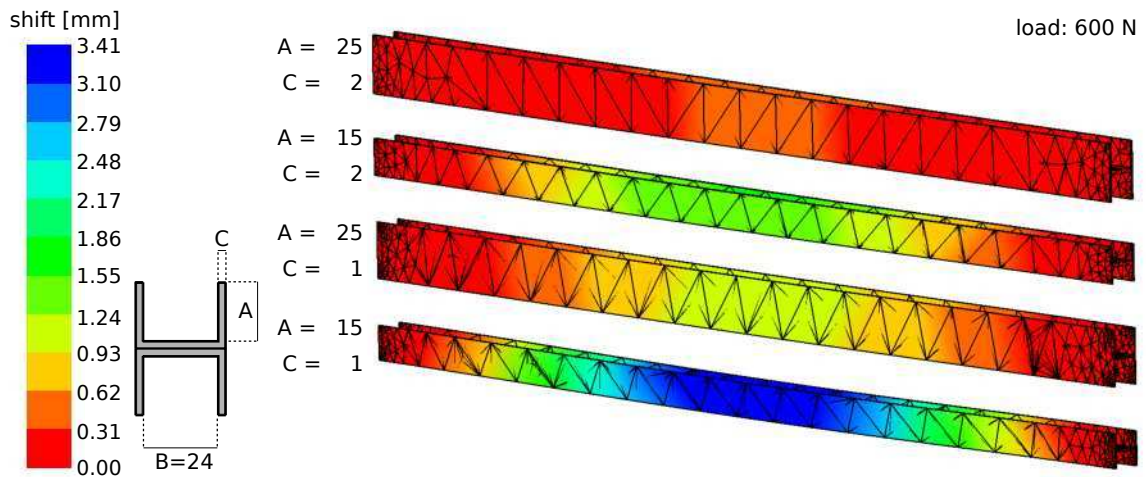


**Figure 5.4:** Impact of the profile thickness ( $C$ ) and height ( $A$ ) for a linear load on the stability of a SC profile. The length of the pieces is 1 m. The finite element analysis was carried out using z88Aurora<sup>®</sup> [z88Aur].

of the Endcap EMC. On the other hand it has to be stiff and robust. In this regard, although foils are a natural choice for a thin seal their proper mechanical assembly is challenging. In case of the Belle II TOP counter a honeycomb panel made of aluminum was used [Suz15]. In this option two ultra-thin aluminum layers are interleaved by perpendicularly oriented hexagons which lends a high stability to this structure. A third possibility is a cover made of carbon fiber. This material combines high stiffness with good machinability and will be used in other PANDA detectors as well [BarTDR, EMCTDR]. Initially it was planned to construct a box containing the radiator which can be slid into the space provided by the SC which is similar to the procedure for existing DIRCs [Ada05, Ina14]. However, such a design would require a more sophisticated construction and hence reduces the acceptance of the EDD and adds more material budget in front of the Endcap EMC. For the abovementioned reasons a thin plate cover represents the best alternative.

## ROM Housing

Like the radiator cover the ROM housing (RH) has to provide a gas- and light-tight environment for the ROMs. One RH will contain nine ROMs. It has to be connected to the radiator cover as the radiator and the FELs form an optical unit. It also has to provide feedthroughs for the high voltage of the MCP-PMTs and the cables which are needed to run and read the soldered ASICs on the PCB. The Front-End Electronics (FEE) are supposed to be placed outside the RH to reduce potential outgassing of the electric components. As the available volume changes the positioning of the FEL-prisms is different for each side of the EDD and the ROM housings have to be individually designed.

	connection	cable	diameter	cross section
<b>HV</b>	108 MCP-PMTs	108 coaxial cables	5 mm	2,700 mm <sup>2</sup>
<b>LV</b>	108 ROMs	216 cables	2.5 mm	1,350 mm <sup>2</sup>
<b>data</b>	108 ROMs	108 fiber cables	5 mm	2,700 mm <sup>2</sup>
<b>gas</b>	4 quadrants	8 pipes	10 mm	800 mm <sup>2</sup>
<b>cooling</b>	4 quadrants	8 pipes	60 mm	28,800 mm <sup>2</sup>
				36,350 mm <sup>2</sup>

**Table 5.1:** Overview of cables and corresponding cross sections for a fully equipped Endcap Disc DIRC with nine ROMs on each side.

### Connection Block

Connection blocks are necessary to support and mount the optical system at the twelve corner positions (see figure also 5.11) as the SC does not provide proper fixation along its geometry. If nine ROMs are connected to each side the lateral area of support will be less than 2.8 cm<sup>2</sup> at the intermediate positions and less than 1.6 cm<sup>2</sup> at the far ends. In case the number of ROMs can be reduced to eight per side this area of support can be doubled (see section 5.4). Like the suspensions in the SC the connection blocks have to be precisely aligned to not add additional forces or torques to the optical system. At this time it is not decided whether the connection blocks will provide a fixed or spring-loaded mount.

### ROM Case

The ROM case contains three FELs and three prisms and provides support at the optically non critical surfaces (see figure also 4.43). It stabilizes the ROM and helps to reduce any torsions between the FELs due to gravitation. In addition it carries a holding structure for the MCP-PMT which has to be precisely mounted on the FEL focal plane. In the case of nine ROMs per side the distance between two neighboring MCP-PMTs is less than 1 mm and the MCP-PMT holder could only support the sensor on two sides. This setup is possible but has only very limited contact surface. Furthermore it is not proven that the MCP-PMTs operate error-free without proper shielding. On the other hand a design with eight ROMs gives additional space between the ROMs and would allow to construct a holder which contacts the MCP-PMT on all four sides including decent shielding of the electromagnetic fields.

#### 5.2.2 Gas System and Cabling

The required cabling depends mainly on the sensors and electronics which are chosen for the final detector. Therefore the presented solution is preliminary and only a baseline de-

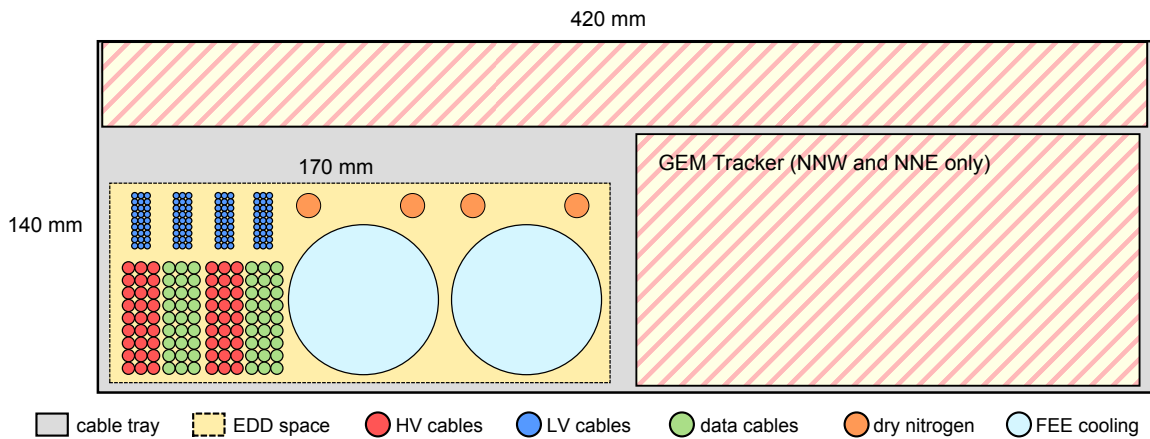


**Figure 5.5:** Cross section of a cable tray and the required space for the Endcap Disc DIRC. The displayed setup routes all electronic and gas cables through the two southern trays but only the cooling is for the two bottom quadrants only. Hence the northern trays have to contain two additional cooling pipes for each quadrant. The top part is occupied by the Muon Detector. The exact placement of the cables has not been defined.

sign. In principle each ROM requires high voltage for the MCP-PMT, low voltage for the operation of the front-end electronics and the ASICs as well as a fiber cable for the data stream. In addition each quadrant requires a gas system to provide a constant flow of dry nitrogen along the radiator surface and towards the FELs. This is necessary to prevent the deposition of outgassing material and avoid condensation on the optical surfaces. The rate will be several liters per hour provided at a light overload pressure compared to the outside air. Depending on the generation of heat by the ASICs additional cooling might be necessary.

Figure 5.5 shows the cross section of an available service duct which leads to the outside of the detector. Inside a reserved area the cables which are required for the EDD are drawn. This setup is not final as the distances between the cables might be changed to prevent overheating. At the same time the bending radius of the cables has to be respected which usually corresponds to a value of about 3 cm. The Forward Endcap of the  $\bar{P}$ ANDA experiment provides eight service ducts which are named according to cardinal points (see figure 5.6) and have a cross section area of  $420 \times 140 \text{ mm}^2$  each. The two eastern and western ducts are mainly occupied by the Forward Endcap EMC [Sni15] whereas the northern ducts are partly used by the GEM tracker. For this reason it is planned to mainly use the southern service ducts for the EDD. In case the quadrants require a separate cooling for the front-end electronics the upper pipes should be introduced via the northern service ducts whereas the cables can still be routed from the southern ducts which allows a better localization of the racks.

Each ROM housing will provide plugs or feedthroughs for the cables. The routing of the cables from south to north can be partly done inside the lateral free space which is pro-

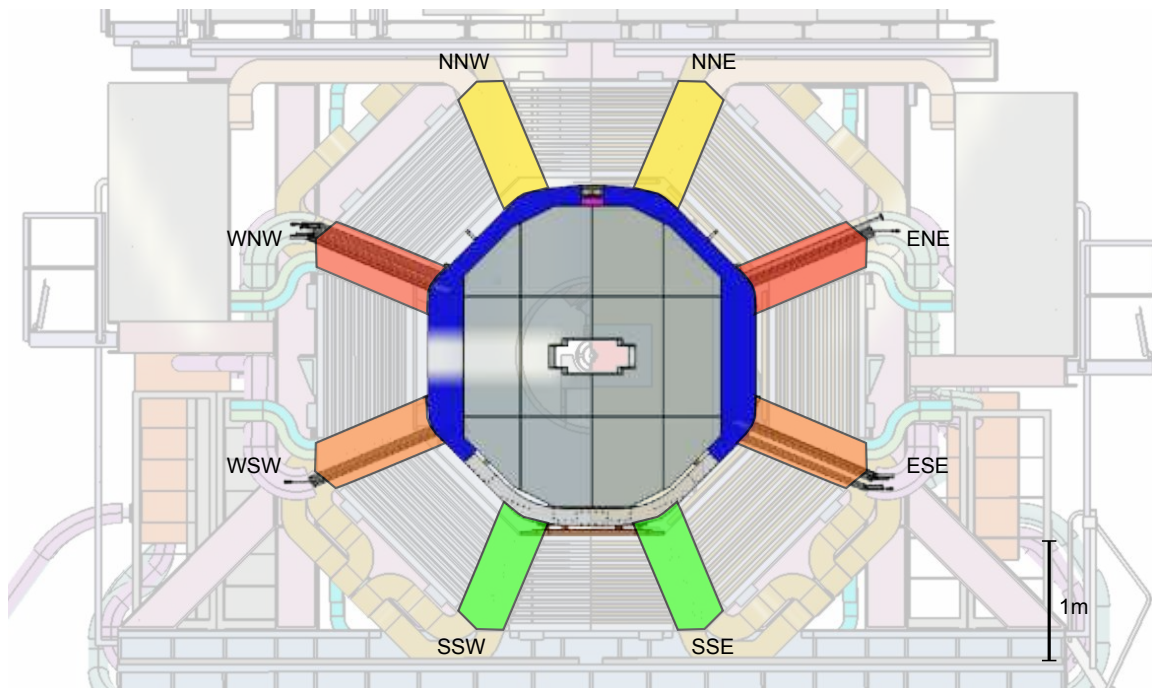


**Figure 5.6:** Upstream view of the  $\bar{P}$ ANDA Target Spectrometer with a highlighted endcap and the available cable trays. The reddish colored trays are mainly occupied by the Endcap EMC (83% for the WNW and ENE and 63% for the WSW and ESE trays). The northern trays will be partly used by the GEM detector whereas the southern trays are not occupied.

vided by the endcap holding structure. The dry nitrogen has to be injected at the radiator surface facing the center of the detector. Hence the incoming tubes will be guided along the SC whereas the outgoing tubes will be connected to the ROM housings. In table 5.1 the required cables and pipes are summarized including their anticipated diameter and total cross section. Cables for a laser calibration system have not been taken into account yet. If the numbers of ROMs are reduced from nine to eight per side the number of cables can be reduced by 10% whereas it does not have an influence on the number of pipes for the dry nitrogen or the front-end cooling.

### 5.3 Assembly

The assembly procedure of the EDD will consist of four stages:

- ROM assembly: preparation of the readout modules for the final assembly
- Quadrant assembly: complete assembly of one detector quadrant
- Horizontal assembly: quadrants are installed and fixed inside the SC on a horizontal table
- Vertical assembly: connecting the EDD to the EMC holding structure in a vertical position

## ROM Assembly

At first the individual ROMs will be prepared. Here the the FEL-prism pairs will be carefully placed inside the ROM case. Before that the components have to be cleaned and be free of dust. For this activity it is important to use a fluffless cloth which is moistened with e.g. isopropyl alcohol. The cloth should be folded and firmly pressed against the surface and moved linearly along the surface. Circulating moves should be avoided. The distance between the optical parts inside a ROM is 1 mm which will be ensured by spacers which keep the FELs and prisms in position by touching them on optically non critical surfaces. An additional spacer will be placed at the far end of the prisms. The prism ends facing the radiator should be parallel and align to the radiator within few  $\mu\text{m}$ . This part of the assembly does not include the MCP-PMTs.

## Quadrant Assembly

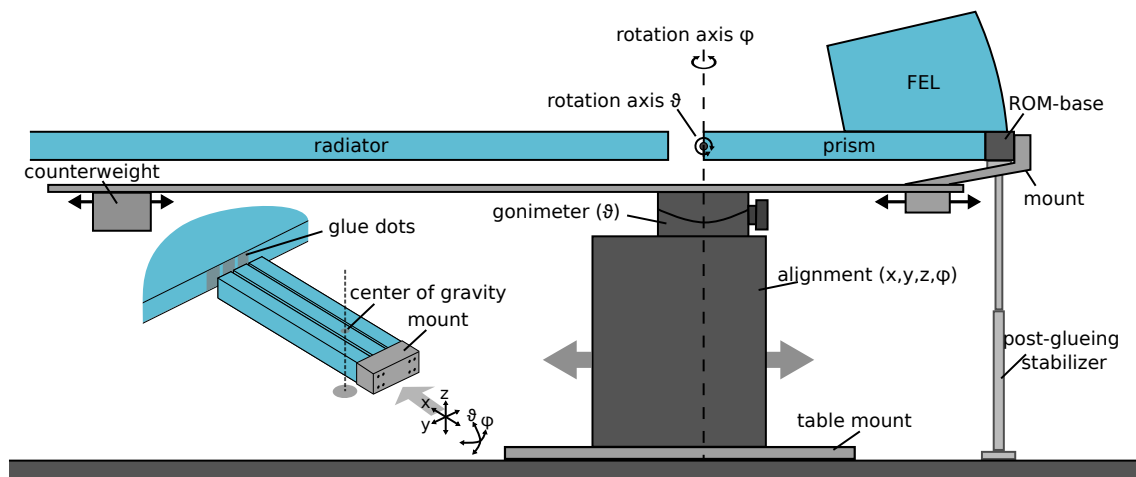


**Figure 5.7:** The schematic drawing illustrates the assembly setup to glue ROMs to a radiator. The rotation axis of the setup coincides with the end of the prism which faces the radiator. The counterweight reduces torque on the goniometer.

In contrast to the present prototypes the available space in the  $\bar{\text{P}}\text{ANDA}$  experiment is not sufficient to install a sophisticated mount for each ROM. Therefore it was decided to glue the FEL-prism pairs to the radiator to form a rigid optical unit. This solution minimizes the space which is necessary to mount the ROMs, does not require a complex recalibration and provides a reliable optical contact between the radiators and the prisms. On the other hand the glue has to meet certain requirements:

- high transmission for the photon wavelengths of interest,
- similar index of refraction to fused silica to avoid Fresnel losses,

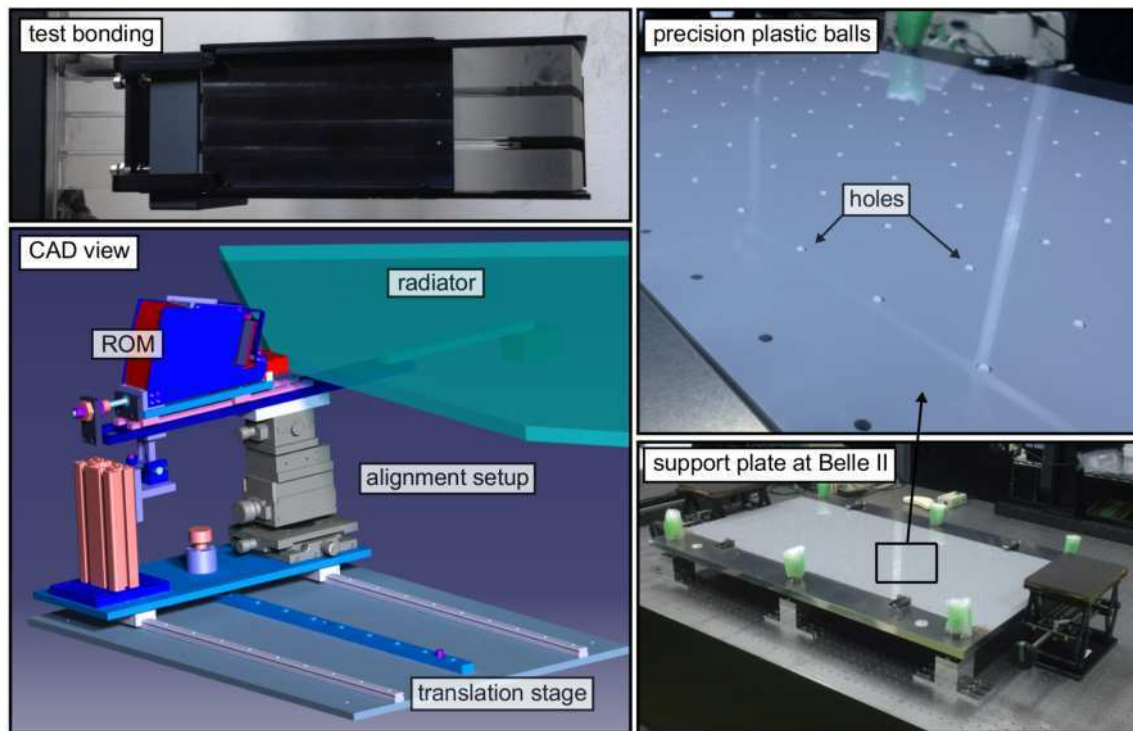


**Figure 5.8:** The left part shows a test bond of a ROM to a thin glass plate (top) and a CAD picture of the final assembly setup. The right part show the support plate that has been used for the Belle II TOP counter.

- radiation hardness,
- strong bonding.

The available options have already been introduced in section 4.6. The most convenient choice would be Epotek 301-2 [EPO301] which has already been used for the BaBar DIRC and the Belle II TOP counter [Wan14]. Due to the size of the components it is not possible to accelerate the curing in a high temperature atmosphere which is why not more than one ROM per day can be glued. NOA-61 [Noa61] on the other hand allows a fast curing with a UV light source. However, its optimum adhesion to glass is reached after about one week of aging and the bond is less strong in comparison to Epotek 301-2.

The gluing has to be done using a special setup which is schematically shown in figure 5.7 and the left side of figure 5.8. Here a ROM is placed on an precision alignment tool with five degrees of freedom (see figure 5.7). The rotation axis  $\theta$  coincides with the center of the prism surface which is bonded to the radiator. For this reason a counterweight is added to the setup as the tilting moment of the goniometer is limited to 1.5 Nm. After a pre-alignment the ROM can be coupled to the radiator and a collimated laser is coupled into the radiator via a coupling prism. This way the laser beam is used to align the ROM with respect to the radiator as shown in figure 4.45. When the angle alignment is completed the ROM can be moved away from the radiator using the linear stage of the alignment tool

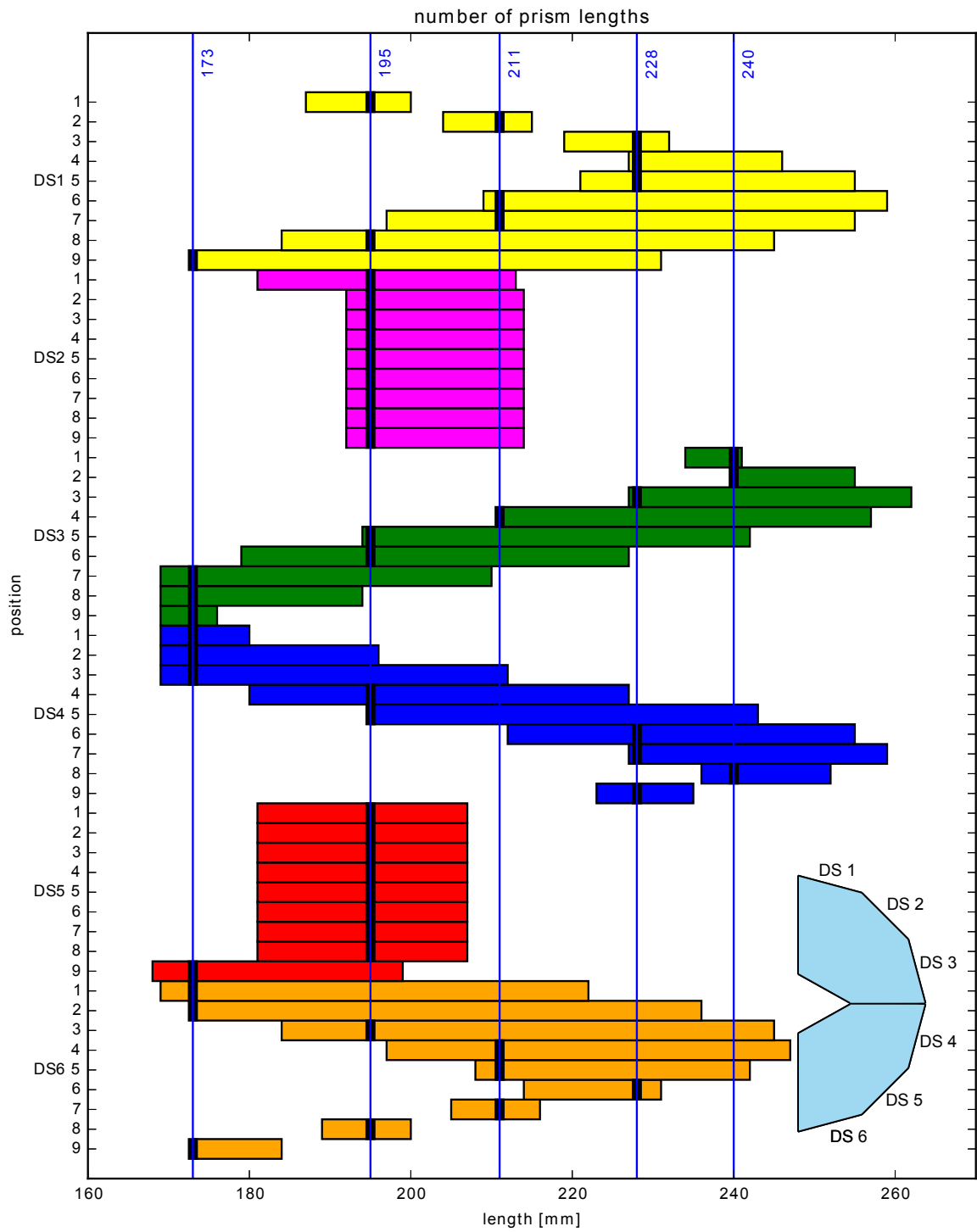


**Figure 5.9:** Allowed prism lengths according to the constraints summarized in figure 5.1. Each color represents one side of a radiator. The plot shows a solution for the minimum number of different lengths of 5. Solutions with more prism lengths allow to reduce the average lever.

if an additional cleaning of the surfaces is required. Afterwards the gap for the glue joint will be adjusted and the glue can be carefully applied. As soon as the joint is hard enough the alignment tool can be moved to the position of the next ROM. Experience has shown

that the glue joint bends because the glue shrinks while curing [San15]. However, this problem can be overcome by adding the opposite of the anticipated bend beforehand.

During the quadrant assembly the radiator has to be stored properly. To avoid sagging of the radiator a special table has to be constructed which equally distributes the weight of the radiator without damaging the surface. In this connection the Belle II collaboration has come up with a solution to produce a plastic plate with periodic holes which are filled with small precision plastic balls (see right side of figure 5.8). The plastic plate is fixed to a large aluminum plate which can be adjusted by micrometer screws which also adds additional degrees of freedom to the alignment setup. This way the radiator can be securely placed without deformation and even be slightly moved into position where it has to be fixed.

Due to the restricted space in the region where the ROMs are placed different prism lengths have to be produced. Figure 5.9 shows the allowed prism lengths for a radiator with radius of 1056 mm and a distance between the back part of the FEL and prism of 20 mm. According to the requirement of staying within the minimum distances shown in figure 5.1 at least five different lengths of the prisms are needed. However, more prism lengths reduce the average lever and improve the available space for the required mechanics. The average length of the prisms could also be reduced by up to 30 mm with a larger radiator. Due to the large size of a fully assembled quadrant it could be advantageous to do this part of the assembly onsite in a dedicated clean room which reduces the risk of damage during transportation. However, this would require that alignment and testing has to be done there as well.

### **Horizontal assembly**

During this step the optical system of each quadrant, which has been bonded during the quadrant assembly, has to be positioned inside the SC. For this purpose the SC is already fixed to the MP in a horizontal position and the radiators are introduced into the available profile which is equipped with dedicated supports. The outside corners of the radiator will be fixed using the connection blocks. During the horizontal assembly the SC has to be stabilized along its arms to not sag. After the optical system is in place the MCP-PMTs will be installed and the ROMs will be covered along with the radiators and sealed. Finally the cabling outside the ROM housings is prepared. At this stage the detector is ready for operation and can in principle be tested using cosmic muons.

### **Vertical assembly**

The last step is to bring the detector into a vertical position. A dedicated heavy table is needed to safely raise the system and move it between the endcap and central part of the

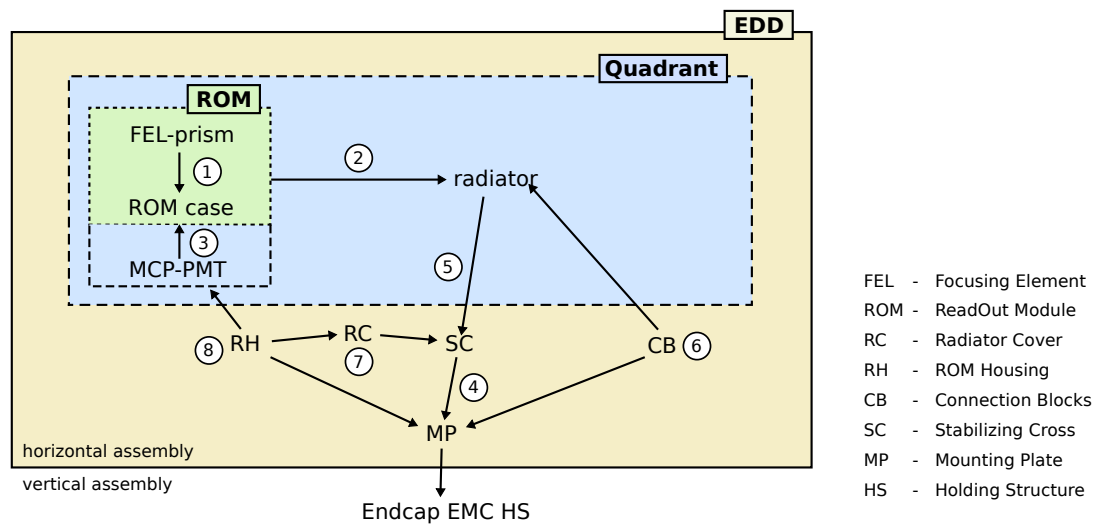


**Figure 5.10:** The schematic shows an overview of the assembly procedure. The different stages are summarized inside the boxes. The circled numbers indicate the order of the assembly.

$\bar{P}$ ANDA Target Spectrometer. The weight of a fully equipped EDD is about 450 kg which requires a very stable construction for this purpose. In front of the endcap the opening of the Endcap EMC holding structure will be approached and the cables coming from the service ducts have to be connected to the detector and placed in the dedicated spots. Once the cabling is completed the EDD has to be carefully joined with the Endcap EMC holding structure by screwing the MP to the support ring. Before the  $\bar{P}$ ANDA Endcap can be closed the heavy table has to be removed. Due to the placement of the endcap inside  $\bar{P}$ ANDA maintenance can only be done by removing the complete EDD using the heavy table.

Figure 5.10 gives a schematic overview and summary of the envisaged assembly procedure.

## 5.4 Optomechanical System

In order to estimate the feasibility of the suggested optical system different aspects have to be taken into account. Although the optical components themselves are rigid objects they are not very elastic and strong permanent forces have to be avoided. Especially for the glue joints between the prisms and the radiator it is important to reduce shear forces or torsional moments. Last fused silica has a very low thermal expansion with respect to aluminum which has to be taken into account as well.

To evaluate the behavior of the optical system as a rigid unit finite element calculations have been carried out. The so-called Finite Element Method (FEM) approximates solutions to boundary value problems by numerically solving partial differential equations. The presented analysis was done using Z88 Aurora [z88Aur] which is a GUI based, platform independent and non-commercial FEM software which is continuously developed since 1986. Besides deformations due to the net weight and gravitation the analysis also tried to in-

clude possible deformations due to the magnetic field. This is important as ferromagnetic materials such as Kovar are used inside the MCP-PMTs and the magnetic field is not ho-

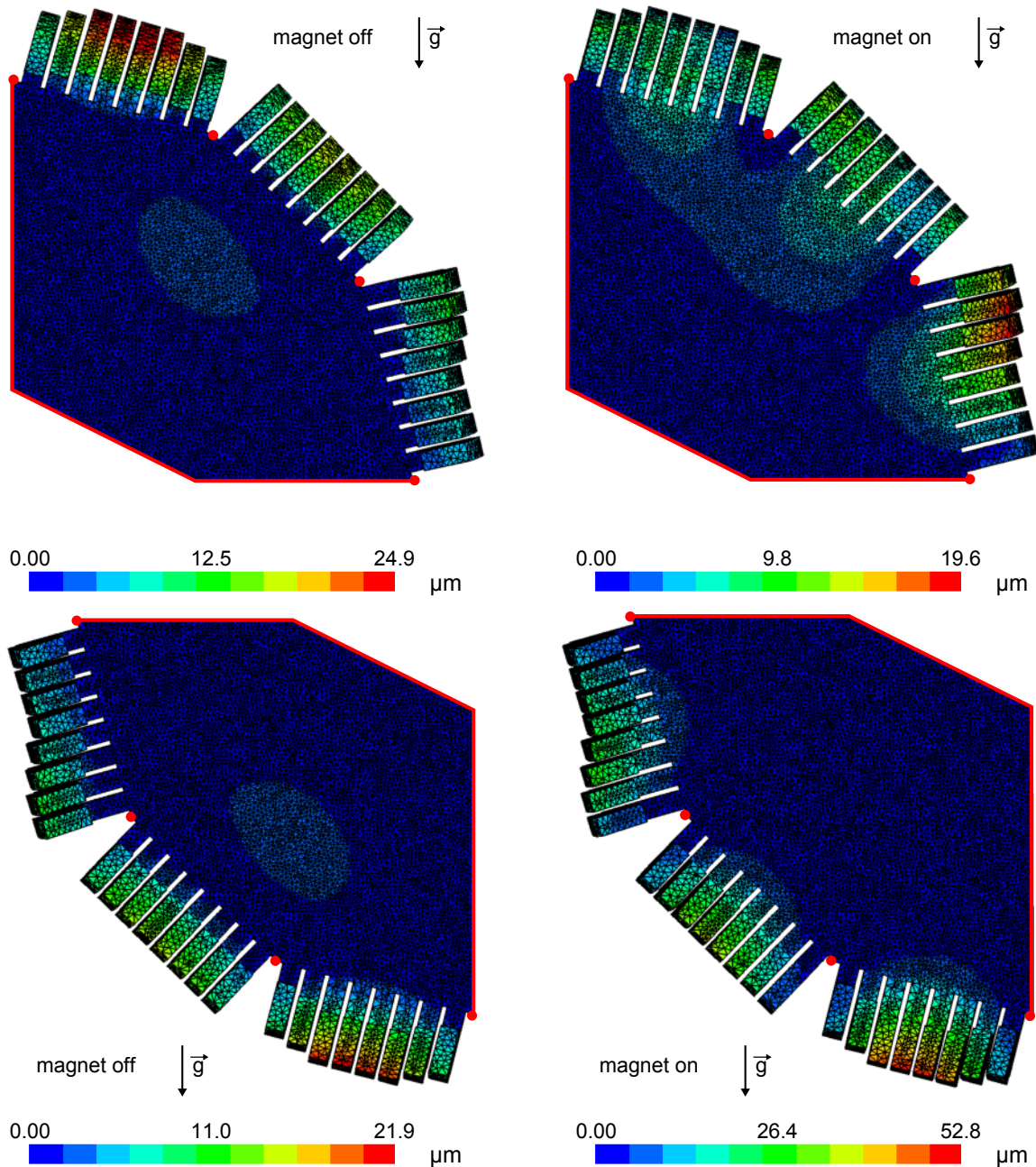


**Figure 5.11:** Results of a FEM analyses for different external configurations. The red lines represent the support coming from the SC, red dots are where the connection blocks are placed. The configurations in the top row show the situation with and without a magnetic field for the upper quadrant positions. The second row shows the two bottom quadrants under the same conditions. The displayed deformations are exaggerated by a factor of 1000.

mogenous. In general the force of an inhomogeneous magnetic field can be calculated ac-

ording to

$$\vec{F} = \vec{\mu} \nabla \vec{B} \approx \mu \cdot \frac{\Delta B}{\Delta x} \quad (5.1)$$

with the magnetic field  $B$  and the magnetic moment  $\mu$  given by

$$\mu = N_A \cdot \frac{m}{M} \cdot \mu_A \quad (5.2)$$

with the mass of the object  $m$ , the molar mass  $M$ , the Avogadro constant  $N_A$  and the magnetic moment of an atom  $\mu_A$ . For the presented analysis a value of 15 N per MCP-PMT was used which corresponds to a change of the magnetic field of 0.1 T over a distance of 1 cm which is about five times higher than the actual value. The radiator is mounted along the sides which are not equipped with ROMs by mounts inside the stabilizing cross and at the outer corners with connection blocks. Figure 5.11 shows the results for calculations with and without a magnetic field and for the top and bottom positions inside the stabilizing cross. For the top positions the magnetic field is capable of reducing the deformation as the orientation of the field is slightly pointing in the opposite direction of the bending which comes from gravitation. However, in case of the bottom quadrants the magnetic field enhances the deformation which is calculated to be up to more than 50  $\mu\text{m}$  for the very outside of the central FELs in the bottom third of the lower radiators.

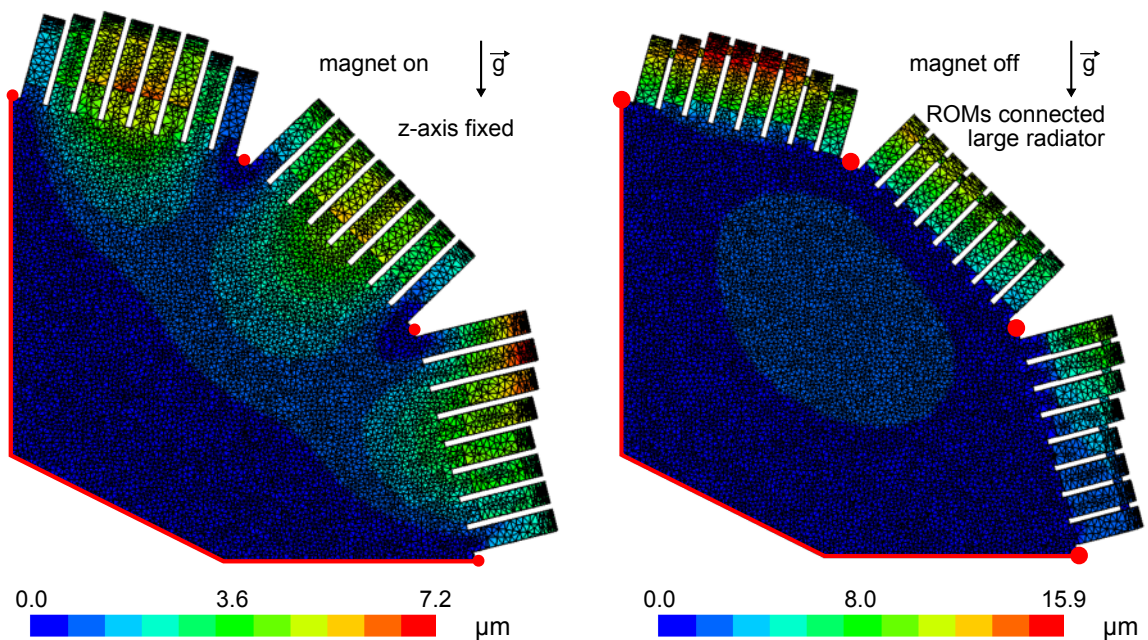


**Figure 5.12:** The left configuration fixes all ROM bases in the z-plane which highly reduces the deformation. In the right configuration the radiator is 3 cm larger and the ROMs are connected by small fused silica blocks.

As mentioned earlier it is necessary to reduce the shear forces and torsional moments which occur. Figure 5.12 shows two options to do so. The first one is to fix the ROMs to the mount-

ing plate such that they can not be moved or shifted out of the z-plane which is parallel to the mounting plate. A full fixation is not recommended as temperature changes can cause unwanted forces. This approach halves the maximum deviation but requires proper mechanics to be realized. A different option is to connect the ROMs such that they form a unit. The connectors can either be done by fused silica or other materials with a low thermal expansion coefficient. This configuration stabilizes the system in a way that it reduces any torsional moments especially on the glue joints. Alternatively the radiator is made 3 cm larger than the original version which reduces the lever arm of the prisms. Whereas in case of the upper quadrants the second option does not make a big difference regarding the maximum deformation the average deformation is differently distributed over the whole radiator surface. For the lower quadrants this option reduces the deformation by more than 50% (see figure 5.13).

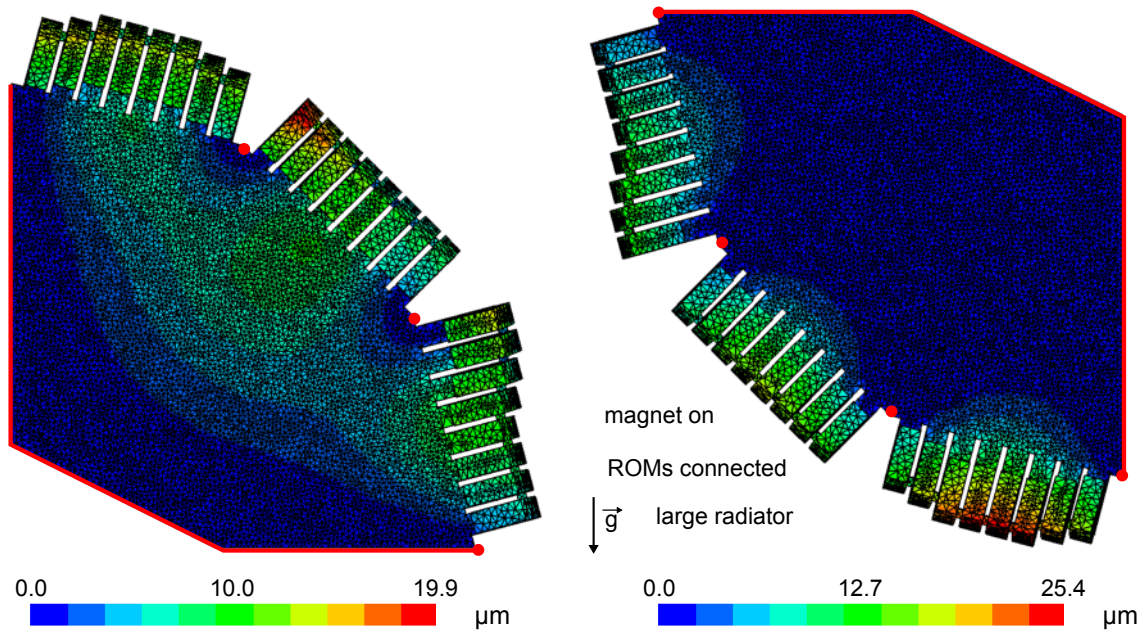


**Figure 5.13:** Upper (left) and lower quadrant (right) with an enlarged radiator and an active magnetic field. In both configurations the ROMs on one side are connected by small blocks.

Special situations occur during the ramping of the magnet or a sudden magnet quench. Due to the rapidly changing magnetic field the forces on the MCP-PMTs are much stronger over a period of a few seconds. For this reason additional mechanical support is desired to reduce the risk of sudden damage to the optical system.

In general the available space for sophisticated mounts for the optical system is scarce. From a mechanical and also economical point of view it is strongly recommended to consider a setup with eight instead of nine ROMs on each radiator side. In this connection it is important to evaluate if the available number of photons can be increased such that it is sufficient

radius radiator [mm]	#ROMs	space between ROMs [mm]	space at corners [mm]	
			inside	outside
1056	9	10	9.0	7.6
1086	9	10	16.8	15.4
1086	9	12	8.7	7.4
1056	8	15	22.0	20.6
1086	8	15	30.0	27.6

**Table 5.2:** The table gives an overview of the space between ROMs and the available space for mounting the radiator along the outside for different radiator sizes and number of ROMs.

to get the expected performance and at the same time does not exceed the allowed accumulated charge during the expected detector lifetime. Table 5.2 summarizes the space which is available between the prisms of two ROMs and at the corners where the connection blocks will be attached. One option, which has already been introduced in the FEM calculations, is to build a larger radiator. To allow enough space for a proper assembly the radius of the radiator can be enlarged up to 3 cm which adds 16 mm per side. This results in a diagonal span of 1536 mm or 60.5". In case of nine ROMs this would allow to introduce a gap between two MCP-PMTs which enables to add some shielding and an improved mount for the MCP-PMTs. On the other hand by placing the ROMs farther apart the available space for the connection blocks cannot be improved. If a setup with eight ROMs per side can be realized the space between the MCP-PMTs can be increased to 5 mm or more with sufficient space at the corners.

## 5.5 Prototype Development

Since the beginning of the development of the  $\bar{\text{P}}\text{ANDA}$  Disc DIRC different prototypes have been constructed. Mostly the mechanics were tailored to the needs of the current setup without taking into account requirements or constraints which are essential for the final detector inside the  $\bar{\text{P}}\text{ANDA}$  experiment. The 2016 prototype was designed with the proviso that some of the concepts that were introduced in section 5.2.1 are tested.

Figure 5.14 shows a CAD picture of the developed setup. In comparison to earlier versions the prototype is build much slimmer measuring  $100 \times 70 \times 37 \text{ cm}^3$ . The top can be opened by simply removing a closure head which is equipped with foam to make the housing light-tight. The large sides can be quickly opened by sliding doors which have special overlaps on each side to also prevent light from the outside to enter the housing. The medium-sized door has a cut-out which has to be equipped with a plate that provides all necessary cable feedthroughs (readout, high voltage and laser calibration). The light-tightness has been carefully tested by placing a camera inside the closed housing and taking pictures using a

long exposure time while shining light directly at critical parts of the cover. In the meantime tests with MCP-PMTs have confirmed this measurement. Besides the doors one side wall can be unscrewed to get access to the back side of the stabilizing cross of the prototype. This is necessary to access several small holes which allow to couple a laser beam into the radiator for the calibration of the ROMs during the assembly. The back side is also equipped with a fiber plug for a calibration system (PiLas connector) and a preparation for a future gas system.

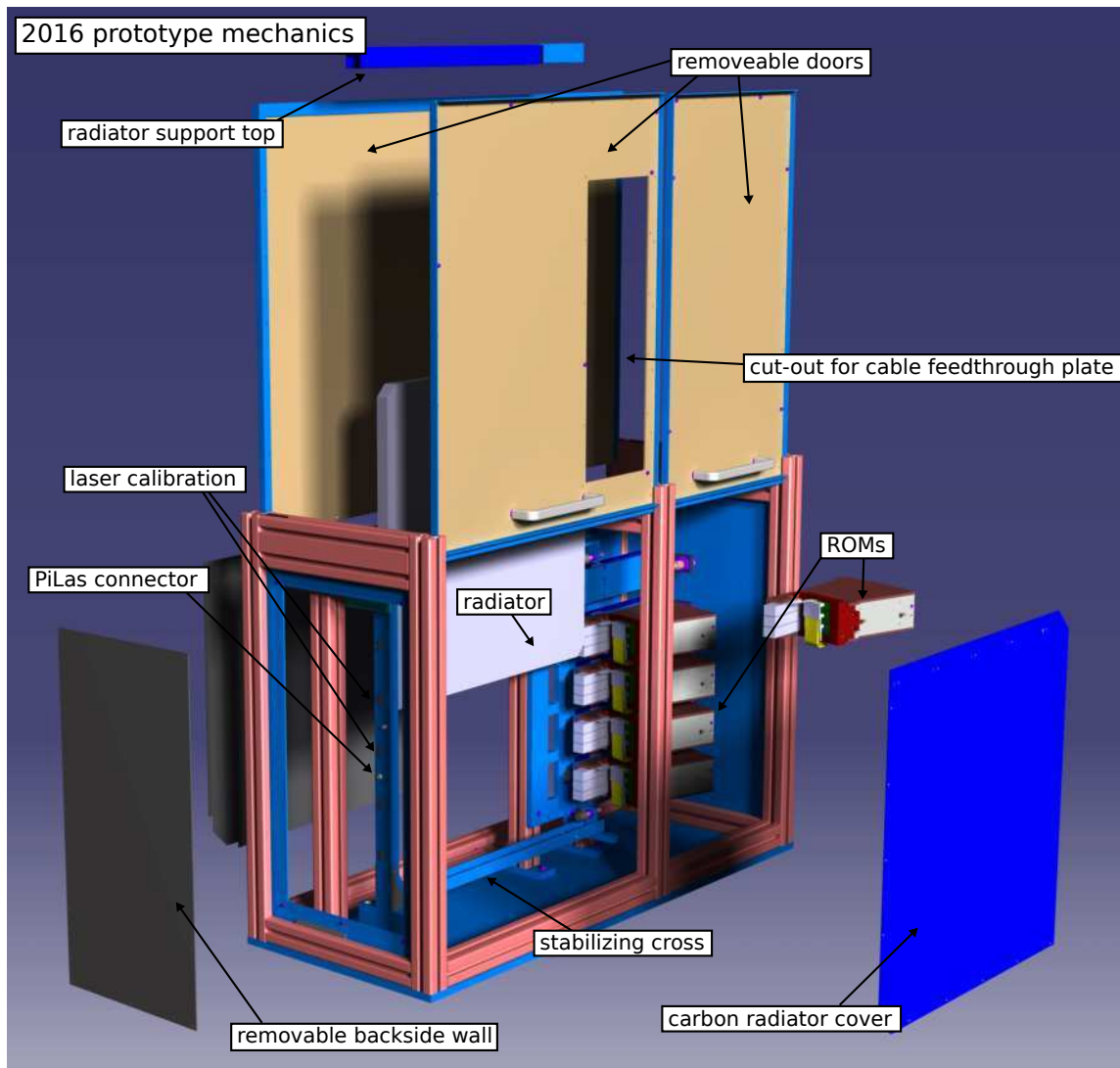


**Figure 5.14:** This exploded view drawing shows the main components of the 2016 prototype. The doors on the front and back side of the prototype housing can be easily removed. The left door on the front side has a cut-out where the cable feedthrough will be placed. The radiator has to be introduced from the top into the stabilizing cross prototype and is additionally protected by two carbon plates once the radiator is fixed inside the stabilizing cross. A removable back side wall allows access to tiny openings in the stabilizing cross which allow laser calibration and provide connections for a future gas system and a PiLas calibration system.

Inside the housing the ROMs are placed on a large plate which replaces the mounting plate. In contrast to the final detector the ROMs are not yet glued to the radiator but placed on spring-loaded precision tracks which can be adjusted in two axes. Before the ROMs are mounted the radiator has to be introduced into the stabilizing cross from the top. The floor of the stabilizing cross is equipped with thin plastic bars and rounded plastic buttons on the side to avoid contact between the glass and the aluminum. Small plastic screws are used to fix the radiator inside the U-profile of the stabilizing cross together with two large bumpers on the side of the mounting plate (see also bottom row in figure 5.14). As soon as the radiator is in position a top part completes the structure and two carbon covers can be attached to the stabilizing cross to protect the surface during the remaining assembly steps.

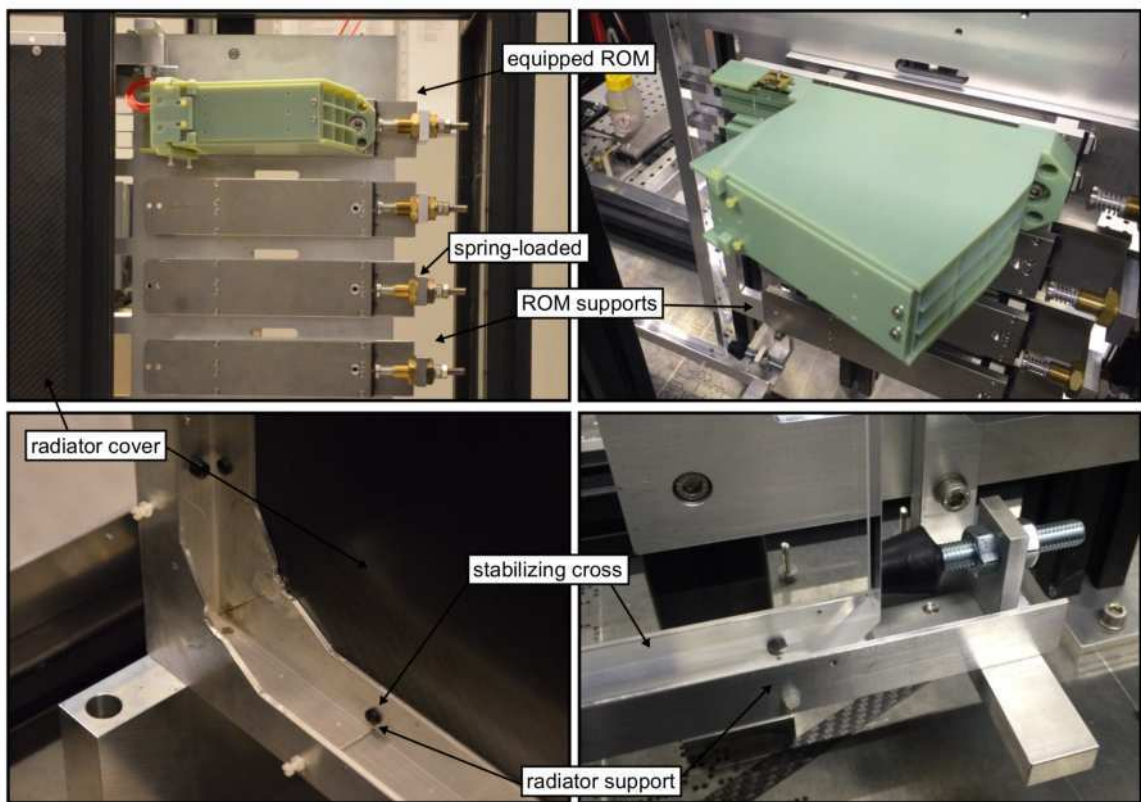


**Figure 5.15:** The pictures show different views during a pre-assembly of the prototype. The top pictures show one equipped ROM which is mounted onto the ROM supports which allow a precise movement of the ROMs. The bottom pictures show the welded stabilizing cross and the buttons and areas of support for the fused silica radiator which is already mounted in the bottom right picture.

The ROMs can be mounted on a carriage which slides on the precision tracks by two screws. First they are mounted without the MCP-PMT to be calibrated. Afterwards they are removed from the carriage which remains in the calibrated position such that no re-calibration is needed once the MCP-PMT is mounted. The ROMs themselves consist of a case which houses the FEL-prism pairs and which provides a mount for the MCP-holder.

All large parts have been fabricated in a 3D printer at the Technische Hochschule Mittelhessen (THM). The concept of a ROM has already been addressed in the 2015 prototype

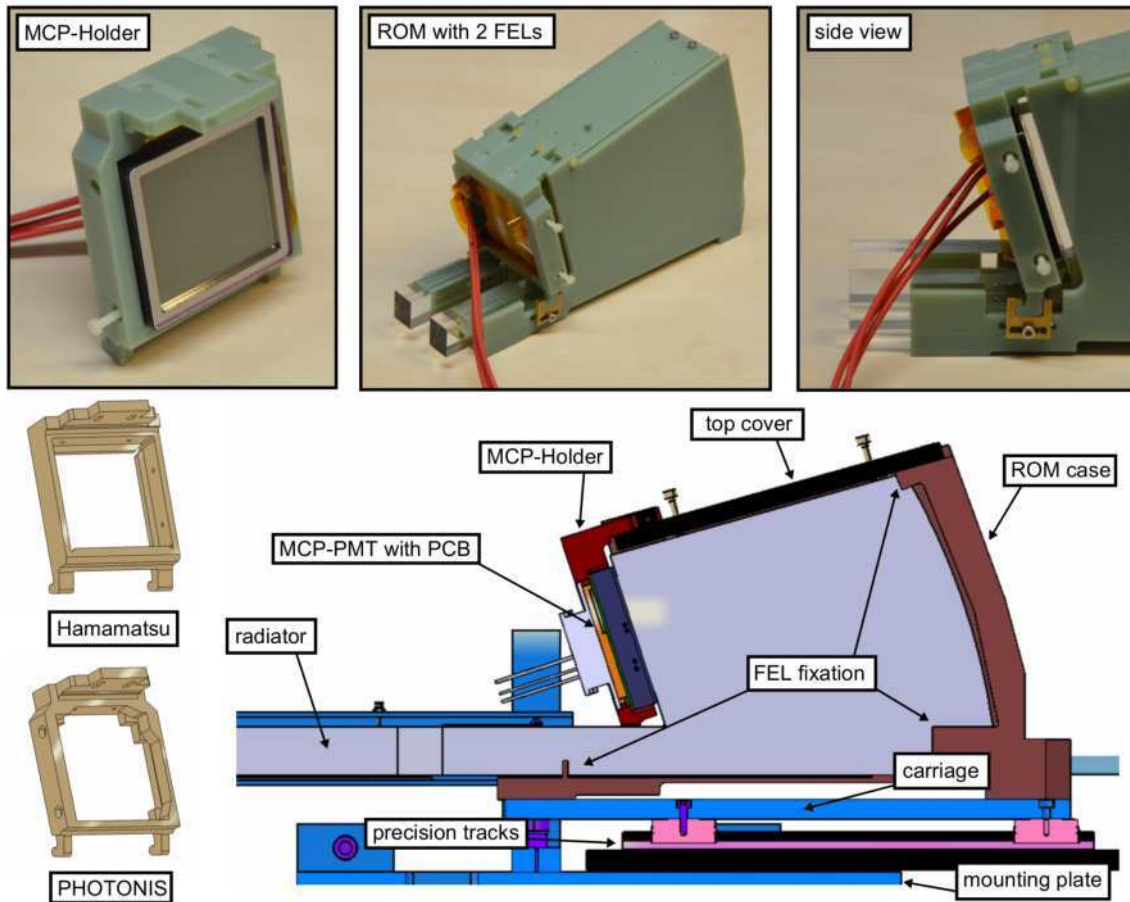


**Figure 5.16:** The top row of pictures shows a partly equipped ROM for the 2016 prototype. Below the backside of the MCP-holders for the PHOTONIS and Hamamatsu sensors are shown. A cross section of a ROM indicates the spots where the optics are mounted.

(see section 6.2.1). However, the new approach allowed to include several features which are necessary to provide proper mounting of the sensors and optics and reduced the number of parts. The ROM case provides 1 mm thin spacers at various positions to align the FEL-prism pairs. They touch the glass at several non critical spots (see figures 4.41 and 4.43) and at the far end of the prisms near the radiator. Here round pins were printed to minimize the area of contact. After the optics are placed inside the ROM case it is closed by a top cover after which the MCP-Holder can be mounted. Each MCP-Holder is designed differently to provide space for the HV cables and respect the different entry window sizes. Before the MCP-PMT is placed into the MCP-Holder the PCBs can be plugged onto the pins. As the signal cable plugs require a certain force to be connected it is recommended to add them before the MCP-PMT is coupled to the FEL. The FELs for the testbeam are designed for 6 mm entry windows hence an additional coupling window has to be put in front of

the MCP-PMT. Afterwards the ROM can be fixed to the mounting plate and coupled to the radiator using optical grease. Before the prototype box can be closed the cables have to be connected to the feedthrough plate which has to be screwed onto the respective door.

The 2016 prototype can also be operated in a horizontal position and fits into the group's cosmic test stand [Muh13]. This way it is possible to evaluate the performance using cosmic muons and being independent of a high energy particle beam.



## 6 Testbeam Analysis

### 6.1 Introduction

The presented analysis is based on data from a testbeam in May 2015 at the T9 beam line at CERN. The beam line is located at the Proton Synchrotron (PS) East Area and delivers a secondary beam of mixed hadronic particles with momenta of up to 15 GeV/c. Besides the 2015 Disc DIRC prototype other detectors were used during the beam time, including a Barrel DIRC prototype from GSI [Swa16], a MicroChannel Plate Time-Of-Flight System (MCP-TOF) and Silicon Fiber Tracker (SFT) from the University of Erlangen-Nuremberg [Uh15] and a segmented highly precise start counter (FLASH) from the University of Mainz. All detectors shared the TRBv3 (a general purpose Trigger and Readout Board) as their common Data Acquisition (DAQ) system. The TRBv3 is a multi-purpose time-to-digital DAQ system developed at GSI [Nei13]. All TRBv3 boards inside the T9 beam area were synchronized by a Central Trigger System (CTS).

The main goal of the testbeam was to evaluate the current detector system and compare it to Monte-Carlo data. The Monte-Carlo data which was generated used a standalone version of Geant 4 [All06]. It includes all relevant sources for photon loss and smearing. The quantum efficiency of the photocathodes is included as a function of wavelength but no readout related features such as dark count noise, cross talk or charge sharing are implemented [SmM16].

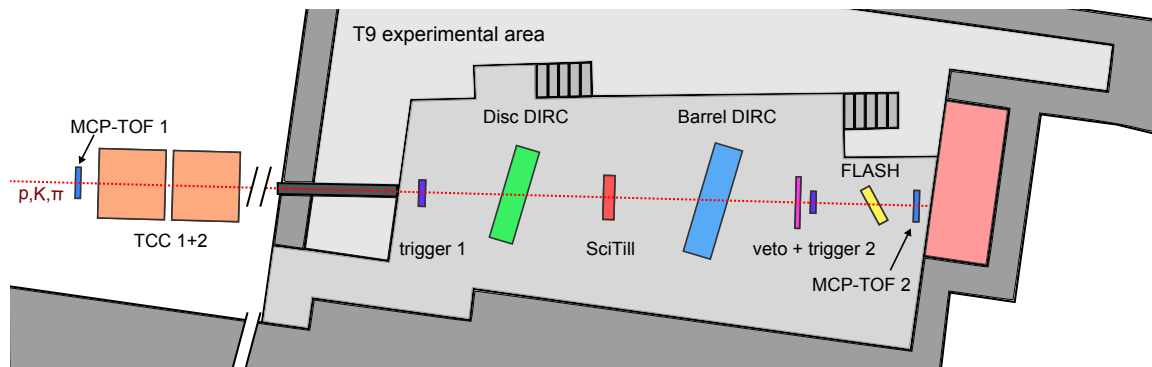


**Figure 6.1:** The experimental setup inside the T9 experimental area. The sizes of the detectors are not to scale.

### 6.2 Setup

#### 6.2.1 Components

The 2015 Disc DIRC prototype had a position about 190 cm downstream of the end of the beam pipe at T9. The first MCP-TOF station was located about 22 m further upstream even

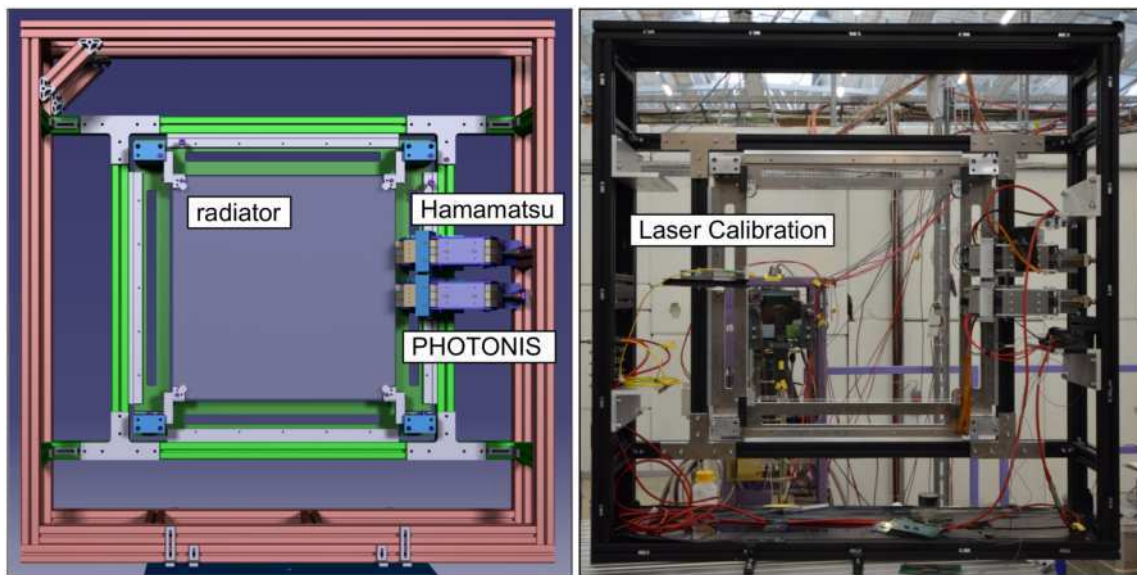


**Figure 6.2:** Upstream view of the 2015 testbeam setup extracted from CAD (left) and photographed on-site (right).

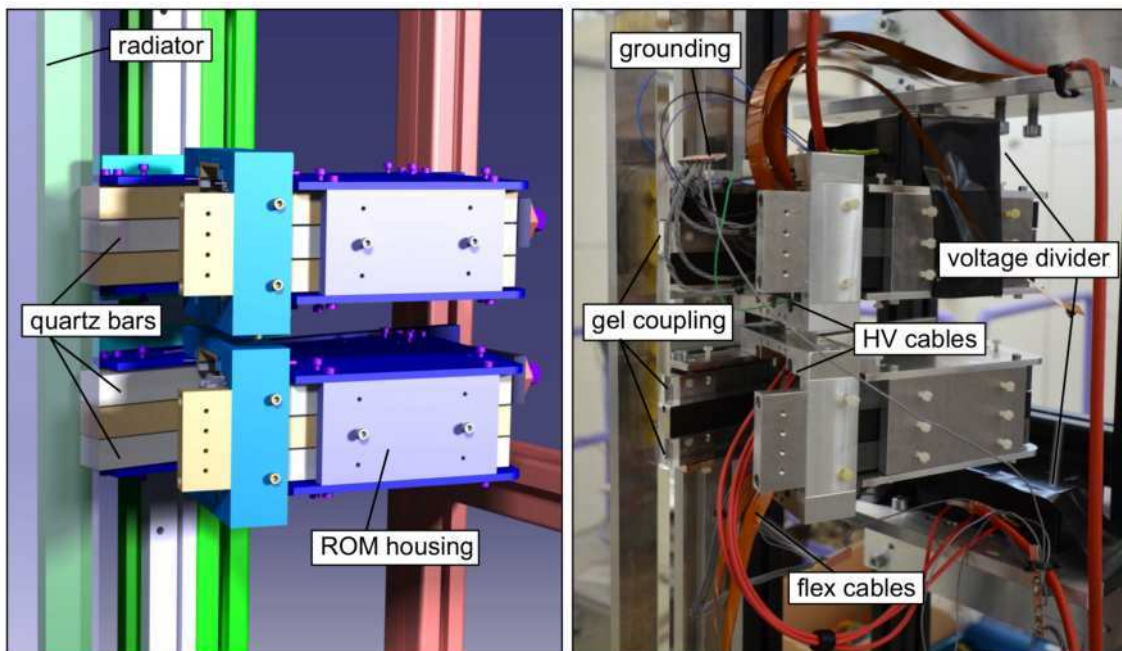


**Figure 6.3:** Close view of the ROMs coupled to the radiator extracted from CAD (left) and photographed on-site (right). The top (bottom) ROM is equipped with the Hamamatsu (PHOTONIS) sensor and contains one (two) fused silica FEL.

before the Threshold Cherenkov Counter (TCC). Between the beam pipe and the EDD prototype a first trigger station was located. After the Disc DIRC prototype the SFT followed before the Barrel DIRC prototype. At the end of the testbeam area a second trigger station, the FLASH detector and the second MCP-TOF station were installed (see figure 6.1). In comparison to previous prototypes the 2015 Disc DIRC prototype consisted of relatively

few but high-quality components such as the optical parts and the MCP-PMTs with highly segmented anodes which meet the requirements of the final detector (see figure 6.2). A square radiator provided by Nikon (see section 4.3 for more details) and three FEL-prism pairs which were manufactured by Berliner Glas (see section 4.4) made up the optical system which for the first time consisted of fused silica components only. The coupling of the optics was done using Cargille optical gel code 0607 [COG607] (see section 4.6).

In total two semi-equipped ROMs were used in the setup as shown in figure 6.3. One ROM consisted of one FEL which was coupled with the prism via optical contact bonding, two plastic dummies and a Hamamatsu MCP-PMT with  $6 \times 128$  pixels. The other ROM consisted of two remaining FELs which were coupled to the prisms using NOA-61 and Epicol 348990, one plastic dummy and a PHOTONIS MCP-PMT with  $3 \times 100$  pixels. Both sensors are candidates for the final detector and have been further investigated regarding their gain and their performance in a magnetic field [Rie16].

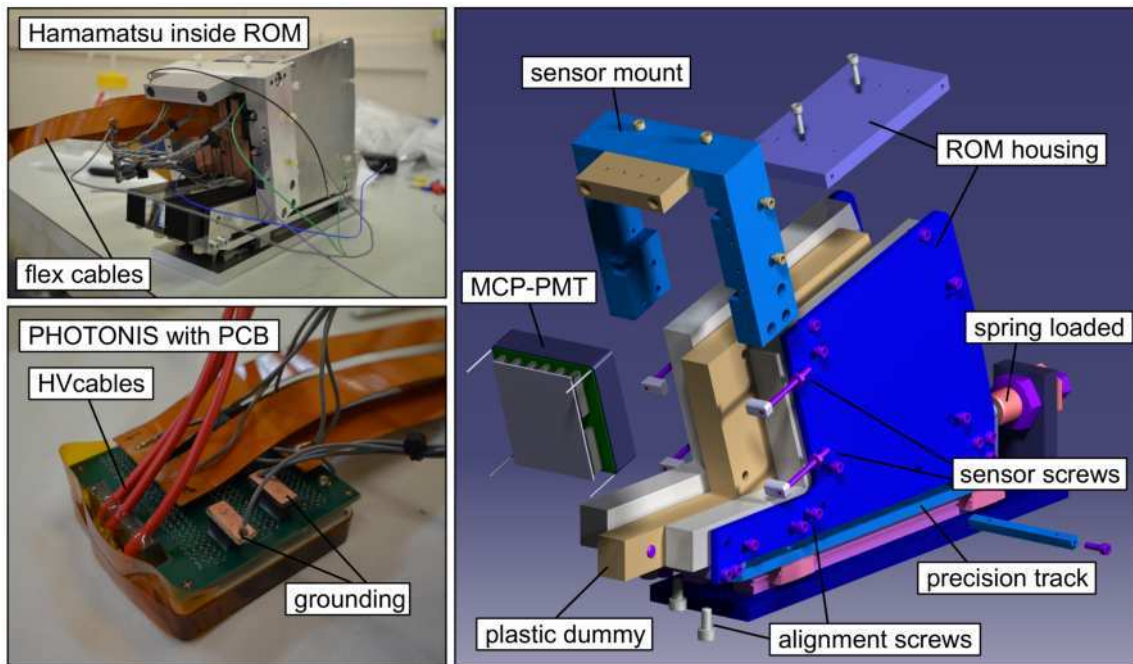


**Figure 6.4:** Setup of a ROM. The top left shows a fully equipped ROM with one FEL and the Hamamatsu sensor. The bottom left is a photograph of the back side of the PHOTONIS sensor with the PCB and flex cables attached. The right picture was extracted from CAD and shows all relevant components used for the ROMs.

Figure 6.4 shows different views of the ROMs including images extracted from a CAD drawing. The pins which carry the electric signals to the back side of each MCP-PMT are connected to a custom-made Printed Circuit Board (PCB). This board reroutes the channels and contains soldered plugs for flex cables which process the signal to the PaDiWa boards [Nei13] which are plugged into another set of PCBs which are mounted onto the light-tight Disc DIRC cover (see figure 6.5). The PaDiWa boards amplify and discriminate the signals

before they are forwarded to the TRBv3 via LVDS cables. Due to technical limitations not all available channels could be read out. In case of the PHOTONIS MCP-PMT only 80 channels per column were read out. The central column as well as the remaining channels in the two outer columns were grounded. In case of the Hamamatsu sensor only  $2 \times 64$  channels were read out which correspond to the top half of the two central columns. Because of the acute angle between the focal plane of the FEL and the prism, the MCP-PMT position had to be shifted upwards which means that some channels lay outside the image on the focal plane and very flat Cherenkov angles cannot be detected.

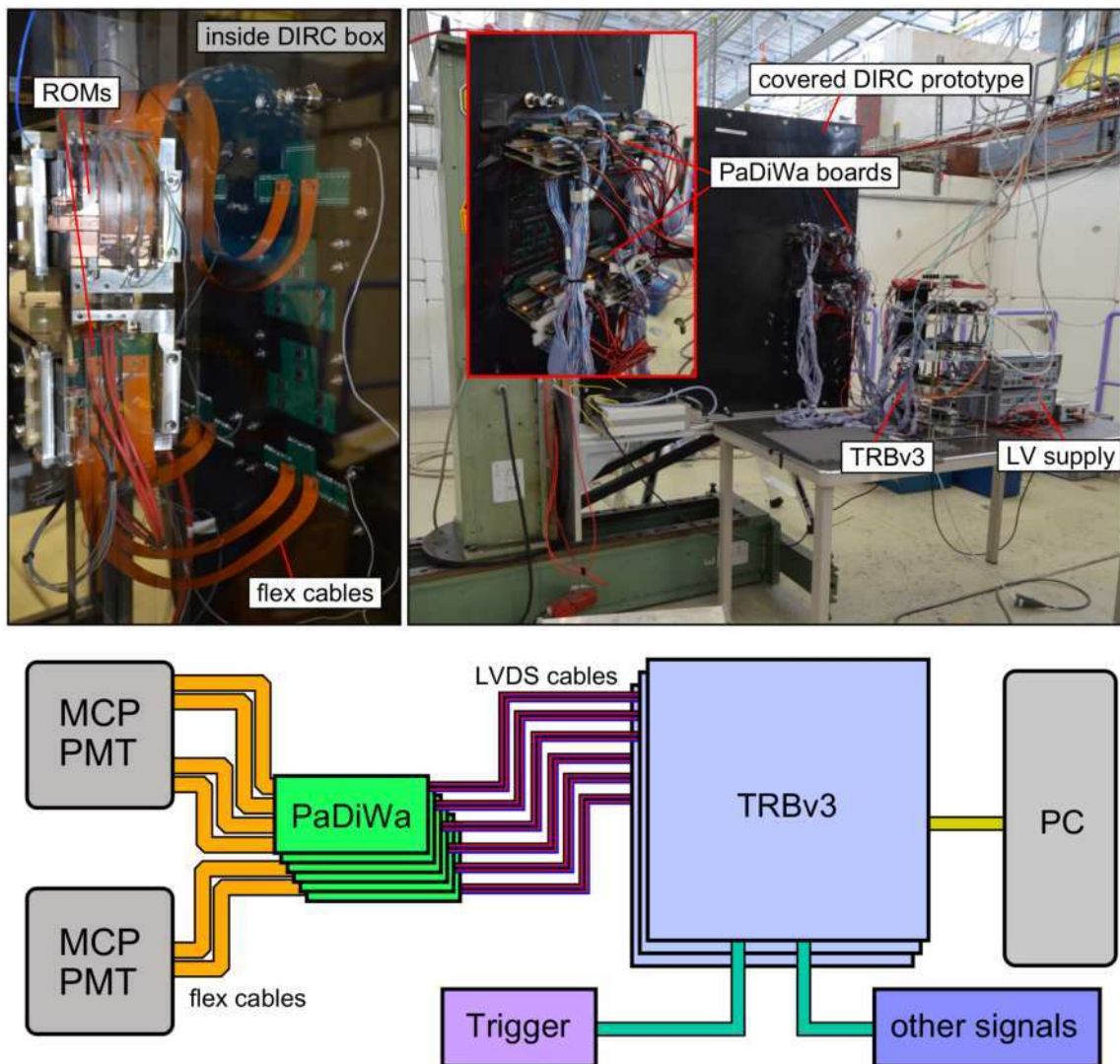


**Figure 6.5:** Bottom: DAQ scheme for the 2015 testbeam. The number of boards and cables does not correspond to the real setup. The top left photograph shows a view through the radiator where the flex cables are connected to the feedthroughs which are integrated into the downstream cover. The top right shows an upstream view of the detector placed on the x-y-stage. The PaDiWa boards are plugged to the outside of the feedthroughs.

### 6.2.2 Installation

As the first step the radiator was fixed inside its frame. For this purpose four connectors which are coated with foam and fit into the cut-outs at the four corners of the radiator were used. Afterwards the ROMs were prepared. The flex cables were connected to the back side of the PCBs and the unconnected plugs were grounded. Next the FEL-prism pairs were put into their respective positions. As each ROM could house three FEL-prism pairs empty positions were equipped with plastic dummies as placeholders which was necessary to properly mount the fused silica optics. Before the sensors were added the ROMs were pre-mounted to the radiator for alignment. For this purpose the ROMs were fixed on the precision tracks and screwed onto a base plate which was connected to the frame. A laser was coupled into the far side of the radiator to imitate the path of the Cherenkov photons and is aligned such that the beam reflects off both sides of the gap between the radiator and the prism (see figure 6.6). If the ROM is not properly aligned two spots are visible on the focal plane of the FEL. The ROM is then aligned using three alignment screws inside the base plate which allow to tilt the ROM such that the spots coincide.

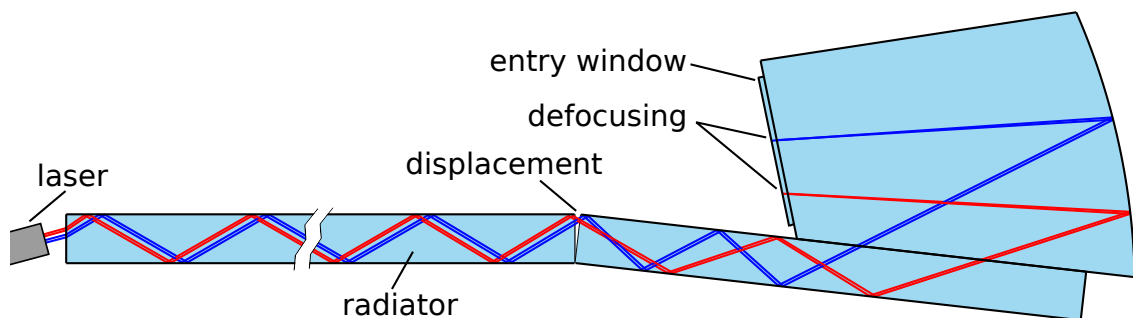


**Figure 6.6:** The drawing illustrates the defocusing that is caused by misaligning the ROM with respect to the radiator. To align the ROM properly a laser is coupled into the radiator such that the beam reflects off both sides of the gap between the radiator and the prism (here drawn as red and blue lines). The ROM is aligned when both lines coincide on the focal plane. The width of the entry window is taken into account by adding a glass plate with the same thickness.

Next the ROM was dismantled to add the MCP-PMT. The MCP-PMT was fixed inside the sensor mount and optical grease was applied to the FEL. Afterwards the loaded sensor mount was mounted on the ROM housing and carefully contacted with the FELs. The gap between the MCP-PMT and the FEL was adjusted by four sensor screws. The complete ROM was then remounted on the base plate. The correct position was provided by the alignment screws whose positions were fixed. The reproducibility of the alignment was checked during earlier tests by remounting the sensor without a MCP-PMT. In order to contact the ROM with the radiator optical grease was applied to the prism surface facing the radiator and the ROM was slowly guided towards the radiator over the precision tracks.

After the contact was initiated the ROM was pressed against the radiator using a spring-loaded plunger (see also 6.4). On the side of the radiator which was opposite to the ROMs a fiber coming from a PiLas (Picosecond Laser) was coupled to the radiator. Next the flex and high-voltage cables for the MCP-PMTs were connected to the corresponding plugs and the prototype housing was closed and sealed by screwing plastic walls to the outer frame and adding black tape to the lateral faces.

Due to the height of the beam pipe two setups were used during the test beam. A first setup used a fixed angle of  $11.2^\circ$  between the beam and the normal of the radiator. With this setup the x and y position of the prototype could be altered within a restricted area (see left part of figure 6.7). In the second setup the prototype was lifted by a crane and placed on a concrete block with a rotary table on top. For this setup the position of the beam was fixed but the angle of incidence could be changed.

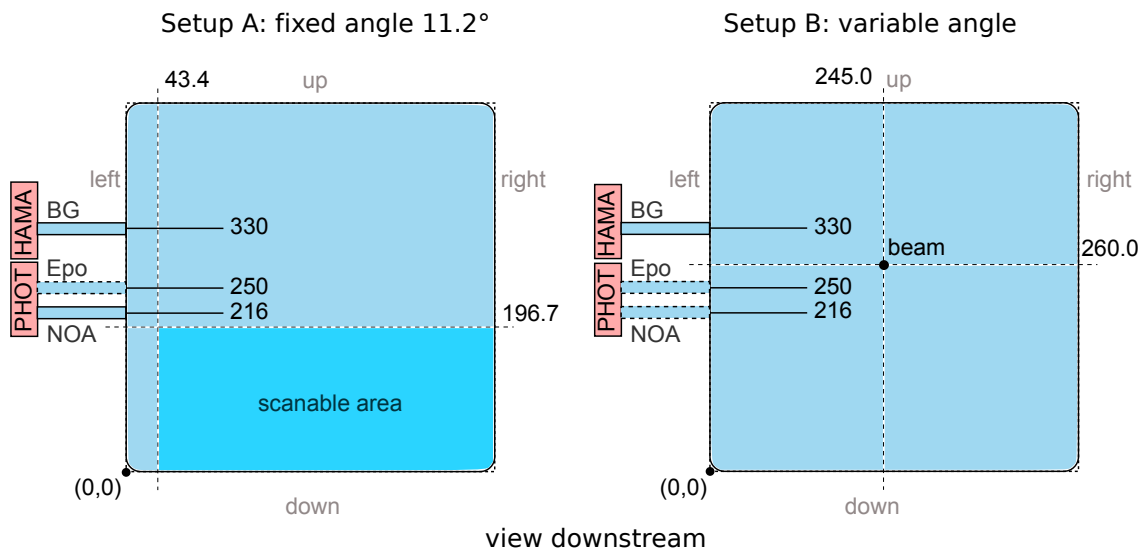


**Figure 6.7:** The figure shows the setups that were used during the testbeam. The left setup A was fixed at a beam angle of  $11.2^\circ$  but allowed a free movement of the detector to position the beam inside the scanable area. The right setup B had a fixed beam position but allowed a variable beam angle of incidence. The number next to the horizontal lines corresponds to the distance of the center of the FELs to the lower edge of the radiator in mm. The PHOTONIS column which is coupled to the FEL/prism with NOA-61 bonding is called PHOTONIS A or outer column whereas the column with the epoxy bonding is called PHOTONIS C or inner column.

## 6.3 Calibration and Data Quality

### 6.3.1 Laser Calibration

The installed PiLas was used as a photon source to set the thresholds of the individual channels and allowed to calibrate the timing of the signals. Whereas the thresholds were

set using an automated routine provided by the TRBv3 system the time calibration was done offline in preparation for the presented analysis. Although a start time is given by the leading edge of the first MCP-TOF station the time-of-propagation of the signal varies for every channel. By calibrating the timing it is possible to apply a narrow time cut for all channels and check the consistency of the data acquisition offline. The procedure is carried out by the following scheme:

- Choose a channel with high statistics (reference channel).
- For each channel: Find the mean of the difference  $\bar{t}_{rel,i}$  between the time of the leading edge of the channel of interest  $t_{chi,i}$  and the reference channel  $t_{ref}$  (where  $i$  stands for the channel of interest).
- To eliminate the shift caused by different times of propagation and signal processing  $\bar{t}_{rel,i}$  can be subtracted.

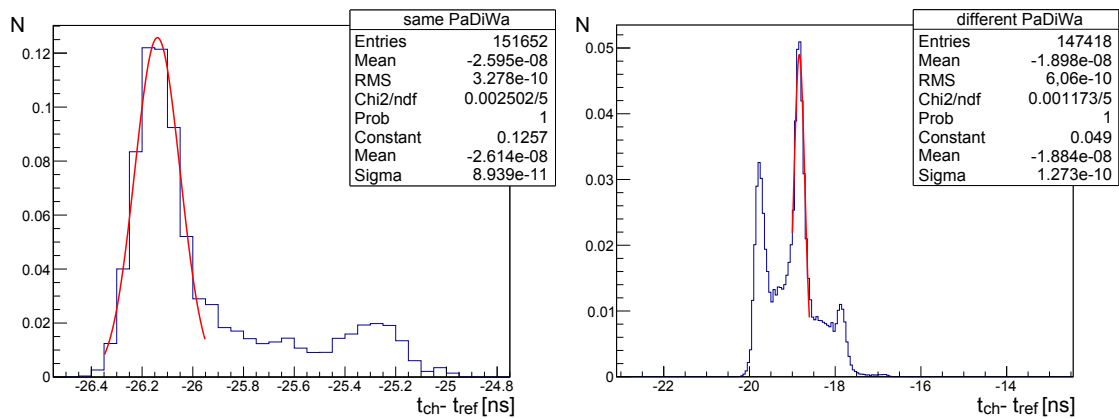


**Figure 6.8:** The left plot shows a single peak with a time resolution of 89.4 ps. The plotted channel is connected to the same PaDiWa board as the reference channel. The right plot contains three peaks which are separated by 1 ns and shows a channel which was connected to a different PaDiWa board than the reference channel.

Due to firmware problems the TRBv3 system was not running reliably which led to missing events in several detectors. Furthermore missing edges in the timing signal did not allow a time-over-threshold measurement and therefore time-walk corrections were not possible. In case of the Disc DIRC prototype it was planned to use the MCP-TOF system for external PID but even at lower momenta no clean separation was possible and the statistics were drastically reduced. In figure 6.8 the time resolutions for two channels with respect to a reference channel are shown. The left plot shows a prominent peak with small background where the mean can be determined by a Gaussian fit. In comparison to the left plot in figure 6.8 the channel in the right plot is processed by a different PaDiWa. Here three peaks are visible at intervals of roughly 1 ns. In this case the central peak with the highest amplitude is chosen and a Gaussian fit applied to determine the mean. This behavior could be obser-

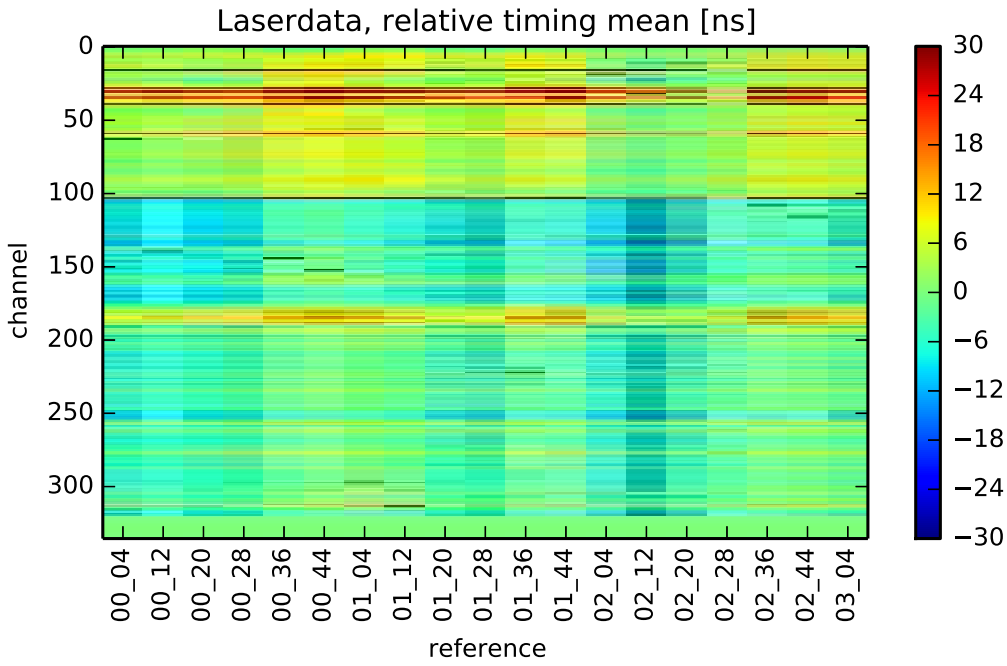


**Figure 6.9:** The plot shows the relative timing of all channels with respect to different reference channels (plotted on the x axis). Reference channel 02\_28 did not record data which results in a shift of 0 ns for all channels.

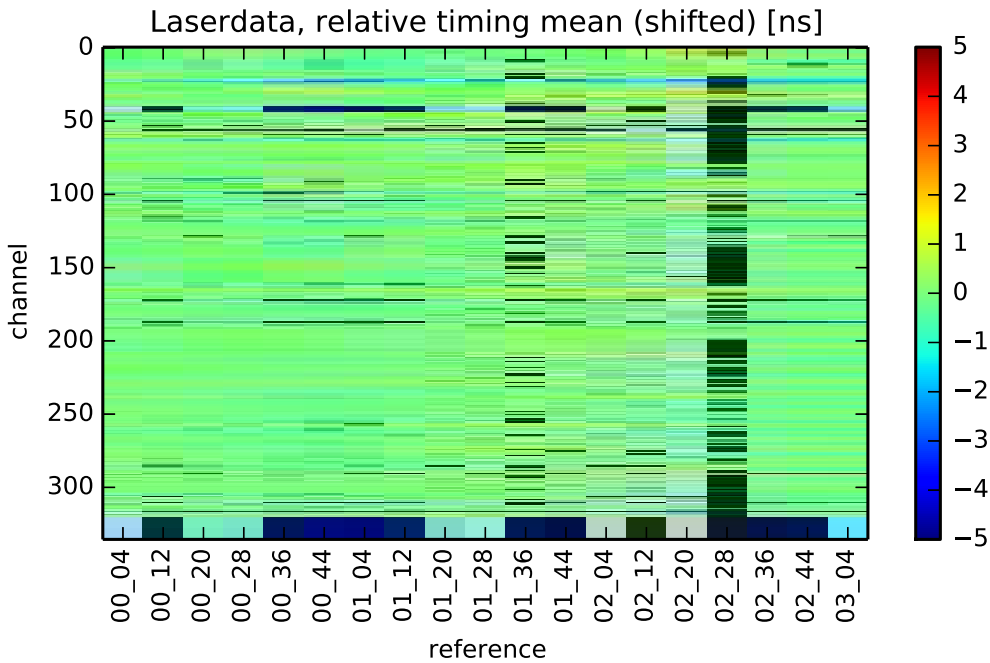


**Figure 6.10:** The plot contains the same data basis as shown in figure 6.9. In comparison to the previous plot each channel was shifted by  $\bar{t}_{rel,i}$  for a chosen reference channel such that all channels have the same relative timing mean. In a second step the mean of each column was calculated and subtracted from each entry which should result in a completely green distribution if all channels were perfectly calibrated.

ved for almost all channels which were processed by a PaDiWa different from the reference channel and must be traced back to issues with the TRBv3 firmware. The problem could not be fixed until the end of the May 2015 beam time but was solved for a second beam time during July 2015 which was done without the presence of the Disc DIRC prototype [Lhm15].

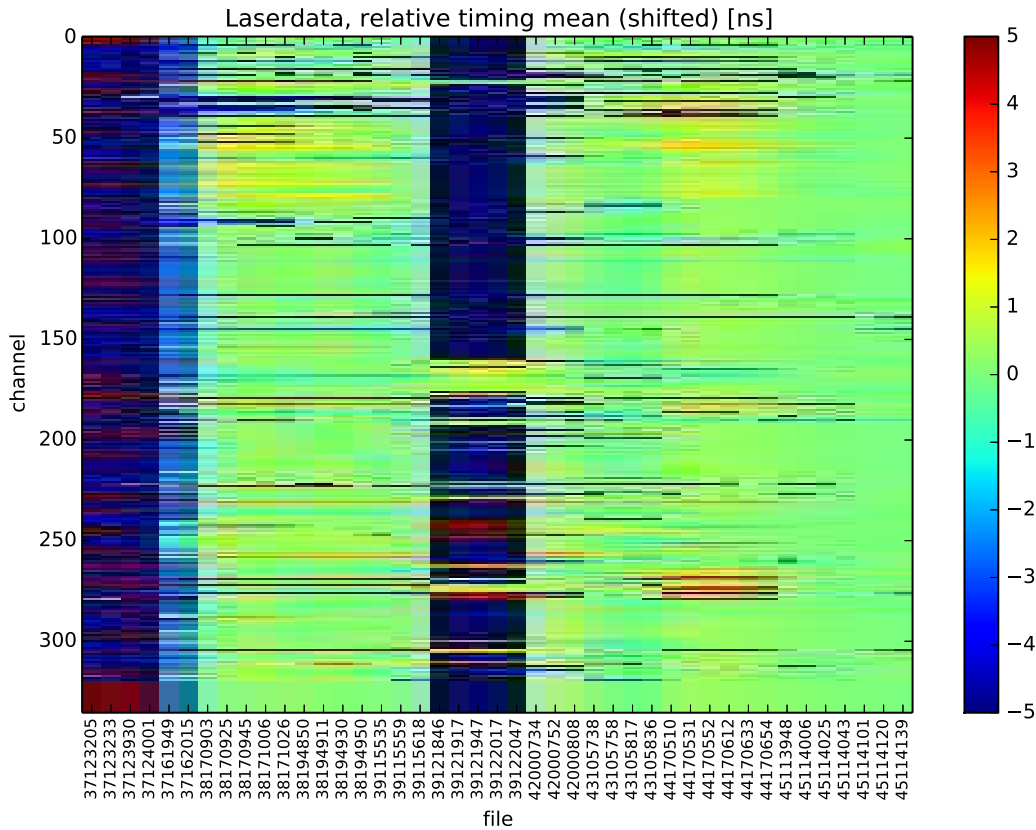


**Figure 6.11:** Relative timing with shifts applied for all recorded laser runs. Sequenced runs show a similar shift as they are using the same settings.

To check the consistency of this procedure and the overall performance  $\bar{t}_{rel,i}$  was calculated for all channels using various reference channels. Figure 6.9 shows the result for selected reference channels. This plot already reveals bad channels such as the reference channel 02\_28 which does not contain any data. For the remaining channels the data shows a reasonable behavior. This becomes clearer if one subtracts the individual channel mean  $\bar{t}_{rel,i}$  of a fixed reference channel for each entry. After this each column should be more or less uniform in color in the two-dimensional histogram which means that the time of arrival of the leading edge is now calibrated. The difference between the columns is now given by the relative timing between the reference channels. Therefore, in a second step, a mean for each column is calculated and subtracted from its entries. In case of a perfectly working detector all entries should now have the same color in the two-dimensional histogram which is the

case for most of the channels as can be seen in figure 6.10. The actual pattern suggests that besides some channels which are dark blue or red the timing is working within an interval of 10 ns. However, it seems that there are some instabilities which are connected with the multiple peak structures shown in figure 6.8.

During the testbeam campaign different setups were tested regarding the voltage settings of the photo sensors, the threshold settings of the individual channels and also the PaDiWa boards that were used. After each change laser runs were recorded to allow a calibration of the data if needed. In the style of the previous plots the relative time of arrival of the leading edge was calibrated for each run using the same reference channel of the same run. This technique allows to exclude strong deviations or bad runs from the analysis. Figure 6.11 gives an overview for the available laser data. It can be clearly seen that the runs at the very left, which correspond to the very first runs of the testbeam, and in the middle are not in agreement with the rest. In case of the runs between file 39121846 and 39122047 the thresholds for the channels were intentionally set by hand to test if the automatic routine to set the thresholds is working reliably.

### 6.3.2 Additional Offline Calibration

The additional offline calibration applies the calibration to the beam data and aims at further improving the data quality. In figure 6.12 three different versions of the relative leading edge versus channel number are plotted for one Hamamatsu column. The data contains all 10 GeV/c runs in order to have the highest statistics and a good coverage of all relevant channels. Due to low statistics all channels below 40 are excluded from the analysis (the same behavior was observed for the neighboring Hamamatsu column and the outer PHOTONIS column). In addition the channels 50 and 70 do not operate properly. Almost all channels show a periodic pattern at intervals of several ns which has been seen by other detectors as well. Both problems were not observed outside the testbeam environment when the MCP-PMTs were tested and have to be attributed to the previously mentioned firmware error [Lhm16b].

The top left plot shows the distribution if no additional calibration is applied and hence the means vary for each channel. The top right plot uses the information gained with the laser calibration by subtracting  $\bar{t}_{rel,i}$  for each channel which leads to a narrower distribution of the means. In order to further reduce the time cut width an additional calibration step was applied by centering the mean values for each channel as shown in the bottom left plot of figure 6.12. In the bottom right plot the projections for each calibration method are shown at an angle of incidence of  $8^\circ$ .

As a next step, the corresponding time cuts were determined to reduce the background which comes from dark counts or scattered light. For each angle and MCP-PMT column a

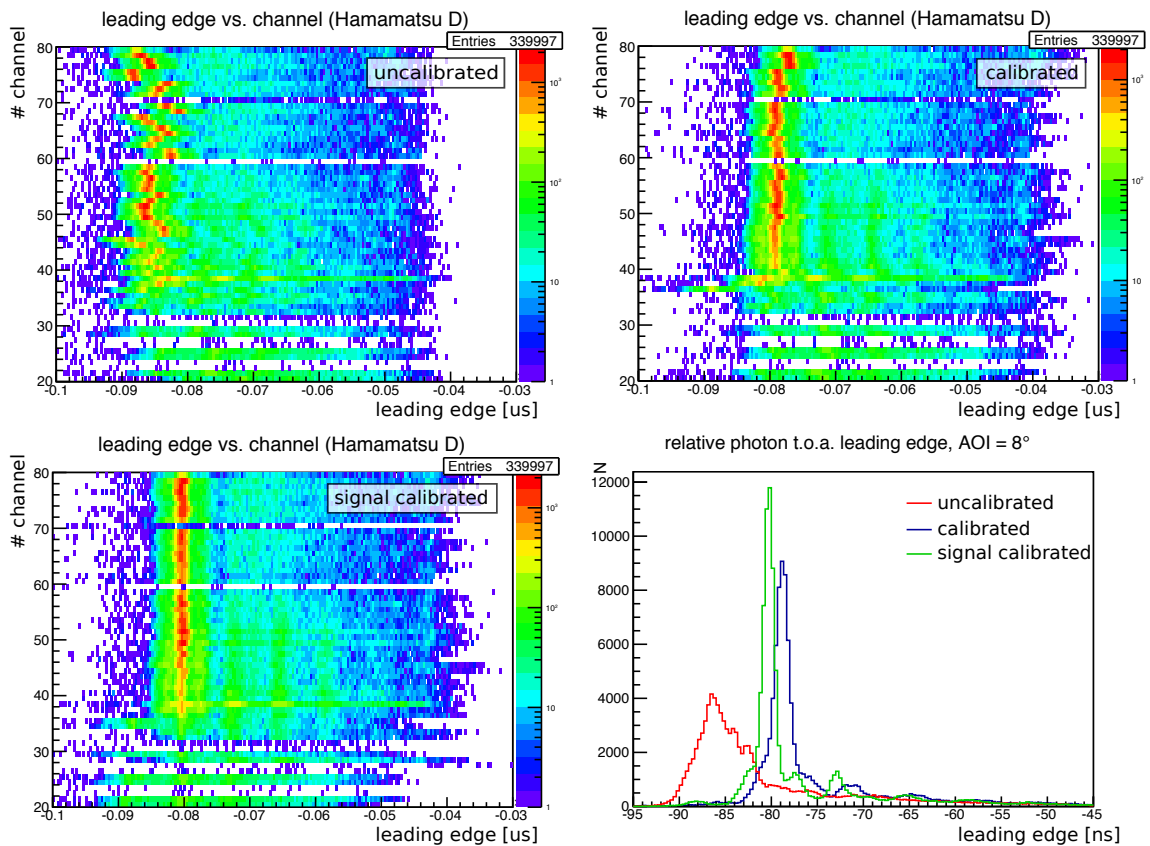


**Figure 6.12:** The plots show the leading edge of the relative timing ( $t_{\text{ch}} - t_{\text{ref}}$ ) without any correction (upper left), with laser calibration (upper right), with laser calibration and additional signal calibration (lower left). The histograms in the lower right plot show a projection of all three options at an angle of incidence of  $8^\circ$ . Two channels above channel 40 are not working properly for this sensor column. No channel below 40 is used in the analysis. The periodic pattern which causes a cluster of events every 7 ns is caused by a firmware error of the TRB system.

signal region was defined. Therefore the accumulated channel distribution with a coarse time cut was fitted by a Gaussian and all events which lay inside a  $3\sigma$  region around the mean value were treated as signal events whereas the remaining events are background. Then all possible time cut intervals around the relative time distributions were evaluated and the interval at the highest signal bin was chosen which simultaneously had the lowest background contribution. Figure 6.13 contains an illustration of this method in the top row. The central row shows the influence of a relative timing on the timing distributions. The left plot contains the coarse timing which is more than 10 ns wide. In comparison to the coarse timing the relative timing which takes into account the first MCP-TOF station narrows down the signals and hence the intervals of interest which helps to reduce the background. Finally the bottom row shows the channel distributions for the events selected as signal and rejected as background. The background distribution is mostly flat and contains no clear peak at the signal position. Both plots again suggest to remove events below chan-

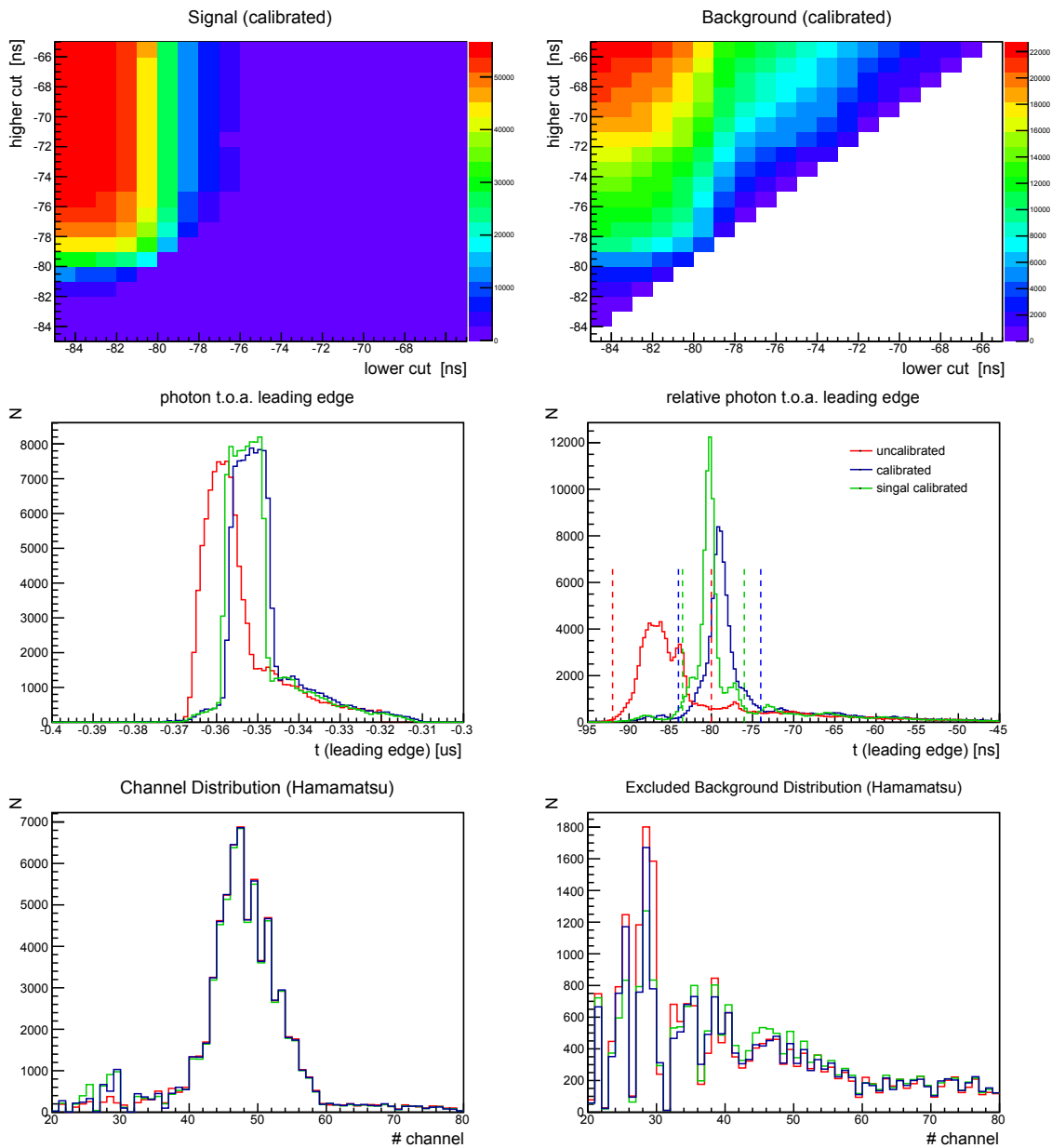


**Figure 6.13:** The top row displays the determination of the time cuts at an angle of incidence of  $6^\circ$ . Events within  $3\sigma$  around the mean of the peak in the channel distribution are counted as signal events whereas the rest is treated as background. The central row shows the time of the leading edge without (left) and with the first MCP-TOF station as a start timer (right). Without the MCP-TOF station the reference time was taken from the physics trigger. The final time cuts are indicated by dashed lines. The bottom row shows the signal events which lay within the cuts (left) and the background events that are rejected by the time cuts (right). All three methods lead to a similar result.

nel 40. All methods show a similar purity of the signal. The width of the time interval for the uncalibrated signal was selected to be 12 ns whereas for the signal calibrated event selection the width was narrowed down to 8 ns. The timing plays only a minor part in the

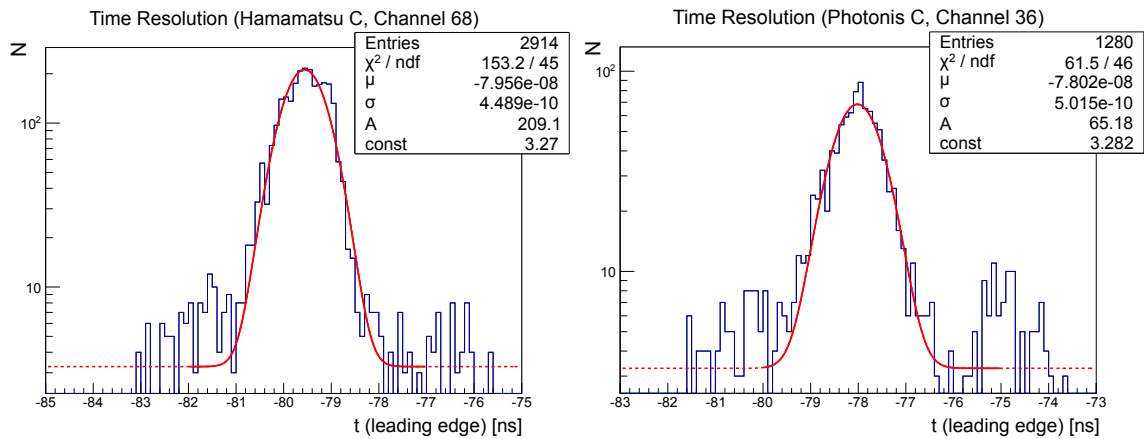


**Figure 6.14:** The histograms show the time resolution for a channel of the Hamamatsu sensor (left) and the PHOTONIS sensor (right). In both cases the achieved time resolution is approximately 500 ps.

data selection at the current stage. As shown in figure 6.14 the time resolution amounts to 500 ps which is the combination of the MCP-TOF and the time resolution of the prototype. Because the time-over-threshold information was missing time-walk corrections could not be applied. The final detector envisages a time resolution of less than 100 ps [Mer14b]. After the calibration was completed overview plots have been created to check the sanity of each set of runs. The following observations were made:

- The photon yield for the PHOTONIS channels is much lower than for the Hamamatsu which is mainly caused by the applied high voltage settings.
- Especially the outer column of the PHOTONIS which was equipped with the FEL-prism pair that was bonded using NOA-61 shows very low statistics. This was expected due to the measurements shown in section 4.4.2.2.
- Some runs have very low statistics (see below).

In order to find the source of the low number of hits the available data for each run was checked on a single event basis. Figure 6.15 gives a detailed overview of the available data for different runs for a 10 GeV/c angle scan between  $6^\circ$  and  $9^\circ$ . A continuous recording of Cherenkov hits can be obtained over the whole period of data taking. The stepwise decrease of the black line can be explained by the acceptance which becomes smaller for higher angles of incidence. If a relative timing is required to apply the previously discussed cuts to reject background hits the leading edge of the first MCP-TOF station must be available. Besides a reduced number of recorded events there are periods where no particles were detected by the MCP-TOF. During some periods the interval of time-of-arrival of the leading edge is shifted by about 30 ns. This shift can be corrected for but is also an example of the problems that arose from the malfunctioning DAQ. In case of an external PID

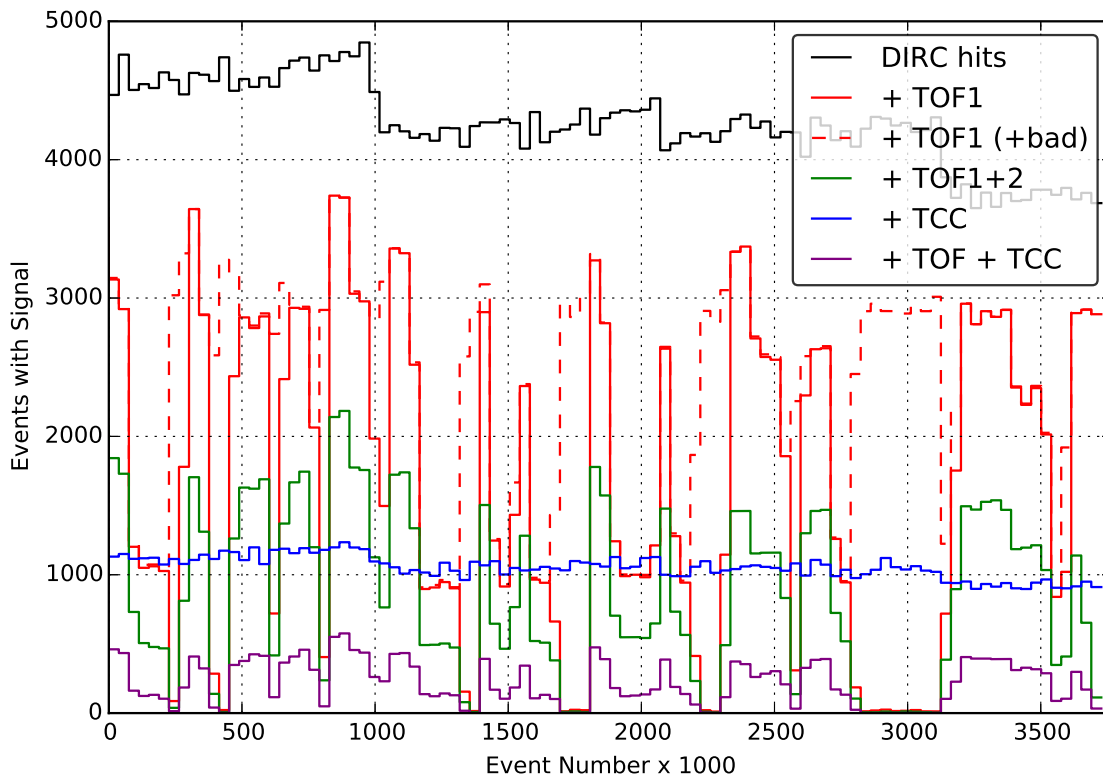


**Figure 6.15:** Data quality for 10 GeV/c runs at angles of incidence between 6 and 9°. The black line corresponds to the total number of events where the Disc DIRC prototype recorded at least one hit. The number of events decreases stepwise as the acceptance of the ROMs becomes smaller for higher angles of incidence. The red line corresponds to events where an additional leading edge in the MCP-TOF is registered. The plot clearly shows that the system did not work continuously and in some periods a large shift of about 30 ns (dashed lines) was recorded. The availability of a signal from both MCP-TOF stations (green line) would reduce the number of events by another factor of two. The blue line corresponds to events recorded with the TCC and violet correspond to events requiring both, TCC and TOF.

information based on the time-of-flight of the particles the second MCP-TOF station has to be included. This requirement lowers the number of events by another 40%. Furthermore the external PID information is corrupt because many events are shifted by multiples of 5 ns at both MCP-TOF stations. This creates ambiguous peaks that do not allow a particle identification even at low momenta. A second option for an external PID signal was given by two pre-installed TCCs. The threshold velocity for the emittance of Cherenkov light can be adjusted by the gas pressure inside the tanks. In the presented runs for 10 GeV/c the TCCs are supposed to record a hit for every pion that traverses the detectors. As can be obtained from figure 6.15 the data taking worked continuously but with a low efficiency. A look at data with lower momentum and comparison with selected MCP-TOF signals and Cherenkov data suggests that the PID information of the TCCs is not reliable as well. For

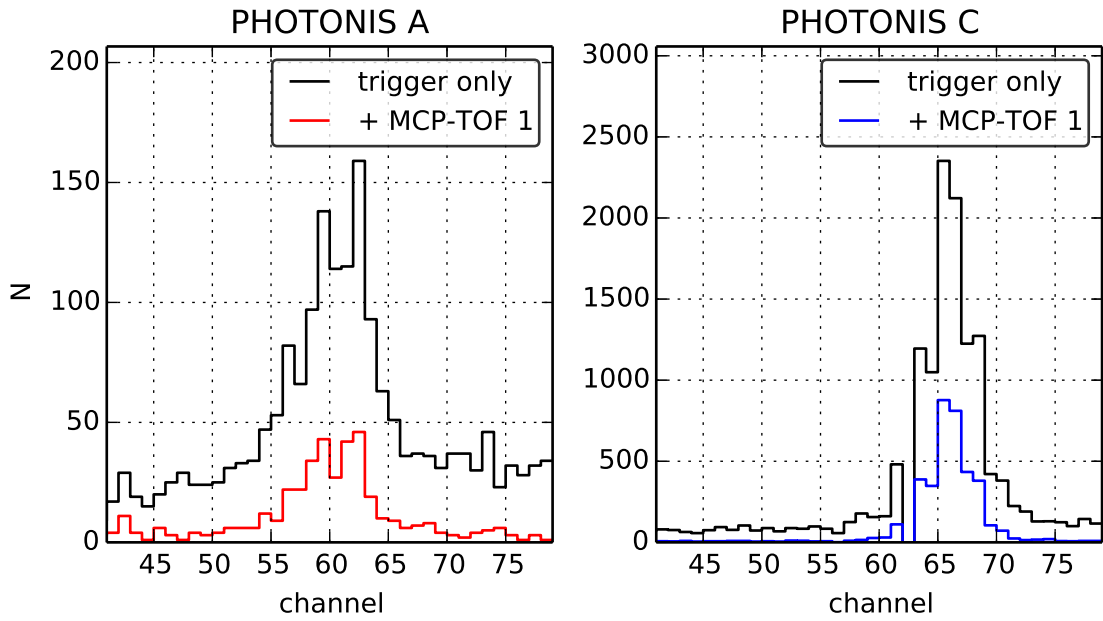


**Figure 6.16:** Recorded photon hits for a 10 GeV/c run at 14° on the outer (left) and inner PHOTONIS column (right). The colored histograms use only events where a leading edge from the first MCP-TOF station is available and are selected using the time cuts. The black histograms use the physics trigger only and are selected by a coarse time cut. Hence the background cannot be rejected efficiently.

setup	$x_{\text{plate}}$ [mm]	$y_{\text{plate}}$ [mm]	$\theta_{\text{beam}}$	$p_{\text{beam}}$ [GeV/c]	focus [m]	description
A	200	196.7	11.2°	5	$\infty$	HV scan
A	200	196.7	11.2°	2-10	+9.5	momentum scan
A	200-300	125-196.7	11.2°	5	$\infty$	transversal scan
B	245	260	5 – 15°	10	$\infty$	angle scan at 10 GeV/c
B	245	260	0 – 20°	5	$\infty$	angle scan at 5 GeV/c
B	245	260	0 – 20°	3	$\infty$	angle scan at 3 GeV/c

**Table 6.1:** Summary of the measured scans during the 2015 test beam. Setup A corresponds to a fixed angle of incidence whereas in setup B the angle can be varied but the beam position is fixed.

this reason the presented analysis only uses the leading edge of the first MCP-TOF station for a relative timing of the events and does without external PID.

To not lose the runs where the MCP-TOF part did not record proper data it was decided to also take data without external timing information into account. Therefore the data was selected by a coarse time cut without demanding a leading edge time from the first MCP-TOF station. In figure 6.16 this coarse distribution is plotted along with the calibrated data sam-

ple. With this method one gains more events in the signal region but also has to deal with higher background. As this analysis mostly aims at the single photon angular resolution at the different MCP-PMT positions the background plays only a subordinate role and can be included in the fit. This method is especially useful in case of the outer PHOTONIS column which has very low statistics in comparison to the other columns.

Table 6.1 summarizes the main measurements that were carried out during the 2015 test beam. With the exception of the transversal scan, which was done to coarsely check the behavior of the detector before one changed to setup B (see figure 6.7), all measurements are explained in more detail in the following section.

## 6.4 Analysis

### 6.4.1 Photon Yield

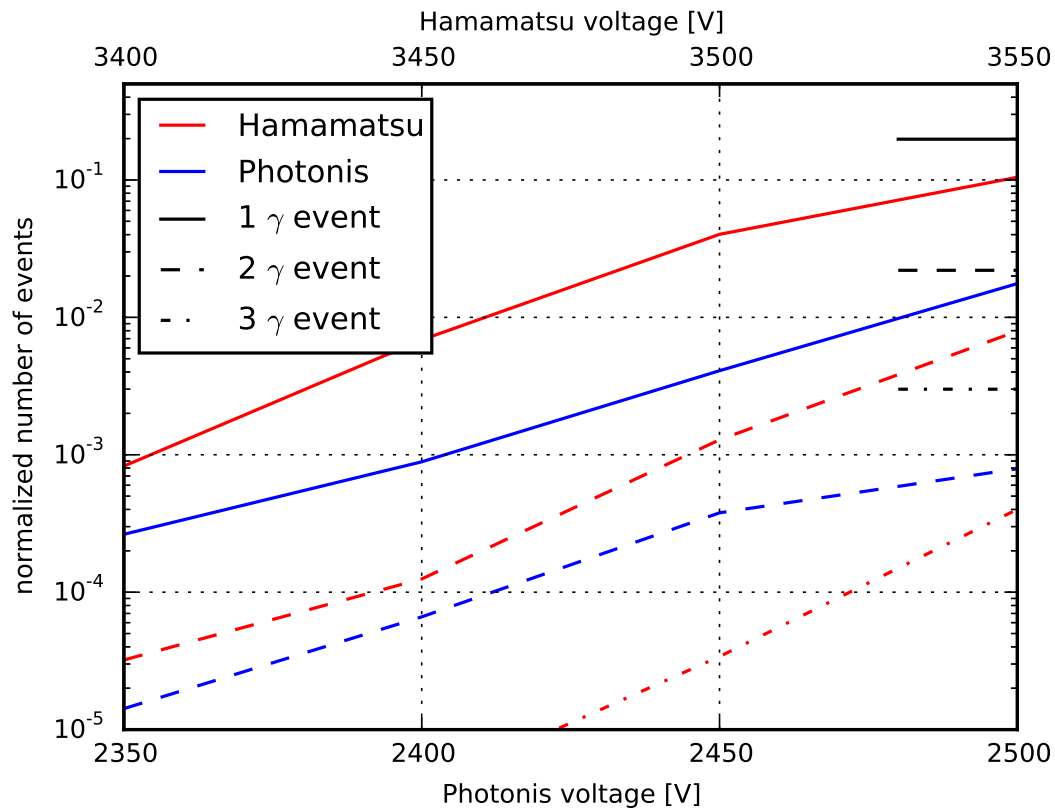


**Figure 6.17:** Photon yield at 5 GeV/c at different high voltage settings for both sensors. The lines correspond to events with 1, 2 or 3 recorded pixel hits per column. The black horizontal lines at the right side of the plot represent the numbers obtained by Monte-Carlo simulations.

The photon yield is an important quantity for the Disc DIRC performance as the resolution of the mean Cherenkov angle scales with the detected number of photons per charged particle track once the wavelength range is fixed. Besides the phenomena and defects that

lead to an actual loss of photons in the optical system further effects can cause a reduction of the recorded number of photons. In connection with an MCP-PMT the quantum efficiency gives the probability of a photon to be converted into an electron inside the photocathode. Furthermore the so-called collection efficiency describes the probability that a generated photoelectron produces enough secondary electrons which reach the anode layer to generate an electric signal. The number of secondary electrons and hence the gain can be controlled by the high voltage applied. At last the threshold settings in the data acquisition determine which pulses are forwarded. In case of the PHOTONIS sensor the maximum high voltage given by the data sheet amounts to 2800 V whereas the Hamamatsu sensor needs a high voltage of up to 3600 V. During a 5 GeV/c run four different high voltage settings were used for each sensor to compare the photon yield as shown in figure 6.17. Although the collection efficiency value for the Monte-Carlo simulations was set to be only 30% the measured photon yield is clearly below the anticipated number of photons.

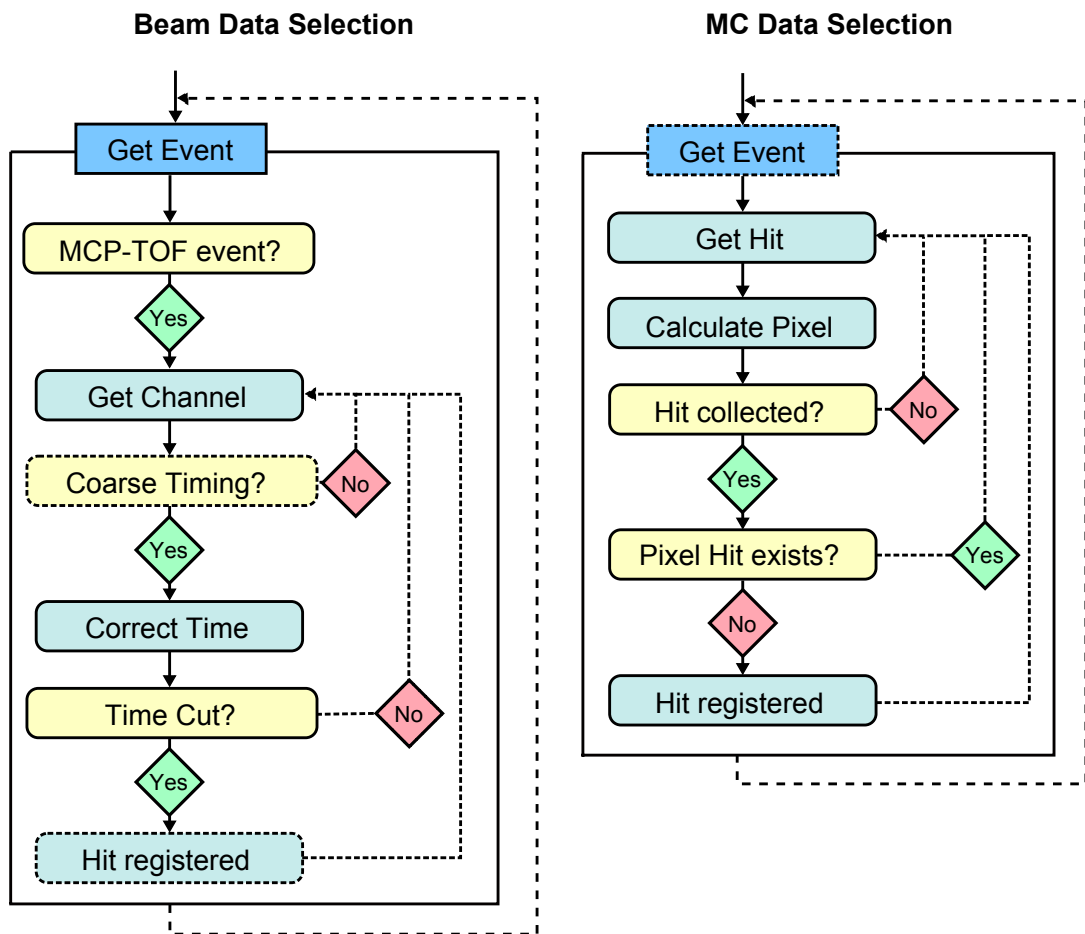


**Figure 6.18:** The flow diagram schematically illustrates the data selection for beam and Monte-Carlo data. In case of the Monte-Carlo data no additional time cut is applied as the spread is small in comparison to the time cut interval of the beam data.

The data format for the Monte-Carlo and the beam data differs hence different selection methods had to be applied for the analysis (see figure 6.18). In case of the beam data a MCP-TOF signal has to be available. As shown in the previous section 6.3.2 only this method allows to efficiently reduce the background. Then every channel is checked for signals within a wide time interval (coarse time cut) which are hit candidates. The time of these signals is then corrected and has to lie within the narrow time cut interval to be registered as a Cherenkov photon hit. In case of the Monte-Carlo data selection a pixel position is calculated for each hit. Next a collection efficiency of 30% is applied and the hit might be rejected. If it is not rejected the algorithm checks whether the pixel has already been hit during this event and in case it has not been hit the Cherenkov photon hit is registered. This step was introduced because without a proper time over threshold measurement multiple photon hits on one pixel cannot be distinguished from single hits. The time spread of the simulated Cherenkov hits is smaller than the chosen time cut interval for the beam data this is why no additional time cut has been applied.

Although the Hamamatsu sensor with 3550 V is used at 96% of its maximum voltage the photon yield has not yet saturated and lies about a factor 2 below the Monte-Carlo expectation. In case of the PHOTONIS MCP-PMT the sensor was used only up to 87% of its maximum voltage and hence has an even lower photon yield. The statistics for 2-photon and 3-photon events are very low which means that only in rare cases more than one hit is registered in one sensor column during a single event. Therefore it is not possible to derive a more sophisticated interpretation of the data using Poisson statistics. The possibility that the photon yield is negatively influenced by problems with the DAQ system cannot be excluded. It will be one of the major tasks for future testbeam campaigns to make out the source of the deviation in the number of photons and to verify the predicted photon yield.

### 6.4.2 Momentum and Transversal Scan

The first scans were done with setup A which had the prototype fixed to an angle of incidence of  $11.2^\circ$ . Horizontal and vertical scans were used to preliminarily verify the correct behavior of the prototype. For this purpose the relative positions and widths of the Cherenkov photon distributions was checked. As the longitudinal distance between the beam and the prism grows the width of the distribution becomes smaller whereas for a larger lateral distances the width of the distribution increases. At the same time the position between the prism and the beam determines  $\alpha_{\text{FEL}}$  which shifts the position of the Cherenkov photon distribution on the MCP-PMT anode (see section 3.3.3). Next a momentum scan was performed at a fixed position which is plotted in figure 6.19 along with Monte-Carlo data. The runs below 4 GeV/c did not collect sufficient data. The particle fractions used in the Monte-Carlo data were set according to predictions shown in [Gat15].

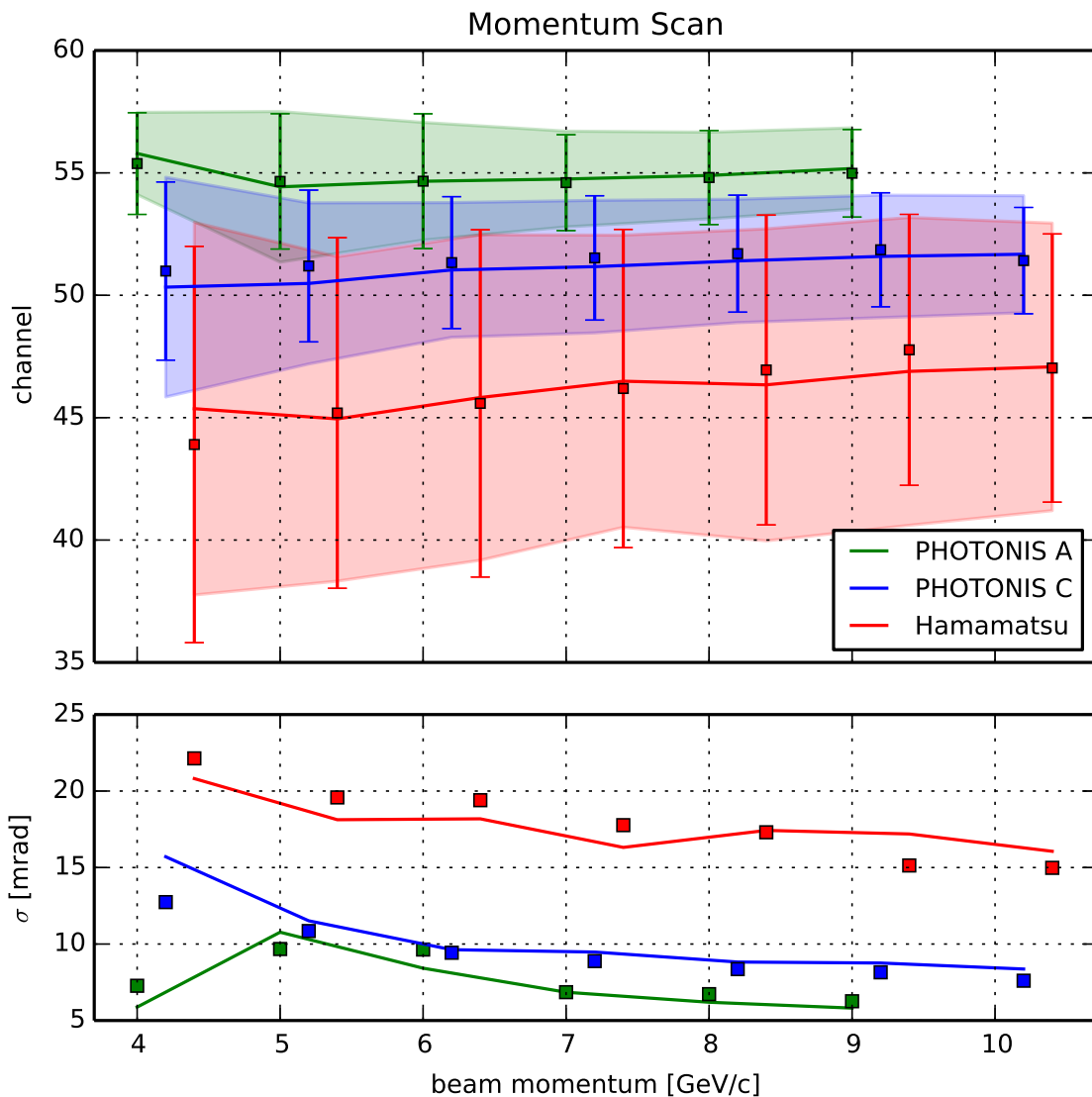


**Figure 6.19:** Summary plot for the momentum scan. The top plot contains the mean positions of the fitted photon distribution for each sensor column (colored squares) and their standard deviation/single photon resolution (corresponding error bars). The lines and shaded areas correspond to the mean value and standard deviation of the Monte-Carlo generated distributions. The lower plot again shows the single photon resolution in mrad for each momentum (colored squares) along with the Monte-Carlo predictions (lines).

The amount of protons in the beam rises almost linearly from about 35% at 4 GeV/c to 70% at 10 GeV/c. In case of the pions their fraction falls from 60% to 25% in the same region. The contributions for kaons is only about 5%. The Cherenkov angles for the different hadrons differ less at higher momenta why the measured single photon resolution becomes smaller. The single photon resolution is determined by the standard deviation  $\sigma$  of a Gauss fit to the Cherenkov photon distribution which is recorded on the MCP-PMT anode. As no reliable external PID was available the distribution was most of the time fitted by a single

Gaussian function although the distribution is technically a superposition of two individual distributions (three if the kaons are included). This method was also chosen because the distributions are only few channels wide which leaves few degrees of freedom in case of a more complex fit function.

Because of the position of the beam the individual single photon distributions for the different hadrons strongly overlap. An exception is the PHOTONIS A at 4 GeV/c where the pion and proton peak are nicely separated and only the pion peak is fitted which results in a drop regarding the single photon resolution. Considering the circumstances of a missing external PID and no precise beam information regarding its exact position and shape a good agreement between beam data and Monte-Carlo can be observed.

### 6.4.3 Angle Scans

#### 6.4.3.1 10 GeV/c Angle Scan

The angle scan at 10 GeV/c contains the highest statistics and has the advantage of overlapping Cherenkov angle distributions for protons and pions. Their Cherenkov angles differ by less than 4 mrad which corresponds to 1.14 (1.46) pixels or channels on the PHOTONIS

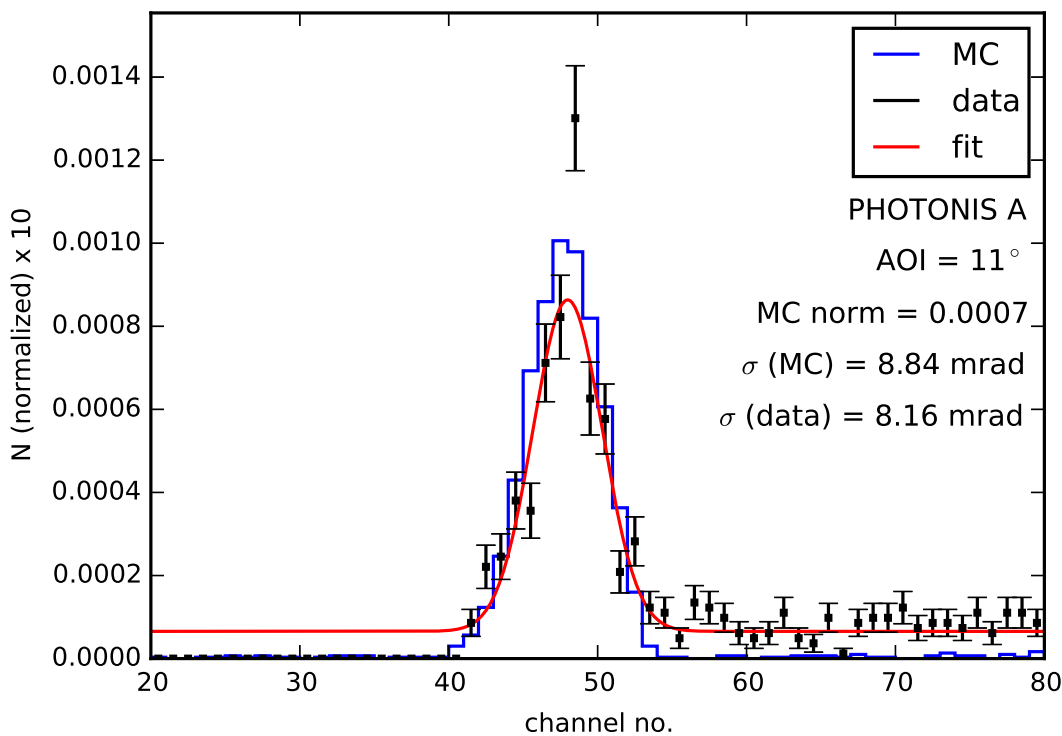


**Figure 6.20:** The Cherenkov photon distribution for the PHOTONIS A (outer column) at a beam angle of incidence of  $11^\circ$  during the angle scan at 10 GeV/c.

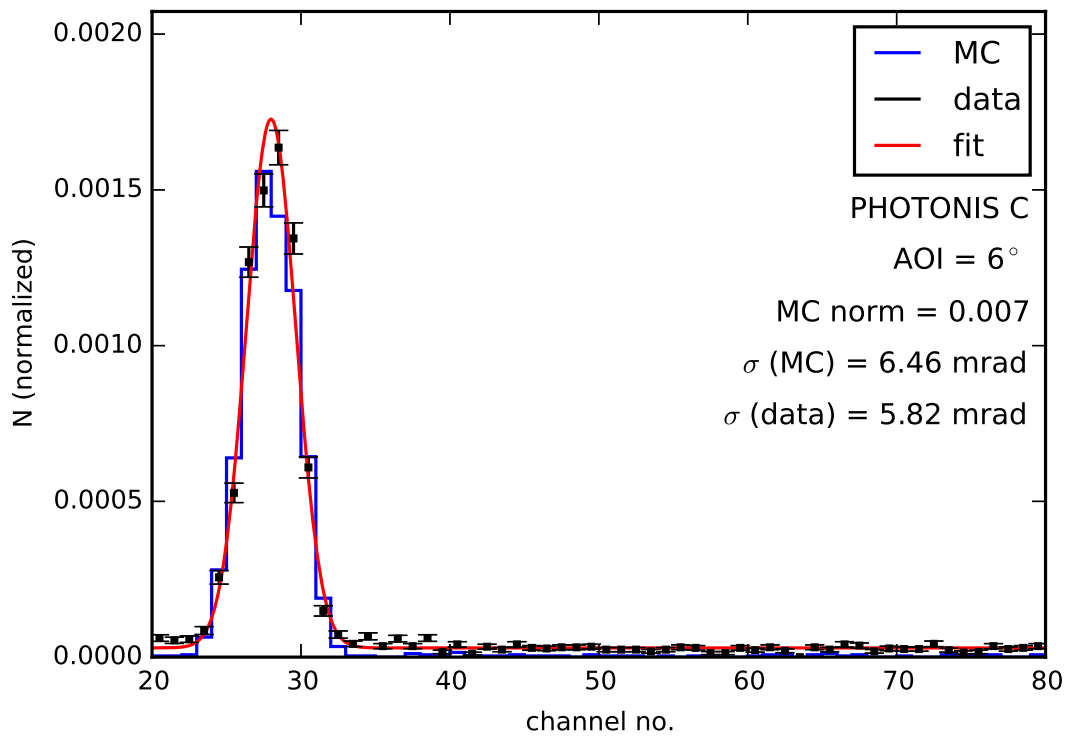


**Figure 6.21:** The Cherenkov photon distribution for the PHOTONIS C (inner column) at a beam angle of incidence of  $6^\circ$  during the angle scan at 10 GeV/c.

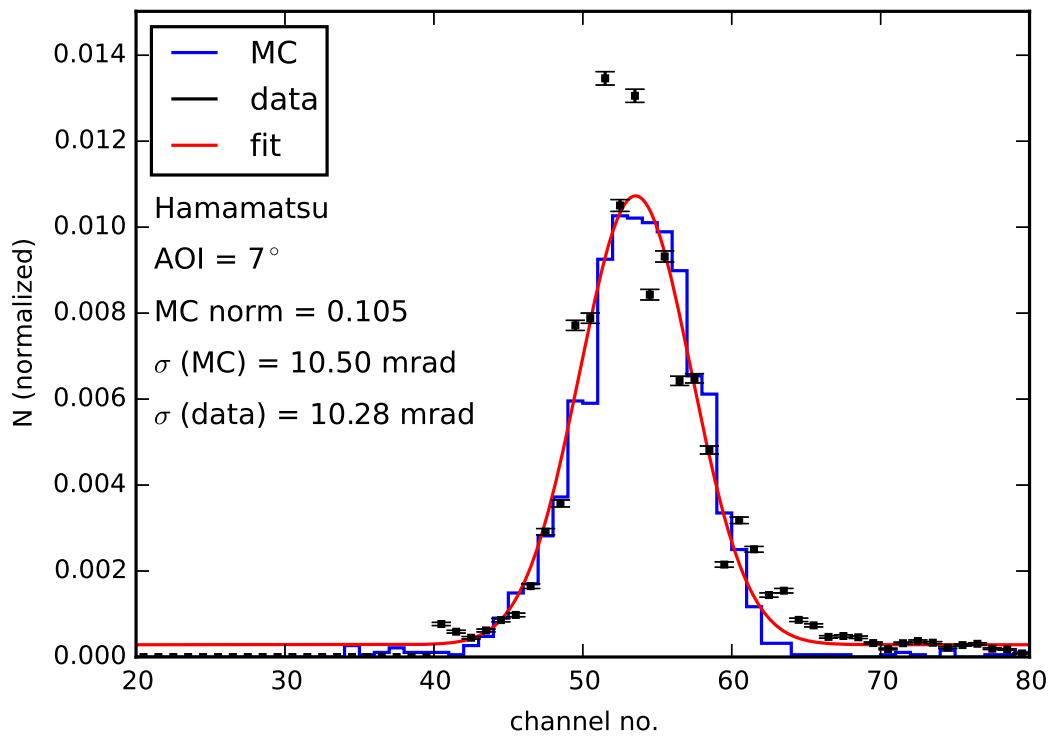


**Figure 6.22:** The Cherenkov photon distribution for the Hamamatsu MCP-PMT column at a beam angle of incidence of  $7^\circ$  during the angle scan at 10 GeV/c.

(Hamamatsu) anode. Furthermore protons are 3.5 times more frequent than pions. During the scan the angle of incidence was manually set by a rotary table. It was equipped with a nonius scale which allows to adjust the prototype with an accuracy of 0.5 mrad. The data selection was done as in the previously described studies. The PHOTONIS (Hamamatsu) MCP-PMT was operated at 2450 V (3450 V) which corresponds to 87.5% (95.8%) of its maximum voltage. Figures 6.20-6.22 show single photon distributions for all three sensor columns and different angles. Each plot shows the measured photon distribution (black circles with error bars) and the corresponding Gaussian fit (red line) which is used to determine the resolution. The blue histogram in the background corresponds to Monte-Carlo data. The sensor column and Angle-Of-Incidence (AOI) is written below the legend. The *MC norm* value is an additional scale factor applied on the Monte-Carlo data in order to match the beam data inside the histogram.

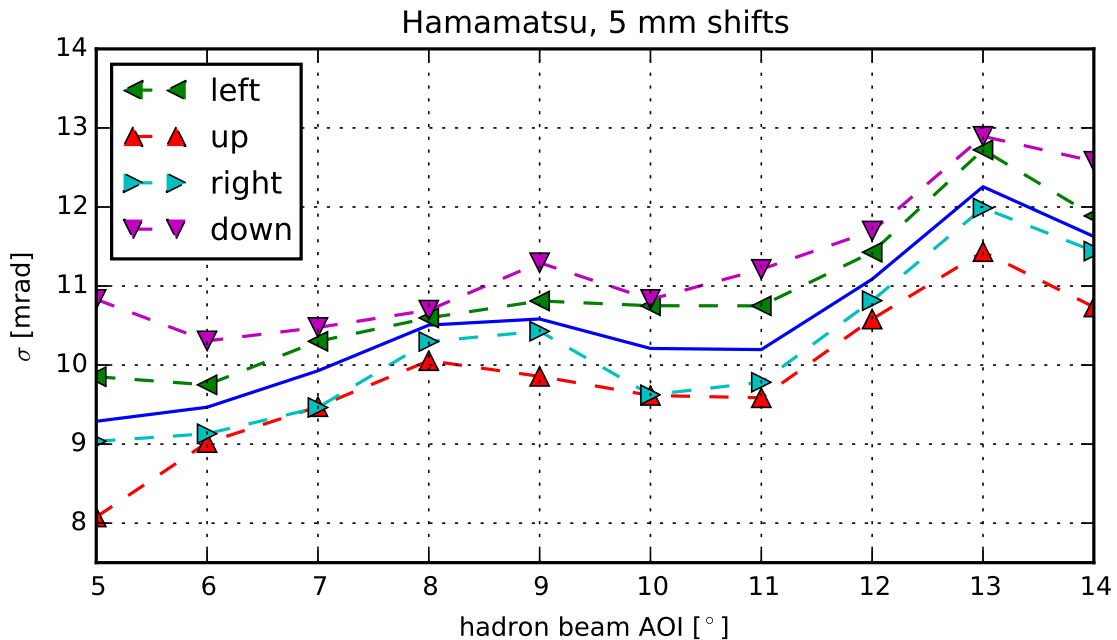


**Figure 6.23:** The plot shows the predicted single photon resolution for the Hamamatsu sensor at 10 GeV/c (blue line). The dashed lines correspond to the single photon resolution if the beam is shifted by 5 mm. The triangular data points point to the four direction of the shift. Left and up corresponds to positions closer to the FEL.

A look at these numbers reveals that the number of detected photons for the PHOTONIS C column is about 15 times below the yield for the Hamamatsu column which is caused by low high voltage settings of the PHOTONIS MCP-PMT. In case of the PHOTONIS A the output drops by another factor of 10 due to the bad optical coupling between the prims and FEL. Otherwise a good agreement between beam and Monte-Carlo data is reached regarding the achieved single photon resolution. In the case of the PHOTONIS A and the

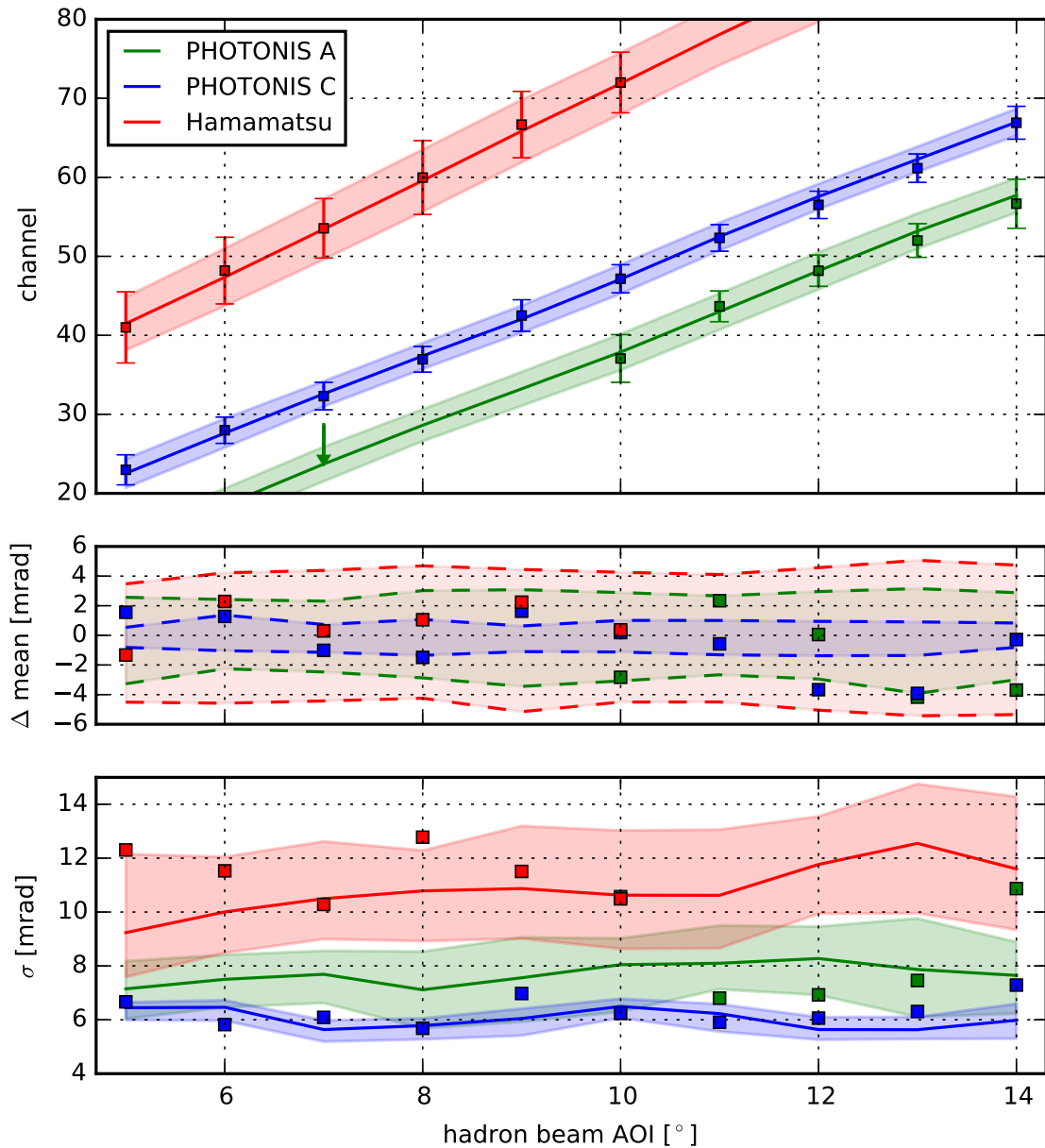


**Figure 6.24:** Overview plot for the 10 GeV/c angle scan. The top panel contains the mean positions of the fitted photon distribution for each sensor column (colored squares) and their standard deviation/ single photon resolution (corresponding error bars). The lines and shaded areas correspond to the mean value and standard deviation of the Monte-Carlo generated distributions. PHOTONIS A values are shifted downwards by 5 channels to give a better overview. The middle panel shows the deviation of the mean values with respect to the Monte-Carlo prediction (colored squares). The bottom panel compares the fitted resolution of the beam data (squares) to the Monte-Carlo data (lines). The values for the PHOTONIS A were determined without a relative timing. The shaded areas in the middle and bottom part correspond to the possible deviation of the mean and the standard deviation of the fitted Cherenkov distribution due to a shift of the beam spot within a radius of 5 mm and a variation of the beam diameter of  $\pm 5$  mm. This band also gives a coarse estimation of the systematic uncertainty.

Hamamatsu columns some channels show a large deviation from a smooth distribution. This can be traced back to the threshold settings of the individual channels which were set automatically during laser runs. Except for the PHOTONIS A column the background is small compared to the signal peak. The best single photon resolution is reached by the PHOTONIS C with 5.7 mrad at  $8^\circ$  because its lateral distance to the beam spot is the smallest with 10 mm. It is important to mention that the difference in the measured single photon resolutions primarily depends on the geometry of the setup. A bad channel or threshold setting is only a second order effect. In case of the PHOTONIS A column only photons with wavelengths above 350 nm were taken into account due to the NOA-61 glue joint (see section 4.5).

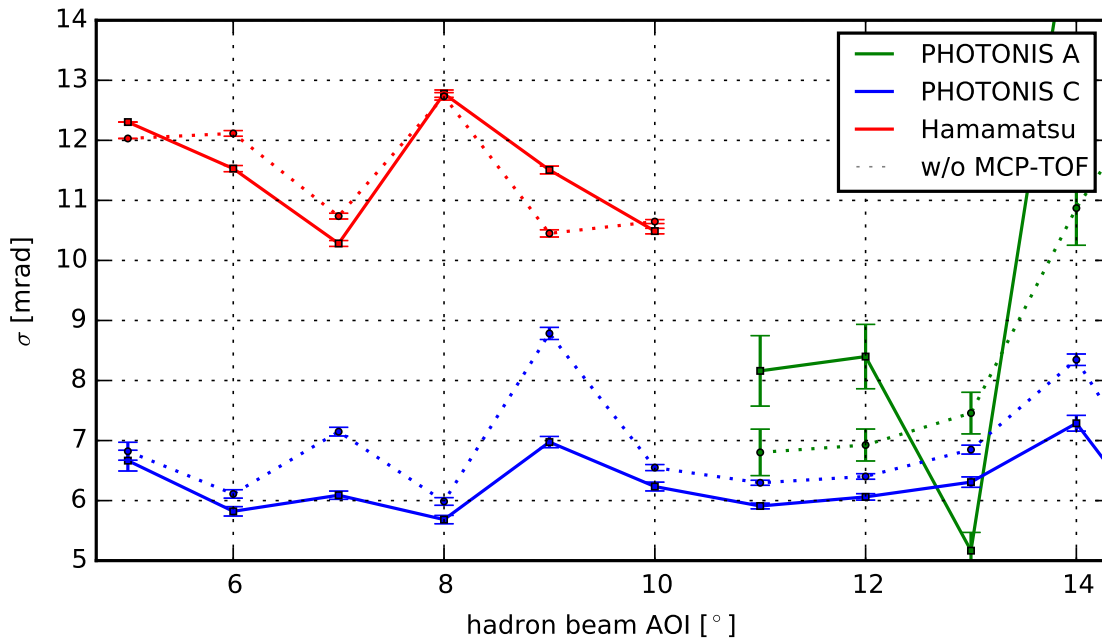


**Figure 6.25:** The measured single photon resolutions at 10 GeV/c with (continuous line) and without (dashed line) MCP-TOF information obtained by a Gaussian fit with constant background.

An overview of the 10 GeV/c angle scan is shown in figure 6.24. It consists of three plots which show the channel overview, the position of the mean and the single photon resolution for all measured angles of incidence (AOI) and all available sensor columns. The top plot contains the mean positions (squares) and standard deviations (error bars) of each Gaussian fit to the beam data. The continuous line and the shaded band correspond to the Monte-Carlo values. In the second plot the difference between the mean of the beam data and Monte-Carlo is drawn (squares). The shaded bands indicate the maximum variation of the mean value if the beam is shifted by  $\pm 5$  mm in x- and y-direction and its diameter is varied by  $\pm 5$  mm. The deviations are partly driven by the nonius scale. The third plot again shows the measured single photon resolutions (squares) along with the Monte-Carlo values

(continuous lines) and the maximum variation due to different beam parameters (shaded areas). An example of the impact of the beam on the single photon resolution is shown in figure 6.23. The continuous line corresponds to values which are obtained with the measured position whereas the dashed lines are shifted beam positions at which the triangle points to the direction of the shift. As expected the resolution becomes smaller if beam is positioned closer to the prism laterally (red triangles) or farther longitudinally (turquoise triangles). In addition the exact beam profile and size was neither precisely known nor was a sufficient measurement available. In figure 6.24 one can also see that the impact is different for each sensor. In case of the PHOTONIS C the variation is small as the beam is almost perpendicular with respect to the prism and FEL. Here the best agreement was reached between data and Monte-Carlo as well.

As mentioned in section 6.3.2 the analysis can be done without a narrow time cut by ignoring the MCP-TOF information. This is especially interesting for runs or columns with low statistics such as the PHOTONIS A. Figure 6.25 compares the single photon resolutions that are obtained with (continuous lines) and without (dashed lines) using the MCP-TOF for a relative timing. In case of the PHOTONIS C the resolution is slightly worse with spikes at 7 and 9° whereas the PHOTONIS A and Hamamatsu do not show a consistent behavior between the two selection methods. Different to the overview plot from figure 6.24 also the statistical errors from the Gaussian fits are included in this plot.

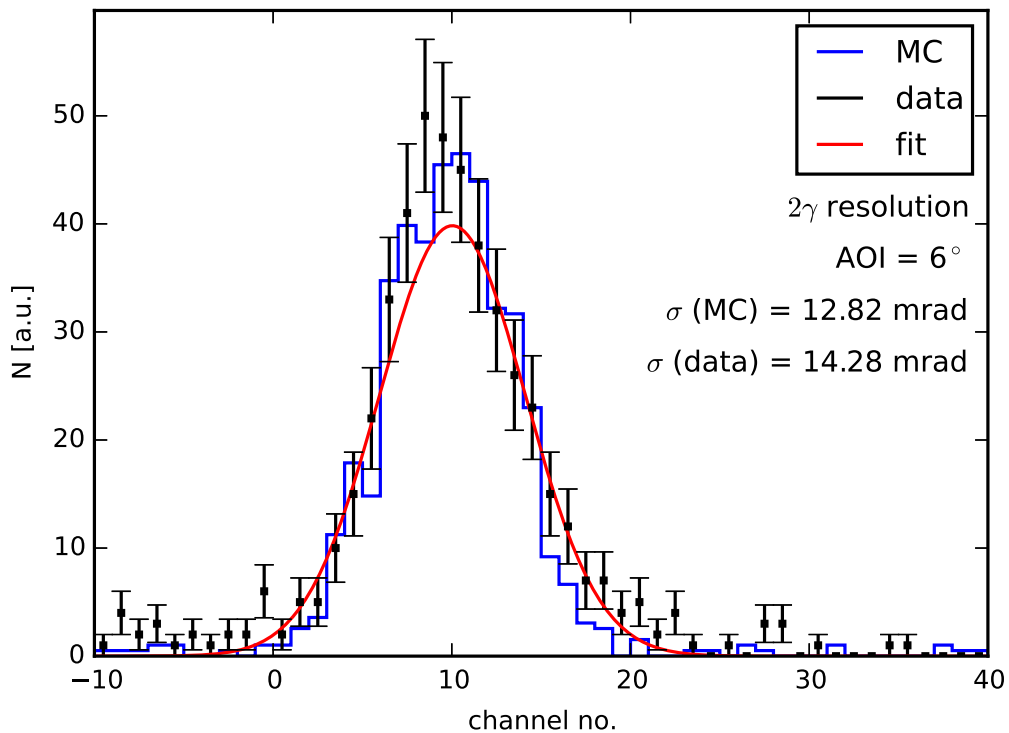


**Figure 6.26:** 2-photon resolution between the inner PHOTONIS and Hamamatsu columns at a beam angle of incidence of 6° during the angle scan at 10 GeV/c.

Besides the single photon resolution the so-called 2-photon resolution is used to check the detector performance. It is defined as the difference between the hit positions of two different sensor columns during a single event. In comparison to the single photon resolutions errors which are connected to the smearing of the beam or the uncertainty of the beam position are correlated and partly cancel. Due to the low statistics this analysis was done for hits in the Hamamatsu and PHOTONIS C only. In the rare case that a column recorded more than one photon a mean was calculated. Figure 6.26 shows the 2-photon resolution at an angle of incidence of  $6^\circ$ . Again the beam data is represented by black circles with error bars and the Monte-Carlo is drawn as a blue histogram in the background. An overview of all available angles is shown in figure 6.27. Besides the results for the individual 2-photon resolutions the quadratic addition of the single photon resolutions  $\sqrt{\sigma_{PHOC}^2 + \sigma_{Hama}^2}$  is plotted.

For the available data no improvement in case of the 2-photon resolution can be obtained as the width of the distribution is dominated by other error sources. Within the large statistical error bars the measured data points agree with the Monte-Carlo predictions. However, all measured values lie above the corresponding simulated data points. All measured single and 2-photon resolutions are summarized in table 6.2.

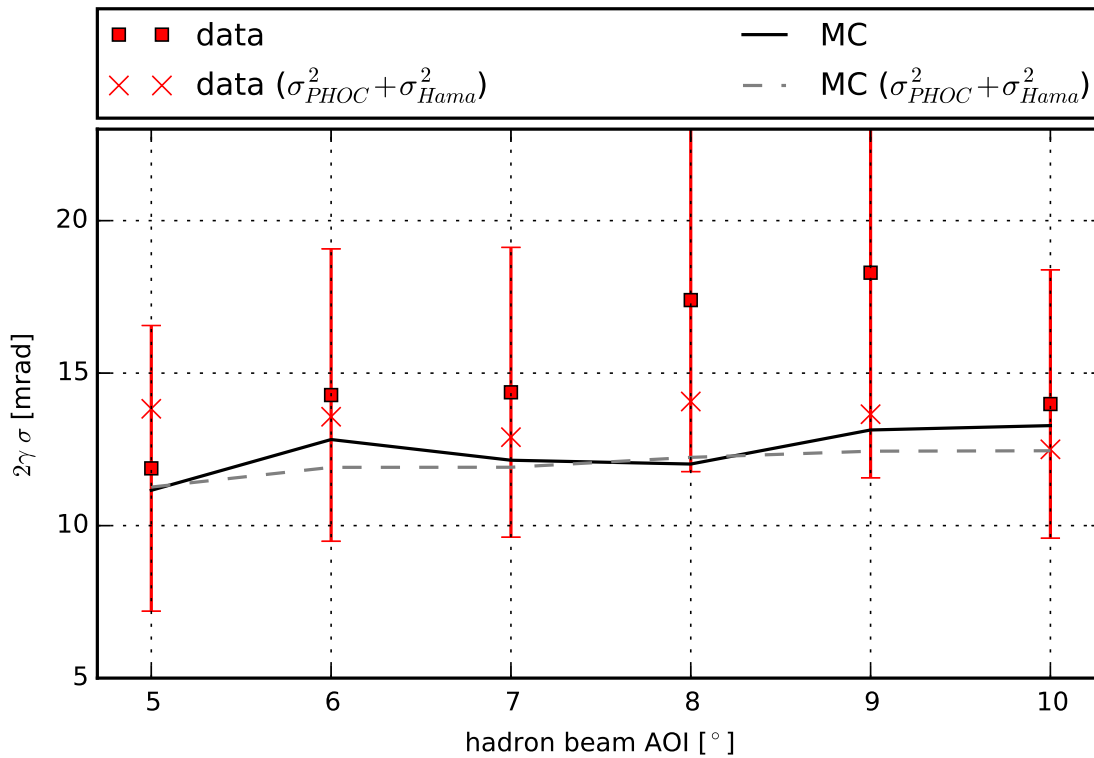


**Figure 6.27:** Overview plot for the 2-photon resolution at 10 GeV/c. The continuous line and squares are the standard deviation of the fit of the 2-photon distribution. The dashed line and crossed data points correspond to the sum of the individual single photon resolutions.

AOI	single photon resolution [mrad]			$2\gamma$ res. [mrad]
	PHOTONIS A	PHOTONIS C	Hamamatsu	
5°	-	$6.67 \pm 0.17$	$12.30 \pm 0.04$	$11.9 \pm 4.7$
6°	-	$5.82 \pm 0.08$	$11.53 \pm 0.05$	$14.3 \pm 4.8$
7°	-	$6.09 \pm 0.07$	$10.28 \pm 0.05$	$14.4 \pm 4.8$
8°	-	$5.68 \pm 0.07$	$12.78 \pm 0.06$	$17.4 \pm 5.6$
9°	-	$6.97 \pm 0.09$	$11.51 \pm 0.06$	$18.3 \pm 6.7$
10°	$10.57 \pm 1.48$	$6.23 \pm 0.07$	$10.49 \pm 0.05$	$14.0 \pm 4.4$
11°	$6.8 \pm 0.4$	$5.91 \pm 0.05$	-	-
12°	$6.9 \pm 0.3$	$6.06 \pm 0.05$	-	-
13°	$7.5 \pm 0.4$	$6.31 \pm 0.09$	-	-
14°	$10.9 \pm 0.6$	$7.29 \pm 0.13$	-	-

**Table 6.2:** Overview of the the measured single and 2-photon resolutions at 10 GeV/c as plotted in figure 6.24 along with the corresponding statistical errors. The values for the PHOTONIS A column are determined without MCP-TOF information.

#### 6.4.3.2 5 GeV/c Angle Scan

The second angle scan was done at a beam momentum of 5 GeV/c. The scan was done with 2° steps between 0° and 20°. Due to the coverage of the available channels of the MCP-PMT the measurements below 6 and above 14° did not show any Cherenkov photon distribution. At 5 GeV/c the separation between the means of the pion and proton distribution corresponds to 16.0 mrad which converts into 4.6 channels for the PHOTONIS and 5.9 channels for the Hamamatsu MCP-PMT. For this reason a fit with a single Gaussian is not advisable. However, due to low statistics and high fluctuations of some channels the two Gaussian fits did not converge properly unless strict boundary conditions were manually applied. Figure 6.28 shows the Cherenkov photon distribution on the PHOTONIS C at a beam angle of incidence of 10°. The black circles with error bars represent the measured data whereas the blue histogram corresponds to Monte-Carlo data. The red dashed lines represent the fitted individual Gaussians distributions. The same was done for the Hamamatsu sensor (see figure 6.29). Although the fitted functions and simulated distributions show some agreement and consistency the data points are fluctuating strongly. Without external PID the 5 GeV/c angle scan does not serve as benchmark scan for the detector performance und is shown for the sake of completeness.

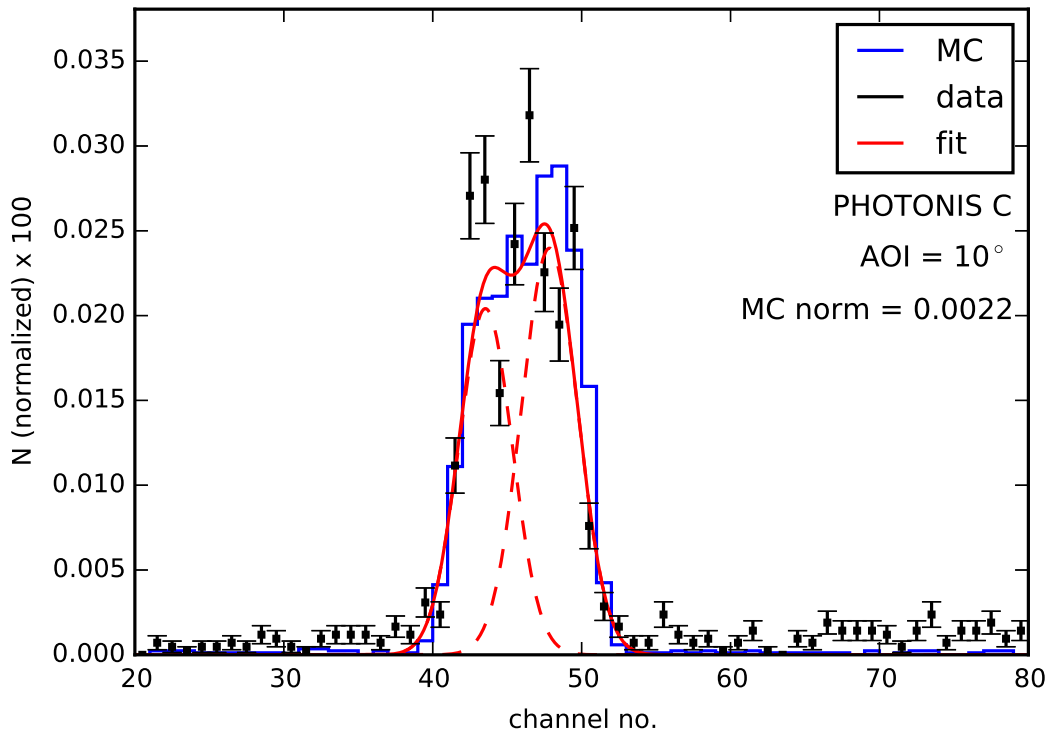


**Figure 6.28:** The Cherenkov photon distribution for the PHOTONIS C (inner column) at a beam angle of incidence of  $10^\circ$  during the angle scan at 5 GeV/c.

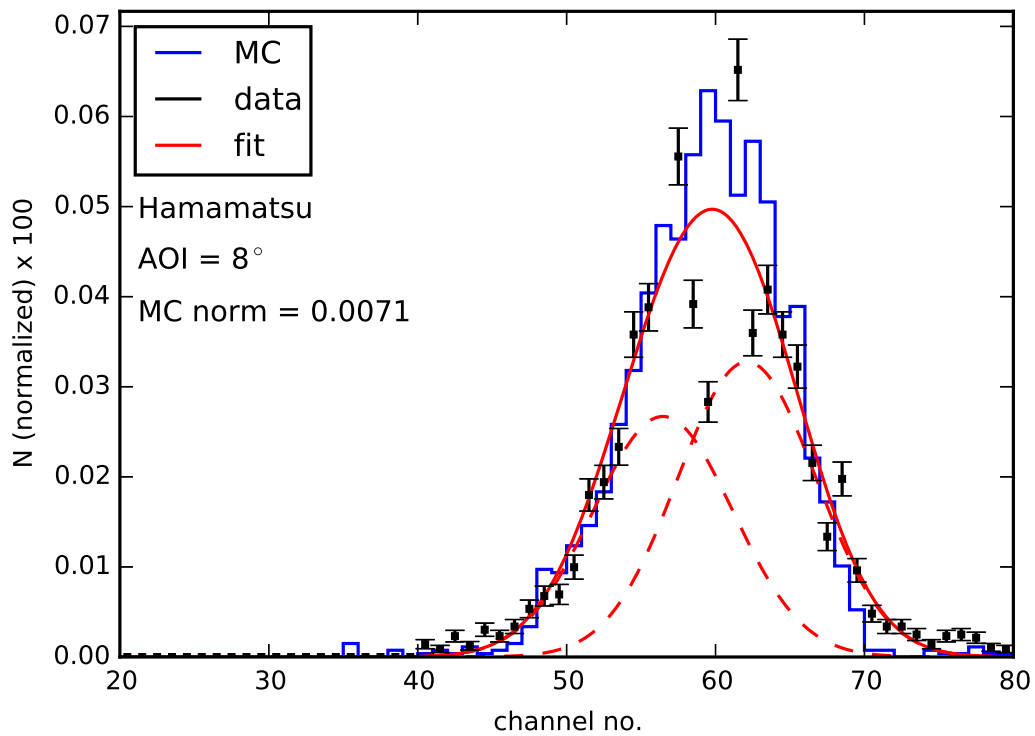


**Figure 6.29:** The Cherenkov photon distribution for the Hamamatsu sensor column at a beam angle of incidence of  $8^\circ$  during the angle scan at 5 GeV/c.

### 6.4.3.3 3 GeV/c Angle Scan

The 3 GeV/c angle scan was done analogously to the previously presented 5 GeV/c angle scan. The difference between the Cherenkov angles for pions and protons at this momentum amounts to 44.3 mrad or 12.7 (16.2) channels in the PHOTONIS (Hamamatsu) MCP-PMT which should result in two clearly separable peaks on the MCP-PMT anode.

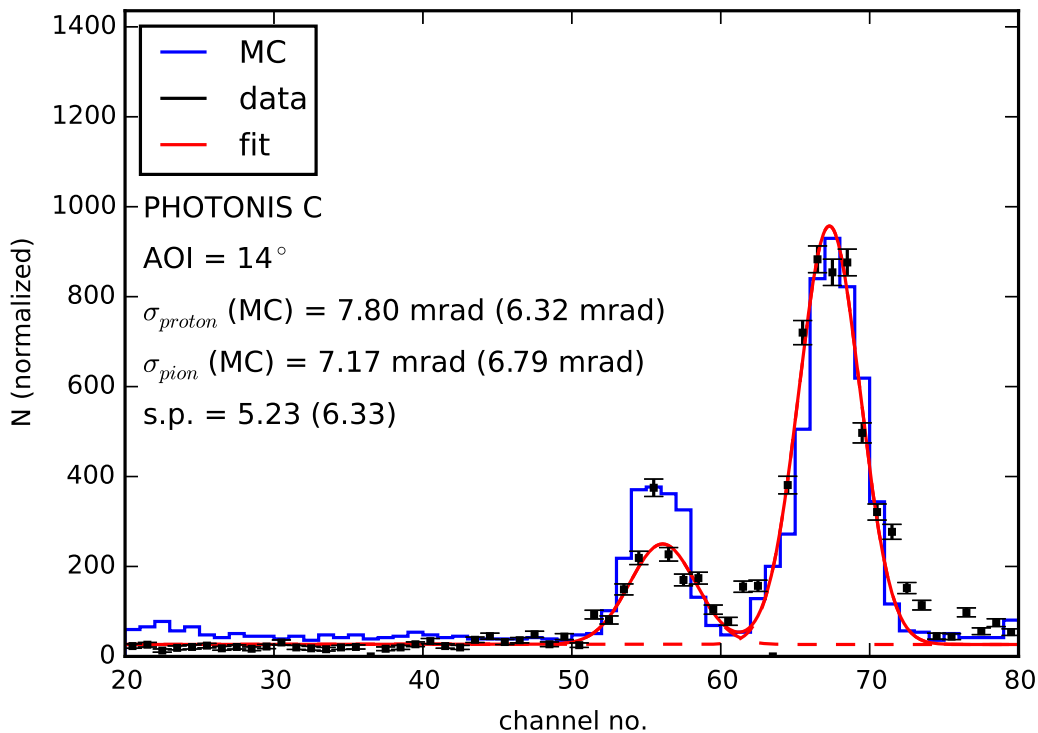


**Figure 6.30:** The Cherenkov photon distribution for PHOTONIS C (inner column) at a beam angle of incidence of  $14^\circ$  during the angle scan at 3 GeV/c. The values in parentheses were obtained by a Monte-Carlo simulation.

Figure 6.30 shows the Cherenkov photon distribution on the PHOTONIS C. As expected two individual peaks can be recognized. The smaller peak around channel 55 comes from the proton fraction of the beam whereas the Cherenkov photons that form the larger peak at channel 67 were emitted by pions. At the momentum of 3 GeV/c pions are about twice as frequent as protons which was considered in the Monte-Carlo. In case of the Hamamatsu column (see figure 6.31) the separation is not as clear due to the larger width of the individual peaks which is caused by the positioning of the FEL-prism pair relative to the beam. However, the measured data matches well the Monte-Carlo prediction. The data base of the presented plots does not use a relative timing from the MCP-TOF which increases the available statistics. Therefore in both cases a constant background was added to the Monte-Carlo data sample.

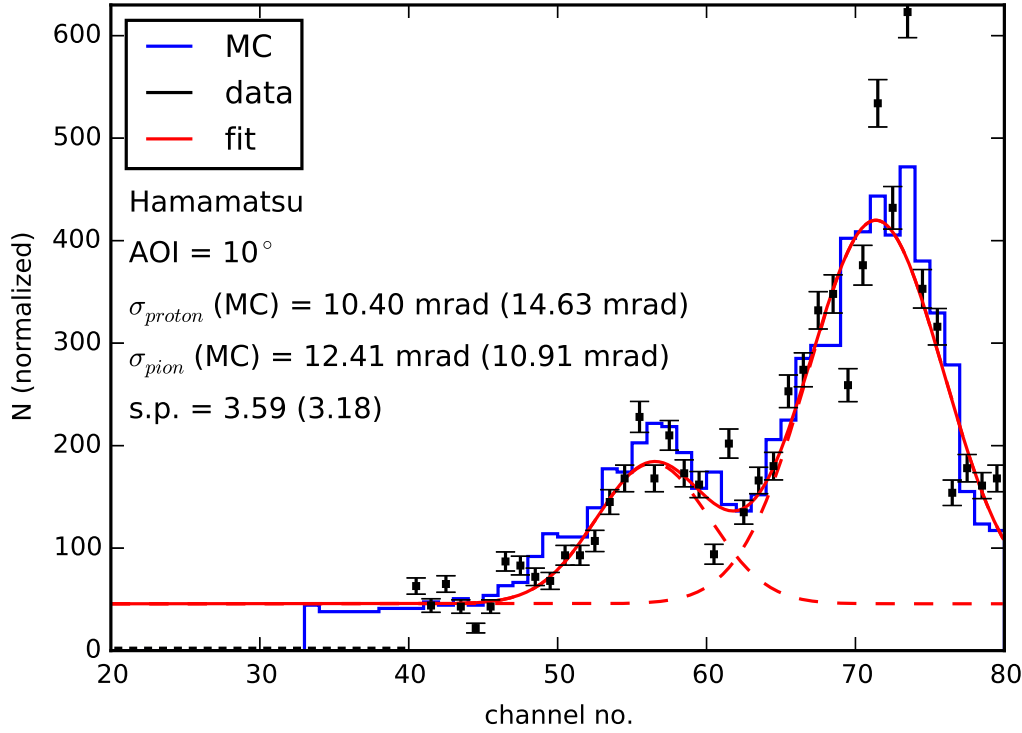


**Figure 6.31:** The Cherenkov photon distribution for the Hamamatsu sensor column at a beam angle of incidence of  $10^\circ$  during the angle scan at 3 GeV/c. The individual Cherenkov photon distributions for pions protons (left peak) and pions (right peak) are drawn as dashed lines.

In principle the Disc DIRC prototype is able to provide PID on a single photon base at low momenta. For both figures the separation power (s.p. or  $n_\sigma$ ) is added to the plot. It is calculated according to [Mer14b]

$$n_\sigma = \frac{|\mu_\pi - \mu_p|}{\frac{1}{2}(\sigma_\pi + \sigma_p)}, \quad (6.1)$$

where  $\mu_i$  is the mean of the Cherenkov photon distribution for the particle type  $i$  and  $\sigma_i$  the corresponding standard deviation. In case of the PHOTONIS C column a separation power of  $4.9\sigma$  and better was reached. The separation power for the Hamamatsu column was calculated to be  $3.6\sigma$  (see figure 6.31). Table 6.3 contains the single photon resolutions  $\sigma_\pi$  and  $\sigma_p$  between 8 and  $14^\circ$  for both peaks along with the measured separation power  $n_p$ . The values are consistent and in good agreement with the Monte-Carlo predictions.

Figure 6.32 summarizes the results for the 3 GeV/c angle scan. In comparison to figure 6.24 for the angle scan at 10 GeV/c the values for the mean and the standard deviation (single photon resolution) correspond to the pion peak only. However, the values are similar to the results during the 10 GeV/c angle scan where the Cherenkov photon distributions almost completely overlap.

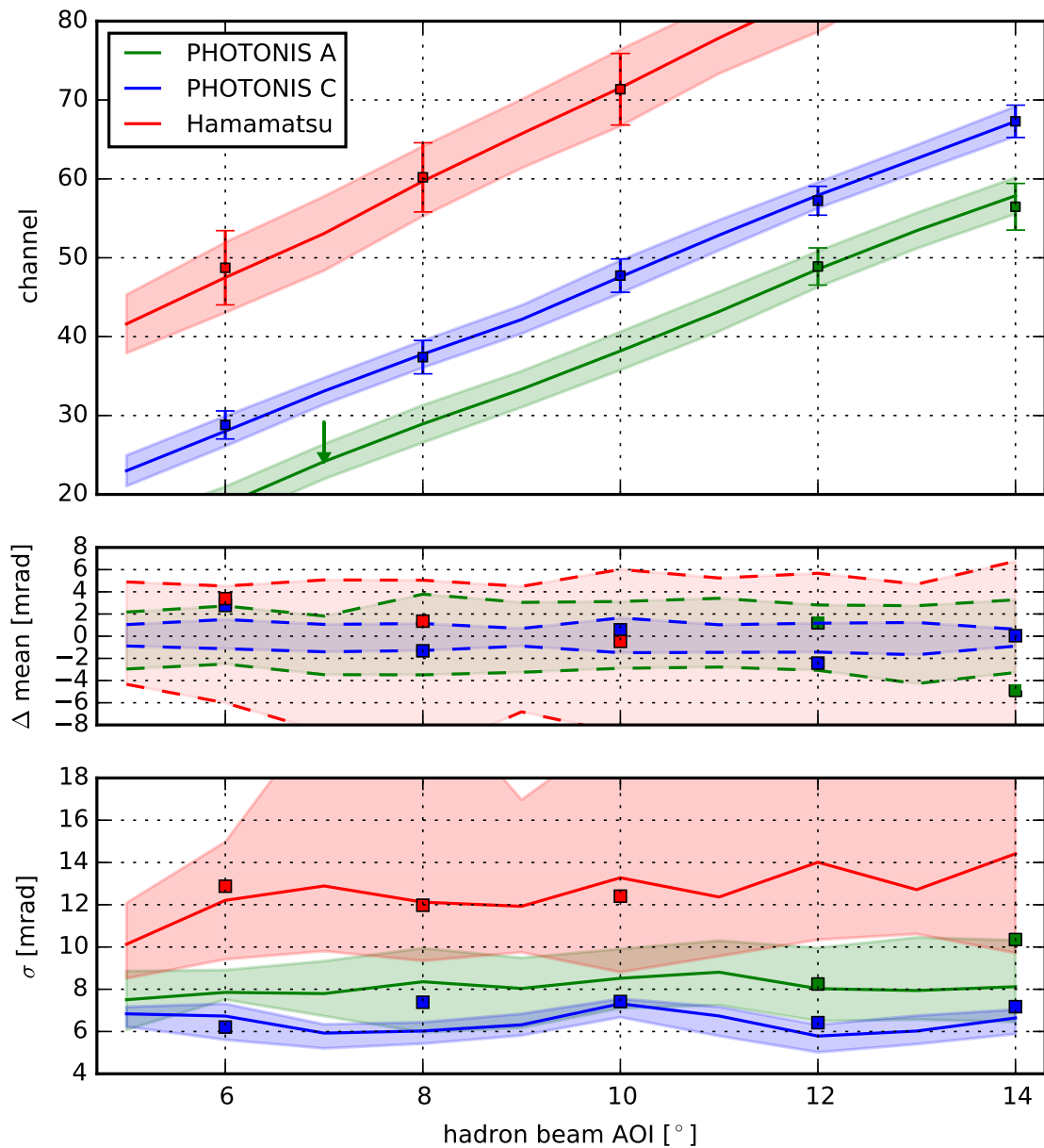


**Figure 6.32:** Overview plot for the 3 GeV/c angle scan. The top part contains the mean positions of the pion's fitted photon distribution for each sensor column (colored squares) and their standard deviation/ single photon resolution (corresponding error bars). The lines and shaded areas correspond to the mean value and standard deviation of the Monte-Carlo generated distributions. PHOTONIS A values are shifted downwards by 5 channels to give a better overview. The middle part shows the deviation of the mean values with respect to the Monte-Carlo prediction (colored squares). The bottom part compares the fitted resolution of the beam data (squares) to the Monte-Carlo data (lines). The values shown were determined without a relative timing. The shaded areas in the middle and bottom part correspond to the possible deviation (see also figure 6.24).

AOI	PHOTONIS C			Hamamatsu		
	$\sigma_\pi$ [mrad]	$\sigma_p$ [mrad]	$\sigma_n$	$\sigma_\pi$ [mrad]	$\sigma_p$ [mrad]	$\sigma_n$
8°	7.39	6.48	5.1	11.98	10.77	3.5
10°	7.42	7.35	5.6	12.41	10.40	3.6
12°	6.41	7.00	5.8	-	-	-
14°	7.17	7.80	4.9	-	-	-

**Table 6.3:** Overview of the measured single photon resolutions for the pion and proton peak from the 3 GeV/c angle scan. The third column for each sensor contains the measured separation power  $n_\sigma$  for the two peaks.

## 6.5 Interpretation and Summary

The prototype for the 2015 testbeam was the first to use high quality components for the photon transport and detection which satisfy the demands for the final detector. All optical components were made of fused silica and MCP-PMTs with highly segmented anodes were used for the detection of Cherenkov photons. Unfortunately the envisaged TOFPET ASIC readout [Rol13] was not yet available for the data acquisition. It was replaced by the TRBv3 system which, due to firmware problems, did not provide a reliable timing. Therefore external PID and time walk correction was not available.

Different scans at different momenta were performed to verify the detector resolution. Most data was collected during an angle scan at 10 GeV/c where a good agreement between Monte-Carlo and beam data was achieved. The single photon resolution for the inner PHOTONIS column was measured to be as low as 5.68 mrad where the main contribution comes from the spot size of the hadron beam. Although measured with low statistics the 2-photon resolution showed a reasonable behavior and was in agreement with the Monte-Carlo data. In case of the 3 GeV/c angle scan a clear separation of the pion and proton peak could be observed with a separation power above  $5\sigma$ . This measurement was mainly done without a start time coming from the MCP-TOF which increased the number of signal events but added a flat but non-negligible background. However, in this connection already a wide time cut allowed to reduce the anyhow small background to a minimum level.

The presented analysis underlines the capabilities of a Disc DIRC detector and verified the single photon resolution for the performed scans. Key to an improvement is a better read-out system including a good understanding of the individual channel efficiencies which in case of this analysis was a main reason for the measured deviations in the single photon resolution values. Also the position of incidence of the hadron is crucial for a further improvement of the single photon resolution. In this respect either a dedicated tracking system or a more narrow beam is required.

## 7 Summary and Outlook

The work in hand was written in the context of constructing a novel Cherenkov detector for efficient  $\pi/K$  separation inside the  $\bar{P}$ ANDA experiment at the future Facility for Antiproton and Ion research (FAIR) at Darmstadt, Germany. The experimental setup including a brief presentation of its components and the envisaged physics program was presented in chapter 2 followed by an introduction to particle identification techniques in chapter 3. Here different detector concepts were discussed with a focus on Cherenkov detectors. The last section of this chapter gave an elaborate introduction to the evolution and final design of an Endcap Disc DIRC (EDD) for  $\bar{P}$ ANDA along with a detailed description of its working principle.

The optical system, thoroughly presented in chapter 4, is a key component of any DIRC detector. It has to provide a low-loss and angle-preserving transport of the Cherenkov photons which requires highly transparent materials with high demands on their surface quality. In section 4.2 a new material, Nikon Fused Silica (NIFS), was introduced and tested for radiation hardness. Irradiations with a  $^{60}\text{Co}$ -source with 1000 and 5000 Gy did not show a significant reduction of the transmission above 300 nm which makes this material suitable for DIRC applications inside  $\bar{P}$ ANDA and other high energy physics experiments. Furthermore a long-term study regarding the recovery potential of the material was carried out showing an exponential behavior in the self healing process. This implicates that statements regarding the radiation hardness of fused silica have to consider long-term effects if probes are exposed to radiation doses in a comparably short time.

The radiator is the largest active detector part of the Disc DIRC and at the same time has to fulfill tight constraints regarding its geometry and surface quality. The corresponding specifications were presented in section 4.3 along with different methods to verify them experimentally with in-house measurements. In this context the flatness of the surface was one of the main concerns regarding the system performance. The developed setup can be used to scan the profile of a large radiator with a sub- $\mu\text{m}$  precision and derive the relative slope between the surfaces with a sub- $\mu\text{rad}$  precision. Measurements of two prototype radiators helped to understand the influence of the polishing process on the radiator profile and the specifications could be improved according to these findings.

Prisms extend the radiator and are coupled to the Focusing Elements (FELs). Both components were introduced in section 4.4 along with their specifications. The imaging quality of available full-scale prototypes was evaluated with a custom setup and compared to theoretical predictions. All components showed the expected performance. For further tests two FELs and prisms were manually bonded using a UV-curing adhesive and a two-component

epoxy. A third FEL-prism pair had already been coupled via optical contact bonding which showed the best performance in a subsequent scan. It is recommended to outsource the gluing of the FEL-prism pairs and use optical contact bonding to obtain the best result possible.

In the remaining sections of chapter 4 different filter options and optical joints were discussed. The existing list of options to reduce the chromatic error due to dispersion and to keep the number of photons at a reasonable level in order to provide sufficient live time of the photosensors was enlarged by a new type of photocathode for the MCP-PMTs which has the highest quantum efficiency in the visible green spectrum. The calculations reveal that it might be sufficient to use this so-called green photocathode and do without additional filters.

The question of how the Disc DIRC can be mechanically integrated had previously not been addressed and in the context of this thesis a conceptual design was developed in chapter 5. It accounts for the different demands: radiation hardness of the components, low material budget, a safe mounting of optical components and a feasible assembly. One of the main decisions was to build a rigid optical system which is aligned during the assembly by gluing the ROMs to the radiator and that fits into the tight available volume. Different parts of the conceptual design were integrated into a new prototype which aside from implementing custom mechanical structures allows an easy access and improved protection of optical components during test experiments.

A prior prototype with fused silica optics and highly segmented MCP-PMTs was tested during a beam time with a mixed hadron beam at CERN in May 2015. Chapter 6 presented the corresponding analysis which includes a laser calibration and several scans for different parameters like the beam angle of incidence or the beam momentum. Especially in case of the single photon resolution a good agreement between the collected data and Monte-Carlo predictions could be reached. During the 10 GeV/c angle scan a new lower limit for the single photon resolution of 5.68 mrad was set. In addition the prototype showed a  $\pi/p$  separation above  $5\sigma$  at 3 GeV/c on a single photon level.

Future testbeam campaigns are expected to further reduce the lower limit of the single photon resolution by using narrower beams or dedicated tracking of the traversing particles. In addition the measured number of photons has to be in agreement with Monte-Carlo simulations for any position on the radiator. The final  $\pi/K$  separation can only be shown with a full size prototype. However, if the single photon resolution and the photon yield are well understood all relevant parameters for the functionality of the detector are identified. En route to a fully equipped quadrant which can be mounted inside the  $\bar{P}$ ANDA detector several details have yet to be worked out. For example the concepts of the mechanical in-

tegration have to be transferred into a detailed design. In this connection it is required to have additional information on the readout system which is under development in parallel to this thesis work.

From a mechanical point of view the feasibility of reducing the number of ROMs per side from nine to eight should be evaluated. On the one hand this decreases the costs for the detector and clears space for a proper mounting, especially in case of the radiator and the MCP-PMTs which is beneficial for a safe operation. On the other hand such a setup reduces the number of photons per event. As the EDD will deliberately limit the detected number of photons this number can be manipulated by the choice of an optical filter which is more transparent towards higher wavelengths to not increase the chromatic error. However, this would cause a higher integrated anode charge on the MCP-PMTs. Taking into account recent measurements which indicate an acceptable quantum efficiency of the MCP-PMTs far above an integrated anode charge of  $5 \text{ C/cm}^2$  and changes regarding the integrated luminosity of  $\bar{\text{P}}\text{ANDA}$  due to a delayed SIS-300, this setup could have the potential to perform according to the demands for the anticipated  $\pi/K$  separation.

In the context of optical filters the green photocathode, whose quantum efficiency peaks at the visible green spectrum, seems like a promising substitute for the currently proposed system of a blue photocathode paired with a optical bandpass or edge filter. It is highly suggested to further investigate this option in terms of Monte-Carlo simulations but also regarding the lifetime of the photocathode.

The findings in connection with the quality of the optical components are essential for the technical design of an Endcap Disc DIRC detector inside  $\bar{\text{P}}\text{ANDA}$  and can hopefully encourage other groups which are either dealing with complex optical geometries or evaluating to use such for other detector systems. Furthermore the possibility of providing particle identification even on a single photon level shows the capability of this detector type and might be of interest for future applications as well.



## A Appendix

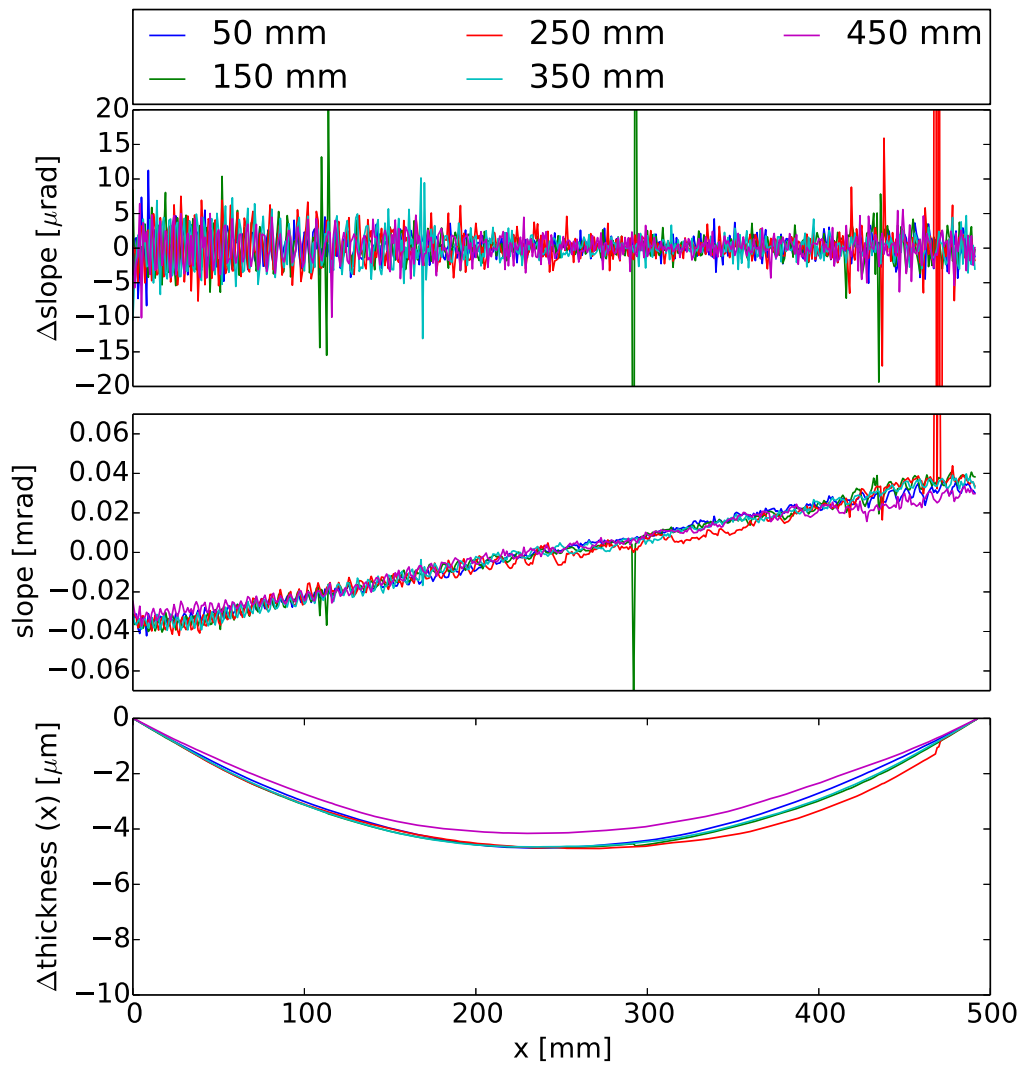


**Figure A.1:** Fine horizontal scan of the Nikon prototype radiator at different x positions as indicated in the legend. Data was obtained with the measuring setup facing the other side of the radiator as in figure 4.34.

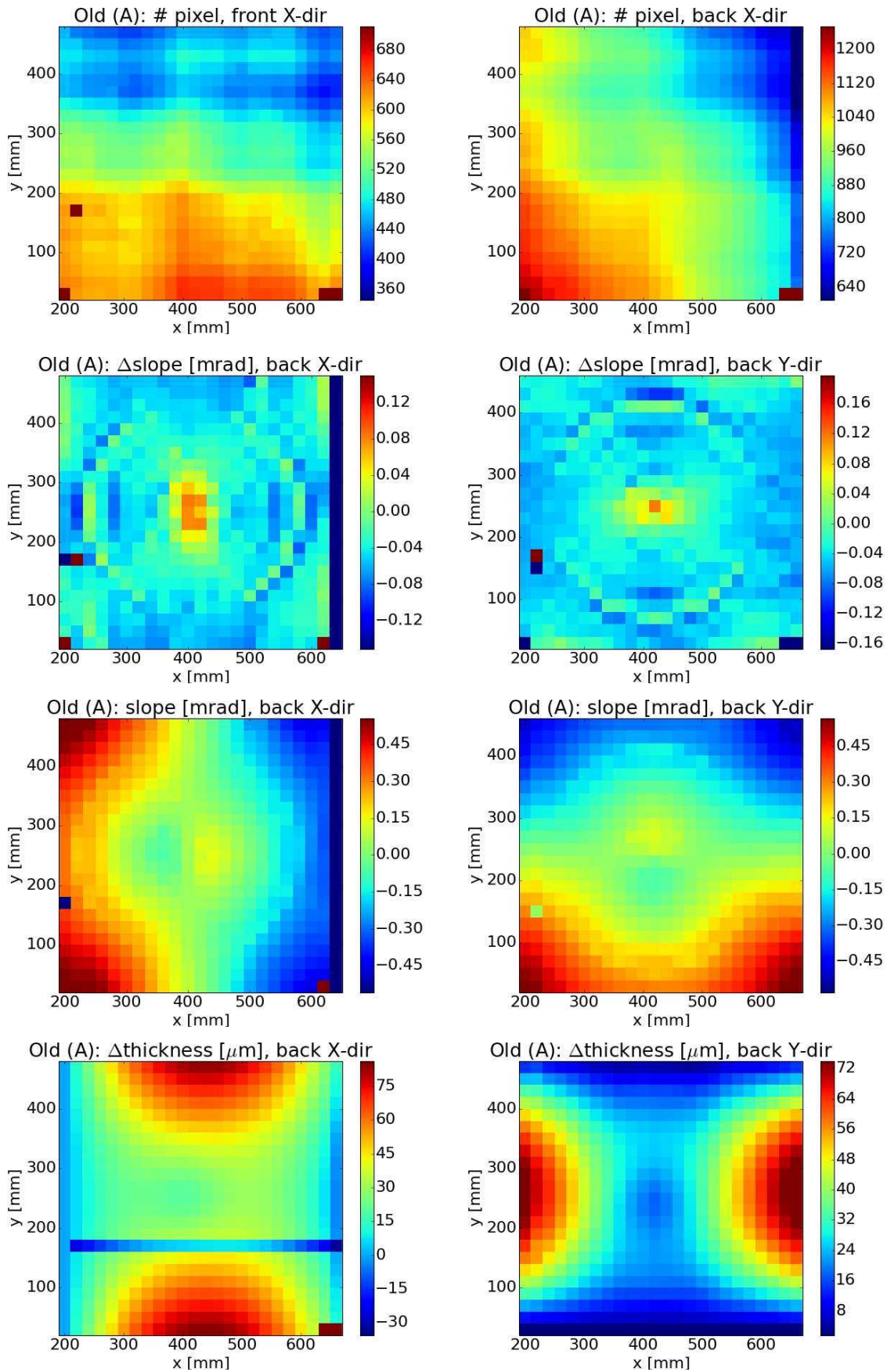


**Figure A.2:** In comparison to 4.29 the measurement was done facing the opposite side of the radiator. The propagation of the erroneous pixel measurement can be clearly followed in the subsequent plots.

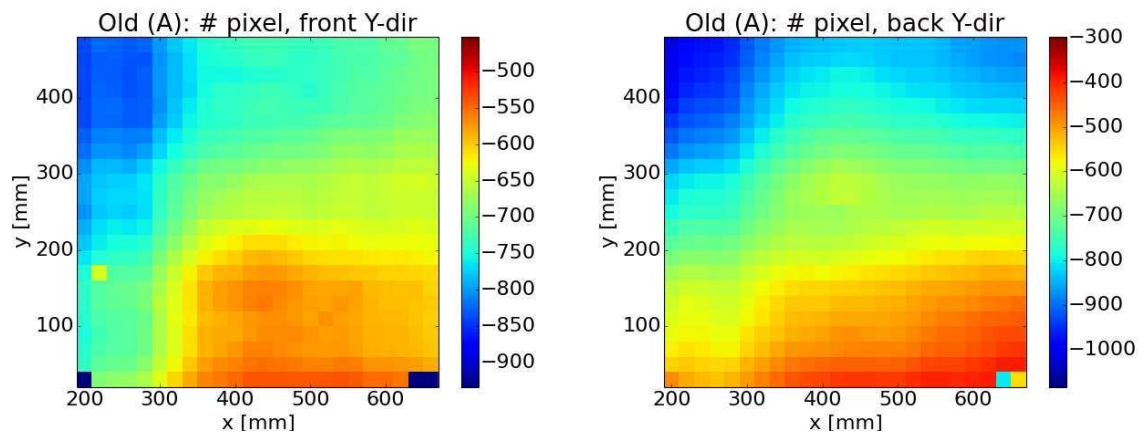


**Figure A.3:** Same plots as shown in the top row of figure A.2 but for the vertical positions of the reflections on the CCD-chip which is used as input for subsequent plots in the right column of figure A.2.

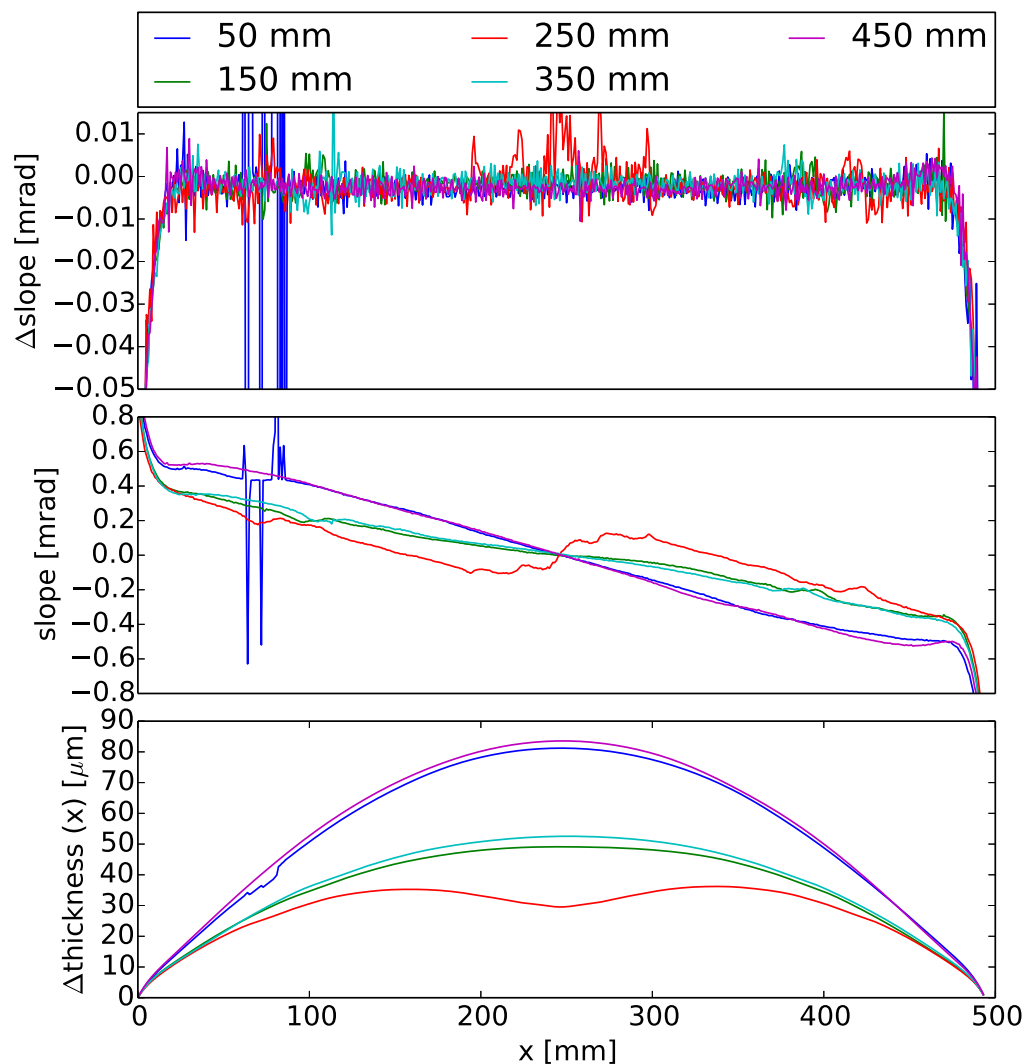


**Figure A.4:** Fine horizontal scan of the old prototype radiator at different y positions as indicated in the legend (compare figure 4.31).

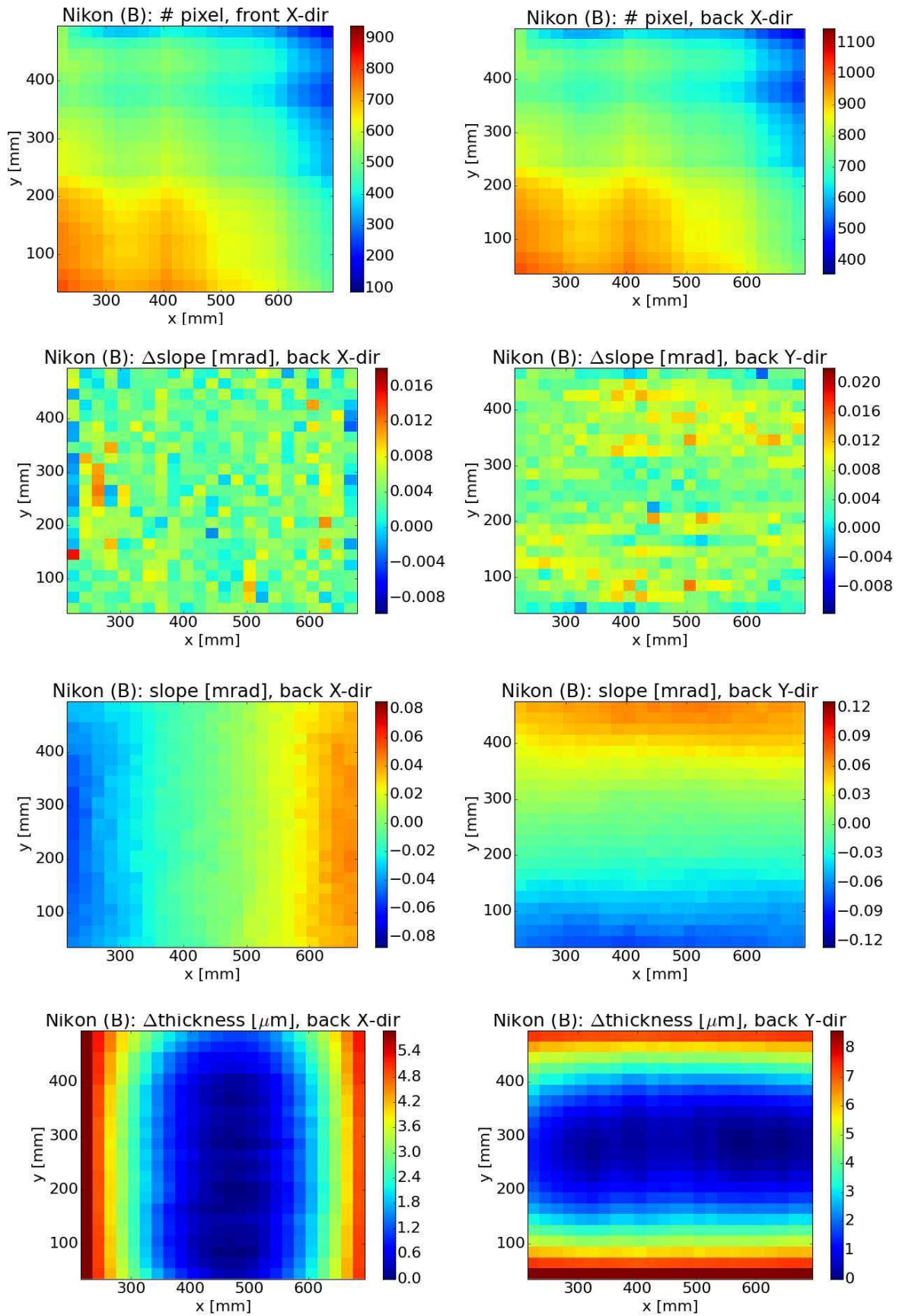


**Figure A.5:** In comparison to 4.32 the measurement was done facing the opposite side of the radiator.

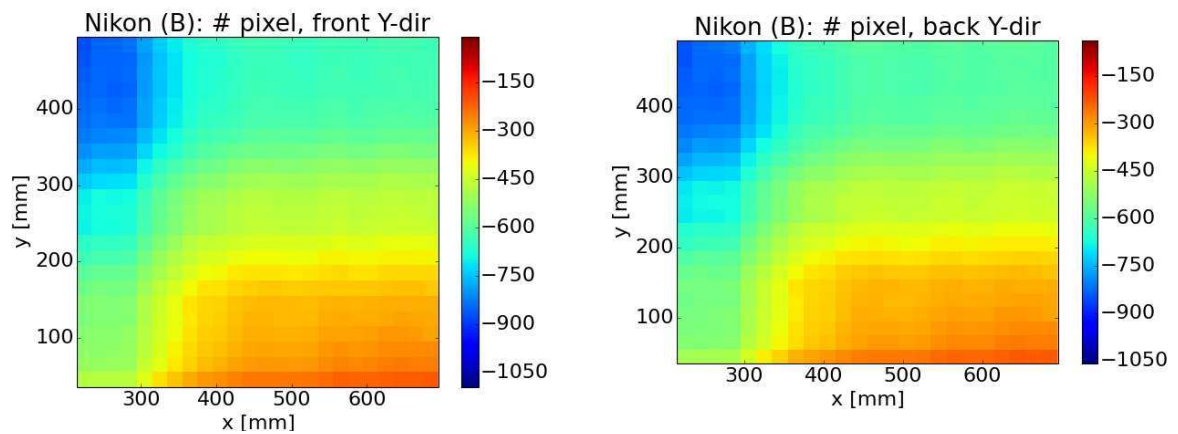


**Figure A.6:** Same plots as shown in the top row of figure A.5 but for the vertical positions of the reflections on the CCD-chip which is used as input for subsequent plots in the right column of figure A.5.

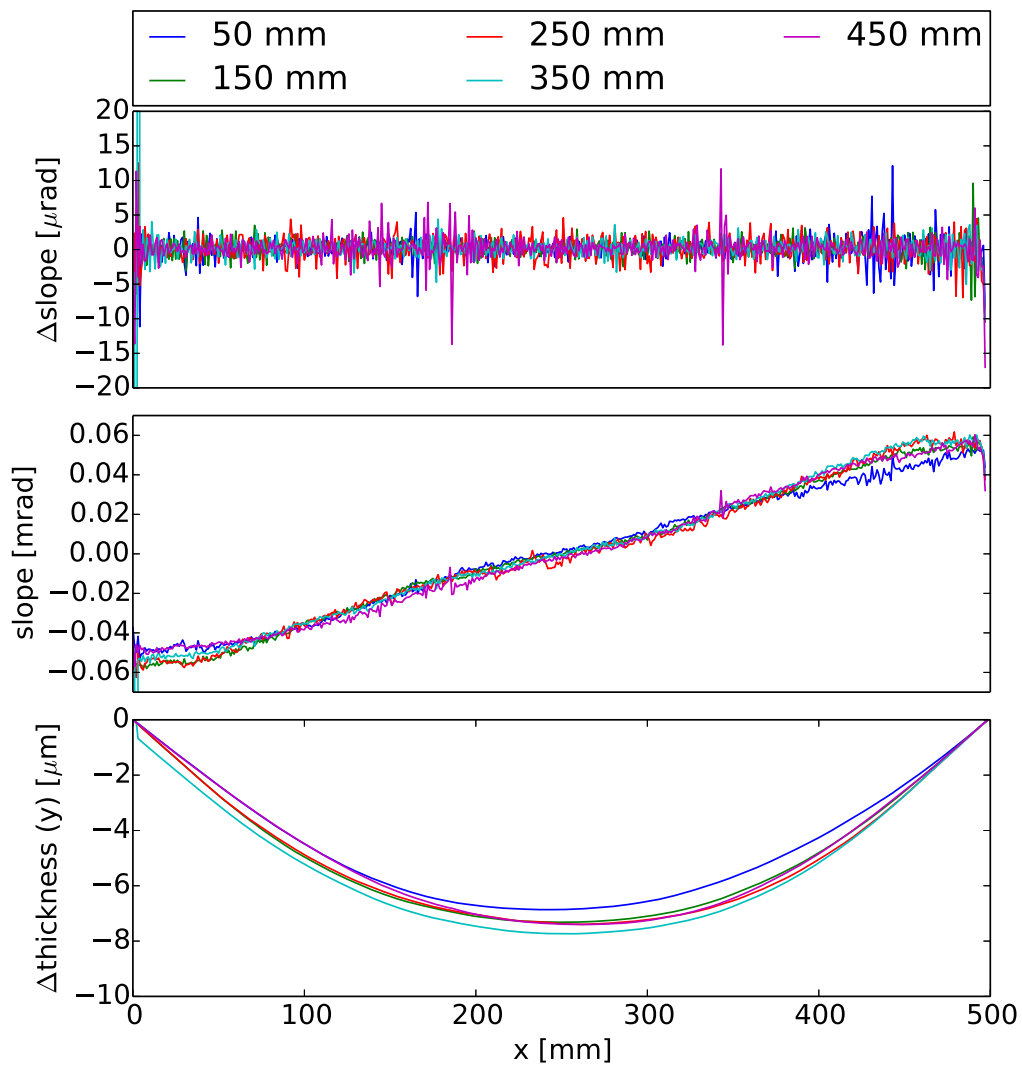


**Figure A.7:** Fine vertical scan of the Nikon prototype radiator at different x positions as indicated in the legend (compare figure 4.34).

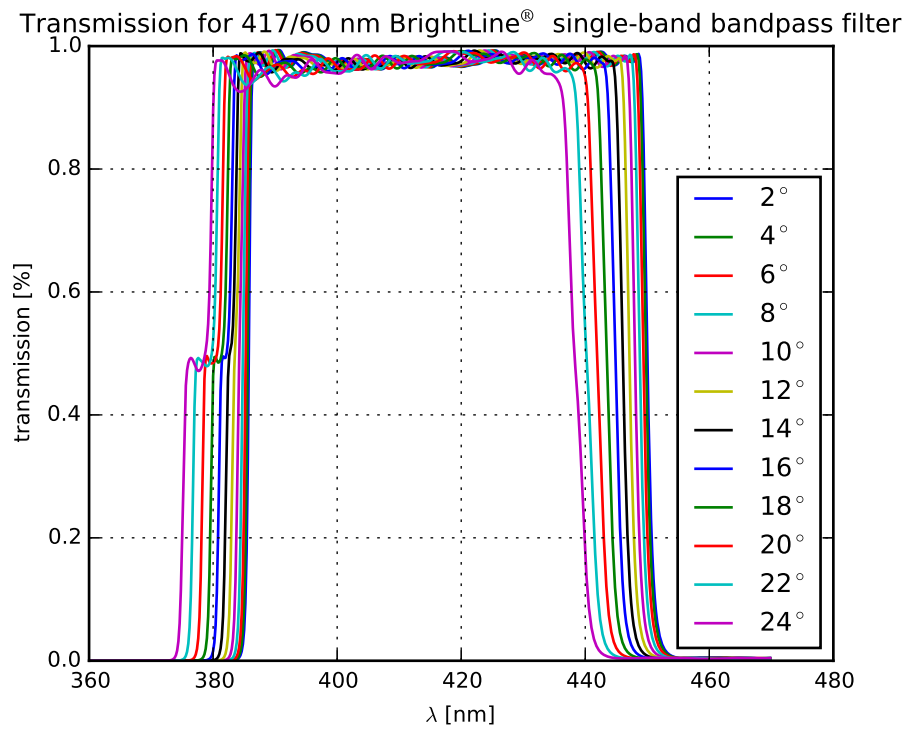


**Figure A.8:** Transmission for 417/60 nm BrightLine® single-band bandpass filter for angles of incidence between 2° and 24° degrees.

## List of Acronyms

- ALD** Atomic Layer Deposition
- AOI** Angle-Of-Incidence
- APPA** Atomic, Plasma Physics and Applications
- ASIC** Application-Specific Integrated Circuit
- BoPET** Biaxially-oriented PolyEthylene Terephthalate
- CAD** Computer-Aided Design
- CBM** the Compressed Baryonic Matter experiment
- CCD** Charge-Coupled Device
- CR** Collection Ring
- CTS** Central Trigger System
- DAQ** Data Acquisition
- DIRC** Detection of Internally Reflected Cherenkov light
- dSiPM** digital Silicon Photomultipliers
- DVCS** Deep Virtual Compton Scattering
- EDD** Endcap Disc DIRC
- EMC** ElectroMagnetic Calorimeter
- FAIR** Facility for Antiproton and Ion Research
- FDIRC** Focusing DIRC
- FEA** Finite Element Analysis
- FEE** Front-End Electronics
- FEL** Focusing Element
- FEM** Finite Element Method
- FS** Forward Spectrometer
- FSC** Forward Spectrometer Calorimeter
- GDA** Generalized Distribution Amplitude
- GEM** Gas Electron Multiplier
- GPD** Generalized Parton Distributions

**GSI** Gesellschaft für SchwerIonenforschung

**GUI** Graphical User Interface

**HEM** Hard Exclusive Meson production

**HESR** High Energy Storage Ring

**HL** High Luminosity

**HR** High Resolution

**HV** High Voltage

**HV-MAPS** High Voltage Monolithic Active Pixel Sensor

**LAAPD** Large Area Avalanche Photo Diode

**MaPMT** Multianode PhotoMultiplier Tube

**MC** Monte-Carlo

**MCP** MicroChannel Plate

**MCP-PMT** MicroChannel Plate PhotoMultiplier Tube

**MCS** Multi Coulomb Scattering

**MDT** Mini Drift Tube

**MP** Mounting Plate

**MVD** Micro Vertex Detector

**NBOHC** Non-Briding Oxygen Hole Center

**NIFS** NIkon Fused Silica

**NOA** Norland Optical Adhesive

**NuSTAR** Nuclear STructure, Astrophysics and Reactions

**ODC** Oxygen-Deficient Center

**PANDA** antiProton ANnihilation at DARMstadt

**PCB** Printed Circuit Board

**PID** Particle IDentification

**PiLas** Picosecond Laser

**PMT** PhotoMultiplier Tube

**PV** Peak-to-Valley

---

**PWO** lead tungstate

**QE** Quantum Efficiency

**QCD** Quantum ChromoDynamics

**QED** Quantum ElectroDynamics

**RESR** Recycled Experimental Storage Ring

**RH** ROM Housing

**RICH** Ring-Imaging CHerenkov

**RMS** Root Mean Square

**ROM** ReadOut Module

**SC** Stabilizing Cross

**SFT** Silicone Fiber Tracker

**SODA** Synchronization Of Data Acquisition

**STT** Straw Tube Tracker

**TCC** Threshold Cherenkov Counter

**THM** Technische Hochschule Mittelhessen

**TIFF** Tagged Image File Format

**TOF** Time Of Flight

**TOFPET** Time-Of-Flight Positron Electron Tomography

**TOP** Time-Of-Propagation

**TORCH** Time Of internally Reflected CHerenkov light

**TRB** Trigger and Readout Board

**TS** Target Spectrometer

**TTV** Total Thickness Variation

**UV** UltraViolet

**VPTT** Vacuum Photo TeTrode



## List of Figures

1.1	Kaon phase space at open charm threshold . . . . .	2
2.1	FAIR and GSI . . . . .	6
2.2	The $\bar{P}$ ANDA experiment . . . . .	7
2.3	Micro Vertex Detector and Straw Tube Tracker . . . . .	8
2.4	Gas Electron Multiplier detector . . . . .	9
2.5	Magnets and Muon Detection . . . . .	10
2.6	The Barrel and Forward Endcap EMC . . . . .	12
2.7	Overview of hadronic states . . . . .	14
2.8	Handbag diagrams of GPDs and GDAs . . . . .	15
3.1	PID topology . . . . .	17
3.2	PID utilizing $dE/dx$ vs. $E$ . . . . .	19
3.3	Schematic drawing of the Cherenkov cone . . . . .	20
3.4	Plot of $\theta_c(p)$ including dispersion . . . . .	21
3.5	Plot of $\theta_c(p)$ for different refractive indices . . . . .	23
3.6	RICH detector types . . . . .	24
3.7	DIRC detector types . . . . .	25
3.8	Barrel DIRC example . . . . .	25
3.9	MCP-PMT working principle . . . . .	27
3.10	Endcap Disc DIRC overview . . . . .	29
4.1	Extrapolated energy deposit in the optical system . . . . .	32
4.2	Typical defects in fused silica . . . . .	33
4.3	Monochromator setup for NIFS samples . . . . .	34
4.4	NIFS transmittance before irradiation . . . . .	36
4.5	Influence of cleaning on transmittance measurement . . . . .	36
4.6	Normalized transmittance loss after irradiation with 1000 Gy . . . . .	37
4.7	Absorption length after irradiation with 1000 Gy . . . . .	38
4.8	Recovery of transmittance loss after irradiation with 1000 Gy for NIFS-V . . . . .	39
4.9	Recovery of absorption length after irradiation with 1000 Gy for NIFS-V . . . . .	39
4.10	Recovery of transmittance loss after irradiation with 1000 Gy for NIFS-V' . . . . .	40
4.11	Recovery of absorption length after irradiation with 1000 Gy for NIFS-V' . . . . .	40
4.12	Relaxation plot after irradiation with 1000 Gy . . . . .	41
4.13	Normalized transmittance loss after irradiation with 5000 Gy . . . . .	42
4.14	Absorption length after irradiation with 5000 Gy . . . . .	42
4.15	Recovery of transmittance loss after irradiation with 5000 Gy for NIFS-V . . . . .	43
4.16	Recovery of transmittance loss after irradiation with 5000 Gy for NIFS-V' . . . . .	43
4.17	Oxygen-deficient center and germanium impurity in fused silica . . . . .	44
4.18	Relaxation plot after irradiation with 5000 Gy . . . . .	45

4.19	Technical drawing of the radiator . . . . .	46
4.20	Picture of a Disc DIRC radiator . . . . .	47
4.21	Schematic setup for transmittance and reflectance measurements . . . . .	49
4.22	Fresnel losses for a transition between vacuum and quartz . . . . .	50
4.23	Fresnel losses for a transition between quartz and vacuum . . . . .	51
4.24	Illustration of wave form error and roughness . . . . .	53
4.25	Total transmittance depending on the surface roughness and absorption length . . . . .	54
4.26	Total transmittance for different path lengths and wavelengths . . . . .	55
4.27	Schematic setup for the profile measurement . . . . .	56
4.28	Profile scan of old prototype radiator for different step sizes . . . . .	60
4.29	Profile scan of old prototype radiator . . . . .	61
4.30	Total thickness variation of the old prototype radiator . . . . .	63
4.31	Fine vertical scan of the old prototype radiator . . . . .	63
4.32	Profile scan of Nikon prototype radiator . . . . .	65
4.33	Total thickness variation of the Nikon prototype radiator . . . . .	66
4.34	Fine horizontal scan of the Nikon prototype radiator . . . . .	66
4.35	Slope error of the Nikon prototype radiator . . . . .	67
4.36	Systematic error of the profile measurement . . . . .	68
4.37	Example of the surface profile impact . . . . .	69
4.38	Transport error for different radiator parameters . . . . .	70
4.39	Total thickness variation for different radiator parameters . . . . .	71
4.40	Different FEL types . . . . .	72
4.41	Technical drawing of the prism . . . . .	73
4.42	Geometrical smearing due to FEL width . . . . .	73
4.43	Technical drawing of the Focusing Element (FEL) . . . . .	74
4.44	Setup quality measurement (SiPM FEL) . . . . .	76
4.45	Calibration of imaging for FEL scan . . . . .	77
4.46	Conversion for coupling into prism . . . . .	77
4.47	Data taking for FEL quality measurements . . . . .	78
4.48	Angle shift for prism and laser . . . . .	79
4.49	Quality measurement (SiPM FEL) . . . . .	80
4.50	Setup quality measurement (MCP-PMT FEL) . . . . .	81
4.51	Long time exposure of FEL . . . . .	81
4.52	Drawing of FEL gluing device . . . . .	83
4.53	FEL gluing procedure . . . . .	83
4.54	Pictures of FEL glue joints . . . . .	84
4.55	FEL-prism pair scan . . . . .	85
4.56	Comparison of FEL performance at 21° . . . . .	85
4.57	Comparison of FEL performance at 26° and 31° . . . . .	86

---

4.58	Comparison of FEL performance at 36° and 41° . . . . .	87
4.59	Reflectivity of coated mirror . . . . .	88
4.60	Quality measurement (MCP-PMT FELs) . . . . .	89
4.61	Realtive quality measurement (MCP-PMT FELs) . . . . .	90
4.62	Transmission for 355 nm EdgeBasic™ long-pass edge filter . . . . .	91
4.63	Transmission for 375/110 nm BrightLine® single-band bandpass filter . . . . .	92
4.64	Transmission for different filter and photocathode options . . . . .	93
4.65	Chromatic error for different filter and photocathode options . . . . .	93
4.66	Overview optical grease . . . . .	95
4.67	Setup for optical pad production . . . . .	96
4.68	Refraction indices for NIFS, NOA-61 and Epotek 301-2 . . . . .	97
5.1	Constraining distances to surrounding detectors . . . . .	102
5.2	Large-scale components . . . . .	103
5.3	Endcap EMC support . . . . .	104
5.4	Profile options for the stabilizing cross . . . . .	105
5.5	Cable tray cross section . . . . .	107
5.6	Endcap cable trays . . . . .	108
5.7	Schematic drawing of assembly setup for radiator/prism joint . . . . .	109
5.8	Assembly setup and support plate . . . . .	110
5.9	Allowed prism lengths . . . . .	111
5.10	Assembly overview . . . . .	113
5.11	FEM analyses for different quadrant configurations . . . . .	114
5.12	FEM analyses for additional ROM fixation . . . . .	115
5.13	FEM analyses for a larger radiator . . . . .	116
5.14	CAD picture of the 2016 prototype . . . . .	118
5.15	Pictures of the 2016 prototype . . . . .	119
5.16	ROMs for the 2016 prototype . . . . .	120
6.1	Experimental setup T9 beam line . . . . .	123
6.2	Testbeam setup 2015 (upstream view) . . . . .	124
6.3	Close view of coupled ROMs . . . . .	124
6.4	Setup of ROMs . . . . .	125
6.5	Testbeam DAQ scheme . . . . .	126
6.6	Calibration of ROM . . . . .	127
6.7	Testbeam setups . . . . .	128
6.8	Timing example of laser run . . . . .	129
6.9	Relative timing for laser run . . . . .	130
6.10	Relative shifted timing for laser run . . . . .	130
6.11	Relative timing for different laser runs . . . . .	131
6.12	Calibration of leading edge timing . . . . .	133

6.13	Time cuts and background reduction . . . . .	134
6.14	Time resolution for different channels . . . . .	135
6.15	Data quality for different selection methods . . . . .	136
6.16	Cherenkov photon distribution with and without MCP-TOF . . . . .	137
6.17	HV-Scan and photon yield . . . . .	138
6.18	Flow diagram for data selection . . . . .	139
6.19	Momentum scan . . . . .	141
6.20	Cherenkov photon distribution for PHOTONIS A at 10 GeV/c . . . . .	142
6.21	Cherenkov photon distribution for PHOTONIS C at 10 GeV/c . . . . .	143
6.22	Cherenkov photon distribution for the Hamamatsu at 10 GeV/c . . . . .	143
6.23	Beam spot dependency of the single photon resolution . . . . .	144
6.24	10 GeV/c angle scan overview . . . . .	145
6.25	Comparison of the resolution with and without MCP-TOF . . . . .	146
6.26	2-photon resolution at 10 GeV/c . . . . .	147
6.27	2-photon resolution overview for the 10 GeV/c angle scan . . . . .	148
6.28	Cherenkov photon distribution for PHOTONIS C at 5 GeV/c . . . . .	150
6.29	Cherenkov photon distribution for Hamamatsu at 5 GeV/c . . . . .	150
6.30	Cherenkov photon distribution for the PHOTONIS C at 3 GeV/c . . . . .	151
6.31	Cherenkov photon distribution for Hamamatsu at 3 GeV/c . . . . .	152
6.32	3 GeV/c angle scan overview . . . . .	153
A.1	Fine vertical scan of the Nikon prototype radiator (opposite side) . . . . .	159
A.2	Profile scan of old prototype radiator (opposite side) . . . . .	160
A.3	Vertical positions of measured reflections off the old prototype radiator . . . . .	161
A.4	Fine horizontal scan of the old prototype radiator . . . . .	161
A.5	Profile scan of Nikon prototype radiator (opposite side) . . . . .	162
A.6	Vertical positions of measured reflections off the Nikon prototype radiator . . . . .	163
A.7	Fine vertical scan of the Nikon prototype radiator . . . . .	163
A.8	Transmission of 417/60 nm BrightLine <sup>®</sup> single-band bandpass filter . . . . .	164

## List of Tables

4.1	Summary of requirements for optical components . . . . .	31
4.2	Overview of available NIFS samples . . . . .	35
4.3	Surface specifications of the radiator . . . . .	47
4.4	Specifications and inspection results for the Nikon prototype radiator . . . . .	64
4.5	Surface specifications of the prism . . . . .	73
4.6	Surface specifications of the FEL . . . . .	75
4.7	FEL tolerances . . . . .	75
4.8	Chromatic error for different filter and photocathode options . . . . .	94
4.9	Summary of the optical system . . . . .	98
5.1	Cabling overview . . . . .	106
5.2	Available space for different EDD configurations . . . . .	117
6.1	Summary of measurements . . . . .	137
6.2	10 GeV/c angle scan overview . . . . .	149
6.3	3 GeV/c angle scan overview . . . . .	154



## Bibliography

- [Ada05] I. Adam et al., *The DIRC particle identification system for the BaBar experiment*, Nucl. Instr. Meth. Phys. Res. **A 538** (2005) 281-357 [25](#), [48](#), [97](#), [105](#)
- [Alb15] M. Albrecht et al., *The Forward Endcap of the Electromagnetic Calorimeter for the PANDA Detector at FAIR*, JPCS **587** (2015) 012050 [12](#)
- [All06] J. Allison et al., *Geant4 developments and applications*, IEEE Trans. Nucl. Sci. **53** No. 1 (2006) 270-278 [123](#)
- [And12] A. Andronica, J.P. Wessels, *Transition radiation detectors*, Nucl. Instr. Meth. Phys. Res. **A 666** (2012) 130-147 [22](#)
- [APMEpi] APM Technica, *APM Epicol 348990*, data sheet, <http://www.apm-technica.com> [82](#), [85](#), [97](#)
- [Ava75] A.L. Avakian, G.M. Garibian, C. Yang, *On the optimal choice of the laminar medium substance for ultrarelativistic particle transition radiation detectors*, Nucl. Instr. Meth. **128** (1975) 601-602 [22](#)
- [Bar07] R. Bär et al., *The new FAIR accelerator complex at GSI* proceedings of ICALEPCS 2007, Knoxville, TN (2007) [1](#), [5](#)
- [BarTDR] The PANDA Collaboration, *Technical Design Report for the: PANDA Barrel DIRC*, technical design report, to be published [11](#), [49](#), [71](#), [105](#)
- [BC634] Saint-Gobain Ceramics & Plastics, Inc., *Detector Assembly Materials*, data sheet, <http://www.crystals.saint-gobain.com> [96](#)
- [Bec63] P. Beckmann, A. Spizzichino, *The Scattering of Electromagnetic Waves from Rough Surfaces*, 1st edition, Pergamon press (1963) [54](#)
- [Blb15] K. Beloborodov, *The Forward Rich Project at PANDA*, presentation, DIRC2015: Workshop on fast Cherenkov detectors (2015) [11](#), [23](#)
- [BlS15] S. Belostotski, *Status of FTOF wall detectors*, presentation, Plenary Session at PANDA CM LV. (2015) [11](#)
- [Brn05] T. Barnes et al., *Higher Charmonia*, Phys. Rev. **D 72** (2005) 054026
- [Che34] P. Cherenkov, *Visible emission of clean liquids by action of gamma radiation*, Dokl. Akad. Nauk. SSSR **2** (1934) 451 [20](#)

- [Cho03] S.-K. Choi et al., *Observation of a Narrow Charmoniumlike State in Exclusive  $B^\pm \rightarrow K^\pm \pi^+ \pi^- J/\Psi$  Decays*,  
Phys. Rev. Lett. **91** (2003) 262001 [14](#)
- [CML6350] Cargille Labs, *Fused Silica Matching Liquid Code 06350*,  
data sheet, <http://www.cargille.com/CODE-06350.pdf> [76](#), [95](#), [97](#)
- [Coh00] J. Cohen-Tanugi et al., *Study of the Internal Reflection Coefficient of DIRC bars as a Function of Quartz Surface Pollution*,  
Internal Group Note, BaBar Dirc Note **131** (2000) [102](#)
- [Coh03] J. Cohen-Tanugi et al., *Optical properties of the DIRC fused silica Cherenkov radiator*,  
Nucl. Instr. Meth. Phys. Res. **A 515** (2003) 680-700 [33](#), [34](#), [48](#), [55](#)
- [COG607] Cargille Labs, *Optical Gel Code 0607*,  
data sheet, <http://www.cargille.com/og0607.PDF> [95](#), [97](#), [125](#)
- [Cor14] Corning, Inc., *Corning<sup>®</sup> HPFS<sup>®</sup> 7979, 7980, 8655 Fused Silica*,  
data sheet, <https://www.corning.com/media/worldwide/csm/documents/5bf092438c5546dfa9b08e423348317b.pdf> [33](#)
- [Cow11] E. N. Cowie et al., *The Focusing Disc DIRC for the PANDA experiment at FAIR*,  
JPCS **312** (2011) 052011 [72](#)
- [Coy94] P. Coyle et al., *The DIRC counter: a new type of particle identification device for B factories*,  
Nucl. Instr. Meth. Phys. Res. **A 343** (1994) 292-299 [1](#), [24](#)
- [Dey15] B. Deya et al., *Design and performance of the focusing DIRC detector*,  
Nucl. Instr. Meth. Phys. Res. **A 775** (2015) 112-131 [26](#)
- [Die03] M. Diehl, *Generalized Parton Distributions*,  
arXiv:hep-ph/0307382 (2003) [15](#)
- [Dij14] M. W. U. van Dijk et al., *TORCH – a Cherenkov based time-of-flight detector*,  
Nucl. Instr. Meth. Phys. Res. **A 766** (2014) 118-122 [26](#)
- [Dur09] M. Düren et al., *The PANDA time-of-propagation disc DIRC*,  
J. Instrum. **4** (2009) C12013 [26](#)
- [Dur12] M. Düren et al., *The PANDA 3D Disc DIRC*,  
J. Instrum. **7** (2012) C01059 [26](#), [72](#)
- [Dzh14] R. Dzhygadlo et al., *Simulation and reconstruction of the PANDA Barrel DIRC*,  
Nucl. Instr. Meth. Phys. Res. **A 766** (2014) 263-266 [26](#)

- [EJ550] Eljen Technology, *Silicone grease EJ-550, EJ-552*, data sheet, [http://www.eljentechnology.com/images/products/data\\_sheets/EJ-550\\_EJ-552.pdf](http://www.eljentechnology.com/images/products/data_sheets/EJ-550_EJ-552.pdf) 95
- [EMCTDR] The PANDA Collaboration, *Technical Design Report for: PANDA Electromagnetic Calorimeter*, technical design report (2008) 12, 101, 103, 105
- [EPO301] Epoxy Technology, *EPO-TEK<sup>®</sup> 301-2*, data sheet, [http://www.epotek.com/site/administrator/components/com\\_products/assets/files/Style\\_Uploads/301-2RevXII.pdf](http://www.epotek.com/site/administrator/components/com_products/assets/files/Style_Uploads/301-2RevXII.pdf) 97, 110
- [Etz16] E. Etzelmüller et al., *Test and developments of the PANDA Endcap Disc DIRC*, J. Instrum. **11** (2016) C04014 35
- [FAIR09] FAIR GmbH, *The Modularized Start Version*, green paper (2009) 5
- [FAIRweb] FAIR GmbH, *Facility for Antiproton and Ion Research*, website, <http://www.fair-center.eu> 6
- [Fie17] J. Fiedler, Berliner Glas, *private communication*, January 2017 88
- [Foh07] K. Föhl et al., *The DIRC detectors of the PANDA experiment at FAIR*, Nucl. Instr. and Meth. **A 595** (2008) 88-91 72
- [Foh09] K. Föhl et al., *The focussing light guide disc DIRC design*, J. Instrum. **4** (2009) C11026 26, 91, 101
- [Foh11] K. Föhl et al., *The WASA focussing light guide disc DIRC*, J. Instrum. **7** (2011) C01002 57, 72
- [Fra37] I. Frank, I. Tamm, *Coherent visible radiation of fast electrons passing through matter*, Dokl. Akad. Nauk. **14** (1937) 109 20, 21
- [Fri11] B. Friman, C. Höhne, J. Knoll, S. Leupold, J. Randrup, R. Rapp, P. Senger, *The CBM Physics Book - Compressed Baryonic Matter in Laboratory Experiments*, 1st Edition, Lecture Notes in Physics, Vol. 814, Springer (2011) 5
- [FSCTDR] The PANDA Collaboration, *Technical Design Report for the PANDA Forward Spectrometer Calorimeter*, technical design report (2016) 13
- [Fur14] D. Furumura, K. Inami, *Status of the optical cookie studies* presentation, TOP Session at 17th Belle II General Meeting (2014) 96

- [Gat15] L. Gatignon, CERN, *private communication*,  
November 2015 140
- [Gin46] V. L. Ginzburg, I. Frank, *Theory of transition radiation*,  
Zh. Eksp. Teor. Fiz. **16** (1946) 15 22
- [Gol59] P. Goldsmith, J. V. Jelley, *Optical transition radiation from protons entering metal surfaces*,  
Phil. Mag. **4** (1959) 836-844 22
- [Gri86] D.L. Griscom, *Nature Of Defects And Defect Generation In Optical Glasses*,  
Proc. SPIE **0541** (1985) 38; 34
- [Gru16] L. Gruber et al., *Barrel time-of-flight detector for the PANDA experiment at FAIR*,  
Nucl. Instr. and Meth. **A 824** (2016) 104-105 11
- [Guz93] M. Guzzi et al., *Neutron irradiation effects in amorphous SiO<sub>2</sub>: optical absorption and electron paramagnetic resonance*,  
J. Phys. Condens. Matter **5** (1993) 8105 34
- [Hae12] Y. Haemisch et al., *Fully Digital Arrays of Silicon Photomultipliers (dSiPM) - a Scalable Alternative to Vacuum Photomultiplier Tubes (PMT)*,  
Phys Procedia **37** (2012) 1546 27
- [Her16] Heraeus, GmbH, *Heraeus Spectrosil<sup>®</sup> 2000*,  
data sheet, [http://heraeus-quarzglas.de/media/webmedia\\_local/downloads/broren\\_mo/Spectrosil\\_syntheticfusedsilica.pdf](http://heraeus-quarzglas.de/media/webmedia_local/downloads/broren_mo/Spectrosil_syntheticfusedsilica.pdf) 33, 60
- [Hir15] S. Hirose et al., *Development of the micro-channel plate photomultiplier for the Belle II time-of-propagation counter*,  
Nucl. Instr. Meth. Phys. Res. **A 787** (2015) 293-296 28
- [Hok11] M. Hoek et al., *Tailoring the radiation hardness of fused silica*,  
Nucl. Instr. Meth. Phys. Res. **A 639** (2011) 227-230 34, 35, 37
- [Hol11] R. Hohler, *Prototyp-Radiatoren eines Barrel-DIRC für das PANDA -Experiment*,  
PhD thesis, Goethe-Universität Frankfurt am Main (2011) 32, 33, 49
- [Hon14] C. Höhne et al., *The CBM-RICH detector*,  
J. Instrum. **11** (2014) C05016 23
- [Ina14] K. Inami et al., *TOP counter for particle identification at the Belle II experiment*,  
Nucl. Instr. Meth. Phys. Res. **A 766** (2014) 5-8 26, 48, 105
- [Jin11] T. Jinno et al., *Lifetime-Extended MCP-PMT*,  
Nucl. Instr. Meth. Phys. Res. **A 629** (2011) 111-117 28

- [Kal10] Y. S. Kalashnikova et al., *Quark and Meson Degrees of Freedom in the X(3872) Charmonium*,  
Phys. Atom. Nucl. **73** (2010) 1592-1611 [14](#)
- [Kam96] T. Kamae et al., *Focussing DIRC - A new compact Cherenkov ring imaging device*,  
Nucl. Instr. Meth. Phys. Res. **A 382** (1996) 430-440 [1](#), [26](#)
- [Kon10] I. Konorov et al., *SODA: Time distribution system for the PANDA experiment*,  
IEEE Nucl. Sci. Symp. Conf. Rec. (2009) 1863 [13](#)
- [Kra15] D. Krambich, Justus-Liebig-Universität Gießen *private communication*,  
February 2015 [35](#)
- [Lhm09] I. Lehmann, *Physics Programme of PANDA at FAIR*,  
arXiv:hep-ph/0909.4237 (2009) [14](#)
- [Lhm15] A. Lehmann, *CERN MCP-TOF results*,  
presentation, PID Cherenkov Session at PANDA CM LV. (2015) [131](#)
- [Lhm16a] A. Lehmann et al., *Lifetime of MCP-PMTs*,  
J. Instrum. **11** (2016) C05009 [28](#)
- [Lhm16b] A. Lehmann, Friedrich-Alexander-Universität Erlangen-Nürnberg, *private communication*,  
July 2016 [132](#)
- [Lhr06] A. Lehrach et al., *Beam Performance and Luminosity Limitations in the High-Energy Storage Ring (HESR)*,  
Nucl. Instr. and Meth. **A 561** (2006) 289-296 [6](#)
- [LumTDR] The PANDA Collaboration, *Technical Design Report for the PANDA Luminosity Detector*,  
technical design report (preliminary version) (2016) [13](#)
- [MagTDR] The PANDA Collaboration, *Technical Design Report for the PANDA Solenoid and Dipole Spectrometer Magnets*,  
technical design report (2009) [10](#)
- [Mai11] R. Maier et al., *The High-Energy Storage Ring (HESR)*,  
proceedings PAC'11, New York, NY (2011) 2104 [6](#)
- [Mer09] O. Merle, *Development of Reconstruction Methods and Algorithms for the PANDA Disc DIRC*,  
diploma thesis, Justus-Liebig-Universität Gießen (2009) [26](#), [30](#)
- [Mer14a] O. Merle, *Development of an Endcap DIRC for PANDA*,  
Nucl. Instr. Meth. Phys. Res. **A 766** (2014) 96-100 [72](#), [101](#)

- [Mer14b] O. Merle, *Development, design and optimization of a novel Endcap DIRC for PANDA*, PhD thesis, Justus-Liebig-Universität Gießen (2014) [1](#), [2](#), [30](#), [32](#), [64](#), [69](#), [74](#), [94](#), [135](#), [152](#)
- [Mer14c] O. Merle, Justus-Liebig-Universität Gießen *private communication*, April 2014 [46](#)
- [Mrd07] A. A. Maradudin, *Light Scattering and Nanoscale Surface Roughness*, 1st edition, Springer (2007) [53](#)
- [Mrs97] C. D. Marshall et al., *Induced optical absorption in gamma, neutron and ultraviolet irradiated fused quartz and silica*, J. Non-Cryst. Solids **212** (1997) 59-73 [33](#)
- [Muh13] D. Mühlheim, *Design und Aufbau eines Teststandes für den PANDA 3D Disc DIRC*, master thesis, Justus-Liebig-Universität Gießen (2009) [121](#)
- [MuoTDR] The PANDA Collaboration, *Technical Design Report for PANDA Muon System*, technical design report (2012) [11](#)
- [MVDTR] The PANDA Collaboration, *Technical Design Report for: PANDA Micro Vertex Detector*, technical design report (2011) [8](#)
- [Nei13] A. Neiser et al., *TRB3: A 264 Channel High Precision TDC Platform and Its Applications*, J. Instrum. **8** (2013) C12043 [123](#), [125](#)
- [NIFS] Nikon Corporation, *Nikon NIFS Series Synthetic Silica Glass*, data sheet, <http://www.nikon.com/products/glass/lineup/materials/sio2/pdf/sio2-e.pdf> [35](#), [97](#)
- [Noa61] Norland Products, *Norland Optical Adhesive 61*, data sheet, <https://www.norlandprod.com/adhesives/noa61pg2.html> [82](#), [85](#), [94](#), [97](#), [110](#)
- [NuS12] The NUSTAR Collaboration, *NUSTAR Progress Report*, progress report (2012) [5](#)
- [PAN09] The PANDA Collaboration, *Physics Performance Report for PANDA: Strong Interaction Studies with Antiprotons*, arXiv:hep-ph/0903.3905 (2009) [1](#), [5](#), [15](#)
- [PDG14] K.A. Olive et al. (Particle Data Group), *Particle Physics Booklet*, Chin. Phys. C **38** (2014) 090001 [102](#)
- [Pes13] R. Pestotnika et al., *Aerogel RICH for forward PID at Belle II*, Nucl. Instr. Meth. Phys. Res. A **732** (2013) 371-374 [23](#)

- [PHO16] PHOTONIS, *Hi-QE Photocathode Technology*, brochure, <https://www.photonis.com/uploads/datasheet/pd/Hi-QE-Brochure.pdf> 92
- [Pin16] S. Duarte Pinto, PHOTONIS, *private communication*, January 2016 93
- [Rat99] B. N. Ratcliff, S. Spanier, *DIRC dreams: research directions for the next generation of internally reflected imaging counters*, Nucl. Instr. Meth. Phys. Res. A **433** (1999) 456-463 25
- [Rie16] J. Rieke et al., *Resolution changes of MCP-PMTs in magnetic fields*, J. Instrum. **11** (2016) C05002 125
- [Rie17] J. Rieke, *Design of a compact photon detection system for the PANDA Disc DIRC*, PhD thesis, Justus-Liebig-Universität Gießen, in preparation 28, 31
- [Rol13] M. D. Rolo et al., *TOFPET ASIC for PET applications*, J. Instrum. **8** (2013) C02050 28, 154
- [RT601] Wacker Chemie AG, *ELASTOSIL® RT 601 A/B*, data sheet, <http://www.wacker.com> 96
- [RTV615] Momentive Performance Materials Inc., *RTV615*, data sheet, <http://www.momentive.com/> 96
- [San15] S. Sandilya, *Status of alignment and gluing*, presentation, TOP Session at 20th Belle II General Meeting (2015) 112
- [Sau16] F. Sauli, *The gas electron multiplier (GEM): Operating principles and applications*, Nucl. Instr. and Meth. A **805** (2016) 2-24 9
- [Sel71] W. Sellmeier, *Zur Erklärung der abnormen Farbenfolge im Spectrum einiger Substanzen*, Annalen der Physik und Chemie **219** (1871) 272-282 20
- [Semweb] Semrock, Inc, *Optical Filter Product Families*, website, <https://www.semrock.com/product-families.aspx> 91, 92
- [Shi14] T. Shibata et al., *Ring imaging Cherenkov counter of HERMES for pion, kaon, proton and anti-proton identification*, Nucl. Instr. Meth. Phys. Res. A **766** (2014) 267-269 23
- [Sie12] P. Sievers et al., *Concept for the Antiproton Production Target at FAIR* proceedings IPAC2012, New Orleans, LA (2012) 2570 5
- [Sig06] P. Sigmund, *Particle Penetration and Radiation Effects*, Springer Series in Solid State Sciences 151, Springer (2006) 18

- [Sku05] L. Skuja et al., *Defects in oxide glasses*,  
Phys. Stat. Sol. (c) **2**, No. 1 (2005) 15-24 37
- [SmM16] M. Schmidt, Justus-Liebig-Universität Gießen *private communication*,  
March 2016 123
- [SmR06] R. Schmidt, *Computer Simulation of a DISC-DIRC Cherenkov Detector for PANDA*,  
diploma thesis, Justus-Liebig-Universität Gießen (2006) 26
- [Sni15] C. Schnier, *Forward Endcap Services and Routing*,  
presentation, PANDA Mechanics Workshop (2015) 107
- [SotLAK] Schott AG, *N-LAK33B*,  
data sheet, [http://www.schott.com/advanced\\_optics/german/abbe\\_datasheets/schott-datasheet-n-lak33b.pdf](http://www.schott.com/advanced_optics/german/abbe_datasheets/schott-datasheet-n-lak33b.pdf) 26
- [SotZER] Schott AG, *ZERODUR® Extremely Low Expansion Glass Ceramic*,  
data sheet, [http://www.schott.com/advanced\\_optics/english/products/zerodur-extremely-low-expansion-glass-ceramic/index.html](http://www.schott.com/advanced_optics/english/products/zerodur-extremely-low-expansion-glass-ceramic/index.html) 101
- [Ste15] J. Stevens, *The GlueX DIRC project*,  
J. Instrum. **11** (2016) C07010 26
- [Sto15] T. Stöhlker et al., *APPA at FAIR: From fundamental to applied research*,  
Nucl. Instr. Meth. Phys. Res. **B 365** (2015) 680-685 5
- [Sug15] H. Sugisaki (Nikon Corporation), *Introduction of Nikon's Large Silica Glass Plate*,  
presentation, DIRC2015: Workshop on fast Cherenkov detectors (2015) 47
- [Suz15] K. Suzuki, *QBB Assembly for Module02-05*,  
presentation, TOP Session at 21st Belle II General Meeting (2015) 105
- [Swa16] C. Schwarz et al., *The PANDA Barrel DIRC*,  
J. Instrum. **11** (2016) C05013 1, 11, 25, 48, 123
- [Swi05] J. Schwiening et al., *Performance of the BaBar-DIRC*,  
Nucl. Instr. and Meth. **A 533** (2005) 317-322 25
- [TarTDR] The PANDA Collaboration, *Technical Design Report for the PANDA Internal Targets*,  
technical design report (2012) 7, 8
- [TrkTDR] The PANDA Collaboration, *Technical Design Report for the: PANDA Straw Tube Tracker*,  
technical design report (2012) 8, 9
- [TSE3032] Momentive Performance Materials Inc., *TSE3032*,  
data sheet, <http://www.momentive.com/> 96

- [Uhl15] F. Uhlig, *Charakterisierung und Anwendung von schnellen Photosensoren im Hinblick auf ihren Einsatz im PANDA-Experiment*,  
PhD thesis, Friedrich-Alexander-Universität Erlangen-Nürnberg (2015) 28, 123
- [Vav01] J. Va'vra, *Measurement of EPOTEK-301-2 Optical Glue Refraction Index and a Reflectivity from EPOTEK-301-2/Fused Silica Interface*,  
DIRC Note #140, internal group note (2001) 97
- [Wag16] M. Wagner, *Studies towards the Data Acquisition of the PANDA experiment & Measurement of a new Upper Limit of the Production Cross Section of  $p\bar{p} \rightarrow hc$* ,  
PhD thesis, Justus-Liebig-Universität Gießen (2016) 13
- [Wan14] B. Wang et al., *The assembly of the Belle II TOP counter*,  
Nucl. Instr. Meth. Phys. Res. **A 766** (2014) 204-207 110
- [Wan16] B. Wang, *Optics Quality Summary*,  
presentation, 23rd Belle II General Meeting (2016) 49
- [z88Aur] F. Rieg et al. *z88Aurora*<sup>®</sup>,  
homepage, <http://z88.de/> 105, 113



## Acknowledgements

This work would not have been possible without many people and I would like to dedicate the following lines to thank them for their support and assistance during the past few years. First of all I would like to thank Michael Düren for providing a liberal work environment but also for his guidance and for being a very collaborative conversational partner when I looked for advice. I would also like to thank the other people at Gießen for their support: Daniela Museaus for taking care of a lot of paperwork, Katja Wolf for software support, Thomas Wasem for his aid in terms of CAD, Rainer Weiss and his workshop colleagues for the on-time completion of mechanical components, Klaus Föhl for mentoring and proof-reading, Oliver Merle for his prior work and advice at the beginning, Mustafa Schmidt for his support regarding simulations, Avetik Hayrapetyan and Kristof Kreutzfeldt for the good times during lunch and breaks as well as their help when it was needed. A special thanks goes to Julian Rieke for adding a lot of fun to our daily grind.

I want to thank HGS-HIRe for the financial support as well as the graduate school program which was a pleasant and fruitful change to the daily work. HGS-HIRe also required regular committee meetings and I was lucky to have Jochen Schwiening, a real DIRC veteran with great experience, as an external expert who also established the contact with the people from Belle II. In this connection I would like to thank Toru Iijima, Kazuhito Suzuki and their colleagues for their time and hospitality during my visit to the KEK. I would also like to kindly thank Nikon Corporation for their collaboration and for providing the samples for evaluation.

Finally, I want to express my deepest gratitude to my family, especially to my parents Christina and Klaus for their continuous support and to my wife Anke for her encouragement, understanding and love throughout all these years. I am deeply grateful to have you in my life.



## **Erklärung**

Ich erkläre: Ich habe die vorgelegte Dissertation selbstständig und ohne unerlaubte fremde Hilfe und nur mit den Hilfen angefertigt, die ich in der Dissertation angegeben habe. Alle Textstellen, die wörtlich oder sinngemäß aus veröffentlichten Schriften entnommen sind, und alle Angaben, die auf mündlichen Auskünften beruhen, sind als solche kenntlich gemacht. Ich stimme einer evtl. Überprüfung meiner Dissertation durch eine Antiplagiat-Software zu. Bei den von mir durchgeführten und in der Dissertation erwähnten Untersuchungen habe ich die Grundsätze guter wissenschaftlicher Praxis, wie sie in der „Satzung der Justus-Liebig-Universität Gießen zur Sicherung guter wissenschaftlicher Praxis“ niedergelegt sind, eingehalten.

Erik Etzelmüller

Gießen, im Dezember 2016